The Influence of the Curing Process on the Response of Textile Composites

by

Christian Heinrich

A dissertation submitted in partial fulfillment
of the requirements for the degree of
Doctor of Philosophy
(Aerospace Engineering)
in The University of Michigan
2011

Doctoral Committee:
Professor Anthony M. Waas, Co-Chair
Professor Alan S. Wineman, Co-Chair
Professor John Kieffer
Assistant Professor Veera Sundararaghavan
Khaled W. Shahwan, Chairman-ACC Board of Directors, and Chrysler Group LLC

to my parents

Acknowledgments

I would like to thank my advisor Professor Anthony Waas for his guidance through the last four years. I want to especially mention is ability to always excite me about engineering problems. I want to thank my advisor Professor Alan Wineman. I appreciate his thorough approach to solid mechanics and careful derivations. He is also a great person to go to, to just discuss life's problems, away from engineering. I want to thank Professor John Kieffer and Michael Aldridge for their support during the ACC project and for providing me with experimental data that could not be found elsewhere. I also want to thank Assistant Professor Veera Sundararaghavan for his service on my committee.

Benjamin Jensen and Greg Odegard from Michigan Technological University deserve acknowledgement for providing me with experimental data for my nanoindentation work.

Many staff members of the aerospace department helped me during my time here, especially Denise Phelps , Suzanne Smith and Dave McLean. Brock Palen from the Center of Advanced Computing was extremely helpful, as well.

It was a pleasure to have many great lab mates, many of whom are also my friends: Pavana Prabhakar, Scott Stapleton, Amit Salvi, Mark Pankow, Paul Davidson, Siva Shankar Rudraraju, Brian Justusson, Evan Pineda, Wooseok Ji, Eugene Kheng, Dianyun Zhang, Pascal Meyer, Zach Kier, Lucas Hansen, Peter Gustafson, Chris Attard, Wei Ng,

I am very happy that I got the chance to be friends with some very special people: my incoming class mates Devesh Kumar and Charles Barbour, my SHPE community service co-chair Brittany Smith and my favorite roommates Daniel Zaide and Brain Garcia. I am also thankful for the friendship of Gayathri Seenumani, Abhilasha Anna, Kalyan Nadella, Abhijit Gogulapati, Nicolas Lamorte, Tim Deschenes and Yeon Baik.

Finally, I wouldn't be here without the love and support of my parents, Karin & Karl-heinz. They had always infinite faith in my abilities and they always supported me in pursuing any interest I might have.

Part of this research was supported by the Automotive Composites Consortium (ACC)

under a United States Automotive Materials Partnership (USAMP) Cooperative Agreement No. DE-FC05-95OR22363 with the U.S. Department of Energy (US-DoE). The author is grateful for the support and monitoring of Dr. Khaled Shahwan of Chrysler Group LLC, and Chairman of the Predictive Technology Development and Composites Crash Energy Management Group (ACC100) of the ACC. The author acknowledges that this research was funded, in whole or in part, by the US-DoE, and such support does not constitute an endorsement by the US-DoE of the views expressed herein.

Table of Contents

List of Tables

Table

List of Figures

Figure

List of Appendices

Appendix

List of Symbols

$\underline{b}$	Body force
c, c_p	Specific heat
c_{pf}, c_{pm}	Specific heat of fiber and matrix
e	Internal energy per unit mass
$k_1, k_2(T)$	Function describing phenomenological cure of epoxy
l	Length
ℓ	Length scale parameter
l^e	Element length
m, n	Parameters parameter describing cure of epoxy
p	Pressure
p_0	Reference pressure
q_i	ith component of the heat flux vector
r	Rate of heat supply
r	Location in radial coordinates
s	Time history, $0 \leq s \leq t$
t	(Current) time
$\underline{t}$	Traction
t_0	Gelation time
$\underline{u}$	Displacement vector
v_f, v_m	Fiber and matrix volume fraction

$\underline{w}$	Displacement due to phase change
x_i, $\underline{x}$	Position vector
α	Linear coefficient of thermal expansion
α_{liq}	Linear coefficient of thermal expansion of liquid epoxy resin
β	Parameter to describe global shape of shear and plane wave modulus
ε_{ij}, $\underline{\underline{\varepsilon}}$	Strain tensor
ε_c	Cure shrinkage strain component
$\underline{\underline{\varepsilon}}_c$	Cure shrinkage strain tensor
ε^{mech}	Mechanical strain
ε_f	Damage onset strain
ε_u	Ultimate strain
η	Local field related to invariant of strain
$\overline{\eta}$	Nonlocal field
$\underline{\overline{\eta}}$	"Displacement" of nonlocal field at nodes
η_{vM}	Scalar related to deviatoric part of strain tensor
λ	Lamé constant
μ	Shear modulus
$\phi(t)$	Degree of cure up to time t
ρ	Density
ρ_f, ρ_m	Fiber and matrix density
σ_{ij}, $\underline{\underline{\sigma}}$	Stress tensor
$\underline{\sigma}$	Vector representation of stress tensor
$\overline{\sigma}$	Degree of randomness
$\underline{\underline{\sigma}}_{eff}$	Effective stress tensor
$\sigma_{\max}$	Maximum principle strain
σ_{vM}	Von Mises stress

σ_{tot}	Total stress in all networks
A	Cross sectional area
A_1, A_2	Frequency-like parameter describing cure of epoxy
A_d	Damaged cross sectional area
A_{eff}	Effective area
$\underline{\underline{B}}$	Left Cauchy-Green tensor
B_u	Derivative of displacement shape functions
$B_{\overline{\eta}}$	Derivative of shape functions of nonlocal field
$\underline{\underline{\underline{\underline{C}}}}$	Stiffness tensor
$\underline{\underline{\underline{\underline{C}}}}_{eff}$	Effective stiffness tensor
D	Damage
E	Elastic modulus
E_{ij}	Macroscopic strain
$\underline{F}$	Force vector
$\underline{F}_u$	Residual vector associated with nodal displacement degrees of freedom
$\underline{F}_{\overline{\eta}}$	Residual associated with nodal nonlocal field values
$H(t)$	Heat generated till time t
H_r	Total heat of reaction
$\underline{\underline{I}}$	Second order unit tensor
K	Thermal conductivity
K	Bulk modulus
K	Stiffness matrix
K_{liq}	Bulk modulus of liquid epoxy resin
L	Length
L	Linear operator representation of divergence
M	Plane wave modulus

$\underline{N_u}$	Shape functions of displacement
$\underline{N_{\overline{\eta}}}$	Shape functions of nonlocal field
R	Gas constant, 8.314 J/K/mol
R_0	Outer radius
T	Temperature
$\underline{T}$	Traction vector
T_{BC}	Temperature applied at boundary
$\underline{T}_{eff}$	Effective traction
T_i	Initial temperature
$\underline{U}$	Nodal displacements
V	Volume
$\underline{X}_{NAT}$	Undeformed natural configuration position vector
$\underline{X}_{SYS}$	System configuration position vector
ΔE_1, ΔE_2	Activation energy
ΔV	Activation volume
Σ_{ij}	Macroscopic stress tensor

List of Acronyms

2DTBC 2 dimensional triaxially braided composite

CCM Concentric cylinder model

CDM Continuous damage mechanics

CTE Coefficient of thermal expansion

DCZM Discrete cohesive zone model

DSC Differential scanning calorimetry

EMD Equilibrium molecular dynamics

FE Finite element

FEM Finite element method

HETVAL User defined heat generation in ABAQUS Standard

NEMD Non-equilibrium thermodynamics

PDE Partial differential equation

RTM Resin transfer molding

RUC Representative unit cell

RUV Representative unit volume

UMAT User defined material model in ABAQUS Standard

VARTM Vacuum assisted resin transfer molding

VUEL User Defined Element in ABAQUS Explicit

VUSDFLD User Defined Field in ABAQUS Explicit

Abstract

Textile composites are a promising engineering material that offer high specific strength and improved fracture toughness. To make full use of its potential, to allow for rapid development of new products made of textile composites and to allow for virtual testing using numerical simulations, a thorough understanding of material state at all times and the material response to external load is necessary.

In previous numerical and experimental studies it has been observed that the use of "virgin" matrix properties leads to predictions of composite behavior that is not in accord with experimental observations. It was concluded that presence of fibers during the curing process of the epoxy alters the matrix material properties, the latter being termed "in-situ" matrix properties.

The current study investigates these effects further. Different physical effects are taken into consideration for a detailed model of the problem. First, the evolution of temperature and degree of cure is investigated through the heat conduction equation and an empirical curing law. Both effects depend strongly on each other and need to be solved for concurrently. The combined model is used to investigate the influence of curing parameters, geometry and thermal conductivity on the curing time and maximum temperature in the epoxy.

In a next step, a novel curing model for epoxy, to describe the phase transition of liquid epoxy resin and hardener mixture to a solid epoxy, has been developed. The model treats the curing of epoxy as a continuous creation of non-interacting networks that occupy the same volume, but which have different material properties. The model accounts for an evolution of elastic properties as cure progresses and predicts resulting cure stresses. It allows for gradients in temperature and varying curing histories and degrees of cure throughout the composite as determined by the thermo-chemical model. It has been shown that considerable stresses develop during the curing process in the epoxy inside the composite. The stresses in unidirectional and woven composites are investigated.

To account for non-linear material behavior during cure and after full cure upon applying external load, the model has been augmented by a continuum damage mechanics formulation. To allow for mesh objective results and to prevent strain localization, a nonlocal formulation

has been chosen. Here the damage not only depends on the state of the material at a point, but it also depends on the state of the material in a finite volume around it. The combined curing and damage model has been applied to a woven composite unit cell and it is shown that cure at elevated temperatures and large chemical shrinkage can cause damage and degradation of the epoxy material inside the composite prior to the application of external load. As a result, the onset of nonlinear effects occur at lower applied mechanical loads and the ultimate strength of the composite is significantly reduced.

Previous studies, [3], relied on the proper determination of "in-situ" material properties to simulate the response of textile composites. Whenever the fiber architecture, fiber volume fraction, curing cycle or resin system changes, new experiments and inverse modeling procedures need to be performed to characterize the "in-situ" properties. The current study aims to eliminate the need for additional experiments to predict the effective composite properties by modeling the curing process through "first principles". The matrix and fiber materials are characterized individually, and effects that lead to an apparent degradation of material properties such as residual stress creation and damage evolution are explicitly accounted for. As a result, if the epoxy material exhibits large shrinkage due to chemical or thermal effects, large stresses and damage develop during cure and the effective ultimate stress that can be applied to the composite part is reduced. It is shown that in a plain weave carbon fiber composite with 6% cure shrinkage in the epoxy and a 30°C temperature change between cure and service temperature, the ultimate tensile load is reduced by over 30% compared to the case where such effects are not included.

Chapter 1
Introduction

The increasing demand for more lightweight structures in aerospace, automotive and other applications drives the need for more sophisticated engineering materials. Composites are such a class of materials that has regained interest in recent decades, albeit it has been used as an engineering material for centuries [4]. By definition, a composite is a combination of two or more distinct materials. By combining them in a specific manner, the overall material properties are enhanced as desired. In the following study, fiber-polymer-matrix composites will be examined as a specific class of composites. Here a strong fiber material, typically glass or carbon, is used to carry maximum stress along its axial direction. The fiber is surrounded by a matrix material, such as polymer epoxy, which provides stiffness in shear and compression, and holds the fibers together. Such fiber composites can be divided into three broad categories depending on their fiber architecture: prep-reg, stitched fabric and 2D and 3D woven composites.

In pre-preg materials, the fibers are all aligned in one direction and the matrix material is already applied to the fabric before it is placed in a mold. Typically, layers of pre-preg lamina are stacked at different angles to create a laminate. Such laminates require an oven to cure, where the viscous liquid like matrix material solidifies. Parts manufactured from laminates offer high specific strength due to the stiffness of the fibers and they are used in aerospace applications. However they are very expensive to produce. They also exhibit poor interlaminar behavior.

Stitched fabrics on the other hand are significantly cheaper compared to pre-preg material. They are comprised of unidirectional layers of dry fibers that have not been wetted by matrix material yet. The layers are stitched together by non-load bearing yarn, to improve handling. During the manufacturing of a composite part from stitched fabrics, the dry fabric is placed in the mold and than the liquid resin is inserted into the mold afterwards using resin transfer molding (RTM) process. The wetting of the fibers may be aided with the help of vacuum. The corresponding process is called Vacuum Assisted Resin Transfer Molding (VARTM). Here, a vacuum is created inside the mold. Liquid epoxy resin is ejected through

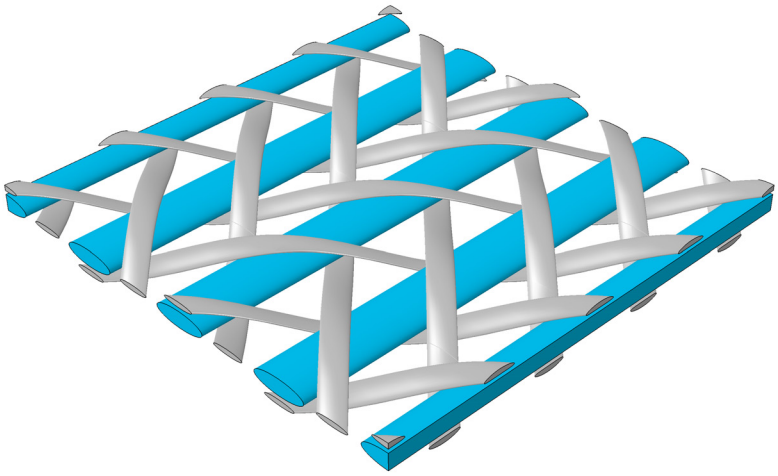

Figure 1.1 Tow architecture of dry 2DTBC fabric, bias tows are shown in grey and axial tows are in blue

one or several ports on one side of the mold and pulled to other ports that are used to create the vacuum. RTM and VARTM can be performed at room temperature, thus eliminating the need for an oven and allowing to manufacture large parts such as wind turbine blades.

In 2D and 3D woven composites, the fibers are combined as fiber tows consisting of thousands of individual fibers. These fiber tows are woven or braided using many different weaving patterns, e.g. in plain weave fiber tows are perpendicular to each other and every fiber tow is braided over and under perpendicular fiber tows in an alternating fashion. Another braiding pattern of interest is 2 dimensional, triaxially braided composite (2DTBC) [3, 5–8]. Here bias tows are braided at an angle over and under an axial tow, as shown in figure 1.1. What makes woven composites an interesting material for engineering applications is their increased fracture toughness compared to pre-preg and stitched composites due to the lack of a clear path for a crack to progress. Due to their complicated geometry, cracks progressing along a fiber direction can be arrested at intersections of fiber tows. Thus, woven fiber composites are of great interest in the design of vehicles, as they can help to dissipate energy during a crash.

1.1 Manufacturing dependent properties

Like stitched fabric, woven composite parts can be manufactured through a RTM or VARTM process at room temperature. Parts can be produced cost-effectively and in high volumes, which are needed for certain industries such as automotive industry or for wind turbine

blades. There are various parameters in the curing process that might be changed in order to reduce process time, such as using different curing agents, different pressure applied to the mold or different temperature cycles applied to the mold. For example, when curing a large wind turbine blade, it is desirable to keep the liquid epoxy resin at a low temperature during the infusion process to keep viscosity low, which will keep the infusion time short, and also for achieving flow for longer bigger parts. Once the entire fabric is wetted, the temperature of the mold is increased, to accelerate the curing. It is expected that the material properties of the final part will depend on all the parameters of the manufacturing process. In previous studies, [3], the material properties have been treated to be independent of the curing process. However, when epoxy is cured in the presence of fibers, the observed effective epoxy properties are different compared to the bulk properties. Parameters that can have an impact on the change of observed epoxy matrix properties include the fiber architecture, the temperature profile during cure, fiber volume fraction, the shrinking of the resin during cure and the thermal mismatch between the fiber and the matrix material. It is important to understand the role of these parameters in order to successfully predict the post cure response of textile composites subjected to applied external mechanical load.

1.2 Previous work

1.2.1 Mechanical properties of textile composites

The mechanical properties of textile composites have been extensively studied in the past and a summary can be found in the work by Song, [3]. Early investigations were aimed mostly at predicting elastic properties of plain weave composites, [9–13]. The inelastic response of plain weave composites was considered by Karkkainen and Sankar, [14]. They constructed the failure envelope of a plain weave woven unit cell and noted a close relation to the Tsai-Wu failure criterion [15]. Whitecomb and Srirengan, [16], investigated progressive damage of plain weave composite. They used a static finite element simulation to determine the locations of largest stress and failure onset. At these points the material properties were modified and a new equilibrium state was calculated. This process was repeated until no further damage occurred and the global strain was increased till the next onset of damage.

Recently, the elastic properties and failure response of 2D triaxial braided composites (2DTBC) received a considerable attention. Quek et al., [17], developed an analytical model to predict the stiffness of 2DTBC. Each tow is first modeled as a transversely isotropic material, where the effective elastic material properties were determined using the concentric

cylinder model (CCM). Then the undulating tows were idealized as sinusoidal waves. To calculate compression response a finite element analysis of a representative unit cell was performed, [18]. The fiber material was treated as an elastic material and the epoxy matrix was modeled using elastic-plastic stress-strain relations and incremental J_2-flow theory of plasticity. Song and co-workers investigated the compressive response of 2DTBC experimentally and through finite element simulations, [3,5–8]. The finite element model used was of an idealized representative unit cell (RUC) consisting of fiber tow and matrix. The fibers were treated as elastic and the matrix material was treated as plastic or plastic-damaging. The resulting nonlinear fiber tow behavior was modeled using Hill's anisotropic plasticity, [19].

1.2.2 Cure of epoxy resin and composites

Manufacturing induced effects have usually been studied in the context of cure induced stresses and potential failure during cure. Rabearison et al. [20] give an example of how gradients in cure develop in a thick carbon epoxy tube and subsequently cause defects such as cracks. Rabearison et al. than developed a numerical model for curing of an epoxy. They calculate the curing of the epoxy in a glass beaker and conclude that stresses large enough to cause cracks are developed during the curing process. In a similar fashion Corden et al. [21] have developed a curing model to predict the residual stresses in thick resin transfer molded laminated cylinders. They identified chemical shrinkage due to cure as a major contributing mechanism for stress build up as they cured all parts at room temperature. During the experimental validation of the results with different laminate layouts it was noted that interlaminar cracking can occur due to differential shrinkage. Plepys and Ferris, [22], noted the creation of cracks during isothermal cure of three-dimensionally constrained epoxy resin in a glass cylinder. Chekanov et al., [23], have identified different defect types that may occur during the constrained cure of epoxy resins. At high temperature, cohesive defects intersecting the resin were observed, at medium temperatures uneven voids were found and at low temperatures zigzag defects and cohesive smaller defects were seen.

Besides stress generation and possible cracking during cure, geometric tolerances are another important issue that needs to be considered. For example a thick composite may be cured on a metal tool with two perpendicular side faces to give an L-shaped composite part. Upon removal of the part from the mold, a "spring-in" can be observed. Here the two sides of the L-shaped part bend inwards giving a smaller angle then the anticipated 90°, [24–27]. Equivalently when a composite part is cured on a flat tool, bending or warpage can be observed due to thermal gradients and residual stresses build up during cure, [28–30]. The dimensional accuracy and stress generation in woven composites has been studied in

the context of woven circuit boards [31].

Proper knowledge of curing induced distortion can be used to design a mold that will compensate for such effects. Capehart et al., [32], have investigated such an optimized mold design for open mold composites. Due to asymmetric stacking of coating and composite layer and large cure shrinkage of the coating layer, large warpage can be observed. Only small temperature gradients in the described manufacturing process are observed. Therefore only cure shrinkage was considered. Viscoelastic effects were neglected by allowing for sufficient time to relax after removing the manufactured part from the mold. A finite element procedure with shell elements was used to simulate the out-of-mold deformations. The cure shrinkage was incorporated using pseudo-temperature. In a next step an algorithm was implemented that simulates distortion due to cure and adjusts the mold accordingly. Experimental comparison between the standard mold and the optimized mold show a reduction of 45% of undesired distortions. A limitation of the procedure lies in the treatment of residual stresses as a semi-empirical parameter which have to be determined by fitting observed deformation. Also the evolution of the elastic properties and cure shrinkage was neglected by considering long term equilibrium values.

Studies that investigate the curing process of composites are commonly broken down into two parts: chemical reaction, heat generation and heat conduction, and, the evolution of stress and development of structural integrity. In order to understand and optimize the manufacturing process both issues must be understood well. The temperature field is usually modeled using the standard heat equation and Fourier's law. The cure kinetics are usually modeled using a phenomenological model proposed by Kamal, [33]. The evolution of stress on the other hand is modeled through a variety of approaches. Plepys and Farris, [22], and Plepys et al., [34], used incremental elasticity to describe the evolution of stresses and elastic properties as a function of cure. They assume that during each time increment, the stress increment is related to the strain increment as a linear isotropic elastic relation with a changing modulus as a function of cure. Bogetti and Gillespie, [35], used a linear mixing rule based on degree of cure, elastic modulus of uncured and fully cured resin moduli and a parameter to quantify stress relaxation and chemical hardening. Another material model often used involves linear viscoelasticity [36–39]. Here the evolution of the cure dependent and therefore time dependent material properties was modeled with the aid of integral constitutive equations found in linear viscoelasticity. A more sophisticated model has been proposed by Adolf and Chambers, [40] using non-linear viscoelasticity. However, such a model with its large amount of parameters also requires extensive validation and experimental investigation, [41].

The approach that will be further in this work has been developed by Mei et al. [42] and

Mei [43]. He investigated solidification of epoxies using a novel network forming model where networks are continuously created in a new reference configuration as cure progresses and each network had different visco-elastic material properties.

With the different curing and stress generation models presented, various studies have been performed to optimize aspects of the curing cycle. Li et al., [44], solved a coupled thermal and chemical problem to investigate an optimal curing cycle for thermoset matrix composites that was optimized for low curing time, but limiting the maximum temperature found in the epoxy. White and Hahn, [30], optimized the curing process to reduce the residual stress in a composite part using a three-step curing cycle. Gopal et al., [45], also aimed for a reduction in residual stress, but they only used a two step curing cycle. Finally, Zhu and Geubelle, [46], investigated the sensitivities of the curing process parameters on the dimensional accuracy of L-shaped composite parts.

1.3 Motivation and current research objectives

In recent studies that investigated the elastic properties and failure of woven composites, it has been noted that stresses and possibly cracks due to cure are present in the composite part prior to applying external service loads [47]. These stresses may reduce the margin of load that can be applied to the part, before the onset of inelastic response and failure. To capture the correct stress state of the resin inside the fully relaxed (no external load applied) composite, attempts are made to measure the "in-situ" matrix properties, [7, 48]. Here the material is treated to be stress free after cure and prior to loading, but effective material properties are reduced. The "in-situ" properties are extracted using an inverse modeling approach. The idealized complex geometry of the woven composite is created in a finite element (FE) model. Then the material properties of the matrix material in the computer model are changed until the simulation results agree with the experimental findings. Such an approach is suitable to investigate the response of a specific woven composite once the effective "in-situ" material properties have been determined experimentally. However, the experimental procedure has to be repeated every time properties of the woven composite and parameters of the curing process are changed. Just to name a few, the change of fiber architecture, fiber stacking, fiber material, matrix material, curing agent, curing pressure and curing cycle can lead to different stress patterns and possible damage due to cure in the manufactured composite part. Therefore, the inverse modeling approach and experimental procedure needs to be repeated to extract the new "in-situ" properties.

The goal of the current study is to circumvent the need to repeat the extraction of "in-situ"

material properties every time a material property or curing process parameter is changed. Instead a model of the curing of epoxy is needed that is derived from "first principles". The only composite properties used in the numerical model is the geometry. Material properties of fiber and matrix material including the evolution of material properties of the epoxy during cure are found from the constituents individually. As in previous studies that investigated the cure of epoxy resins it is necessary to include various physical concepts to properly determine the importance of the various curing parameters. The curing of epoxy is a highly exothermic reaction [49–51] that can lead to appreciable temperature gradients in thick composites. The chemical evolution is tightly linked to the temperature and finally the evolution of stresses and material properties of the bulk composite depends on both the temperature history and curing history of the resin.

It has been shown previously that the "in-situ" elastic properties are not significantly altered by the curing process. The predicted failure on the other hand is significantly different when FE simulations are based on bulk vs. "in-situ" properties. It is therefore necessary to include a suitable failure model. The computational models employed in the past can roughly be divided into two categories. On the one hand macroscopic cracks and failure have been captured through the use of discrete cohesive zone models (DCZM), [52, 53]. These models usually require a priori knowledge of the crack location to make mesh preparation and computation efficient. The other major model to capture failure is the continuum damage model (CDM), [2, 54]. In CDM micro cracks and voids are not explicitly modeled. Instead damage due to microstructural changes are accounted for in an average sense by degrading material properties. CDM models do not predict the formation of macroscopic cracks. On the other hand, when modeling failure with CDM, the location where damage will occur does not need to be known. Therefore, this approach was pursued in this study to model failure of epoxy during and after cure.

1.4 Thesis Outline

The current study is organized as follows. Chapter 2 investigates the thermo-chemical problem of epoxy cure. The governing equations of thermal conductivity and cure kinetics are solved using finite conductivity and assuming a perfectly conducting material and perfectly insulating material as extreme cases. The cure-kinetic parameters for EPON 862 with EPIKURE 9553 are introduced and that material system is compared to others that can be found in the literature. A parametric study is performed to investigate the influence of boundary temperature, geometry, thermal conductivity and cure kinetics parameters on the

curing time and maximum temperature developed in the epoxy.

Chapter 3 presents a model to predict the stresses generated during cure. The idea of the continuous formation of networks as a modeling tool is introduced. The derivation of the model is presented in two different ways. First, a simple 1D small strain spring model is sufficiently generalized to yield the governing equations of a 3D curing material. Secondly, a general large deformation model is sufficiently specialized to give the same governing equations of a curing epoxy. A method is presented to extract the necessary material properties from Brillouin and Raman Light Scattering Experiments (BLS and RLS). Also the equations necessary to implement the governing equations into the commercial finite element code ABAQUS, [55], are shown.

Chapter 4 uses the 3D curing model to numerically investigate the influence of geometry, temperature history and boundary conditions on the post cure stress state. The cure of a pure epoxy sample, of a cylinder with a single fiber and matrix and cure of a composite with many hexagonally packed fibers are shown. The influence of randomness in fiber packing is discussed, which is important to estimate the amount of representative fibers necessary to model a fiber tow. Finally, the cure and stress creation in a plain weave composite is calculated.

In Chapter 5 the network forming model is extended to allow for inelastic response and damage of the curing epoxy and when applying external mechanical load. Continuum damage mechanics is identified as the material model of choice to allow for failure of the epoxy because the location where damage might occur does not need be known when the finite element model is created. However, it is shown that the use of CDM in classical FE codes can lead to a strongly mesh dependent solution and vanishing energy associated with the formation of cracks. As a remedy to that problem, a nonlocal formulation is introduced. Here the evolution of damage is not a point wise function, but instead coupled to the strain state within a finite volume centered about the point of interest. Finally the steps necessary to implement the governing equations into a ABAQUS user element (UEL) are discussed.

Chapter 6 shows the application of the cure and nonlocal damage model. First the nonlocal damage parameters are derived though a double cantilever beam (DCB) simulation. Then the cure and subsequent response of a plain weave representative unit cell (RUC) is calculated. The influence of stresses generated due to cure shrinkage and thermal mismatch is quantified. It is shown that damage can form already during the curing of the composite which leads to a reduction in load bearing capability when subjected to mechanical load subsequently.

Finally, chapter 7 summarizes the major results and provides directions for further research.

In an effort to extract the material properties of the cure composite nanoindentation experiments have been performed. The results of these experiments are presented in appendix A.

1.5 Unique Contributions in this Dissertation

An itemized list of original contribution presented in this thesis is given below.

1: Phenomenological cure kinetics equation of EPON 862 with EPIKURE 9553 and subsequent investigation of the influence of cure parameters, boundary temperature and thermal conductivity on the evolution of temperature and extend of cure.

2: The use of the notion of a perfect conductor and perfect insulator to give upper and lower bounds regarding the curing time and maximum temperature that can be anticipated.

3: A novel network forming model, that can predict the evolution of stresses as a function of cure and which takes into account the evolution of material properties as a function of cure has been developed. Cure dependent elastic properties have been found from BLS and RLS data.

4: An exploratory study of network forming model to determine the stress state and dimensional accuracy in a composite as a function of geometry, fiber number and arrangement, thermal and mechanical boundary conditions has been presented.

5: Extension the of network forming model with nonlocal damage formulation to account for degradation of material properties during cure has been developed.

6: Numerical investigation of damage during cure and after applying external load to a plain weave representative unit cell has been completed.

7: Nanoindentation experiments to find the visco-elastic plastic material properties of epoxy inside a woven composite fiber tow have been presented.

Chapter 2

The curing process - chemical and thermal effects

2.1 Introduction

This chapter is concerned with modeling the chemical and thermal processes that take place during cure of a polymer matrix. The aim is to compare previously available models for coupled heat transfer and cure, and how the model predictions are influenced by temperature, geometry, heat conduction and the values of their parameters. By obtaining and understanding of how these parameters influence the curing process, in the next chapter they can be incorporated into a model that couples these thermo-kinetic processes to internal stress generation.

The current study investigates Epon862 with curing agent Epikure9553. This epoxy system will be compared to some of the many studies that have been performed on the curing kinetics of various other epoxy and hardener systems: Shanku et al. [50] and O'Brian and White [51] investigated EPON 862 and curing agent W, Ramakrishnan et al. [49] were concerned with EPON 815/EPICURE 3274, and Adolf and Chambers [37] with EPON 828/DEP and EPON 828/Z.

2.2 Heat Conduction and Curing

The curing of an epoxy is a highly exothermic chemical reaction (see for example all before mentioned studies regarding DSC of epoxy, [49–51]). The degree of cure is often measured by placing a small sample in a digital scanning calorimeter, maintaining the sample at a constant temperature and measuring the heat that is generated during cure. Denote the heat generated by $H(t)$ and the degree of cure by $\phi(t)$, both at time t. The degree of cure is often

defined [33] by

$$\phi(t) = \frac{H(t)}{H_r}, \tag{2.1}$$

where H_r is the total heat that is generated. Thus, $\phi(t)$ monotonically increases from $\phi = 0$, at the uncured state, to $\phi = 1$, at the fully cured state. Note that the rate of heat generation per unit mass is

$$r = \frac{\mathrm{d}(H_r\phi)}{\mathrm{d}t}. \tag{2.2}$$

The process is modeled by a curing kinetics equation of the form

$$\frac{\mathrm{d}\phi}{\mathrm{d}t} = f(T,\phi), \tag{2.3}$$

where T is the temperature and $f(T,\phi) \geq 0$. Kamal [33] has suggested that $f(T,\phi)$ be given by,

$$f(T,\phi) = \left(k_1(T) + k_2(T)\phi^m\right)(1-\phi)^n, \tag{2.4}$$

$$k_1(T) = A_1 \exp\left(-\frac{\Delta E_1}{TR}\right), \tag{2.5}$$

$$k_2(T) = A_2 \exp\left(-\frac{\Delta E_2}{TR}\right), \tag{2.6}$$

in which m and n are constants, R is the gas constant, A_1, A_2 are frequency like constants and ΔE_1, ΔE_2 are activation energies. Choices for m, n, $k_1(T)$ and $k_2(T)$ for various epoxy-curing agent systems have appeared in the literature. These will be presented in Section 2.5. In applications, equation (2.3) is used to describe the curing process even when the temperature varies with time [51].

In a curing structural composite, there is both local heat generation due to curing and heat conduction due to the presence of an external surface or along fibers. This process is governed by the *local* form of the first law of thermodynamics, [56, 57],

$$\rho\frac{\mathrm{d}e}{\mathrm{d}t} = -\frac{\partial q_i}{\partial x_i} + \rho r + \sigma_{ij}\frac{\mathrm{d}}{\mathrm{d}t}\varepsilon_{ij} \tag{2.7}$$

where e is the internal energy per unit mass, ρ is the current mass density, q_i are the components of the heat flux vector, r is the rate of heat supply per unit mass, σ_{ij} are the stress components and ε_{ij} are the components of the infinitesimal strain tensor.

For the applications considered here, the rate of mechanical work, $\sigma_{ij}\mathrm{d}\varepsilon_{ij}/\mathrm{d}t$, is as-

sumed to be negligible and the internal energy is assumed to be proportional to temperature, $e = cT$. The heat flux vector is related to the temperature gradient by the Fourier law of heat conduction,

$$q_i = -K\frac{\partial T}{\partial x_i}, \tag{2.8}$$

where K is the thermal conductivity. It is possible that the thermal conductivity depends on the degree of cure and the temperature, i.e. $K = K(T,\phi)$. Equation (2.7), with (2.2), (2.8) and these assumptions, becomes

$$\rho c\frac{\partial T}{\partial t} = \frac{\partial}{\partial x_i}\left(K(\phi,T)\frac{\partial T}{\partial x_i}\right) + \rho H_r\frac{\partial \phi}{\partial t}. \tag{2.9}$$

Equations and (2.3),(2.4) and (2.9) form a system of coupled nonlinear partial differential equations for the spatial distribution and time variation of temperature, $T(\underline{x},t)$, and degree of cure, $\phi(\underline{x},t)$.

2.3 Special Cases

It is useful to have analytical solutions to the system of equations (2.3) and (2.9). This is shown to be possible in the two limiting cases of a perfect conductor and a perfect insulator.

2.3.1 Perfect Conductor $K \to \infty$

In this case, (2.8) implies that $\partial T/\partial x_i = 0$ and the temperature field in the epoxy is homogeneous. Heat generated by curing is instantaneously conducted. If the body was in an infinite bath of temperature T_0, then the temperature in the body would be $T(t) = T_0$ at all times, t. Let the temperature be fixed. Then the degree of cure is determined by solving (2.3). When $f(T,\phi)$ is given by (2.4),

$$\frac{\mathrm{d}\phi}{dt} = (k_1(T) + k_2(T)\phi^m)(1-\phi)^n. \tag{2.10}$$

It is convenient to determine the inverse relation $t = t(\phi)$, which is possible since $f(T,\phi) > 0$. This is obtained from (2.10),

$$t = \int_0^{\phi(t)} \frac{d\bar{\phi}}{\left(k_1(T) + k_2(T)\bar{\phi}^m\right)(1-\bar{\phi})^n}, \tag{2.11}$$

where use was made of the initial condition $\phi = 0$ at $t = 0$. Equation (2.11) holds also if T varies with time. In general, the integral in (2.11) cannot be evaluated analytically for general values of m, n, $k_1(T)$ and $k_2(T)$ such as have been experimentally determined, and a numerical method must be used. However, an analytical solution can be obtained in the special case when $m = n = 1$ and T is constant in time,

$$t = \frac{1}{k_1 + k_2} \ln \left(\frac{k_2 \phi(t) + k_1}{k_1 (1 - \phi(t))} \right). \tag{2.12}$$

This can be inverted to give

$$\phi(t) = \frac{k_1 [\exp(\{k_1 + k_2\} t) - 1]}{k_2 + k_1 \exp(\{k_1 + k_2\} t)}, \tag{2.13}$$

where the arguments of k_1 and k_2 have been suppressed. Note that $k_1 > 0$ and $k_2 > 0$ and as $t \to \infty$, $\phi \to 1$. The rise time depends on k_1 and k_2.

2.3.2 Perfect insulator $K \to 0$

In this case, there is no heat conduction. Heat generated by curing does not conduct away. The temperature field is uniform and its time dependence is determined from (2.9), which reduces to

$$\rho c \frac{\partial T}{\partial t} = \rho H_r \frac{\partial \phi}{\partial t}. \tag{2.14}$$

If curing begins at a uniform temperature $T = T_0$, then

$$T(t) = \frac{H_r}{c} \phi(t) + T_0. \tag{2.15}$$

Thus, in a poor heat conductor such as an epoxy, the change in temperature is proportional to the change in degree of cure. The overall change in temperature is equivalent to the heat that can be produced during the curing process, divided by the specific heat of the material. It is useful to provide a numerical example using (2.15). The total heat during curing is about $227\, kJ/(kg \cdot K)$ (see table 2.2). For Epon 862, $c = 1.2 \quad kJ/(kg \cdot K)$. The temperature rise when fully cured ($\phi = 1$) is then $T(t) - T_0 = \frac{H_r}{c} = 189K$.

As in the case of the perfect conductor, it is convenient to first determine the inverse relation $t = t(\phi)$. This is given by (2.11) with T determined using (2.15),

$$t = \int_0^{\phi(t)} \frac{\mathrm{d}\bar{\phi}}{\left(k_1 \left(\frac{H_r}{c} \bar{\phi} + T_0\right) + k_2 \left(\frac{H_r}{c} \bar{\phi} + T_0\right) \bar{\phi}^m\right) (1 - \bar{\phi})^n}. \tag{2.16}$$

The integral can be numerically evaluated and a plot of ϕ vs. t can be constructed.

2.4 Curing of Epon 862/Epikure 9553

Experimental data has been obtained for the degree of cure as a function of time for Epon862 and Epikure 9553, [58], using Raman light scattering (RLS), [59, 60]. The measurements were taken through isothermal cure cycles at 295K ($22°C$), 303K ($30°C$), 313K ($40°C$) and 323K ($50°C$). The experimental data was scaled such that upon saturation of the curing reaction the final curing value approached 1. Compared to the raw experimental data, the values presented in figures 2.1 and 2.2 have been multiplied by about 1.2. This is necessary because the data was obtained using Raman light scattering which is based on tracking intensities of atomic bond vibrations. On the other hand the typical definition of cure, that is also used in this study is based on the emission of heat during an exothermal reaction as measured with DSC. Another way to account for the fact that only a partially cured state is measured using RLS is by introducing a saturation cure level $\phi_{\max}$, [61], such that,

$$\frac{\mathrm{d}\phi}{\mathrm{d}t} = k_2(T)\phi^m(\phi_{\max} - \phi)^n \tag{2.17}$$

The experimental data was curve fitted using a non-linear least squares approach. Two different models were considered. In one case all parameters in (2.4) were free to vary. In the other case only A_1 and ΔE_1 were free to vary. The other parameters were set to $n = 1$, and $A_2 = \Delta E_2 = m = 0$. The result of only two variables being free is shown in figure 2.1. For simplicity, in future discussions the model using only the two fitting constants ΔE_1 and A_1 will be used. The experimental data indicates that curing temperature and time to full cure are related in a very non-linear fashion. The curing time varies from 40,000 seconds (about 11 hours) at 22°C and 12,000 seconds (3.3 hours) at 30°C to 3,600 seconds (1 hour) at 40°C and only about 1,800 seconds (1/2 hour) at 50°C. Figure 2.2 shows a fit of the experimental data where A_2, ΔE_2, m and n are parameters of the model.

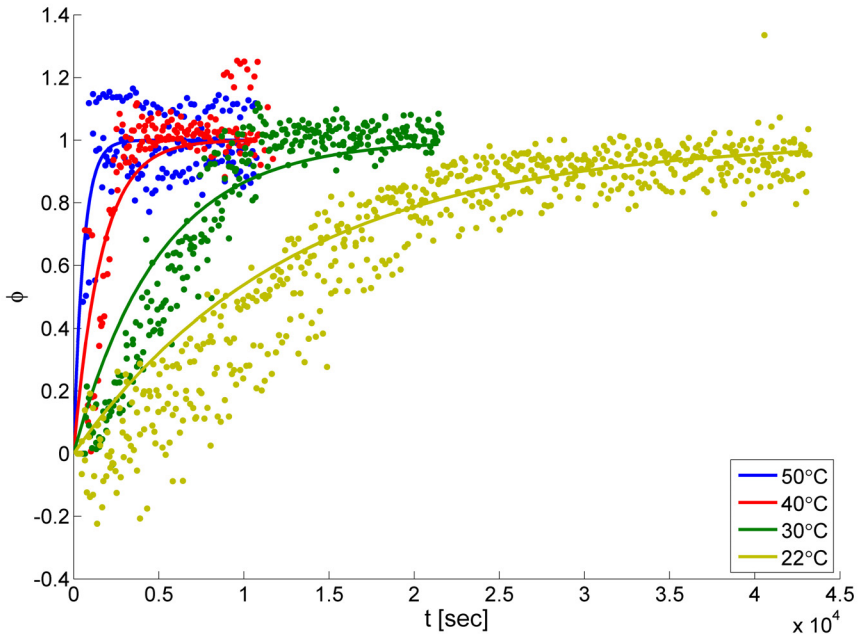

Figure 2.1 Experimental data and curve fit for isothermal cure. A_1 and ΔE_1 are parameters to the curing model. $A_1 = 3.62 \cdot 10^{11}$ sec^{-1}, $\Delta E_1 = 8.854 \cdot 10^4$ J, $n = 1$, $m = A_2 = \Delta E_2 = 0$

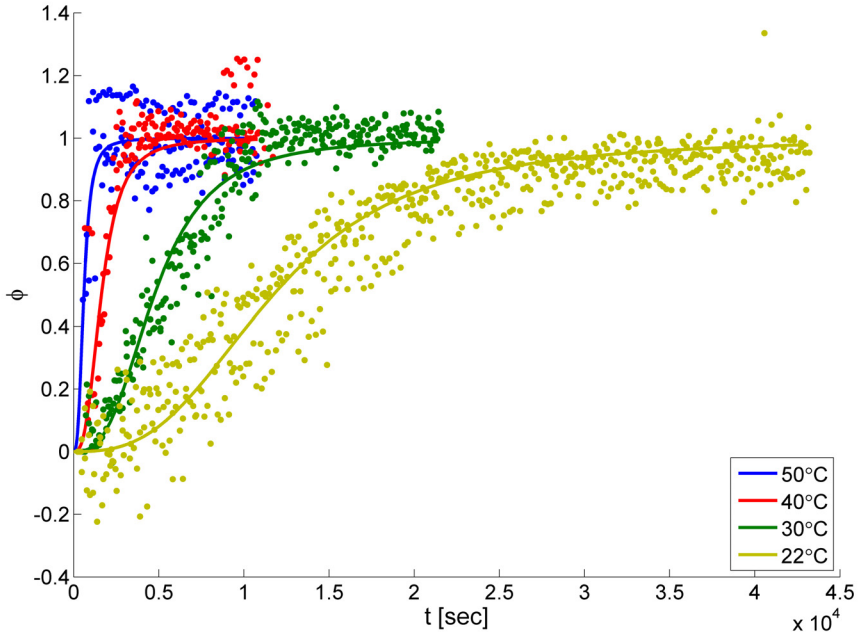

Figure 2.2 Experimental data and curve fit for isothermal cure. A_2, ΔE_3, m, n are parameters to the curing model. $A_1 = 0 = \Delta E_1 = 0$ J, $A_2 = 1.92 \cdot 10^1 1$ sec^{-1}, $\Delta E_2 = 8.415 \cdot 10^4$ J, $m = 0.66$, $n = 1.33$

2.5 Comparison of Different Models

Several authors have investigated the curing behavior of EPON with different curing agents. Shanku et al., [50], and O'Brian and White, [51], investigated EPON 862 (bisphenol F epoxide) with curing agent W (diethyloluene diamine). Adolf and Chambers, [37], were concerned with EPON 828 (bisphenol A based) with curing agent DEP (diethonolamine) and Z (mixture of aromatic amines). Ramakrishnan et al. [49] obtained data for EPON 815 (bisphenol A based) with curing agent EPICURE 3274. They produced values for m and n in (2.4) and expressions for $k_1(T)$ and $k_2(T)$ in (2.5) and (2.6) for the systems that were investigated. This information is summarized in table 2.1.

These values were used in (2.13) and (2.16) to determine the degree of cure vs. time for the cases of a perfect conductor and a perfect insulator. As can be seen in Figures 2.3 through 2.7, the curing reaction predicted by the various models is quite different, not only among different materials, but also within the same epoxy system investigated by different authors.

Figure 2.3 shows the degree of cure versus time for a perfect insulator with an initial temperature of T_0=295 K (22 °C). The temperature is proportional to the degree of cure as stated in equation (2.15). Initially, $\phi = 0$ and the rate of cure is very small. With increasing temperature the rate of cure rises, a self accelerating effect sets in. The heat stays where it is generated which causes the temperature to rise which in turn causes more heat to be released in a shorter time. It is seen that there is a narrow time interval during which the temperature can rise very rapidly. The time when this interval occurs depends strongly on the parameters in k_1 and k_2. EPON 862/EPIKURE 9553 and EPON 815/EPIKURE 3274 cure significantly faster than the other epoxy system considered in figure 2.3. The degree of cure of EPON 862/W and EPON 828 stays close to zero during the time interval shown in figure 2.3.

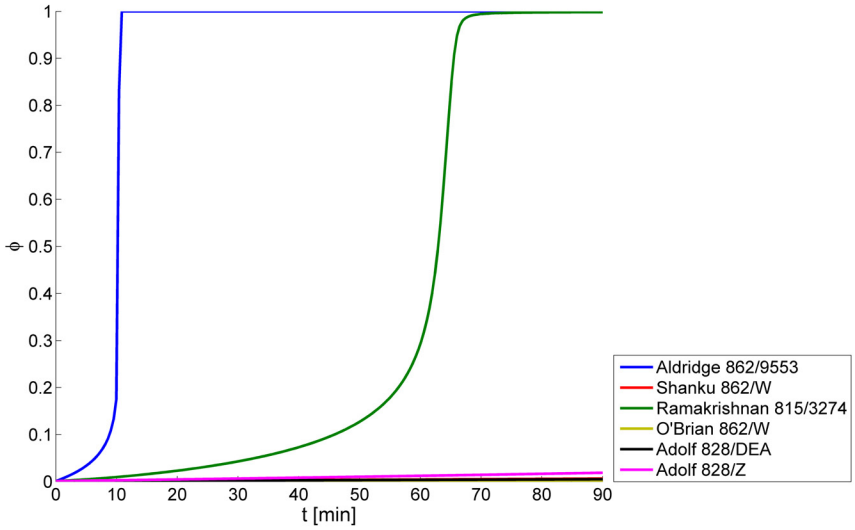

Figure 2.3 Comparison of different curing models for a perfect insulator, $T_0 = 295K$

Figure 2.4 shows the degree of cure versus time for a perfect conductor. The curing reaction is significantly slower. The self accelerating effect cannot be observed since the temperature is fixed. As can be seen from equation (2.10), as $\phi \to 1$, $\mathrm{d}\phi/\mathrm{d}t \to 0$, so that the degree of cure asymptotically approaches one. It should be noted that among all epoxy systems that are considered, Epon862/9553 is by far the most reactive.

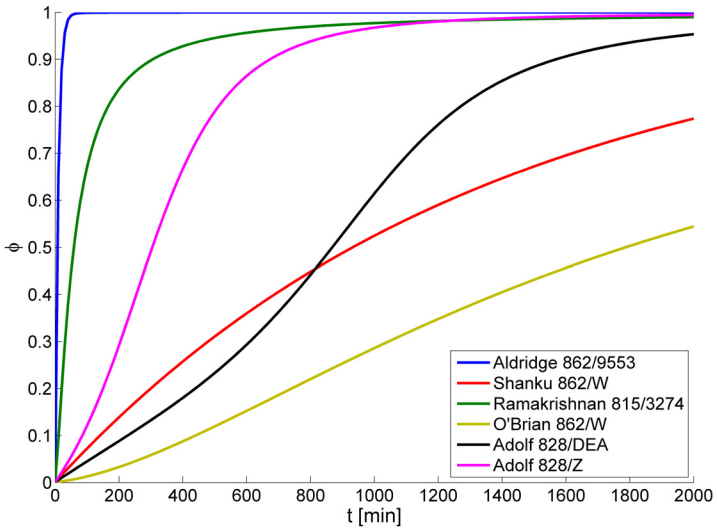

Figure 2.4 Comparison of different curing models for a perfect conductor, $T_0 = 323$ K (50°C)

Figure 2.5 shows the degree of cure vs. time for a perfect conductor using the material parameters of Epon862/9553 at different boundary temperatures. The degree of cure occurs faster at higher temperatures. Since complete cure, $\phi = 1$, is approached asymptotically, a

curing time t_{cure} is defined to be the time corresponding to $\phi = 0.95$.

Figure 2.6 shows how curing time and initial temperature are related for a perfect insulator. The curing time decreases in an exponential fashion. Between an initial temperature of 283K (10 °C) and 373 (100 °C) the curing time drops by two to three orders of magnitude. EPON 862/ EPICURE 9553 cures the fastest, followed by EPON 815/ EPICURE 3274. There is a noticeable difference in the predicted curing behavior of EPON 862 between O'Brian and White [51] and Shanku et al. [50]. One reason for this might be, that the values of O'Brian and White were measured at a higher temperature level, than the measurements by Shanku et al.

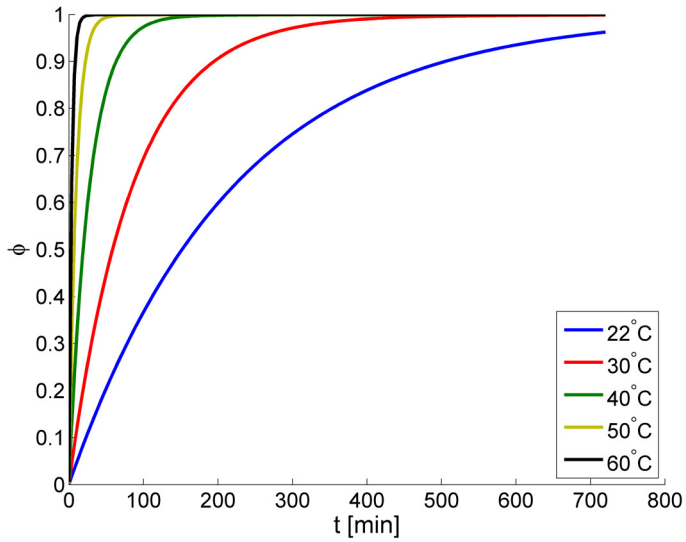

Figure 2.5 Degree of cure vs. time for perfect conductor and Epon862/Epikure9553 at different boundary temperatures

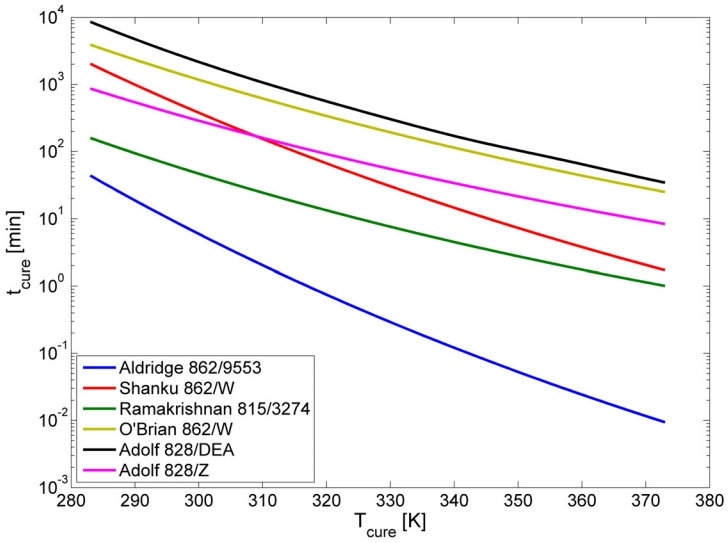

Figure 2.6 Time to 95% cure as function of initial temperature, perfect insulator

Figure 2.7 shows curing time versus epoxy temperature for a perfect conductor (isothermal conditions). As expected the curing time is significantly higher compered to the perfect insulator. Curing temperature and time are again related in an exponential manner and between 283K and 373K the curing time decreases by about two orders of magnitude. Between 338 K and 360 K EPON 828/DEP shows an unexpected behavior with the curing time increasing with temperature. This might be attributed to the piecewise definition of k_2 as given in Table 2.1.

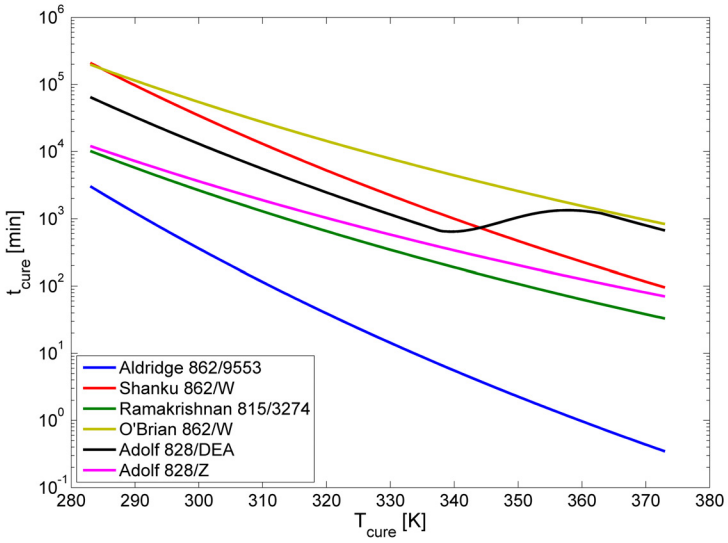

Figure 2.7 Time to 95% cure as function of curing temperature, perfect conductor

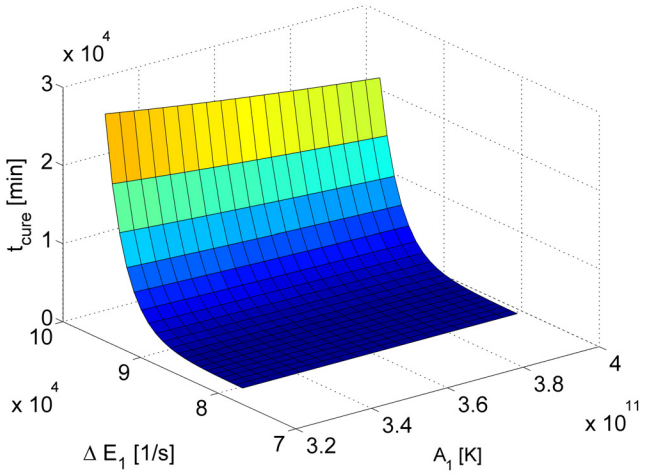

Figure 2.8 Time to 95% cure for different A_1 and ΔE_1, perfect conductor, T_0=295K

2.6 Sensitivity Analysis

A question arises as to the sensitivity of the results in figures 2.3-2.7 to the model parameters, namely A_1, ΔE_1, A_2, ΔE_2 and H_r. This is investigated for the perfect conductor and perfect insulator. H_r does not have any effect in the case of a perfect conductor. In the case of the perfect insulator, a change in H_r has a scaling effect, as seen in equation (2.15). The sensitivity with respect to the activation energy ΔE_1 and frequency parameter A_1 for the epoxy system of interest has been investigated here for a perfect conductor and perfect insulator.

Figure 2.8 shows t_{cure} as a function of A_1 and ΔE_1 for T_0=295 K (22°C) for the perfect conductor and figure 2.9 shows the same for T_0=323 K (50°C). In both cases, an increase in the frequency parameter A_1 causes a linear decrease in curing time. An increase in the activation energy causes an exponential like increase in the time it takes to cure. This is expected. As seen from equation (2.5) and (2.6), an increase in ΔE_1 has the same effect as decreasing the temperature.

Figure 2.10 shows cure histories for a boundary temperature of 323K with some deviation from the values given by the model. All the histories studied show similar behavior, with a faster curing for higher frequency parameter, A_1, and lower activation energy.

In figure 2.11, the dependency of the curing time on A_1 and ΔE_1 is shown for Epon862/Epikure9553 and a perfect insulator at 295K. Figure 2.12 shows the same at 323K. The results are similar to the ones that can be found for the perfect conductor: an increase in frequency parameter causes the curing time to get smaller in a linear fashion, whereas an increase in the activation energy causes the curing time to increase in an expo-

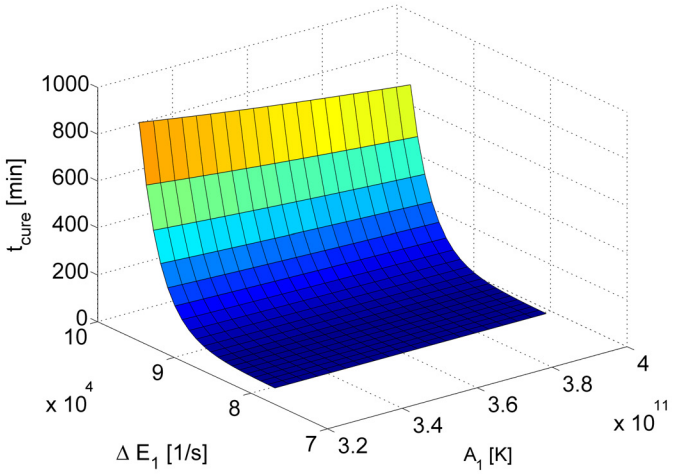

Figure 2.9 Time to 95% cure for different A_1 and ΔE_1, perfect conductor, T_0=323K

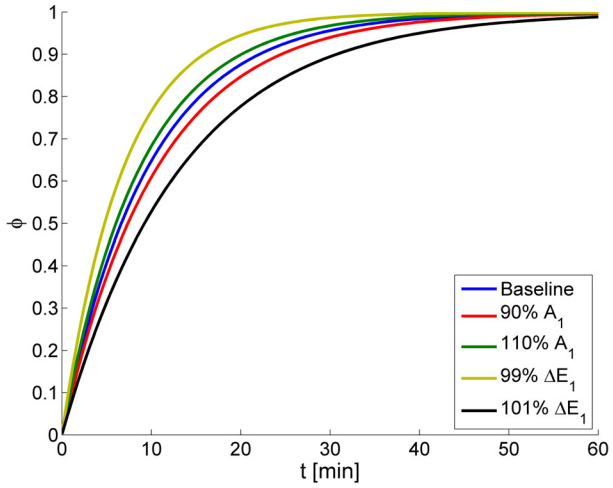

Figure 2.10 Time to 95% cure for different A_1 and ΔE_1, perfect conductor, T_0=323K

nential manner. Figure 2.13 shows ϕ vs. t, for the baseline case and some deviation of the model parameters. The initial temperature is 295K. The curves are similar and compress along the time axis for higher A_1 and lower ΔE_1.

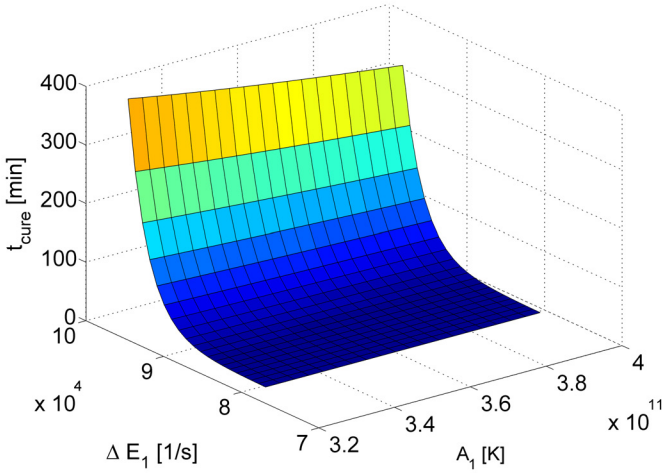

Figure 2.11 Time to 95% cure for different A_1 and ΔE_1, perfect insulator, T_0=295K

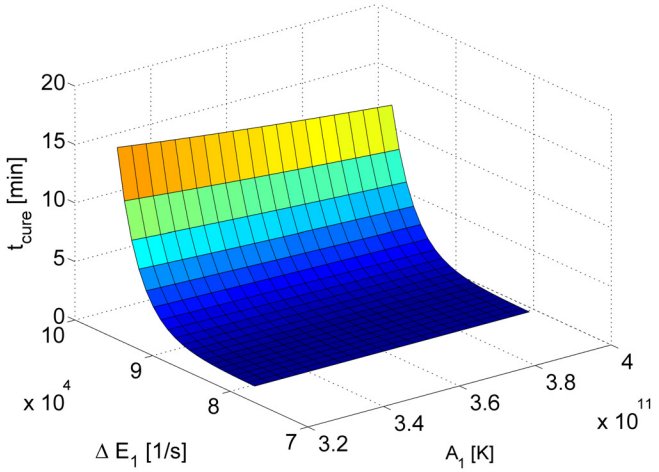

Figure 2.12 Time to 95% cure for different A_1 and ΔE_1, perfect insulator, T_0=323K

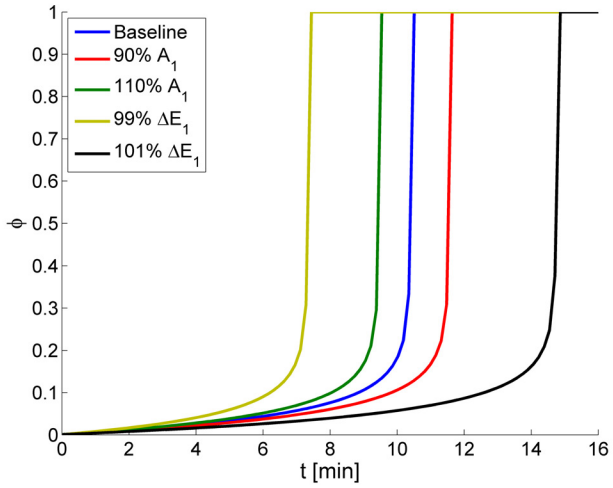

Figure 2.13 Time to 95% cure for different A_1 and ΔE_1, perfect insulator, T_0=295K

2.7 Radial Heat Generation and Conduction in a Solid Cylinder

Consider an infinitely long circular cylinder of radius R_0 that is filled with epoxy at $t = 0$. The cylinder wall is maintained at a constant ambient temperature T_{BC} while the epoxy cures. The degree of cure and temperature vary with radius and time, i.e. $\phi = \phi(r,t)$ and $T = T(r,t)$. Assuming that the thermal conductivity, density and heat of reaction are constants, $\phi = \phi(r,t)$ and $T = T(r,t)$ satisfy the nonlinear coupled system of equations,

$$\frac{\partial \phi}{\partial t} = (k_1(T) + k_2(T)\phi^m)(1-\phi)^n \tag{2.18}$$

$$\frac{\partial T}{\partial t} = \frac{K}{\rho c}\left(\frac{\partial^2 T}{\partial r^2} + \frac{1}{r}\frac{\partial T}{\partial r}\right) + \frac{H_r}{c}\frac{\partial \phi}{\partial t} \tag{2.19}$$

in which $k_1(T)$ and $k_2(T)$ are defined in (2.5) and (2.6). The initial conditions are

$$\phi(r,0) = 0, \quad T(r,0) = T_i, \quad 0 \le r \le R_0 \tag{2.20}$$

The boundary conditions are that there is no heat flow at the centerline and the outer wall is maintained at fixed temperature:

$$\frac{\partial T}{\partial r}(0,t) = 0, \quad T(R_0,t) = T_{BC} \tag{2.21}$$

As it does not appear possible to solve the system of equations (2.18) and (2.19) by analytical methods, they are solved numerically, using a finite differences method and Matlab®, [62]. Choices for values of ρ, c, K and H_r are summarized in table 2.2. The discretized equations are shown in Appendix B.

Numerical results that illustrate the phenomena have been obtained using the data for EPON 862/Epikure 9553. The initial temperature, or temperature of the epoxy when placed in the cylinder is the room temperature $T_i = 295K$ ($22^\circ C$). The outside wall of the cylinder is $T_{BC} = 323K$, as one might find in a heated mold or oven. Figures 2.14 and 2.15 show results for $R_0 = 1$mm .

As shown in figure 2.14, the temperature in the entire sample rapidly increases from room temperature to the boundary temperature. It overshoots a by a small amount due to the heat that is generated during the curing process, but the temperature is largely dominated by the boundary temperature. Heat conduction is rapid compared to heat generation. Figure 2.15 shows the temperature and degree of cure vs. time at the centerline $r = 0$.

A different picture is revealed, when looking at the same example but changing the size

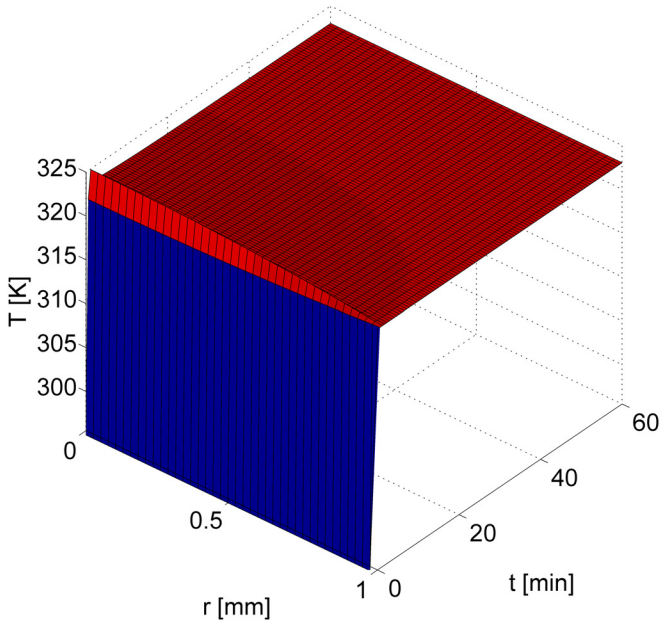

Figure 2.14 Temperature development, R_0=1mm, $T_{ini} = 295$K, $T_{BC} = 323$K

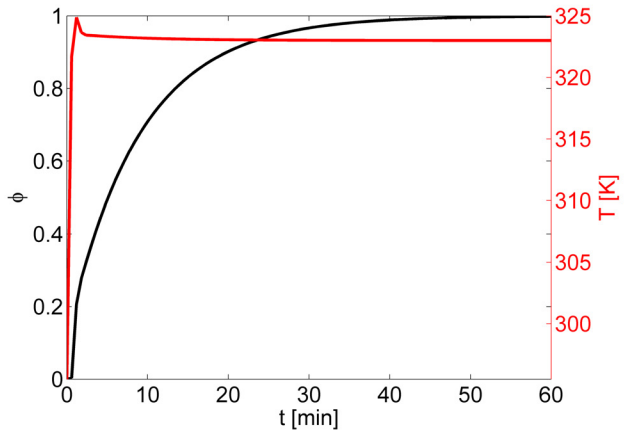

Figure 2.15 Cure and temperature at midline, R_0=1mm, $T_{ini} = 295$K, $T_{BC} = 323$K

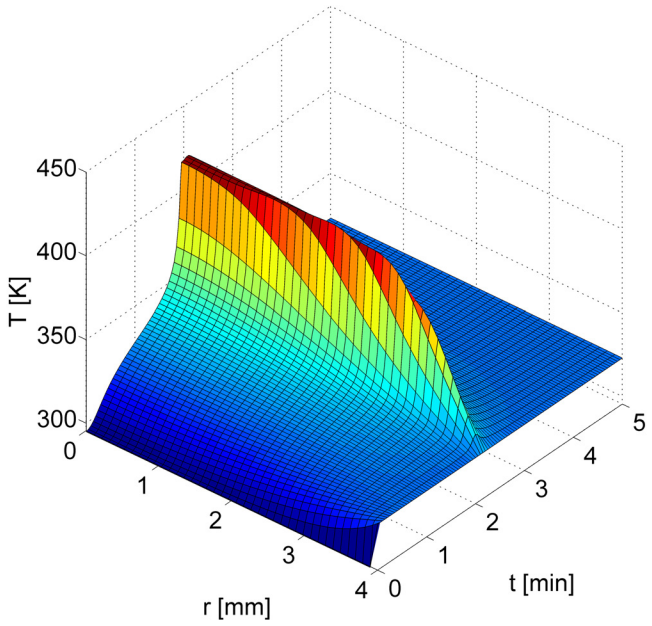

Figure 2.16 Temperature development, R_0=4mm, $T_{ini} = 295$K, $T_{BC} = 323$K

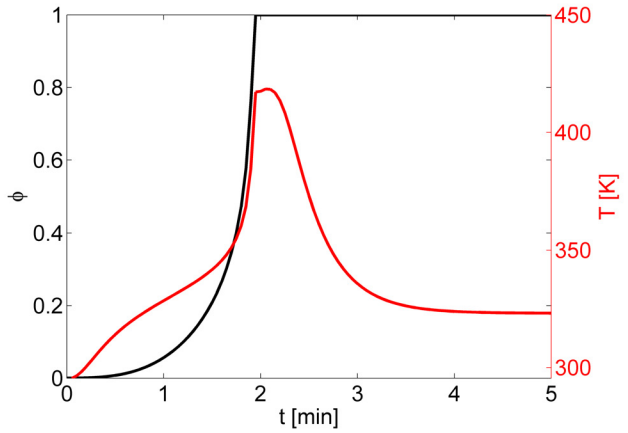

Figure 2.17 Cure and temperature at midline, R_0=4mm, $T_{ini} = 295$K, $T_{BC} = 323$K

of the cylinder to $R_0 = 4$mm. Figure 2.16 shows $T(r,t)$ for the entire cylinder. Figure 2.17 shows temperature and degree of cure vs. t at the centerline $r = 0$. The sample is again initially at room temperature. Due to the large size and small conductivity the temperature field is mainly governed by the heat generation. Heat is generated near $r = 0$ more rapidly than it can be conducted to the boundary and the reaction is accelerating itself. Once the reaction is complete, the sample starts cooling due to the gradient between the center and the boundary. In this particular example the maximum temperature was over 400 K.

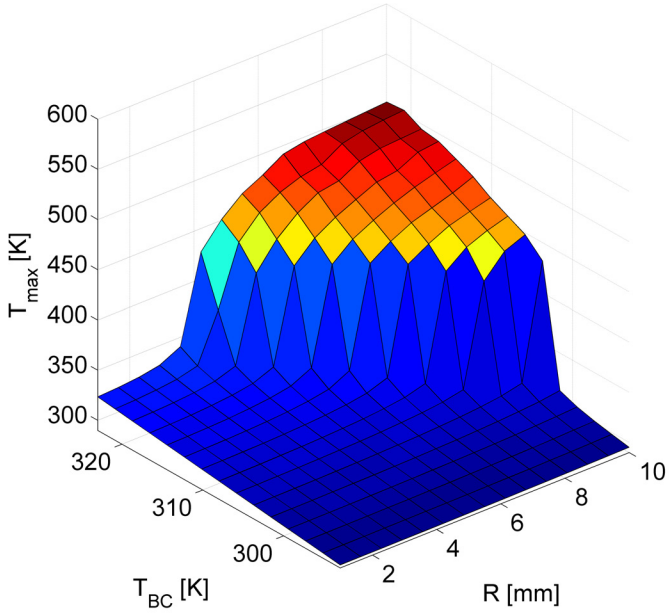

Figure 2.18 Maximum temperature for different sample radii 1mm – 10mm and initial temperatures 293K – 323K, Conductivity 0.20 (W/m/K)

2.8 Parameter Study

It was shown in section 2.7 that a change in the radius of the cylinder can seriously affect the spatial and time variation of the temperature and degree of cure. This suggests an investigation of the effect of the various parameters on the curing time and maximum temperature in the cylinder.

Figure 2.18 shows the maximum temperature in a cylindrical specimen as a function of boundary temperature and the sample radius (the initial temperature was always set to 295K). The maximum temperature is defined as the highest temperature at any radius or time during the process. Generally one can observe that the higher the initial temperature, the higher the maximum temperature (where the linear part of that increase is purely to the increase in temperature and not related to curing effects). Also the larger the radius, the higher is the maximum temperature. It is very interesting to note that there is a transition region where the maximum temperature rapidly increases for small increases in either cylinder radius or initial/ boundary temperature.

Figure 2.19 shows how the curing time t_{cure} varies with sample radius and boundary temperature. The times are plotted on a logarithmic scale since a small change in temperature can cause very large changes in magnitude of the time that it takes to cure. The results are closely related to the ones for the maximum temperature. The higher the temperature

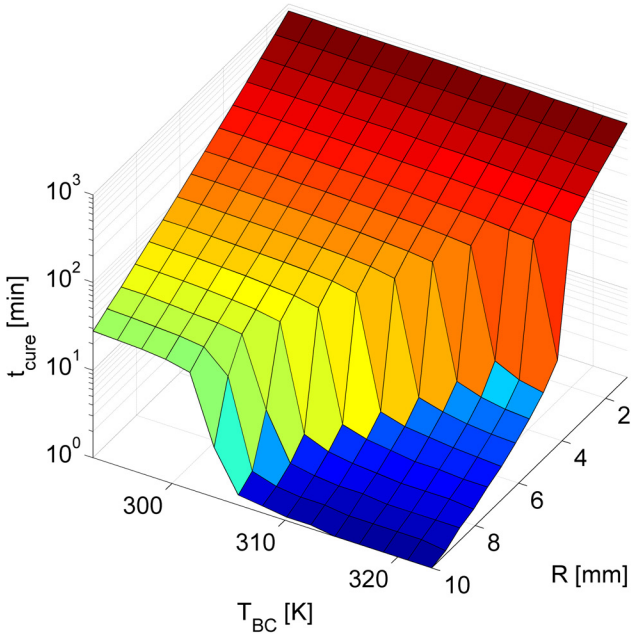

Figure 2.19 t_{cure} for different sample radii 1mm – 10mm and initial temperatures 293K – 323K, Conductivity 0.20 (W/m/K)

and the larger the radius, the faster the sample cures. There is a transition region where the curing time rapidly increases for small increases in either temperature or sample radius. The differences in time span 3 orders of magnitude. At 323K a sample can be cured in minutes, whereas a small sample at room temperature takes half a day.

Figure 2.20 shows the relationship between the maximum temperature in a cylinder, the cylinder radius R and the thermal conductivity K of the epoxy. As expected a large radius and a low conductivity causes the maximum temperature to rise.

Figure 2.21 shows t_{cure} vs. radius and thermal conductivity K. For low conductivity and large radii, the cure progresses rapidly.

The value of the thermal conductivity K has been the subject of past research. Varshney et al. [63] investigated the conductivity of EPON 862, curing agent W (DETDA) and their cross linked network with non-equilibrium (NEMD) and equilibrium molecular dynamics(EMD). The values obtained with NEMD were 0.21, 0.20 and 0.30 W/m/K and with EMD, they were 0.13, 0.15 and 0.13 W/m/K. The authors state that they favor the higher values from the NEMD calculations to be more realistic. According to figures 2.20 and 2.21, these values fall in a range where small changes in K can have a large influence on maximum temperature and curing time.

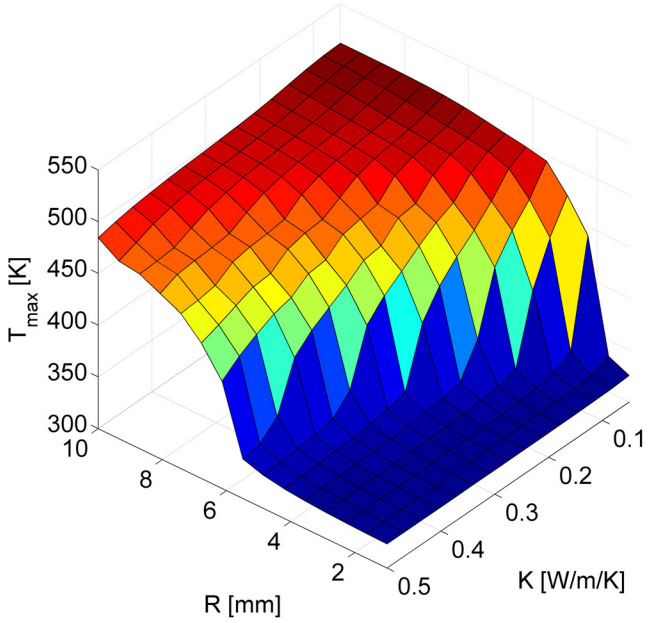

Figure 2.20 Maximum temperature for different sample radii, 5 mm –100 mm, and thermal conductivities 0.05 – 0.5 (W/m/K) with boundary temperature 323 K

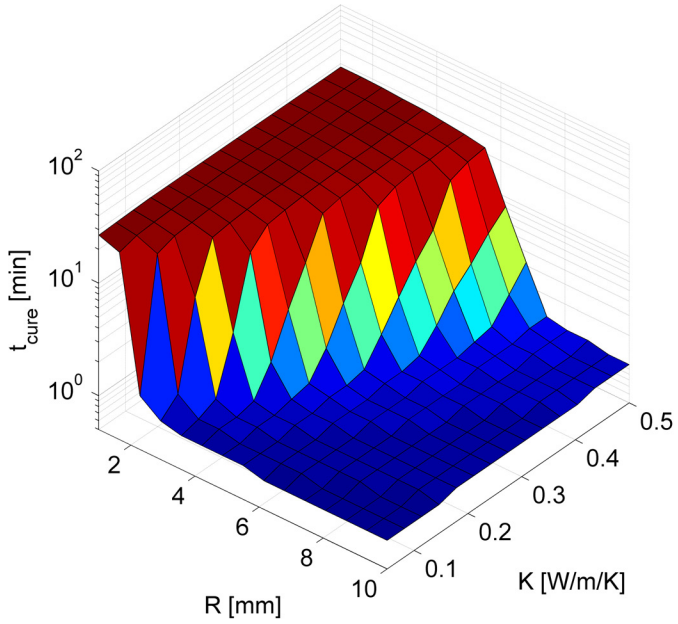

Figure 2.21 t_{cure} for different sample radii, 5 mm – 100 mm, and thermal conductivities ranging from 0.05 to 1 (W/m/K) with initial temperature 303 K

Reference and Material	$H_r\ (J/g)$	m	n	k_1	k_2
Shanku Epon 862/W	341	0	1	$1.76 \cdot 10^7 \exp\left(\frac{-75000}{RT}\right)/\text{sec}$	0
Ramakrishnan Epon 815/ Epikure 3274	384	0.25	1.7	0	$4.18^5 \exp\left(\frac{-55920}{RT}\right)/\text{sec}$
Obrian and White Epon 862/W	399	0.39	1.67	0	$6488 \exp(\frac{-53326K}{RT})/\text{sec}$
Adolf Epon 828/DEP	200	-	1.6	$43333 \exp(-66512K/(RT))/\text{sec}$ $338K < T < 368K$	$\begin{cases} 9.5 \cdot 10^6 \exp(-66512K/(RT))/sec & \text{if } T < 338K \\ 1.5 \cdot 10^6 \frac{363-T}{(T-273K)^6}/\text{secif } 338 \leq T < 363 & \\ 0 & \text{if } 363 < T \end{cases}$
Aldridge Epon 862/Epikure 9553	-	0	1	$3.62 \cdot 10^{11} \exp\left(\frac{-88500}{RT}\right)/\text{sec}$	0

Table 2.1 Curing parameters of various epoxy hardener systems

Property	Unit	Material	Value	Reference
Density ρ	kg/m^3	Epon862/Epikure3234	1230	[64]
		current study	1200	
Specific heat c_p	J/kg/°C	Generic epoxy	1200@109°C	[65]
		Epon862/W	1000	[44]
		Bisphenol F/HHPA	1150@23°C	[66]
		current study	1200	
Heat of reaction	J/kg	Epon862/W	399000±14000	[51]
		Epon862/W	395000	[50]
		Epon862/W	200000	[44]
		Epon862/Epikure3234	121600±6400	[67]
		current study	230000	
Thermal conductivity K	W/m/K	Epon862 resin	0.15-0.20	[63]
		DETDA	0.13-0.21	[63]
		Epon862/DETDA	0.13-0.30	[63]
		Epon862/W	0.195	[68]
		Bisphenol F/HHPA	0.2	[66]
		current study	0.2	

Table 2.2 Thermal properties

2.9 Conclusions

The cure of epoxy polymers was studied, using parameters for cure models that have been presented in the prior literature. These studies included numerical solutions of the coupled equation of cure kinetics and energy balance. Closed form solutions were presented for the cases corresponding to that of a perfect conductor and a perfect insulator. It was found that the curing time between these two extremes differs by more than a factor of ten. A change in initial temperature (perfect insulator) or boundary temperature (perfect conductor) causes an exponential decrease in curing time, spanning more than two magnitudes over a range of 100 degrees Kelvin. These results correspond to available epoxy systems. It was shown that there is a close relation between geometry, thermal conductivity, temperature and time to cure. High initial temperature, low thermal conductivity and a large size (geometry) cause high curing rates and low curing times. In these cases the curing characteristics were similar to one of a perfect insulator with a steep rise of curing rate towards full cure. For smaller sizes, higher conductivity and lower temperatures, the opposite trend was observed. The curing rate declined smoothly for higher degrees of cure. The behavior was very similar to the case of a perfect conductor. These two extremes are very useful in estimating the curing characteristics of components with different size scales. Maximum temperature during cure (T_{max}), and curing time (t_{cure}), can be used as two critical parameters to characterize the

curing process. There is only a small transition band in the size vs. initial temperature "space", where none of these two extremes apply. A detailed quantitative assessment of the polymer curing characteristics is very desirable, because rapid curing due to geometric effects is expected to lead to gradients in temperature, degree of cure and ultimately residual stresses in a structural component of interest. The generation of internal stress, coupled with cure kinetics and internal energy balance, is investigated in section 4.1 for pure epoxy systems, while the corresponding problem for a single fiber idealized composite is presented in section 4.2 and that for a unit cell of a woven composite is presented in section 4.5.

Chapter 3
Stress evolution during cure

Residual self equilibrating stresses in an epoxy used in a structural part can significantly alter its subsequent performance of the part under service loads. Therefore, measurement and prediction of residual stresses during the cure of epoxy has been the subject of many past studies. Plepys and Farris [22] and Plepys et al. [34] have investigated the evolution of residual stresses in a three dimensionally constrained Epon 828 epoxy resin. They used incremental elasticity to account for the change of material properties through the curing history of the epoxy. They measured tensile stresses of up to 28 MPa in the fully cured epoxy resin. The incremental elasticity article of Plepys and Farris has different underlying assumptions from those used here. They assume, that during each time increment, the stress increment is related to the strain increment as a linear isotropic elastic relation, but moduli can change from one increment to another. The strain appears to be measured with respect to the same reference configuration. In the approach presented here, new networks are continuously formed in new reference configurations. Hence strains in different networks are measured with respect to different reference configurations. Bogetti and Gillespie [35] studied the process-induced stress and deformation in thick thermoset composite laminates. The model was evaluated using a one-dimensional cure simulation based on incremental transient finite difference formulation. Instantaneous material properties were used and the cure dependent material properties were found using a cure mixing rule. Circumferential stresses of 60 MPa and more were calculated in a cylindrical specimen.

In this chapter, a model for the stress evolution during cure will be derived in two different ways. First a bottom up approach will be taken, where a small strain model including one dimensional springs will be generalized to yield a small strain result for a three dimensional solid. In a second approach a finite strain, three dimensional model will be specialized to yield the results that can be used to calculate cure induced deformation and stresses.

3.1 Model - Bottom up

To develop an understanding of the stresses and deformations during polymer cure, a network model of a polymer will be adopted. The networks interpenetrate each other, i.e. they occupy the same volume. On the other hand the assumption is made that they do not interact with each other.

A second assumption is related to the interaction of the different physical problems mentioned earlier: heat conduction, chemical change and mechanical response. Curing of epoxy resins is often done under pressure. This has influence on the rate of cure and can be taken into account. Ramos et el., [69], measured and modeled the cure kinetics and shrinkage for a DGEBA/ MCDEA epoxy system. The reaction rate was investigated over a range of 200-600 bar pressure and a shift in reaction rate was noticeable. For this kind of analysis where the stress and chemical composition depend on each other, the term mechanochemistry has been used in the past, [70]. Ramos et al., [69], suggested to augment equations (2.5) and (2.6) such that:

$$k_i(T,p) = A_{i0} \exp\left(-\frac{\Delta E_1}{TR}\right) \exp\left[\left(\frac{-\Delta V}{TR} + \frac{1}{V}\frac{\partial V}{\partial p}\right)(p - p_0)\right], \quad i = 1,2 \tag{3.1}$$

where ΔV is the activation volume and p is the pressure. The dependency of rate of cure on temperature is significantly stronger than on pressure. Ramos et al., [69], measured the evolution of cure at 1 bar pressure over the temperature range from 100°C-180°C and at 160°C over a pressure range from 1 bar to 800 bar. The dependence on pressure can best be observed for intermediate degrees of cure. Therefore the time to reach a degree of cure of 50%, $t_{50\%}$, will be used for comparison in the following. The results for varying the temperature and keeping the pressure constant are: $t_{50\%}(140°\text{C}, 1bar) = 150$ minutes, $t_{50\%}(160°\text{C}, 1bar) = 85$ minutes and $t_{50\%}(180°\text{C}, 1bar) = 35$ minutes. On the other hand the results for varying the pressure and keeping the temperature are: $t_{50\%}(160°\text{C}, 1bar) =$ 85 minutes, $t_{50\%}(160°\text{C}, 200bar) = 75$ minutes and $t_{50\%}(160°\text{C}, 400bar) = 68$ minutes. For further discussion it is useful to consider the magnitudes of pressure that occur during the manufacturing process of woven composites. Rudd cites a mold pressure of up to 15 bar during resin transfer molding (RTM). Ikegawa et al., [71], give 20-50 bar mold pressure after impregnation of the fiber mat during structural resin transfer molding process and Revello, [72], extends these values to 35-140 bar for compression molding of sheet molding compound. Typical values of mold pressure during an RTM process are expected to be significantly below this value. Thus, at 160°C an increase of mold pressure to 200 bar,

as considered by Ramos et al., marks a clear upper bound for mold pressure during the manufacturing process of woven composites. Applying 200 bar pressure will result in a decrease of $t_{50\%}$ from 85 minutes to 75 minutes. On the other hand varying the temperatures between 140°C and 180°C causes a change of $t_{50\%}$ from 35 minutes to 150 minutes. These temperature variations are likely to be observed during the curing process of epoxy. Therefore in the following the dependency on pressure will be ignored. It is also desirable to separate the thermochemical problem from the mechanical one from a numerical point of view. This leads to a one way coupling. The temperature and chemical composition are independent of stress state but the stress state depends on the degree of cure through evolving material properties and on temperature through thermal expansion.

In what follows, a model for stress evolution that incorporates the notion of networks forming and contributing to evolving stiffness is derived for a 1D model and then generalized to 3 dimensions. The creation of the epoxy networks as curing evolves is depicted in figure 3.1, [43]. Initially, hardener and epoxy resin are in a liquid state. They are mixed and poured into a mold with the fibers. Immediately after mixing, the pure epoxy resin starts reacting, building connections and cross links. At some time t_1 the first network forms. It is assumed, that it forms in a stress free configuration. The forming of the network is accompanied by some shrinkage due to cure. There also might be additional strain due to changes in temperature and externally applied loads. At some later time, t_2, another network forms. This network has a different stress free reference configuration. Even later, a new network forms at time t_3. Its stress free reference configuration is different than the one from the networks formed at time t_1 and t_2. Because all networks occupy the same volume, their current configuration is the same. On the other hand their stress free reference configuration is different. As a result, the stress in each network is different. The sum of all stresses within the networks is such that it balances out all externally applied stresses.

Figure 3.2 depicts the formation of networks as one dimensional springs. The following derivation is similar to the ones given in [43] and [73]. A network forms at time t_1 and might experience some external strain due to external load. The response of the network is assumed to be elastic. The stress $\sigma(t,s)$ at time t in a network created at time s is proportional to the mechanical strain $\varepsilon^{mech}(t,s)$ relative to its stress free reference configuration multiplied with the elastic modulus $E(s)$ associated with that network.

$$\sigma(t,s) = E(s)\varepsilon^{mech}(t,s). \tag{3.2}$$

The total strain at time t in the network formed at time s is the sum of all incremental strains since its creation. This is the same as the mechanical strain including thermal effects and shrinkage effects. $\Delta\varepsilon(t_i)$ is the increment in total strain from time t_{i-1} to time t_i.

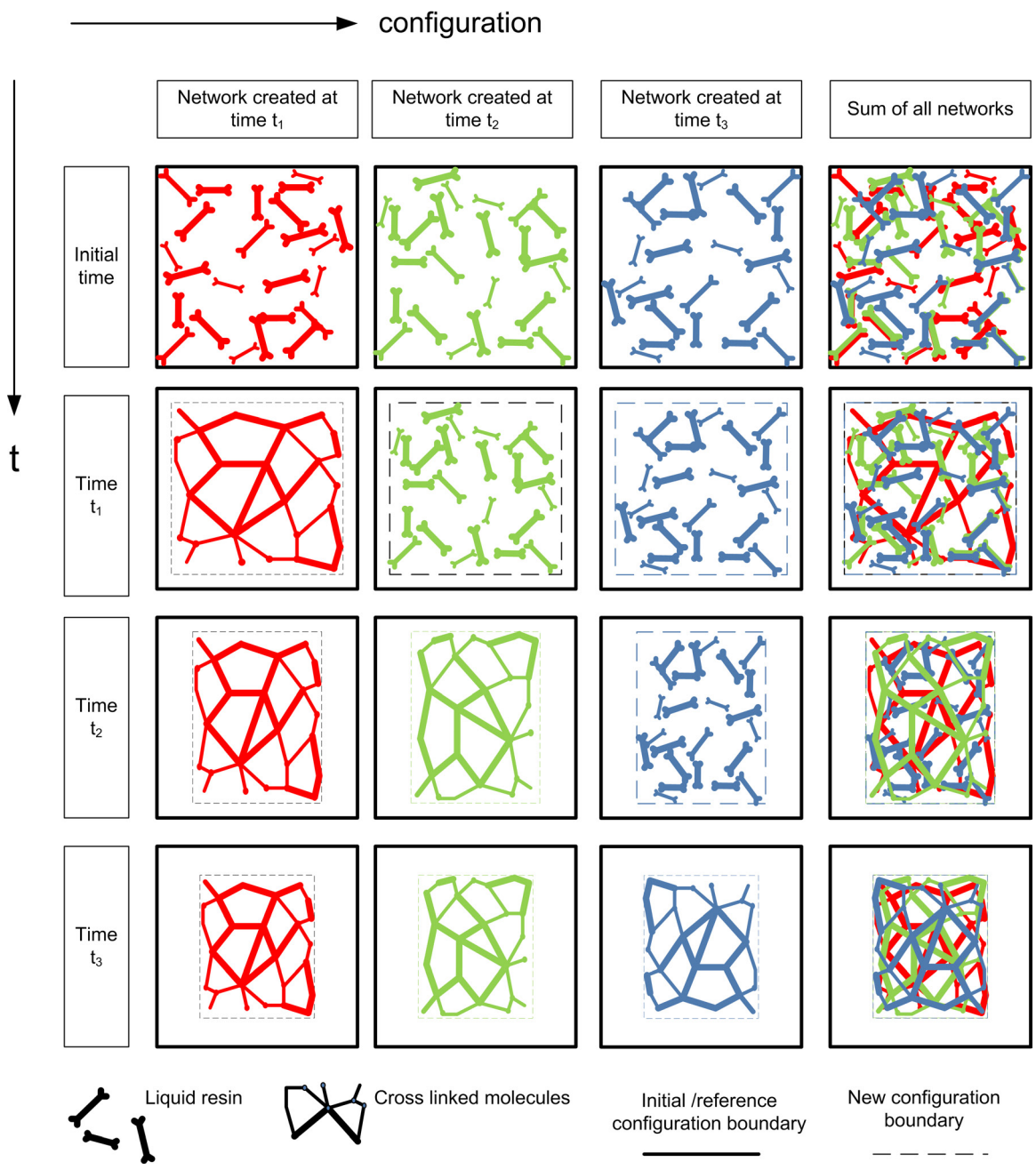

Figure 3.1 A schematic of the forming of networks as curing evolves

$$\varepsilon(t,s) = \Delta\varepsilon(s)+\Delta\varepsilon(s+\Delta t)+\cdots+\Delta\varepsilon(t) \quad (3.3)$$
$$= \varepsilon^{mech}(t,s)+\alpha(s)\Delta(T(t)-T(s))-\varepsilon_c(s) \quad (3.4)$$

Here, $\varepsilon_c(s)$ is the cure shrinkage strain of the network formed at time s. The sign of $\varepsilon_c(s)$ is positive when it decreases the strain. The stress in network 1 created at time t_1 is given by:

$$\sigma(t_1,t_1) = E(t_1)(\Delta\varepsilon(t_1)+\varepsilon_c(t_1)-\alpha(T(t_1)-T(t_1))) \quad (3.5)$$

Curing strains begin to impact each network, after it is formed. Strains due to external loads and temperature difference have to be accounted for at all times. The stresses in network 1 and 2 at the formation time of network 2 are given by:

$$\sigma(t_2,t_1) = E(t_1)(\Delta\varepsilon(t_1)+\Delta\varepsilon(t_2)+\varepsilon_c(t_1)-\alpha(T(t_2)-T(t_1))) \quad (3.6)$$
$$\sigma(t_2,t_2) = E(t_2)(\Delta\varepsilon(t_2)+\varepsilon_c(t_2)-\alpha(T(t_2)-T(t_2)) \quad (3.7)$$

Furthermore, in the next step, the total strains of the reference configuration change by the amount $\Delta\varepsilon_3$ after network 3 is created:

$$\sigma(t_3,t_1) = E(t_1)(\Delta\varepsilon(t_1)+\Delta\varepsilon(t_2)+\Delta\varepsilon(t_3)+\varepsilon_c(t_1)-\alpha(T(t_3)-T(t_1))) \quad (3.8)$$
$$\sigma(t_3,t_2) = E(t_2)(\Delta\varepsilon(t_2)+\Delta\varepsilon(t_3)+\varepsilon_c(t_2)-\alpha(T(t_3)-T(t_2))) \quad (3.9)$$
$$\sigma(t_3,t_3) = E(t_3)(\Delta\varepsilon(t_3)+\varepsilon_c(t_3)-\alpha(T(t_3)-T(t_3))) \quad (3.10)$$

Each network is weighted to contribute to the total load carrying capability in a "rule of mixtures" type sense. During the creation of each network the overall epoxy has cured by an amount of $\Delta\phi(t_i) = \phi(t_i)-\phi(t_{i-1})$. With ϕ denoting the degree of cure as defined in chapter 2. As a reminder the interpretation of the degree of cure ϕ is given by

$$\phi(t) = \frac{\text{mass cured at time } t}{\text{total mass of material that can cure}}$$
$$= \text{mass fraction of cured material}$$

$$\mathrm{d}\phi = \text{mass fraction cured during time interval from } s \text{ to } s+\mathrm{d}s$$

This definition is not same as equation 2.1, but it is assumed, that they are equivalent. The total stress in the epoxy at time t_N is given by:

$$\sigma_{tot}(t_N) = \sum_{i=1}^{N} \Delta\phi(t_i)\sigma(t_N,t_i) = \sum_{i=1}^{N} \Delta\phi(t_i)E(t_i)\left(\varepsilon_c(t_i) - \alpha(T(t_N)-T(t_i)) + \sum_{j=i}^{N}\Delta\varepsilon(t_N,t_j)\right) \tag{3.11}$$

The *tot* subscript will be omitted in the following, when it is clear that the total stress meant. When taking the limit of the above equation, the sums can be converted into integrals:

$$\sum \Delta\phi \to \int \mathrm{d}\phi \quad \text{and} \quad \sum \Delta\varepsilon \to \int \mathrm{d}\varepsilon$$

The discrete quantity $\varepsilon_c(t_i)$ represents the curing strain in the i^{th} network formed at time t_i. It's continuous equivalent is $\varepsilon_c(s)$, the cure shrinkage in the network formed at time s. Equivalent expressions exist for the material properties $E(t_N) \to E(s)$ and $\alpha(t_N) \to \alpha(s)$.With these substitutions, the stress up to a certain amount of cure, represented by the cure fraction, Φ is given by:

$$\begin{aligned} \sigma(\Phi) &= \int_0^{\Phi} \tilde{E}(\phi)\left(\varepsilon_c(\phi) - \alpha(T(\Phi)-T(\phi)) + \int_{\varepsilon(\phi)}^{\varepsilon(\Phi)} \mathrm{d}\overline{\varepsilon}\right)\mathrm{d}\phi & (3.12)\\ &= \int_0^{\Phi} \tilde{E}(\phi)\left(\varepsilon_c(\phi) - \alpha(T(\Phi)-T(\phi)) + \varepsilon(\Phi) - \varepsilon(\phi)\right)\mathrm{d}\phi & (3.13) \end{aligned}$$

The degree of cure $\phi(s)$ increases monotonically with time which allows for the substitution, $\mathrm{d}\phi = \frac{\mathrm{d}\phi}{\mathrm{d}s}\mathrm{d}s$:

$$\sigma(t) = \int_0^t \frac{\mathrm{d}\phi}{\mathrm{d}s} E(s)\left(\varepsilon(t) - \varepsilon(s) + \varepsilon^{cure}(s) - \alpha(T(t)-T(s))\right)\mathrm{d}s \tag{3.14}$$

The elastic modulus $E(s)$ depends directly on the degree of cure, and indirectly on time, by $E(s) = \tilde{E}(\phi(s))$. The above equation can be generalized to three dimensions:

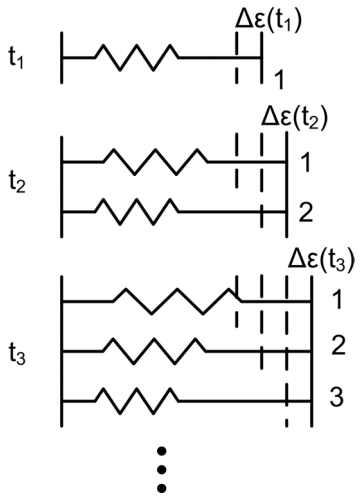

Figure 3.2 Forming of 1D networks, shown schematically

$$\begin{aligned}\underline{\underline{\sigma}} &= \int_0^t \frac{\mathrm{d}\phi}{\mathrm{d}s}\underline{\underline{1}}\Big[K(s)\mathrm{tr}\left(\underline{\underline{\varepsilon}}(t)-\underline{\underline{\varepsilon}}(s)+\underline{\underline{\varepsilon}}_c(s)-\underline{\underline{1}}\alpha(s)\Delta T(t,s)\right) \\ &\quad +2\mu(s)\left(\underline{\underline{\varepsilon}}(t)-\underline{\underline{\varepsilon}}(s)+\underline{\underline{\varepsilon}}_c(s)-\underline{\underline{1}}\frac{1}{3}\mathrm{tr}\left(\underline{\underline{\varepsilon}}(t)-\underline{\underline{\varepsilon}}(s)+\underline{\underline{\varepsilon}}_c(s)\right)\right)\Big] \\ &\quad +(1-\phi(t))K_{liq}\mathrm{tr}(\underline{\underline{\varepsilon}}(t)-\underline{\underline{1}}\alpha_{liq}\Delta T(t))\underline{\underline{1}}\end{aligned} \tag{3.15}$$

where K is the per-network bulk modulus, μ is the per-network shear modulus and α is the linear coefficient of thermal expansion of each network. The notation, $\underline{\underline{(.)}}$ indicates a second order tensor. The last term in the equation is due to the fact that a liquid can hold compressive volumetric stresses.

The tensor quantity $\underline{\underline{\varepsilon}}_c(s)$ describes the cure shrinkage strains of each network. It is assumed that curing only produces normal strains.

$$\underline{\underline{\varepsilon}}_c(s) = \begin{bmatrix} \varepsilon_c(s) & 0 & 0 \\ 0 & \varepsilon_c(s) & 0 \\ 0 & 0 & \varepsilon_c(s) \end{bmatrix} \tag{3.16}$$

$\underline{\underline{\varepsilon}}_c(s)$ can be chosen such that macroscopically a bilinear shrinkage as a function of degree of cure can be observed.

Note that formally $\alpha(s), \mu(s), K(s)$ are functions of time. But actually they are a function of cure, which has to be related to time, so that $\alpha(s) = \tilde{\alpha}(\phi(s))$, $\mu(s) = \tilde{\mu}(\phi(s))$, $K(s) = \tilde{K}(\phi(s))$ and $\varepsilon_c(s) = \tilde{\varepsilon}_c(\phi(s))$. These material functions need to be determined from experiments.

3.2 Model - Top down

The foregoing derivation started with the assumption that the material will only observe small strains. Now, only limited assumptions shall be made about the deformation state of the material and specialization will be introduced when necessary. As before, the idea of overlapping, interpenetrating but non-interacting networks will be used. In order to describe the thermo-mechanical properties of these networks, one considers several different configurations These are shown in figure 3.3.

(a) The configuration of a volume of epoxy in its uncured, non-crosslinked state.
(b) The epoxy at time s when it has crosslinked and become solid. The configuration in (b) is the configuration the solid would have if it was stress free, unconstrained by the remaining material. The volume of the crosslinked solid in configuration (b) is smaller than the volume of the non-crosslinked fluid in configuration (a) due to shrinkage, much as occurs in a phase transition. This is a stress-free or *natural* configuration.
(c) This is the actual configuration taken by the solid at time s due to the interaction with other material. It is no longer stress free.
(d) The configuration of the material at the current time t.

The material is a fluid that is uncross-linked until the critical gel point. At the critical gel point ϕ_0 at time t_0, it can transmit stress. The mass fraction of cured epoxy is ϕ_0.The constitutive equation for the stress at the current time t is:

$$\underline{\underline{\sigma}} = \mathscr{F}\left(\frac{\partial \underline{x}(t)}{\partial \underline{X}_{NAT}(t_0)}, T(t), T(t_0), t_0\right) \tag{3.17}$$

Here t_0 is the parameter used to identify the network to be formed at time t_0. $T(t_0)$ is the temperature at the time of formation and $T(t)$ is the temperature at the current time t. $\partial \underline{x}(t)/\partial \underline{X}_{NAT}(t)$ describes the deformation gradient comparing the configuration at time t to the natural configuration. Note that the material is thermoelastic since it depends only on the current deformation gradient. History effects or viscoelastic effects are not considered.

A new network forms during the subsequent time interval s to $s + \mathrm{d}s$. The mass fraction of the cured epoxy that is formed is $\mathrm{d}\phi$. The constitutive equation is denoted as

$$\underline{\underline{\sigma}} = \mathscr{F}\left(\frac{\partial \underline{x}(t)}{\partial \underline{X}_{NAT}(s)}, T(t), T(s), s\right) \tag{3.18}$$

Here s is a parameter identifying the network formed at time s, where $0 \leq s \leq t$. $T(s)$ is the temperature at the time of formation and $T(t)$ denotes the current temperature. $\partial \underline{x}(t)/\partial \underline{X}_{NAT}(s)$ is the deformation gradient comparing the configuration at time t to the natural configuration (stress free configuration) of the network formed at time s. The

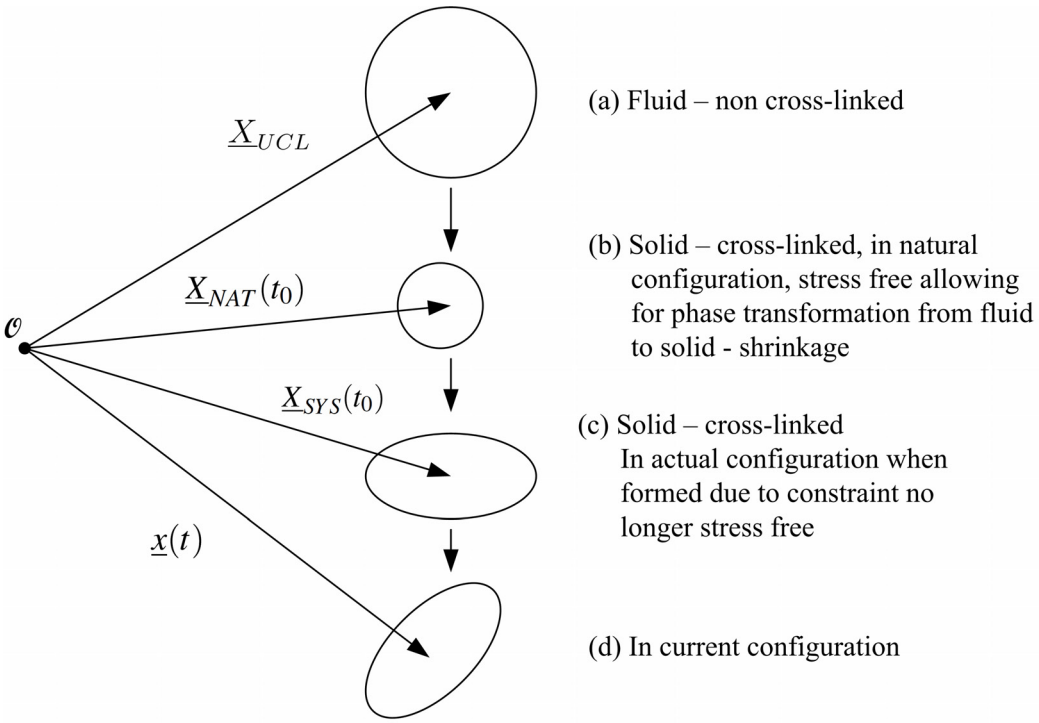

$\underline{X}_{UCL}$	Position vector of particle in fluid phase
$\underline{X}_{NAT}(t_0)$	Position vector in natural or stress-free configuration at critical gel point
$\underline{X}_{SYS}(t_0)$	Position vector in actual configuration of system at time t_0
$\underline{x}(t)$	Position in current configuration

Figure 3.3 Different configurations for a network

network is thermoelastic as well.

Assume that the total stress at time t, in the curing network, is the superposition of the stresses in the networks formed up to time t, to form the integral:

$$\underline{\underline{\sigma}}(t) = \phi_0 \cdot \mathscr{F}\left(\frac{\partial \underline{x}(t)}{\partial \underline{X}_{NAT}(t_0)}, T(t), T(s), t_0\right) + \int_0^t \dot{\phi}(s)\mathscr{F}\left(\frac{\partial \underline{x}(t)}{\partial \underline{X}_{NAT}(s)}, T(t), T(s), s\right) \tag{3.19}$$

The dependence on the parameter s allows the elastic properties of that network formed at that time to depend on s and be different from the elastic properties formed at other times. No assumptions have been made yet about how each network stress depends on its deformation gradient and temperature. Also, note that the stress in each network depends on its own natural configuration. The configuration occupied by the system has not yet been

introduced. The difference between the natural configuration of the network at time s and the system configuration at time s is attributed to the phase transition of the material from its fluid - "non cross-linked" state to its solid "cross-linked state"

Using the restrictions due to frame indifference and isotropy, further statements about the form of the constitutive law of each network can be made. $\mathscr{F}$ now has the form

$$\underline{\underline{\sigma}} = \tilde{\mathscr{F}}\left(\frac{\partial \underline{x}(t)}{\partial \underline{X}_{NAT}(t_0)}\left(\frac{\partial \underline{x}(t)}{\partial \underline{X}_{NAT}(t_0)}\right)^T, T(t), T(s), t_0\right) \tag{3.20}$$

where

$$\frac{\partial \underline{x}(t)}{\partial \underline{X}_{NAT}(t_0)}\left(\frac{\partial \underline{x}(t)}{\partial \underline{X}_{NAT}(t_0)}\right)^T = \underline{\underline{B}}_{NAT(t_0)}(t)$$

denotes the left Cauchy-Green strain tensor of the current configuration with respect to the natural or stress free configuration. $\tilde{\mathscr{F}}$ is and isotropic function of $\underline{\underline{B}}_{NAT}$. When $\underline{\underline{(B)}} = \underline{\underline{I}}$, i.e. $\underline{x}(t) = \underline{X}_{NAT}(t_0)$ and $T(t) = T(t_0)$, the material is in its natural reference state and is stress free. It is assumed that the network undergoes small deformations from its natural reference state, so that a linearized model can be used. The natural configuration is different for each network formed after the critical gel point. Because of this, it is convenient to think of a sequence of different configurations as shown in figure 3.3:

- $\underline{X}_{NAT}(t_0)$: Natural or stress free configuration of network formed at time $s = t_0$
- $\underline{X}_{SYS}(t_0)$: Configuration of system of networks formed up to time s. Each would like to be in its natural configuration, but is constrained from being so by the previously formed networks
- $\underline{x}(t)$: The current configuration occupied by the system
- $\bar{\underline{x}}$: A common reference configuration for all networks chosen for convenience and the ultimate applications

Using the chain rule, the deformation gradient can be expanded, to give

$$\frac{\partial \underline{x}(t)}{\partial \underline{X}_{NAT}(t_0)} = \frac{\partial \underline{x}(t)}{\partial \bar{\underline{x}}}\frac{\partial \bar{\underline{x}}}{\partial \underline{X}_{SYS}(t_0)}\frac{\partial \underline{X}_{SYS}(t_0)}{\partial \underline{X}_{NAT}(t_0)} \tag{3.21}$$

$$= \frac{\partial \underline{x}(t)}{\partial \bar{\underline{x}}}\left(\frac{\partial \underline{X}_{SYS}(t_0)}{\partial \bar{\underline{x}}}\right)^{-1}\frac{\partial \underline{X}_{SYS}(t_0)}{\partial \underline{X}_{NAT}(t_0)} \tag{3.22}$$

Note that $\underline{X}_{SYS}(t_0) = \underline{x}(t_0)$ is the current configuration at time t_0.
Let $\underline{x}(t) = \bar{\underline{x}} + \underline{u}(t)$, where $\bar{\underline{x}}$ is some common configuration and $\underline{u}(t)$ is the displacement from the common configuration to the current configuration at time t. Then $\underline{x}(t_0) = \bar{\underline{x}} + \underline{u}(t_0)$.

$$\underline{X}_{SYS}(t_0) = \underline{X}_{NAT}(t_0) + \underline{w}(t_0) \tag{3.23}$$

where $\underline{w}(t_0)$ is the "displacement" due to phase change from the natural configuration to the system configuration at time t_0.
Then

$$\frac{\partial \underline{x}(t)}{\partial \underline{X}_{NAT}(t_0)} = \left(\underline{I} + \frac{\partial \underline{u}(t)}{\partial \underline{\bar{x}}}\right)\left(\underline{I} + \frac{\partial \underline{u}(t_0)}{\partial \underline{\bar{x}}}\right)^{-1}\left(\underline{I} + \frac{\partial \underline{w}(t_0)}{\partial \underline{X}_{NAT}(t_0)}\right) \tag{3.24}$$

Using the small deformation assumption leads to

$$\left|\frac{\partial \underline{u}(t_0)}{\partial \underline{\bar{x}}}\right|, \left|\frac{\partial \underline{w}(t_0)}{\partial \underline{X}_{NAT}(t_0)}\right| \ll 1$$

The deformation gradient with respect to the natural configuration can be linearized

$$\begin{aligned}
\frac{\partial \underline{x}(t)}{\partial \underline{X}_{NAT}(t_0)} &\approx \left(\underline{\underline{I}} + \frac{\partial \underline{u}(t)}{\partial \underline{\bar{x}}}\right)\left(\underline{\underline{I}} - \frac{\partial \underline{u}(t_0)}{\partial \underline{\bar{x}}}\right)\left(\underline{\underline{I}} + \frac{\partial \underline{w}(t_0)}{\partial \underline{X}_{NAT}(t_0)}\right) && (3.25)\\
&\approx \left(\underline{\underline{I}} + \frac{\partial \underline{u}(t)}{\partial \underline{\bar{x}}} - \frac{\partial \underline{u}(t_0)}{\partial \underline{\bar{x}}} + \frac{\partial \underline{w}(t_0)}{\partial \underline{X}_{NAT}(t_0)}\right) && (3.26)
\end{aligned}$$

and the left Cauchy-Green tensor can be linearized to obtain

$$\begin{aligned}
\underline{\underline{B}}_{NAT(t_0)}(t) &\approx \underline{\underline{I}} + \underbrace{\frac{\partial \underline{u}(t)}{\partial \underline{\bar{x}}} + \left(\frac{\partial \underline{u}(t)}{\partial \underline{\bar{x}}}\right)^T}_{2\varepsilon(t)} - \underbrace{\left(\frac{\partial \underline{u}(t_0)}{\partial \underline{\bar{x}}} + \frac{\partial \underline{u}(t_0)}{\partial \underline{\bar{x}}}\right)^T}_{2\varepsilon(t_0)}\\
&\quad + \underbrace{\frac{\partial \underline{w}(t_0)}{\partial \underline{X}_{NAT}(t_0)} + \left(\frac{\partial \underline{w}(t_0)}{\partial \underline{X}_{NAT}(t_0)}\right)^T}_{2\varepsilon_c(t_0)} && (3.27)\\
&= \underline{\underline{I}} + 2\underline{\underline{\varepsilon}}_{NAT(t_0)}(t_0) && (3.28)
\end{aligned}$$

$$\underline{\underline{\varepsilon}}_{NAT(t_0)}(t) = \underline{\underline{\varepsilon}}(t) - \underline{\underline{\varepsilon}}(t_0) + \underline{\underline{\varepsilon}}_c(t_0) \tag{3.29}$$

This states that

Now, using equation 3.28, linearize the stress in the network about the natural or stress free state

the strain $\underline{\underline{\varepsilon}}_{NAT(t_0)}$ from the natural configuration to the current configuration

=

strain $\underline{\underline{\varepsilon}}_c(t_0)$ from the natural configuration to the configuration of the system at time t_0

+

strain $\underline{\underline{\varepsilon}}(t)$ from the common configuration to the current configuration

-

strain $\underline{\underline{\varepsilon}}(t_0)$ from the common configuration the to configuration of system at time t_0

$$\begin{aligned}\mathscr{F}\left(\underline{\underline{B}}_{NAT(t_0)}(t),T(t),T(t_0),t_0\right) &= \mathscr{F}\left(\underline{\underline{I}}+2\underline{\underline{\varepsilon}}_{NAT(t_0)}(t),T(t)-T(t_0)+T(t_0),T(t_0),t_0\right)\\ &= \lambda(t_0)\mathrm{tr}\left(\underline{\underline{\varepsilon}}_{NAT(t_0)}(t)-\overline{\alpha}(t_0)\left(T(t)-T(t_0)\right)\underline{\underline{I}}\right)\underline{\underline{I}}\\ &\quad +2\mu(t_0)\left(\underline{\underline{\varepsilon}}_{NAT(t_0)}(t)-\overline{\alpha}(t_0)\left(T(t)-T(t_0)\right)\underline{\underline{I}}\right)\end{aligned} \tag{3.30}$$

The material properties are given by the Lamé modulus $\lambda(t_0)$, the shear modulus $\mu(t_0)$ and the coefficient of thermal expansion $\bar{\alpha}(t_0)$. The bulk modulus is introduced by the relation

$$\lambda(t_0) = K(t_0) - \frac{2}{3}\mu(t_0) \tag{3.31}$$

All these properties are associated with the network formed at time t_0.

Note that $\underline{\underline{\sigma}} = 0$ when $\underline{\underline{\varepsilon}}_{NAT}(t_0)(t) = 0$ and $T(t) = T_0$ as it should be. The expression for $\underline{\underline{\varepsilon}}_{NAT(t_0)}$ int terms of $\varepsilon(t)$, $\varepsilon(t_0)$ and $\varepsilon_c(t_0)$ can now be substituted in the constitutive equation.

Next consider the network formed at time s. Frame indifference and isotropy yields the constitutive equation in such a network.

$$\underline{\underline{\sigma}} = \mathscr{F}\left(\frac{\partial \underline{x}(t)}{\partial \underline{X}_{NAT}(s)}\left(\frac{\partial \underline{x}(t)}{\partial \underline{X}_{NAT}(s)}\right)^T, T(t), T(s), t_0\right) \tag{3.32}$$

The deformation gradient can again be decomposed using a common configuration for all networks as well a system configuration of all networks. Also, using a small displacement assumption the deformation gradient can be linearized.

$$\frac{\partial \underline{x}(t)}{\partial \underline{X}_{NAT}(s)} = \frac{\partial \underline{x}(t)}{\partial \underline{\bar{x}}} \frac{\partial \underline{\bar{x}}}{\partial \underline{X}_{SYS}(s)} \frac{\partial \underline{X}_{SYS}(s)}{\partial \underline{X}_{NAT}(s)} \tag{3.33}$$

$$= \frac{\partial \underline{x}(t)}{\partial \underline{\bar{x}}} \left(\frac{\partial \underline{X}_{SYS}(s)}{\partial \underline{\bar{x}}} \right)^{-1} \frac{\partial \underline{X}_{SYS}(s)}{\partial \underline{X}_{NAT}(s)} \tag{3.34}$$

$$\approx \left(\underline{\underline{I}} + \frac{\partial \underline{u}(t)}{\partial \underline{\bar{x}}} \right) \left(\underline{\underline{I}} - \frac{\partial \underline{u}(s)}{\partial \underline{\bar{x}}} \right) \left(\underline{\underline{I}} + \frac{\partial \underline{w}(s)}{\partial \underline{X}_{NAT}(s)} \right) \tag{3.35}$$

Note that $\underline{X}_{SYS(s)} = \underline{x}(s)$ is the current configuration at time s. As before the linearized deformation gradient is given as

$$\frac{\partial \underline{x}(t)}{\partial \underline{X}_{NAT}(s)} = \left(\underline{\underline{I}} + \frac{\partial \underline{u}(t)}{\partial \underline{\bar{x}}} - \frac{\partial \underline{u}(s)}{\partial \underline{\bar{x}}} + \frac{\partial \underline{w}(s)}{\partial \underline{X}_{NAT}(s)} \right) \tag{3.36}$$

and the left Cauchy-Green tensor is

$$\underline{\underline{B}}_{NAT(s)}(t) \approx \underline{\underline{I}} + \underbrace{\frac{\partial \underline{u}(t)}{\partial \underline{\bar{x}}} + \left(\frac{\partial \underline{u}(t)}{\partial \underline{\bar{x}}} \right)^T}_{2\underline{\underline{\varepsilon}}(t)} - \underbrace{\left(\frac{\partial \underline{u}(s)}{\partial \underline{\bar{x}}} + \frac{\partial \underline{u}(s)}{\partial \underline{\bar{x}}} \right)^T}_{2\underline{\underline{\varepsilon}}(s)}$$
$$+ \underbrace{\frac{\partial \underline{w}(s)}{\partial \underline{X}_{NAT}(s)} + \left(\frac{\partial \underline{w}(s)}{\partial \underline{X}_{NAT}(s)} \right)^T}_{2\underline{\underline{\varepsilon}}_c(s)} \tag{3.37}$$

$$= \underline{\underline{I}} + 2\underline{\underline{\varepsilon}}_{NAT(t)}(s) \tag{3.38}$$

$$\underline{\underline{\varepsilon}}_{NAT(s)}(t) = \underline{\underline{\varepsilon}}(t) - \underline{\underline{\varepsilon}}(s) + \underline{\underline{\varepsilon}}_c(s) \tag{3.39}$$

The stress in the network formed at time s is

$$\mathscr{F}\left(\underline{\underline{B}}_{NAT(s)}(t), T(t), T(s), s \right) = \mathscr{F}\left(\underline{\underline{I}} + 2\underline{\underline{\varepsilon}}_{NAT(s)}(t), T(t) - T(s) + T(s), T(s), s \right)$$
$$= \lambda(s) \mathrm{tr}\left(\underline{\underline{\varepsilon}}_{NAT(s)}(t) - \overline{\alpha}(s)\left(T(t) - T(s)\right) \underline{\underline{I}} \right) \underline{\underline{I}}$$
$$+ 2\mu(s)\left(\underline{\underline{\varepsilon}}_{NAT(s)}(t) - \overline{\alpha}(s)\left(T(t) - T(s)\right) \underline{\underline{I}} \right) \tag{3.40}$$

The total stress in all the networks is now given by combining (3.30) and (3.40) in equation (3.19):

$$
\begin{aligned}
\underline{\underline{\sigma}}(t) &= \phi_0 \Big\{ \lambda(t_0) \mathrm{tr}\left(\underline{\underline{\varepsilon}}_{NAT(t_0)}(t) - \overline{\alpha}(t_0)\left(T(t)-T(t_0)\right) \underline{\underline{I}} \right) \underline{\underline{I}} \\
&\quad + 2\mu(t_0) \left(\underline{\underline{\varepsilon}}_{NAT(t_0)}(t) - \overline{\alpha}(t_0)\left(T(t)-T(t_0)\right) \underline{\underline{I}} \right) \Big\} \\
&\quad \int_{t_0}^{t} \dot{\phi}(s) \Big\{ \lambda(s) \mathrm{tr}\left(\underline{\underline{\varepsilon}}_{NAT(s)}(t) - \overline{\alpha}(s)\left(T(t)-T(s)\right) \underline{\underline{I}} \right) \underline{\underline{I}} \\
&\quad + 2\mu(s) \left(\underline{\underline{\varepsilon}}_{NAT(s)}(t) - \overline{\alpha}(s)\left(T(t)-T(s)\right) \underline{\underline{I}} \right) \Big\} \mathrm{d}s
\end{aligned}
\tag{3.41}
$$

Introducing the bulk modulus,

$$
\lambda(s) = K(s) - \frac{2}{3}\mu(s), \tag{3.42}
$$

the final constitutive relation becomes,

$$
\begin{aligned}
\underline{\underline{\sigma}}(t) &= \phi_0 \Big\{ K(t_0) \mathrm{tr}\left(\underline{\underline{\varepsilon}}_{NAT(t_0)}(t) - \overline{\alpha}(t_0)\left(T(t)-T(t_0)\right) \underline{\underline{I}} \right) \underline{\underline{I}} \\
&\quad + 2\mu(t_0) \left(\underline{\underline{\varepsilon}}_{NAT(t_0)}(t) - \frac{1}{3}\mathrm{tr}\left(\underline{\underline{\varepsilon}}_{NAT(t_0)}(t) \right) \underline{\underline{I}} \right) \Big\} \\
&\quad \int_{t_0}^{t} \dot{\phi}(s) \Big\{ K(s) \mathrm{tr}\left(\underline{\underline{\varepsilon}}_{NAT(s)}(t) - \overline{\alpha}(s)\left(T(t)-T(s)\right) \underline{\underline{I}} \right) \underline{\underline{I}} \\
&\quad + 2\mu(s) \left(\underline{\underline{\varepsilon}}_{NAT(s)}(t) - \frac{1}{3}\mathrm{tr}\left(\underline{\underline{\varepsilon}}_{NAT(s)}(t_0) \right) \underline{\underline{I}} \right) \Big\} \mathrm{d}s
\end{aligned}
\tag{3.43}
$$

Equivalence to the previously derived result (3.15) can be established by choosing the completely non-cross-linked configuration as a common reference configuration (i.e. $t_0 = \phi_0 = \underline{\underline{\varepsilon}}_{NAT(t_0)} = 0$). Also the strain from the natural configuration will be given as the difference between the current strain, the strain when the network was created and the addition of the curing strains as given in equation (3.39). Finally, only strains in epoxy networks have been considered. Therefore the capability of the uncured liquid resin and hardener mixture to hold normal stresses needs to be included.

Chose equation (3.43) and substitute $\underline{\underline{\varepsilon}}_{NAT(s)} = \underline{\underline{\varepsilon}}(t) - \underline{\underline{\varepsilon}}(s) + \underline{\underline{\varepsilon}}_c(s)$ or chose equation (3.15) directly and group it into three different terms

$$
\begin{aligned}
\underline{\underline{\sigma}}(t) \;=\; & \left(\int_0^t \frac{\mathrm{d}\phi(s)}{\mathrm{d}s}K(s)\mathrm{d}s\right)\mathrm{tr}(\underline{\underline{\varepsilon}}(t))\underline{\underline{1}} + \left(2\int_0^t \frac{\mathrm{d}\phi(s)}{\mathrm{d}s}\mu(s)\mathrm{d}s\right)\left(\underline{\underline{\varepsilon}}(t) - \frac{1}{3}\mathrm{tr}(\underline{\underline{\varepsilon}}(t))\underline{\underline{1}}\right) \\
& -3\cdot\underline{\underline{1}}\left(\int_0^t \frac{\mathrm{d}\phi(s)}{\mathrm{d}s}K(s)\alpha(s)\mathrm{d}s\right)(T(t)-T(0)) \\
& -\left\{\int_0^t \frac{\mathrm{d}\phi(s)}{\mathrm{d}s}K(s)\mathrm{tr}(\underline{\underline{\varepsilon}}(s))\mathrm{d}s\underline{\underline{1}} + 2\int_0^t \frac{\mathrm{d}\phi(s)}{\mathrm{d}s}\mu(s)\left(\underline{\underline{\varepsilon}}(s) - \frac{1}{3}\mathrm{tr}(\underline{\underline{\varepsilon}}(s))\underline{\underline{1}}\right)\mathrm{d}s\right. \\
& \left. -3\cdot\underline{\underline{1}}\int_0^t \frac{\mathrm{d}\phi(s)}{\mathrm{d}s}K(s)\alpha(s)(T(s)-T(0))\mathrm{d}s\right\} \\
& + \int_0^t \frac{\mathrm{d}\phi(s)}{\mathrm{d}s}K(s)\mathrm{tr}(\underline{\underline{\varepsilon}}_c(s))\mathrm{d}s\cdot\underline{\underline{1}} + 2\int_0^t \frac{\mathrm{d}\phi(s)}{\mathrm{d}s}\mu(s)\left(\underline{\underline{\varepsilon}}_c - \frac{1}{3}\mathrm{tr}(\underline{\underline{\varepsilon}}_c(s))\underline{\underline{1}}\right)\mathrm{d}s \qquad (3.44)
\end{aligned}
$$

Equation (3.44) has the mathematical form

$$
\underline{\underline{\sigma}}(t) = K^*(t)\mathrm{tr}(\underline{\underline{\varepsilon}}(t))\underline{\underline{1}} + 2\mu^*(t)\left(\underline{\underline{\varepsilon}}(t) - \frac{1}{3}\mathrm{tr}(\underline{\underline{\varepsilon}}(t))\underline{\underline{1}}\right) - 3\cdot\underline{\underline{1}}(K\alpha)^*(t)(T(t)-T(0)) + \underline{\underline{S}}^{cure}(t), \qquad (3.45)
$$

in which $\underline{\underline{S}}^{cure}(t)$ represents the last two groups of terms in equation (3.44). This has the appearance of the constitutive equation for linear isotropic elasticity, but with a term $\underline{\underline{S}}^{cure}(t)$ that arises from two sources: contraction due to curing and the preceding strain history. $\underline{\underline{S}}^{cure}(t)$ will be called a "curing" stress. $K^*(t)$ is the bulk modulus of the system is defined by

$$
K^*(t) = \int_0^t \frac{\mathrm{d}\phi(s)}{\mathrm{d}s}K(s)\mathrm{d}s. \qquad (3.46)
$$

$\mu^*(t)$ is the shear modulus for the system of networks and is defined by

$$
\mu^*(t) = \int_0^t \frac{\mathrm{d}\phi(s)}{\mathrm{d}s}\mu(s)\mathrm{d}s. \qquad (3.47)
$$

$(K\alpha)^*(t)$ is a combined bulk-thermal expansion modulus for the system of networks and is defined by

$$
(K\alpha)^*(t) = \int_0^t \frac{\mathrm{d}\phi(s)}{\mathrm{d}s}K(s)\alpha(s)\mathrm{d}s. \qquad (3.48)
$$

Since the extent of reaction ϕ increases monotonically with time, it is possible to change the variable of integration in equation (3.46) – (3.48) from time s to extent of cure $\phi(s)$. The expression for the moduli then become

$$K^*(\phi) = \int_{\phi(t)=0}^{\phi(t)} K(\overline{\phi})\mathrm{d}\overline{\phi} \tag{3.49}$$

$$\mu^*(\phi) = \int_{\phi(t)=0}^{\phi(t)} \mu(\overline{\phi})\mathrm{d}\overline{\phi} \tag{3.50}$$

$$(K\alpha)^*(\phi) = \int_{\phi(t)=0}^{\phi(t)} K(\overline{\phi})\alpha(\overline{\phi})\mathrm{d}\overline{\phi} \tag{3.51}$$

Equation (3.49) – (3.51) relate the moduli of the system to the extend of cure.

It should be noted that choosing the liquid configuration as a common reference configuration is very convenient from a modeling point of view, especially when looking towards finite elements based analysis. However during this manufacturing process the initial (liquid) configuration might undergo large changes. For example when a mold with fiber mats and epoxy is compressed, part of the liquid resin usually spills out. This loss of material is hard to account for. Therefore when simulating the curing process it is convenient to chose the final configuration that can be observed in a real part as the initial liquid configuration for a FE simulation. Using the gelation point as the initial configuration might be more appropriate since from that point on, no loss of material can be expected. However due to temperature gradients in the material the gelation point is different at different points within the material. Therefore the common configuration for the different networks of material points would vary throughout a part.

3.3 Determination of material properties

3.3.1 Mechanical properties

The plane wave modulus, shear modulus and degree of cure are measured as a function of time through concurrent Raman and Brillouin light scattering [59, 60, 74]. The plane wave modulus M is the elastic constant measured in a uniaxial strain field. It is related to the Lamé constants and the bulk modulus by $M = \lambda + 2\mu = K + \frac{4}{3}\mu$. Raman scattering provides cure information and Brillouin light scattering provides mechanical information. This optical measurement method has the advantage of yielding mechanical and chemical properties without touching the sample. In contrast classical methods that measure the mechanical properties during cure, such as rheometers or bending tests [75], actively influence the boundary value problem that is needed to extract the per-network properties for this

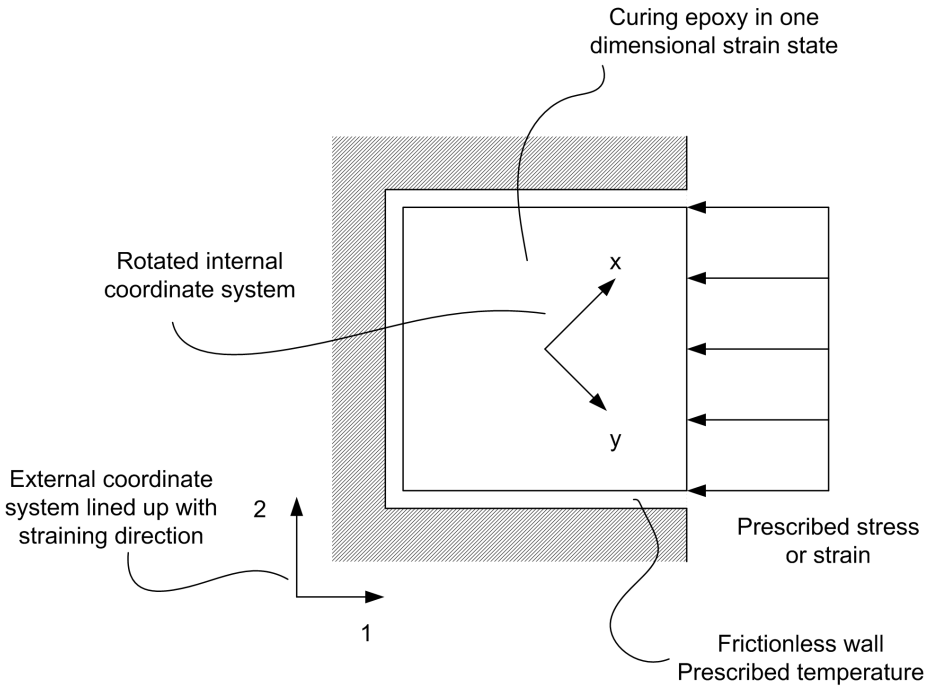

Figure 3.4 Uniaxial strain boundary value problem used to determine material properties

approach.

It is important to note that experimentally, the response of all networks is measured simultaneously. The individual response of each network has to be adjusted so that the total simulated response follows the total experimentally measured response. To this end, assume that the network is cured in a uniaxial strain field. After some time, a sudden jump in strain is applied. The jump needs to be considered for all times during the curing history, because the material properties need to be extracted for all times during the curing history. The stress response is measured in the direction the strain jump is applied, and in the perpendicular direction. The BVP is depicted in figure 3.4. It also shows the meaning of the plane wave modulus, M. Two coordinate systems are shown, one aligned with the strain direction and an internal coordinate system with some arbitrary direction. The latter is a useful tool to ensure the numerical implementation into the finite element program is correct. While reaction forces are reported in the global coordinate system lined up with the axis of deformation, internally the finite element program calculates stresses and strains with respect to the rotated coordinate system. The stress and strain tensor will be fully populated and possible error in the programming of the material model will be easier to find.
Ignoring the influence of temperature, the stresses before and after the jump, respectively,

are:

$$\underline{\underline{\sigma}} = \begin{bmatrix} \sigma_{11} & 0 & 0 \\ 0 & \sigma_{22} & 0 \\ 0 & 0 & \sigma_{33} = \sigma_{22} \end{bmatrix} \tag{3.52}$$

Thus,

$$\sigma_{11} = \int_0^t \dot{\phi} \left\{ K\left[\varepsilon(t) - \varepsilon(s) + 3\varepsilon_c(s)\right] + \frac{4}{3}\mu\left[\varepsilon(t) - \varepsilon(s)\right] \right\} \mathrm{d}s + (1-\phi(t))K_{liq}\varepsilon(t) \tag{3.53}$$

$$\begin{aligned} \sigma_{11} + \Delta\sigma_{11} = \int_0^t \dot{\phi} \left\{ K\left[\varepsilon(t) + \Delta\varepsilon - \varepsilon(s) + 3\varepsilon_c(s)\right] + \frac{4}{3}\mu\left[\varepsilon(t) + \Delta\varepsilon - \varepsilon(s)\right] \right\} \mathrm{d}s \\ + (1-\phi(t))K_{liq}(\varepsilon(t) + \Delta\varepsilon) \end{aligned} \tag{3.54}$$

The difference between the two is

$$\begin{aligned} \Delta\sigma_{11} &= \Delta\varepsilon \int_0^t \dot{\phi} \left\{ K(s) + \frac{4}{3}\mu(s) \right\} \mathrm{d}s + \Delta\varepsilon(1-\phi)K_{liq} && (3.55) \\ &= \Delta\varepsilon \int_0^t \dot{\phi} M(s) \mathrm{d}s + \Delta\varepsilon(1-\phi)K_{liq} && (3.56) \end{aligned}$$

The strain tensor of the uniaxial strain field is:

$$\underline{\underline{\varepsilon}} = \begin{bmatrix} \varepsilon & 0 & 0 \\ 0 & 0 & 0 \\ 0 & 0 & 0 \end{bmatrix} \tag{3.57}$$

This can be written as

$$\Delta\sigma_{11} = \Delta\varepsilon_{11} M_{tot}(t) \tag{3.58}$$

where

$$\begin{aligned} M_{tot} &= \int_0^t \dot{\phi} M(s) \mathrm{d}s + (1-\phi(t))K_{liq} && (3.59) \\ &= \int_0^t \dot{\phi} \left\{ K(s) + \frac{4}{3}\mu(s) \right\} \mathrm{d}s + (1-\phi(t))K_{liq} && (3.60) \end{aligned}$$

is the total plane wave modulus, and $M(s)$ is the plane wave modulus of each network formed at time s. Differentiating with respect to time, t, re-arranging and applying the chain rule yields the per-network properties.

$$M(\phi) = \frac{dM_{tot}(\phi)}{d\phi} + K_{liq} \tag{3.61}$$

The same boundary value problem (BVP) can be used to determine a second set of properties. For the direction perpendicular to the one in which the strain is applied, it follows that:

$$\begin{aligned} \Delta\sigma_{22} &= \Delta\varepsilon \int_0^t \dot{\phi}(K(s) - \frac{2}{3}\mu(s))\mathrm{d}s + \Delta\varepsilon(1-\phi)K_{liq} && (3.62)\\ &= \Delta\varepsilon \int_0^t \dot{\phi}\lambda(s)\mathrm{d}s + \Delta\varepsilon(1-\phi)K_{liq} && (3.63) \end{aligned}$$

For this particular BVP,

$$\Delta\sigma_{22} = \Delta\varepsilon_{11}\lambda_{tot}(t) \tag{3.64}$$

where

$$\lambda_{tot} = \int_0^t \dot{\phi}(s)\lambda(s)\mathrm{d}s + (1-\phi(t))K_{liq} \tag{3.65}$$

so that the per-network Lamé constant is

$$\lambda(\phi) = \frac{d\lambda_{tot}(\phi)}{d\phi} + K_{liq} \tag{3.66}$$

This can be transformed to yield the per network shear and bulk moduli:

$$\begin{aligned} \mu(\phi) &= \frac{d\mu_{tot}}{d\phi} && (3.67)\\ K(\phi) &= \frac{dK_{tot}}{d\phi} + K_{liq} && (3.68) \end{aligned}$$

Figures 3.5 and 3.6 show representative experimental data for M and μ as functions of extent of cure. For mathematical convenience the transition of these material properties is currently modeled with an analytical function:

$$X_{\text{tot}}(\phi) = \frac{\arctan\left(\left(\phi-\frac{1}{2}\right)\beta_X\right)}{\arctan\left(\frac{\beta_X}{2}\right)}(X_f - X_s) + \left(\frac{X_f + X_s}{2}\right) \tag{3.69}$$

$$X = \{\mu, M\} \tag{3.70}$$

This leads to closed form solutions for the per-network properties:

$$\mu(\phi) = \frac{1}{2}\frac{\beta_\mu\left(\mu_f - \mu_s\right)}{\left(1+(\phi-1/2)^2{\beta_\mu}^2\right)\arctan\left(1/2\,\beta_\mu\right)} \tag{3.71}$$

$$M(\phi) = \frac{1}{2}\frac{\beta_M\left(M_f - M_s\right)}{\left(1+(\phi-1/2)^2{\beta_M}^2\right)\arctan\left(1/2\,\beta_M\right)} + K_{liq} \tag{3.72}$$

$$K = M - \frac{4}{3}\mu \tag{3.73}$$

It should be noted that in reality, gelation occurs. Until gelation, the shear modulus of the material is undetectable and the resin behaves like a viscous fluid. This is shown in figure 3.6. In the current model, a small amount of shear stiffness is assumed even for low amounts of curing. Finally, the bulk modulus of the liquid epoxy is the one measured at the beginning of the experiment.

$$K_{liq} = K_{tot}(0) \tag{3.74}$$

The per network shear modulus and the per network bulk modulus as described by equation (3.71) and equation (3.73) are given in figure 3.7 and figure 3.8. Interpreting the shape of the curve belonging to the bulk modulus does not offer any deeper insight. It should merely be stated that the shape is a direct result of the mathematical description chosen to quantify the shear and the plane wave modulus. However it can be noticed that choosing the per network bulk modulus to be constant would be a reasonable starting assumption. A more physically motivated interpretation can be given to the shape of the shear modulus curve. The per network modulus varies widely. The maximum is attained at gelation. This is, in this particular case, at the 50% curing mark. Networks formed at this time have a more important role in the overall stress of the body than networks that are formed earlier or later. Technically, the networks formed before gelation should not carry any shear stress. However this would cause a singularity at gelation. Therefore, also networks formed earlier were made to hold some stress.

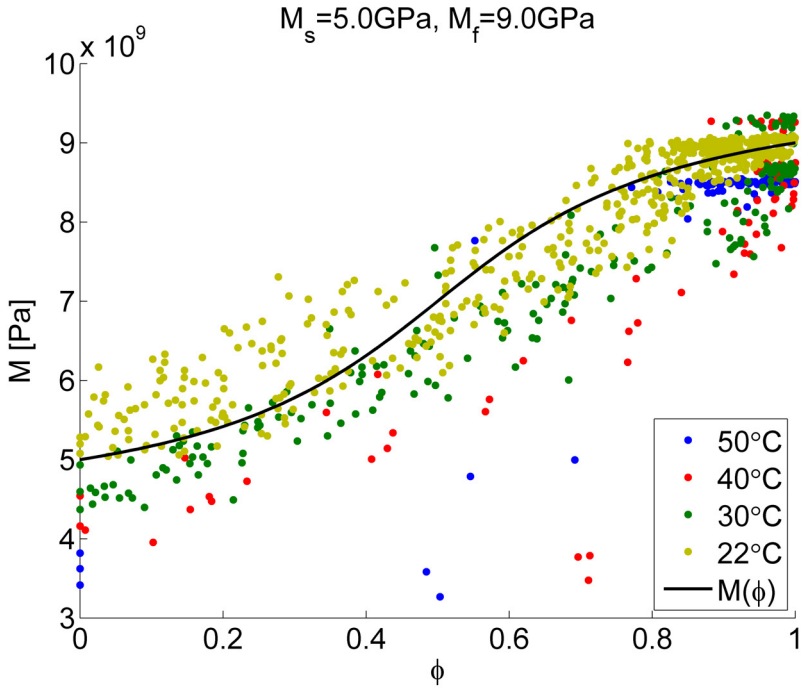

Figure 3.5 Experimental results of Brillouin light scattering

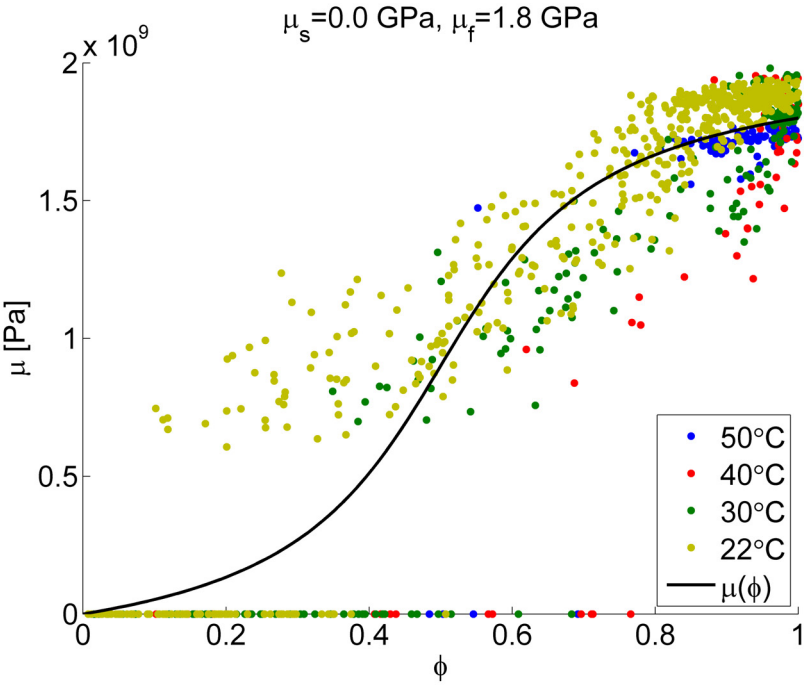

Figure 3.6 Experimental results of Brillouin light scattering

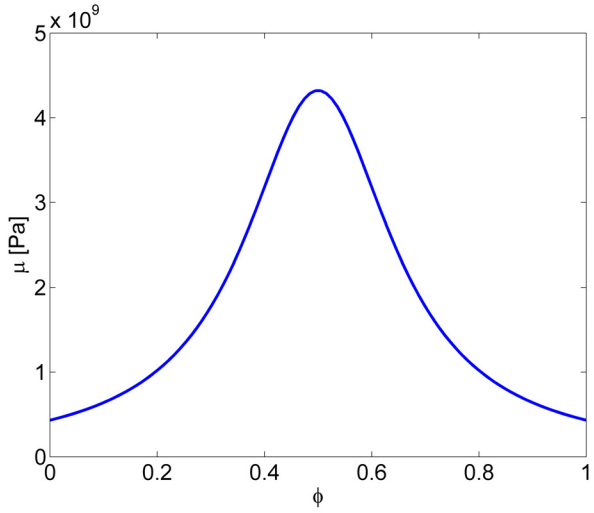

Figure 3.7 Shear modulus of individual networks as a function of the degree of cure

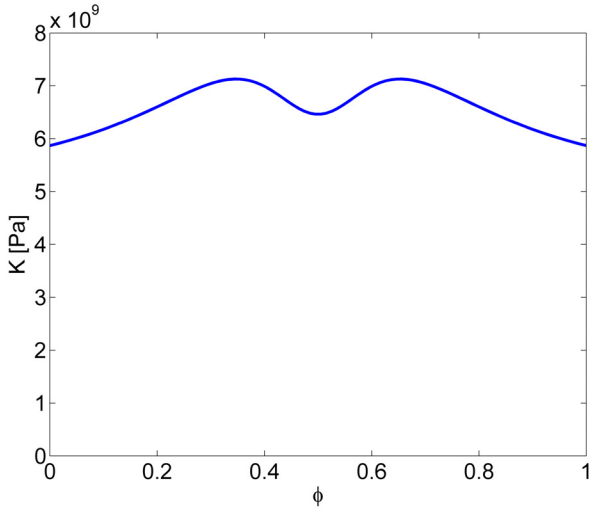

Figure 3.8 Bulk modulus of individual networks as a function of the degree of cure

3.3.2 Cure shrinkage

To determine the correct cure shrinkage a boundary value problem needs to be found, where the change in volume can be measured. Therefore, consider again the uniaxial strain BVP of a curing epoxy sample as shown in figure 3.4. The specimen is free to expand or contract in the 1-direction. No stresses are applied in this direction. The stress and strain tenors are,

$$\underline{\underline{\sigma}} = \begin{bmatrix} \sigma_{11} = 0 & 0 & 0 \\ 0 & \sigma_{22} & 0 \\ 0 & 0 & \sigma_{33} = \sigma_{22} \end{bmatrix} \tag{3.75}$$

Cure shrinkage/volume change	Material	Reference
6.9%	MY750	[76]
4.5@100°C,200 bar	DGEBA/MCDEA	[69]
$>$1%	EPON828/DEP	[37]
2.75% after gelation	Bisphenol F	[77]
$<$2%	Epikote 828/MNA/BDMA	[78]
2%	current study	

Table 3.1 Cure shrinkage in various epoxy materials

and

$$\underline{\underline{\varepsilon}} = \begin{bmatrix} \varepsilon & 0 & 0 \\ 0 & 0 & 0 \\ 0 & 0 & 0 \end{bmatrix} \tag{3.76}$$

The stress in the 1-direction is given by

$$\sigma_{11} = \int_0^t \dot{\phi}(s)M(s)(\varepsilon(t)-\varepsilon(s))\mathrm{d}s + 3\int_0^t \varepsilon_c(s)K(s)\dot{\phi}(s)\mathrm{d}s + (1-\phi(t))\varepsilon(t)K_{liq}, \tag{3.77}$$

and it is equal to zero. There is a monotonic relation between time, t, and degree of cure, ϕ. A change in variables of $t \rightarrow \Phi = \phi(t) =$ and $\dot{\phi}ds \rightarrow d\phi$ leads to:

$$\sigma_{11}(\Phi) = \int_0^\Phi M(\phi)(\varepsilon(\Phi)-\varepsilon(\phi))\mathrm{d}\phi + 3\int_0^\Phi \varepsilon_c(\phi)K(\phi)\mathrm{d}\phi + (1-\Phi)\varepsilon(\Phi)K_{liq} = 0 \tag{3.78}$$

Differentiating with respect to the upper limit, observing that no stress was applied in the 1-direction and rearranging, yields the final answer for the cure shrinkage

$$\varepsilon_c(\Phi) = \frac{1}{3K(\Phi)}\left[\left(\varepsilon(\Phi) - (1-\Phi)\frac{d\varepsilon(\Phi)}{\mathrm{d}\Phi}\right)K_{liq} - \frac{d\varepsilon(\Phi)}{\mathrm{d}\Phi}\int_0^\Phi M(\phi)\mathrm{d}\phi\right] \tag{3.79}$$

The total cure shrinkage of all networks $\varepsilon(\Phi)$ can be measured through a gravimetric test method [76]. Table 3.1 gives an account of the results that have been obtained for various epoxy systems.

The per network shrinkage is shown in figure 3.9. Although the per network properties have been chosen such that overall, a linear cure shrinkage is obtained, choosing a constant cure shrinkage per network would have been a good starting point.

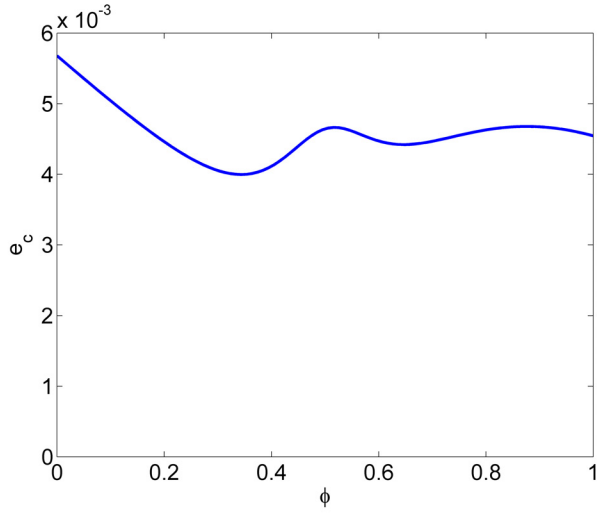

Figure 3.9 Bulk modulus of individual networks as a function of the degree of cure

(Linear) Coefficient of thermal expansion (ppm/K)	Material	Reference
65	Bisphenol F/HHPA	[66]
61	Epon862/Epikure 3234	[64]

Table 3.2 Thermal expansion coefficient of various epoxies

3.3.3 Thermal expansion

Data for thermal expansion is sparse in the literature and cited in table 3.2. Since no data was obtainable for non-crosslinked epoxy the thermal expansion coefficients are the same for cured and uncured networks.

3.3.4 Thermal conductivity

Thermal conductivity can be modeled through a rule of mixture relation.

$$K = K_{liquid}(1-\phi) + K_{\text{all networks}} \tag{3.80}$$

Varshney et al. [63], have investigated the thermal conductivity of EPON 862 resin, curing agent DETDA and their mixture as well as the cross linked epoxy using molecular dynamics simulations. However the data differs more for different types of simulations than for crosslinked vs. non-crosslinked networks. Therefore, currently a constant value is chosen for the thermal conductivity.

3.4 Numerical implementation

The simulations are carried out using the commercial finite element analysis package ABAQUS. Much use has been made of the possibility to first calculate the thermo-chemical problem and in a second step the generation of stresses. Whenever possible quadratic elements were used both for the heat conduction as well as stress balance. Identical meshes were used for both calculations to ease the export of data from one calculation to the other. Of course it is possible to solve the thermal and mechanical problem simultaneously through a fully coupled analysis. At first glance this doesn't impose a significant change in problem size since the number of unknowns increases from six to seven (from force balance to fully coupled analysis). However during the calculations it has been observed that the thermal problem needs significantly more iterations to finish the simulation than the mechanical one. Since each iteration of the mechanical part is much costly to compute one should avoid increasing the number of iterations whenever possible and thus solve the two problems separately.

3.4.1 Heat conduction and cure

The equation describing the extent of cure enters the ABAQUS simulation through the heat source term and can be incorporated through a user defined heat generation subroutine (HETVAL subroutine). The degree of cure constitutes an internal state variable. It only implicitly depends on the surrounding material through the spatial dependence of the temperature.

The starting equations to describe the curing process (for the Shanku Model) of the epoxy is given by

$$\frac{d\phi}{dt} = A_1 \exp\left(\frac{-\Delta E}{RT}\right)(1-\phi) \tag{3.81}$$

This equation is approximated using a central difference scheme around the time $t+\Delta t/2$. Δt is the time step during the solution process. Thus,

$$\left.\frac{d\phi}{dt}\right|_{t+\frac{\Delta t}{2}} = A_1 \exp\left(\frac{-\Delta E}{RT(t+\frac{\Delta t}{2})}\right)\left(1-\phi\left(t+\frac{\Delta t}{2}\right)\right) \tag{3.82}$$

The degree of cure $\phi(t)$ and temperature $T(t)$ are the solution values at the end of the previous increment. The value for the degree of cure at the end of the current increment are solved for. The temperature at the end of the increment is solved by ABAQUS. With this in mind the values in the middle of the step can be approximated

as $\phi(t+\Delta t)/2 = (\phi(t)+\phi(t+\Delta t))/2$ and $T(t+\Delta t)/2 = (T(t)+T(t+\Delta t))/2$.

$$\frac{\phi(t+\Delta t)-\phi(t)}{\Delta t} = A_1 \exp\left(\frac{-\Delta E}{R\left(\frac{T(t+\Delta t)}{2}+\frac{T(t)}{2}\right)}\right)\left(1-\frac{\phi(t+\Delta t)+\phi(t)}{2}\right) \tag{3.83}$$

Rearranging, yields the finial answer,

$$\phi(t+\Delta t) = \frac{\Delta t A_1 \exp\left(\frac{-\Delta E}{R\left(\frac{T(t+\Delta t)}{2}+\frac{T(t)}{2}\right)}\right)(1-\frac{\phi(t)}{2})+\phi(t)}{1+\frac{\Delta t}{2}A_1 \exp\left(\frac{-\Delta E}{R\left(\frac{T(t+\Delta t)}{2}+\frac{T(t)}{2}\right)}\right)} \tag{3.84}$$

An analytical solution is available for the perfect conductor and perfect insulator. Other temperature histories can be checked with the commercial code MATLAB. If a more general form of the curing equation like (2.10) had been chosen the curing equation would be non-linear in the degree of cure and a Newton-Raphson algorithm could be used to solve the problem numerically. A comparison of the FE solutions with analytical solutions is given in the Appendix D.

3.4.2 Consistent Jacobian

The evolution of stress and mechanical properties is incorporated into an ABAQUS user material subroutine (UMAT). The inputs provided to the user are strains at the beginning of the increment and strain increments and the program requires the user to provide the stress at the end of the increment as well the Jacobian (or tangent stiffness matrix) to be used in that increment.

Numerically the integration will be done with the trapezoidal rule:

$$\int_0^{t+\Delta t} f(s)\mathrm{d}s \approx \int_0^t f(s)\mathrm{d}s + \frac{f(t+\Delta t)+f(t)}{2}\Delta t \tag{3.85}$$

The sum that represents the integral can be increased in every time increment in ABAQUS by only the current portion and the entire integral does not have to be recalculated.

Also for the correct implementation in ABAQUS the correct Jacobian is needed. The algorithmic Jacobian (as opposed to the consistent one) is needed since the influence of a change in strain is altered by the choice of integration algorithm. The required Jacobian is $\frac{\partial \Delta\sigma_{ij}}{\partial \Delta\varepsilon_{kl}}$.

To that end find the change in stress as the difference between the new stress (at the end of the increment) and the old stress (at the beginning of the increment).

$$\Delta\sigma_{ij} = \sigma_{ij}^{new} - \sigma_{ij}^{old} \tag{3.86}$$

only keeping terms depending upon $\Delta\varepsilon$:

$$\begin{aligned}
\Delta\sigma_{ij} &= \int_0^{t^{new}} \frac{d\phi}{\mathrm{d}s} \left(\delta_{ij} K(s) \left(\varepsilon_{ij}(t^{new}) - \varepsilon_{ij}(s) + 3\varepsilon_0(s) - 3\alpha(s)(T(t^{new} - T(s))) \right) \right. \\
&\quad \left. + 2\mu(s) \left(\varepsilon_{ij}(t^{new}) - \varepsilon_{ij}(s) + \varepsilon_0(s) - \delta_{ij} \frac{1}{3} \left(\varepsilon_{kk}(t^{new}) - \varepsilon_{kk}(s) + 3\varepsilon_0(s) \right) \right) \right) \\
&\quad + \delta_{ij}(1-\phi(t)) K_{liq} (\varepsilon_{kk}(t) - 3\alpha_{liq}(T(t^{new} - T(0))) \\
&\quad - \int_0^{t^{old}} \frac{d\phi}{\mathrm{d}s} \left(\delta_{ij} K(s) \left(\varepsilon_{ij}(t^{old}) - \varepsilon_{ij}(s) + 3\varepsilon_0(s) - 3\alpha(s)(T(t^{old} - T(s))) \right) \right. \\
&\quad \left. - 2\mu(s) \left(\varepsilon_{ij}(t^{old}) - \varepsilon_{ij}(s) + \varepsilon_0(s) - \delta_{ij} \frac{1}{3} \left(\varepsilon_{kk}(t^{old}) - \varepsilon_{kk}(s) + 3\varepsilon_0(s) \right) \right) \right) \\
&\quad - \delta_{ij}(1-\phi(t)) K_{liq} (\varepsilon_{kk}(t) - 3\alpha_{liq}(T(t^{old} - T(0)))
\end{aligned} \tag{3.87}$$

Now set $t^{old} = t$, $t^{new} = t + \Delta t$ and $\varepsilon(t^{new}) = \varepsilon(t) + \Delta\varepsilon$. The second part of the equation will be ignored in the following, since it does not depend on $\Delta\varepsilon_{ij}$ and will vanish during the differentiation. More specifically integrals that run till time t and all appearance of $\varepsilon_{ij}(t)$ are not functions of $\Delta\varepsilon_{ij}$. Also, terms only depending on temperature will vanish. Thus,

$$\begin{aligned}
\Delta\sigma_{ij} &= \delta_{ij} \int_0^{t+\Delta t} \dot{\phi} K(s) \Delta\varepsilon_{kk} \mathrm{d}s - \delta_{ij} \int_0^{t+\Delta t} \dot{\phi} K(s) \varepsilon_{kk}(s) \mathrm{d}s \qquad (3.88) \\
&\quad + 2 \int_0^{t+\Delta t} \dot{\phi} \mu(s) \Delta\varepsilon_{ij} \mathrm{d}s - 2 \int_0^{t+\Delta t} \dot{\phi} \mu(s) \varepsilon_{ij}(s) \mathrm{d}s \\
&\quad - \frac{2}{3} \delta_{ij} \int_0^{t+\Delta t} \dot{\phi} \mu(s) \Delta\varepsilon_{kk} \mathrm{d}s + \frac{2}{3} \delta_{ij} \int_0^{t+\Delta t} \dot{\phi} \mu(s) \varepsilon_{kk}(s) \mathrm{d}s \\
&\quad + \delta_{ij}(1 - \phi t + \Delta t) K_{liq} \Delta\varepsilon_{kk} \qquad (3.89)
\end{aligned}$$

All time integrals can be split up as follows

$$
\begin{aligned}
\Delta\sigma_{ij} &= \delta_{ij}\int_0^t \dot{\phi}K(s)\Delta\varepsilon_{kk}\mathrm{d}s + \delta_{ij}\int_t^{t+\Delta t} \dot{\phi}K(s)\Delta\varepsilon_{kk}\mathrm{d}s && (3.90)\\
&\quad -\delta_{ij}\int_0^t \dot{\phi}K(s)\varepsilon_{kk}(s)\mathrm{d}s - \delta_{ij}\int_t^{t+\Delta t} \dot{\phi}K(s)\varepsilon_{kk}(s)\mathrm{d}s && (3.91)\\
&\quad +2\int_0^t \dot{\phi}\mu(s)\Delta\varepsilon_{ij}\mathrm{d}s + 2\int_t^{t+\Delta t} \dot{\phi}\mu(s)\Delta\varepsilon_{ij}\mathrm{d}s && (3.92)\\
&\quad -2\int_0^t \dot{\phi}\mu(s)\varepsilon_{ij}(s)\mathrm{d}s - 2\int_t^{t+\Delta t} \dot{\phi}\mu(s)\varepsilon_{ij}(s)\mathrm{d}s\\
&\quad -\frac{2}{3}\delta_{ij}\int_0^t \dot{\phi}\mu(s)\Delta\varepsilon_{kk}\mathrm{d}s - \frac{2}{3}\delta_{ij}\int_t^{t+\Delta t} \dot{\phi}\mu(s)\Delta\varepsilon_{kk}\mathrm{d}s && (3.93)\\
&\quad +\frac{2}{3}\delta_{ij}\int_0^t \dot{\phi}\mu(s)\varepsilon_{kk}(s)\mathrm{d}s + \frac{2}{3}\delta_{ij}\int_t^{t+\Delta t} \dot{\phi}\mu(s)\varepsilon_{kk}(s)\mathrm{d}s\\
&\quad +\delta_{ij}(1-\phi t+\Delta t)K_{liq}\Delta\varepsilon_{kk} && (3.94)
\end{aligned}
$$

All integrals running from 0 to t and not depending on $\Delta\varepsilon$ can be ignored. All integrals between t and $t+\Delta t$ are approximated with the trapezoidal rule according to the actual FE implementation.

$$
\begin{aligned}
\Delta\sigma_{ij} &= \delta_{ij}\Delta\varepsilon_{kk}\left(\int_0^t \dot{\phi}K\mathrm{d}s + \left(\dot{\phi}(t)K(t)+\dot{\phi}(t+\Delta t)K(t+\Delta t)\right)\frac{\Delta t}{2}\right) && (3.95)\\
&\quad -\delta_{ij}\left(\phi(t)K(t)\varepsilon_{kk}(t)+\phi(t+\Delta t)K(t+\Delta t)(\varepsilon_{kk}(t)+\Delta\varepsilon_{kk})\right)\frac{\Delta t}{2} && (3.96)\\
&\quad +2\Delta\varepsilon_{ij}\left(\int_0^t \dot{\phi}\mu\mathrm{d}s + \left(\dot{\phi}(t)\mu(t)+\dot{\phi}(t+\Delta t)\mu(t+\Delta t)\right)\frac{\Delta t}{2}\right) && (3.97)\\
&\quad \phi(t)\mu(t)\varepsilon_{ij}(t)+\phi(t+\Delta t)\mu(t+\Delta t)(\varepsilon_{ij}(t)+\Delta\varepsilon_{ij}) && (3.98)\\
&\quad \frac{2}{3}\delta_{ij}\Delta\varepsilon_{kk}\left(\int_0^t \dot{\phi}\mu\mathrm{d}s + \left(\dot{\phi}(t)\mu(t)+\dot{\phi}(t+\Delta t)\mu(t+\Delta t)\right)\frac{\Delta t}{2}\right)\frac{\Delta t}{2} && (3.99)\\
&\quad -\delta_{ij}\left(\phi(t)\mu(t)\varepsilon_{kk}(t)+\phi(t+\Delta t)\mu(t+\Delta t)(\varepsilon_{kk}(t)+\Delta\varepsilon_{kk})\right) && (3.100)\\
&\quad +\delta_{ij}(1-\phi t+\Delta t)K_{liq}\Delta\varepsilon_{kk} && (3.101)
\end{aligned}
$$

Simplifying and taking the derivative with respect to $\Delta\varepsilon_{kl}$ yields the final answer for the Jacobian.

$$
\begin{aligned}
\frac{\partial\Delta\sigma_{ij}}{\partial\Delta\varepsilon_{kl}} &= \delta_{ij}\delta_{kl}\left(\int_0^t \dot{\phi}K\mathrm{d}s + \frac{\dot{\phi}(t)Kt\Delta t}{2} - \frac{2}{3}\int_0^t \dot{\phi}\mu\mathrm{d}s - \frac{2}{3}\frac{\dot{\phi}(t)\mu(t)\Delta t}{2} + (1-\phi(t+\Delta t))K_{liq}\right)\\
&\quad 2\delta_{ik}\delta_{jl}\left(\int_0^t \dot{\phi}\mu\mathrm{d}s - \frac{\dot{\phi}(t)\mu(t)\Delta t}{2}\right) && (3.102)
\end{aligned}
$$

or in matrix form

$$\begin{pmatrix} \Delta\sigma_{11} \\ \Delta\sigma_{22} \\ \Delta\sigma_{33} \\ \Delta\sigma_{12} \\ \Delta\sigma_{23} \\ \Delta\sigma_{13} \end{pmatrix} = \begin{bmatrix} \tilde{\lambda}(t)+2\tilde{\mu}(t) & \tilde{\lambda}(t) & \tilde{\lambda}(t) & 0 & 0 & 0 \\ \tilde{\lambda}(t) & \tilde{\lambda}(t)+2\tilde{\mu}(t) & \tilde{\lambda}(t) & 0 & 0 & 0 \\ \tilde{\lambda}(t) & \tilde{\lambda}(t) & \tilde{\lambda}(t)+2\tilde{\mu}(t) & 0 & 0 & 0 \\ 0 & 0 & 0 & \tilde{\mu}(t) & 0 & 0 \\ 0 & 0 & 0 & 0 & \tilde{\mu}(t) & 0 \\ 0 & 0 & 0 & 0 & 0 & \tilde{\mu}(t) \end{bmatrix} \begin{pmatrix} \Delta\varepsilon_{11} \\ \Delta\varepsilon_{22} \\ \Delta\varepsilon_{33} \\ \Delta\gamma_{12} \\ \Delta\gamma_{23} \\ \Delta\gamma_{13} \end{pmatrix} \tag{3.103}$$

where,

$$\begin{aligned} \tilde{\lambda}(t) &= \left(\int_0^t \dot{\phi} K \mathrm{d}s + \frac{\dot{\phi}(t) K t \Delta t}{2} - \frac{2}{3}\int_0^t \dot{\phi}\mu \mathrm{d}s - \frac{2}{3}\frac{\dot{\phi}(t)\mu(t)\Delta t}{2} \right. \\ &\quad \left. + (1-\phi(t+\Delta t))K_{liq} \right) \qquad (3.104) \\ \tilde{\mu}(t) &= \left(\int_0^t \dot{\phi}\mu \mathrm{d}s - \frac{\dot{\phi}(t)\mu(t)\Delta t}{2} \right) \qquad (3.105) \end{aligned}$$

Therefore incrementally the curing of the epoxy as presented in this chapter can be described in a form that is similar to the one known from linear elasticity. Finally a very important point can be observed about the proposed model: once the epoxy is fully cured, the material will behave in a linear elastic fashion because $\tilde{\mu}(t) \to \mu_\infty$ and $\tilde{\lambda}(t) \to \lambda_\infty$ as $t \to \infty$. The model as presented so far is capable of describing the evolution of residual stresses due to curing and thermal gradients. However the presence of residual stresses will not have any effect on the response of the fully cured material in the context of the material model presented. This is because the presented material model is related to small strain linear elasticity, where the change in stress due to externally applied loads is independent of existing residual stress. In this case the superposition principle can be used. The incorporation of changes in the response due to pre-existing residual stresses will be discussed in chapter 5.

3.5 Conclusion

A model that can describe the evolution of mechanical properties has been formulated in two different ways. First, a one dimensional spring model was introduced and generalized

to give a three dimensional, small strain model. Then a very general approach from large displacement considerations has been taken and sufficiently specialized to yield a result for small strains. The model is based on the notion of networks, occupying the same body and being generated at different times and in different stress free reference configurations. Brillouin and Raman light scattering data has been used to characterize the material properties of epoxy networks as a function of cure and a way has been described to find the per network cure shrinkage. The proposed model is capable of quantifying residual stresses but it cannot produce a non-linear response to mechanical loading. This latter aspect is re-visited in chapter 5.

Chapter 4
Applications

4.1 Curing of pure epoxy

As a first example, the temperature, degree of cure and cure stress development in a pure epoxy cube will be considered. Two different size cubes are considered in order to show the effect of size on curing. A graphical representation of the cubes is shown in figure 4.1. The cubes have side length of 1 mm and 8 mm, respectively. Due to the symmetric nature of the boundary value problem, the size of the finite element model can be reduced to $1/8^{th}$. The boundary conditions on the original cube are such that the outside surfaces are traction free. The temperature on the entire boundary is prescribed. The epoxy is completely uncured at 295K (22°C) at time $t = 0$. The temperature is ramped up linearly within 100 seconds to 323K (22°C). It is held at that level subsequently for 3,600 seconds. The boundary temperature is then reduced to room temperature within 100 seconds. This temperature time history is shown in figure 4.2. In the symmetric FE model, the boundary conditions on the outside are identical to the original model. The origin of the coordinate system is at a corner on an inner surface. On the inner "cut" planes symmetry demands that the normal displacements are set to zero. Also, the heat flux is zero on these planes, which is equivalent to a perfectly insulating wall.

Figure 4.3 shows the temperature field in the two cubes as they cure. As can be seen in figure 4.3(a), the temperature is uniform in the small sample throughout the entire time and follows the prescribed boundary condition very closely. On the other hand, in the larger sample the temperature is not uniform. During the time at which the boundary temperature is ramped up, the inside temperature lags the outside temperature. That means the during the first 100 seconds, the slope of the degree of cure is lower in the center compared to the outside. The low conductivity of the material puts a limit on how quickly a steady or uniform state is reached. Due to the exothermic reaction of the epoxy, heat or energy will be released into the system. This heat causes the temperature to rise in the large sample. Low conductivity limits the size of the heat flux and excess heat cannot be transported to

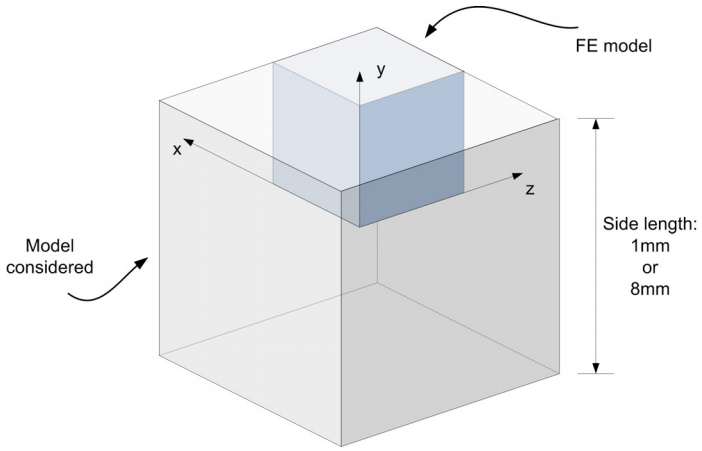

Figure 4.1 Pure epoxy cube, symmetry has been used, to reduce model size to one eights

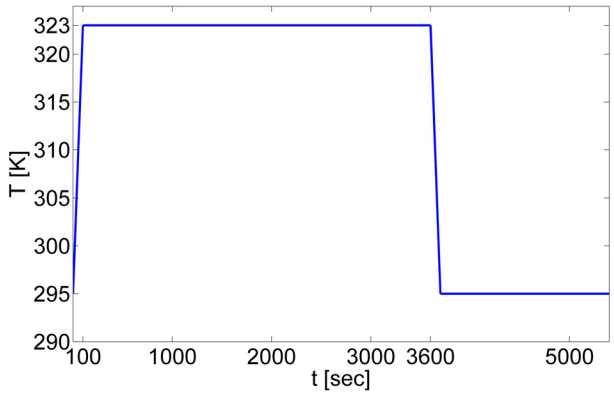

Figure 4.2 Temperature history used for thermal boundary conditions

the boundary quickly enough to reach a uniform distribution. The result is an overshoot in temperature, which itself leads to even quicker cure. Once the curing rate decreases, the heat released into the system diminishes and a uniform distribution is reached eventually. Finally, upon cooling of the sample the center lags again behind the boundary. In this particular case, the center remains at an elevated temperature for a longer time. It should be noted, that upon change of boundary conditions of the small sample, the temperature there is also not uniform. This would occur only for the case for a perfect conductor, but in the actual simulation, temperature gradients are too small to be noticed and properly resolved.

Figure 4.4 shows the curing history of the small and large epoxy samples. Since temperature and cure are closely related, it is not surprising that the uniform temperature distribution in the small sample gives rise to a uniform degree of cure distribution. In the large sample, however, initially the rate of cure is slower at the center compared to the outside. That means, the slope indicating the rate of cure is lower during the first 100 seconds. This is true until the inside temperature reaches the same level as the outside. As mentioned before,

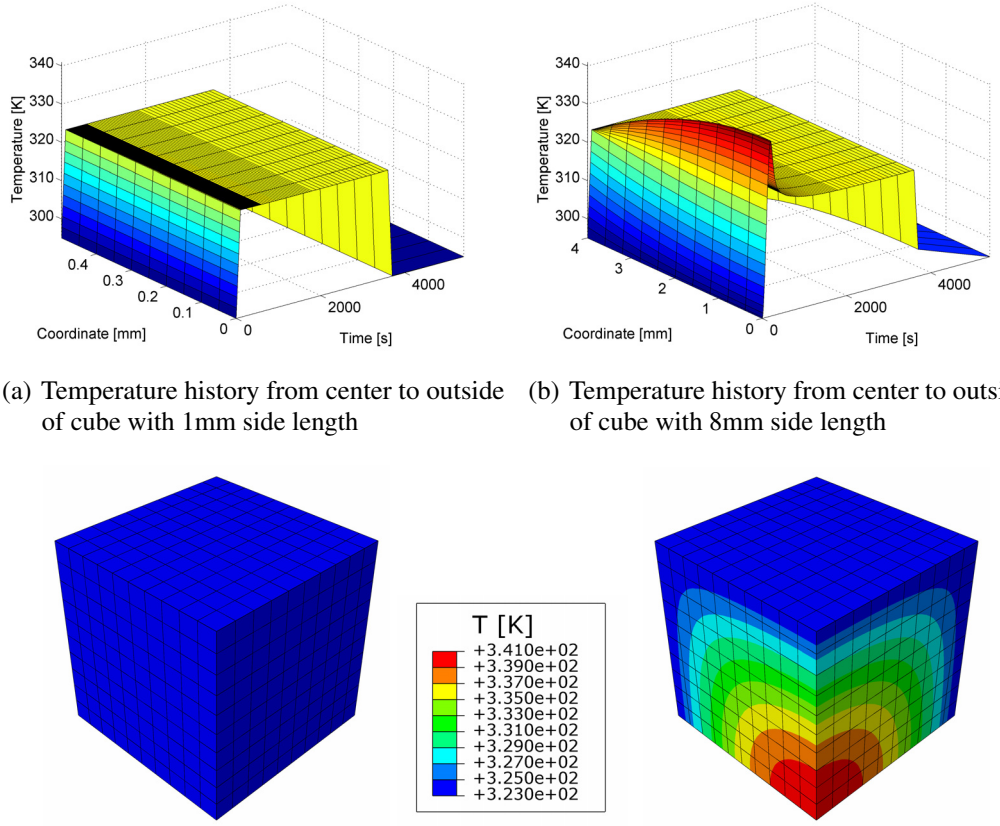

(a) Temperature history from center to outside of cube with 1mm side length

(b) Temperature history from center to outside of cube with 8mm side length

(c) Temperature distribution after 200 seconds in cube with 1mm side length

(d) Temperature distribution after 200 seconds in cube with 8mm side length

Figure 4.3 Temperature history in small and large block of epoxy

since heat emitted to the system cannot be transported to the outside quickly enough, the temperature rises at the center of the specimen. This in turn leads to faster cure and more heat released into the system in a shorter time. Therefore full cure is attained faster on the inside. It should be noted that figure 4.3(d) shows the temperature distribution 200 seconds after the reaction started. At this point the temperature gradient is largest in the specimen. However, figure 4.4(d) shows the time at which the difference in degree of cure is very uneven. This is at 600 seconds. Therefore, an overshoot in temperature should not be mistaken for a large degree of cure obtained. High degree of cure will lag behind that overshoot. The reason for this behavior lies in the fact that heat released into the system is related to the rate of cure, not the degree of cure. For the Kamal model, [33], the rate of cure is typically higher for low degrees of cure, and reduces with increasing amount of cure. The described phenomena are in line with the observations from chapter 2. The numerical results there were obtained through a finite difference method. The results presented in this

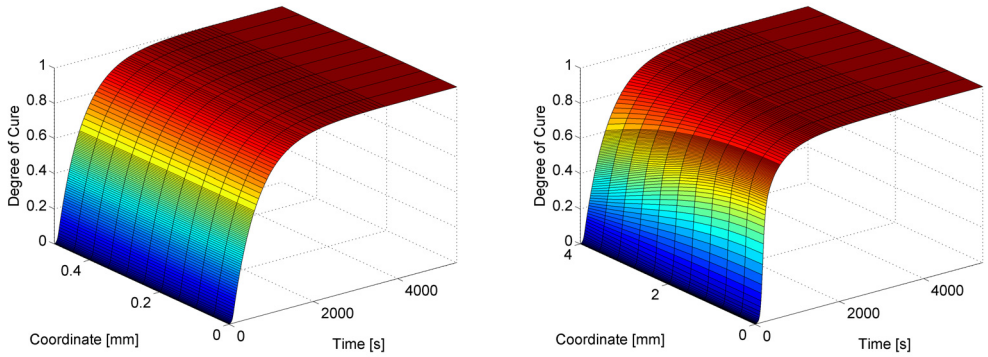

(a) Cure history from center to outside of cube with 1mm side length

(b) Cure history from center to outside of cube with 8mm side length

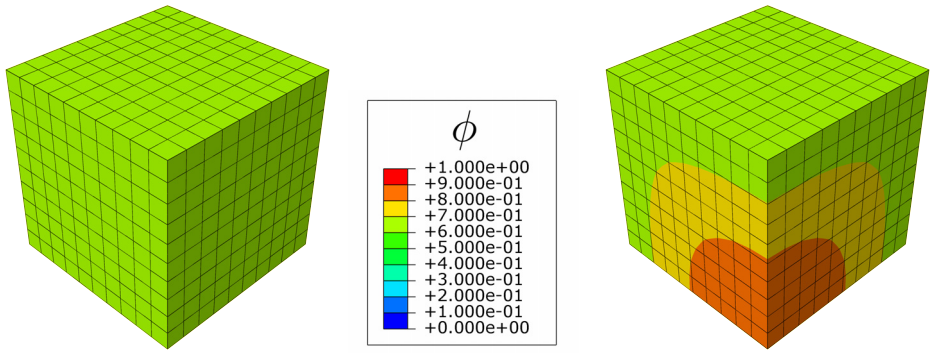

(c) Cure distribution after 600 seconds in cube with 1mm side length

(d) Cure distribution after 600 seconds in cube with 8mm side length

Figure 4.4 Cure history in small and large block of epoxy

chapter are obtained using the finite element method.

Figure 4.5 depicts the von Mises stresses in the small and large epoxy samples. The von Mises stress is a common scalar field to quantify the stress state, it is related to the local shape change and defined as

$$\sigma_{vM}(t,s) = \sqrt{\frac{(\sigma_{xx}-\sigma_{yy})^2+(\sigma_{yy}-\sigma_{zz})^2+(\sigma_{zz}-\sigma_{xx})^2+6(\sigma_{xy}{}^2+\sigma_{xz}{}^2+\sigma_{yz}^2)}{2}}. \quad (4.1)$$

The small sample is stress free. This is expected because no thermal gradients or gradients in degree of cure are present and the sample boundary was traction free. However, the larger sample does exhibit stresses due to the non uniform nature of the temperature and cure. Von Mises stresses are larger on the outside than on the inside. Figure 4.6 gives closer insight into what is happening. Here the maximum principal stress is shown. During the cure

of the large sample the center cures first and the outside follows later. Therefore the center solidifies first. The phase transition from liquid to solid is associated with some degree of shrinkage. However this has little effect on the outer region. Its small degree of cure implies that the epoxy has a very low shear modulus, μ, and will follow any shape change without creating significant stresses. When the outer parts of the cube cure, the center is already solidified. The cure shrinkage will therefore affect the epoxy. A decrease of volume upon phase change from liquid to solid implies that the outer part is "shrink wrapped" around the inner part. The result is the development of tensile stresses in the outer part and compressive stresses on the inside. A traction free boundary implies that the maximum tensile stresses act on an infinitesimal surface perpendicular to the outside surface. Therefore, if a crack or void were to be present in the material, it would have a tendency to open up further. Also, due to the symmetric nature of the boundary value problem, a near hydrostatic stress state can be assumed towards the center of the specimen. This leads to vanishing von Mises stresses at the center. Finally, it should be noted that the von Mises stresses and the maximum principal stresses show a jump in figure 4.5 at 3600 seconds when the sample is cooled down. This is again due to the low thermal conductivity and the temperature gradient. The outside has a lower temperature then the inside. The positive coefficient of thermal expansion of the epoxy implies that the outside contracts more than the inside, amplifying the tensile stresses on the boundary and the compressive stresses in the center.

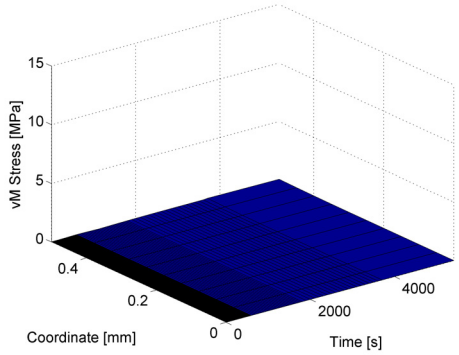

(a) von Mises stress history from center to outside of cube with 1mm side length

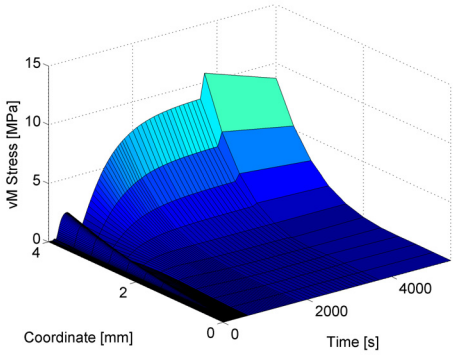

(b) von Mises stress history from center to outside of cube with 8mm side length

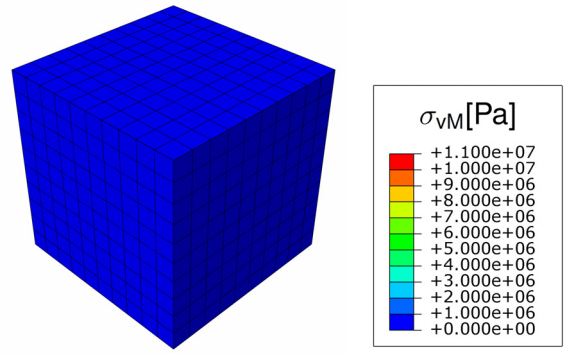

(c) von Mises stress distribution after 3700 seconds in cube with 1mm side length

(d) von Mises stress distribution after 3700 seconds in cube with 8mm side length

Figure 4.5 von Mises stress history in small and large block of epoxy

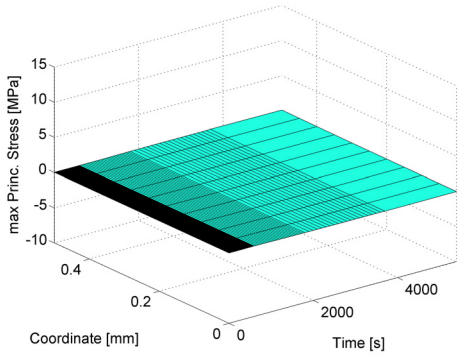

(a) maximum principal stress history from center to outside of cube with 1mm side length

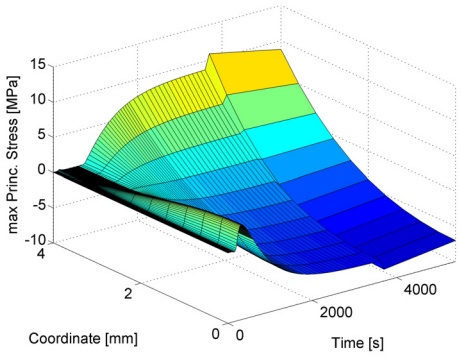

(b) maximum principal stress history from center to outside of cube with 8mm side length

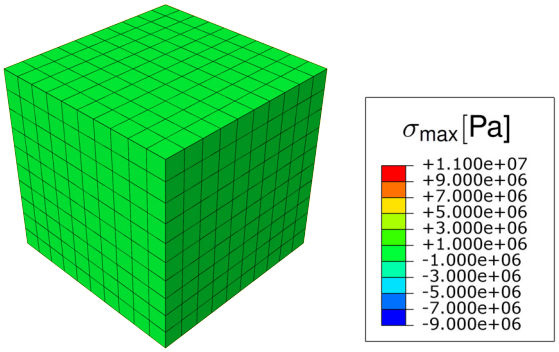

(c) maximum principal stress distribution after 3700 seconds in cube with 1mm side length

(d) maximum principal stress distribution after 3700 seconds in cube with 8mm side length

Figure 4.6 Maximum principal stress history in small and large block of epoxy

4.2 Curing of an idealized single fiber composite

In the next example, the cure and stress development in a single fiber composite, which consists of a fiber-matrix concentric cylinder will be investigated. Table 4.1 summarizes various thermal and mechanical material properties that can be found in the literature for carbon and glass fibers. It should be noted that carbon fibers differ in two important aspects from glass fibers. Carbon fibers are orthotropic. Also their thermal expansion coefficient in the axial direction is negative. Two different sizes of carbon fiber and matrix cylinders will be investigated: one with 1 mm outer radius and one with 8 mm outer radius. The fiber radius is always half of the total (outer) radius. The length is 20 times the total radius. The temperature of the cylinder on the cylindrical outer surface is prescribed. The thermal cycle is identical to the one in the previous section, as shown in figure 4.2. The top and bottom surfaces of the cylinder are insulated, so that there is no heat flux crossing these surfaces. Two different mechanical boundary conditions are chosen. In Case (a) all surface are traction free and free to expand and shrink. In Case (b), the displacements on all sides, except the top of the cylinder were prescribed. At the end of the cure cycle the displacement constraints are removed and the cylinder is free to expand or contract. In figures 4.8-4.13 all images of cross-sections are taken in the middle of the cylinder. When examining cross-sections along the axis of rotation of the cylinder, end effects of the stress field can be noticed, but they vanish quickly due to Saint-Venant's principle.

Figure 4.8 shows the temperature history in the two different cylinders. The observations that can be made are very similar compared to the ones made earlier for a pure epoxy material. In the smaller cylinder the temperature is very uniform throughout the curing history. On the other hand, in the larger sample the temperature in the middle lags behind the

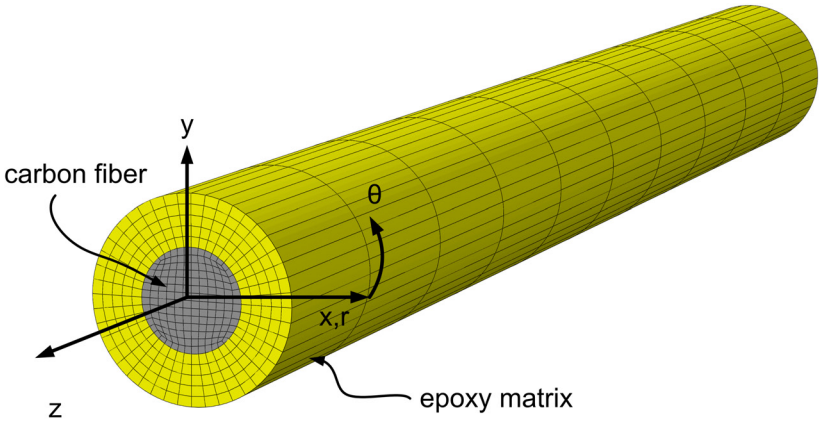

Figure 4.7 Meshed cylinder of individual carbon fiber and epoxy matrix

one that was prescribed on the boundary at the beginning. Due to the exothermic reaction heat gets released into the system, which causes a temperature rise in the center. Here the low heat conduction cannot prevent the development of temperature gradients. It can be seen that the temperature in the carbon fiber is uniform at all times and identical to the temperature of the bordering matrix. The second fact is a direct consequence of the interface condition. Since carbon is an excellent conductor, its conductivity is orders of magnitude higher, compared to the epoxy, and heat conduction can be regarded almost instantaneous compared to the cure cycle time and the time for heat conduction in the epoxy. It should also be noted that the carbon serves as a reservoir for the heat that is generated by the curing process. As an example, consider the following: it has been previously shown that for a perfect insulator, the temperature rise can be calculated, assuming constant properties as a function of temperature, as

$$\rho c_p \Delta T = \rho H_r \tag{4.2}$$

This could be generalized to a composite with fiber and matrix to obtain

$$(v_f \rho_f c_{pf} + (1 - v_f)\rho_m c_{pm})\Delta T = (1 - v_f)\rho_m H_r \tag{4.3}$$

The left hand side of equation 4.3 quantifies the temperature rise and contains information about the entire composite. The right hand side of the equation deals with the heat released into the system due to the exothermic reaction. It only contains information about the epoxy. As a result the temperature rise in a composite with 50% fiber volume fraction, v_f, is 90 K compared to 189 K in a pure epoxy. The overall temperature rise in the composite will be significantly lower compared to the one in a pure epoxy.

Figure 4.9 shows the curing history in the two different sized fiber-matrix cylinders. Due to the uniform nature of the temperature field, the degree of cure is uniform in the smaller of the two cylinders. The overshoot in temperature at the center of the larger cylinder is accompanied by faster cure. It can be again noticed that a peak in temperature does not correspond to high degree of cure. A high degree of cure will lag behind the peak in temperature. In this particular example the temperature is highest around 450 seconds. But full cure in the center is not achieved until 600 seconds.

Figure 4.10 depicts the development of the circumferential stresses in the cylinders that were allowed to cure with traction free boundary conditions. The stress levels at the end of the curing cycle are quite comparable. In the large cylinder the maximum value of $\sigma_{\theta\theta}$ is 40.4 MPa. In the smaller cylinder it is 35.0 MPa. In this particular case cure shrinkage has a stronger effect on the stress development compared to thermal effects, because thermal

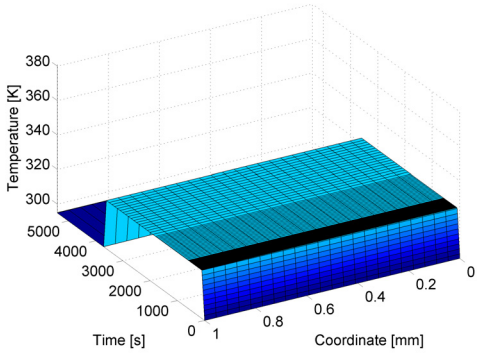

(a) Temperature history from center to outside of fiber-matrix cylinder with 1 mm radius

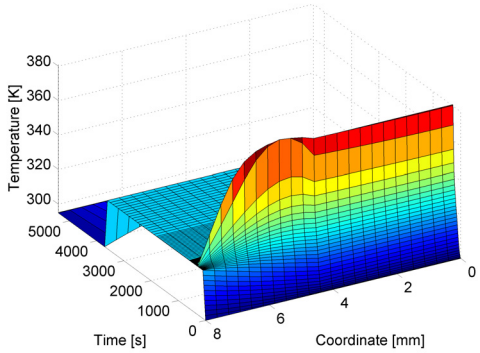

(b) Temperature history from center to outside of fiber-matrix cylinder with 8 mm radius

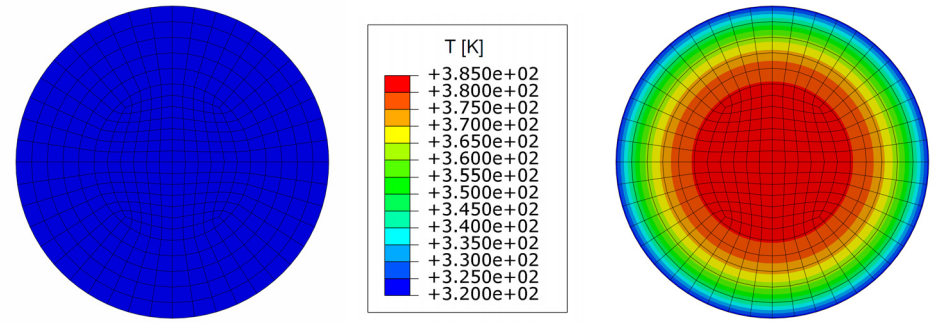

(c) Temperature distribution after 300 seconds in fiber-matrix cylinder with 1 mm radius

(d) Temperature distribution after 450 seconds in fiber-matrix cylinder with 8 mm radius

Figure 4.8 Temperature history in small and large fiber-matrix cylinder

gradients are small..

In the following, the stress components corresponding to boundary conditions of Case (a) and Case (b) will be discussed. First it should be mentioned that the boundary conditions have a surprisingly small effect on the final stresses. The stress fields have been compared for the 8 mm radius cylinder. The stress field for Case (b), after removing the displacement constraints, is similar, albeit not the same, compared to Case (a). However, before relaxing the boundary conditions in Case (b), the stress fields in Case (a) and Case (b) are significantly different, as shown in figures 4.11, 4.12 and 4.13.

Figure 4.11(b) depicts the radial stresses in Case (a). They are all negative, with the largest magnitude in the center and decreasing to zero on the boundary. This is of course expected since the outward normal to the traction free surface points in the radial direction. The compressive nature of the radial stress is due to cure shrinkage. The outer parts of the cylinder press onto the inner parts and the fiber in an attempt to shrink. It can also be

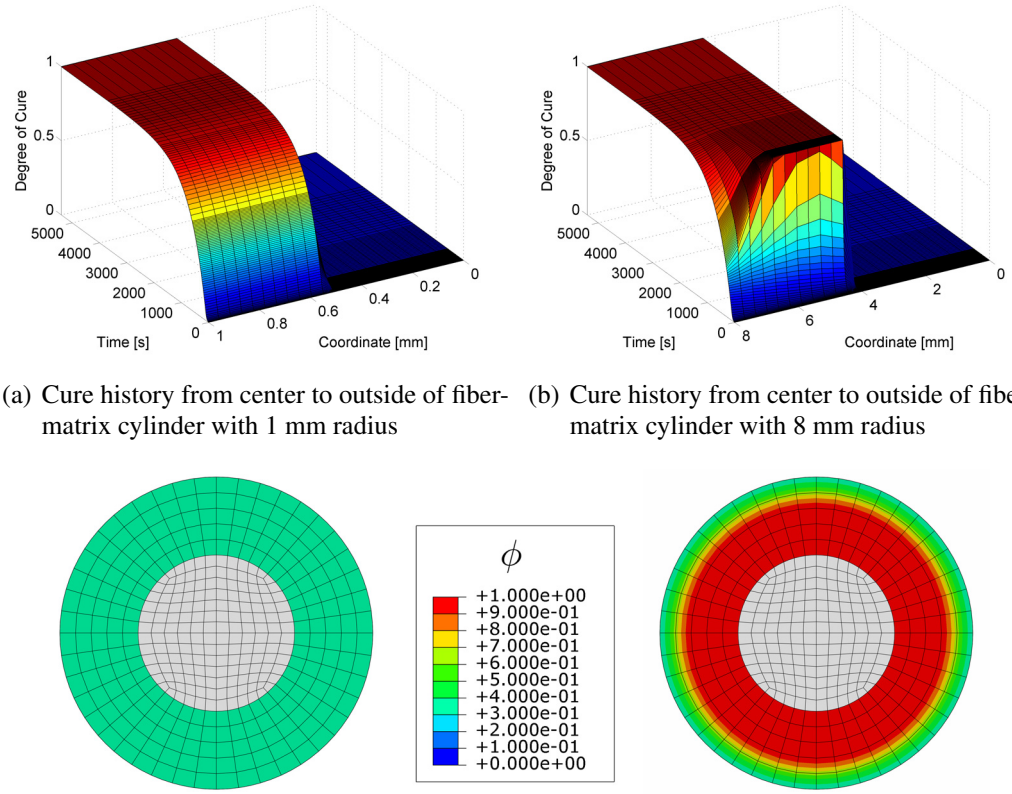

(a) Cure history from center to outside of fiber-matrix cylinder with 1 mm radius

(b) Cure history from center to outside of fiber-matrix cylinder with 8 mm radius

(c) Cure distribution after 300 seconds in fiber-matrix cylinder with 1 mm radius

(d) Cure distribution after 300 seconds in fiber-matrix cylinder with 8 mm radius

Figure 4.9 Cure history in small and large fiber-matrix cylinder

seen that bringing the temperature at the end of the cure cycle after 3600 seconds back to room temperature further increases the stress magnitudes. This is due to the fact that the coefficient of thermal expansion (CTE) of the epoxy is almost an order of magnitude larger than the in plane CTE of carbon fibers. It should be noted that the radial stresses predicted for Case (b), shown in figure 4.11(c), in which the boundary is constrained is so large, that in reality the interface between the epoxy and the outside surface will fail. This has been observed in the past, when Hetron resin was cured in a glass cylinder. The epoxy debonded and just fell out of the tube, [79].

Figure 4.12 depicts the circumferential stress distribution in the 8 mm cylinders. In Case (a) the circumferential stress is in tension, because it shrinks around the fiber. The circumferential stress in the fiber, in turn, goes into compression. Compressive stresses from the matrix onto the fiber are uniform everywhere in the fiber interior which causes a plane strain state, uniform and independent of coordinate system chosen within the fiber. Specifically, the circumferential and radial stresses are the same throughout the fiber. All

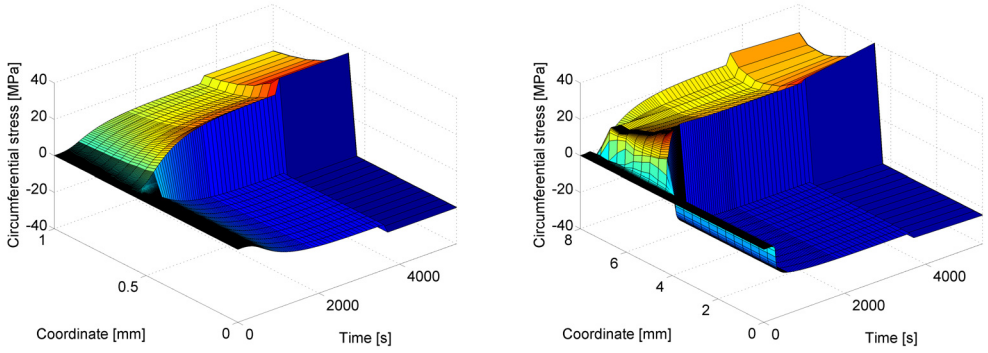

(a) Circumferential stress history from center to outside of fiber-matrix cylinder with 1 mm radius

(b) Circumferential stress history from center to outside of fiber-matrix cylinder with 8 mm radius

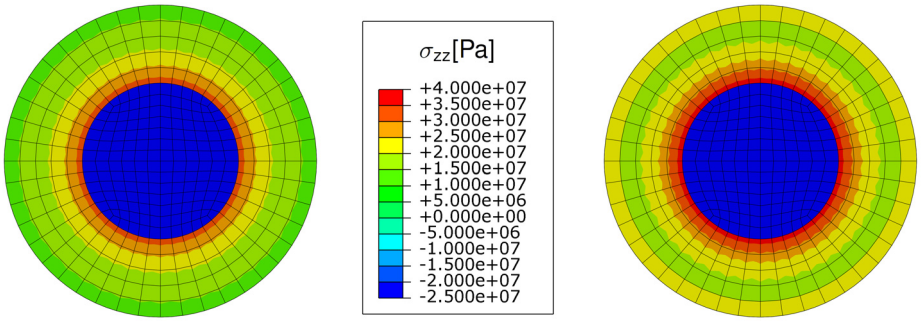

(c) Circumferential stress distribution after 5400 seconds in fiber-matrix cylinder with 1 mm radius

(d) Circumferential stress distribution after 5400 seconds in fiber-matrix cylinder with 8 mm radius

Figure 4.10 Circumferential stress history in small and large fiber-matrix cylinder

stress magnitudes increase further upon cooling down the cylinder to room temperature due to the CTE mismatch in the fiber and the matrix. It should be noted that tensile stresses in the matrix are undesirable because they will support crack growth. As opposed to the case of the pure epoxy, where tensile stresses were confined to the outer part of the matrix, here the circumferential stresses in the matrix are tensile in the entire region between the outer surface and the fiber-matrix interface.

Finally, figure 4.13 shows the axial stresses in the two cases. In Case (a) the situation is similar to that presented earlier for circumferential stresses. The curing matrix shrinks around the fiber, which tries to resist this. The matrix axial stress is tensile and the fiber axial stress is compressive. In the circumferential direction, the tensile stresses, $\sigma_{\theta\theta}$, are largest at the interface between fiber and matrix, whereas the tensile stresses in the axial direction, σ_{zz}, are uniform throughout the matrix. The maximum axial and circumferential

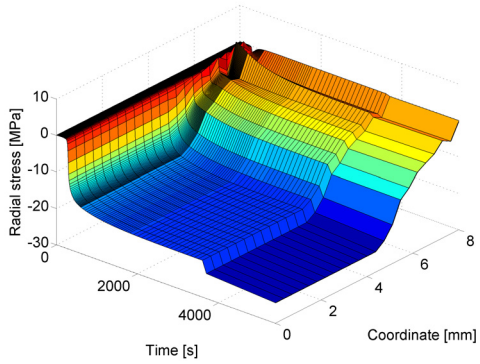

(a) Radial stress history from center to outside of fiber-matrix cylinder with 8 mm radius that has not been constrained (Case a)

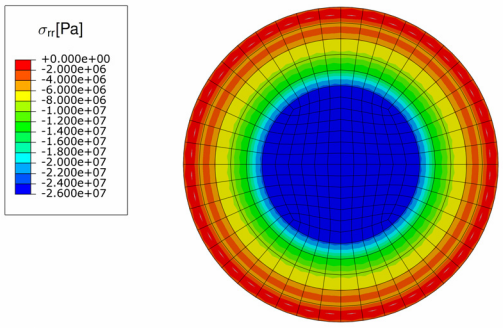

(b) Radial stress distribution after 5400 seconds in fiber-matrix cylinder with 8 mm radius that has not been constrained (Case a)

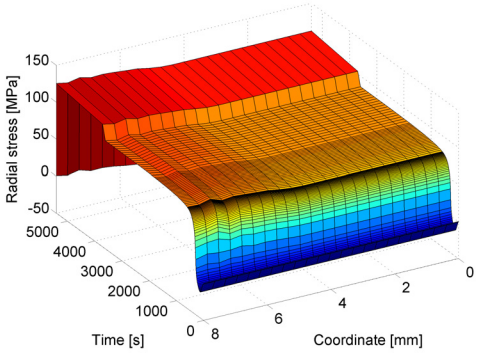

(c) Radial stress history from center to outside of fiber-matrix cylinder with 8 mm radius that has been constrained (Case b)

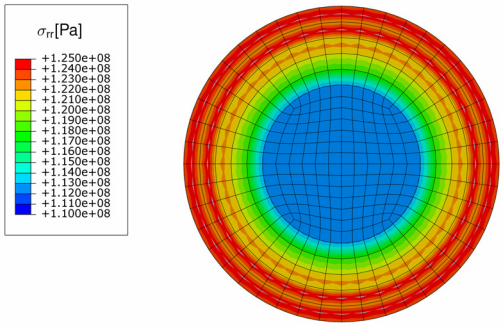

(d) Radial stress distribution after 5400 seconds in fiber-matrix cylinder with 8 mm radius that has been constrained (Case b)

Figure 4.11 Radial stress history in large constrained and unconstrained fiber-matrix cylinder

tensile stresses in the matrix are comparable, while the axial compressive stress in the fiber is significantly larger. Upon cooling, the stresses increase further. In the axial direction, the fiber expands and the epoxy shrinks. In the case of the constrained cylinder, the stresses are tensile in the matrix and the fiber. The stress magnitude is larger in the matrix than in the fiber. This tensile stress jump at the fiber-matrix interface would aid debonding between fiber and matrix by forming mode II cracks.

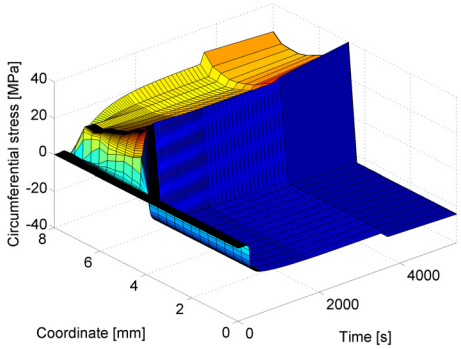

(a) Circumferential stress history from center to outside of fiber-matrix cylinder with 8 mm radius that has not been constrained (Case a)

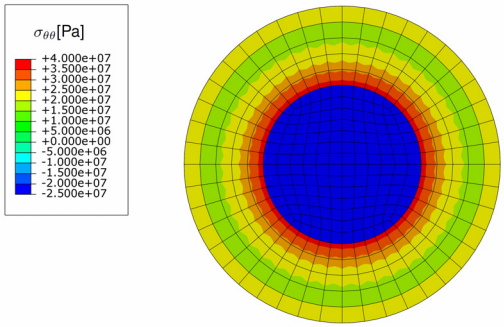

(b) Circumferential stress distribution after 5400 seconds in fiber-matrix cylinder with 8 mm radius that has not been constrained (Case a)

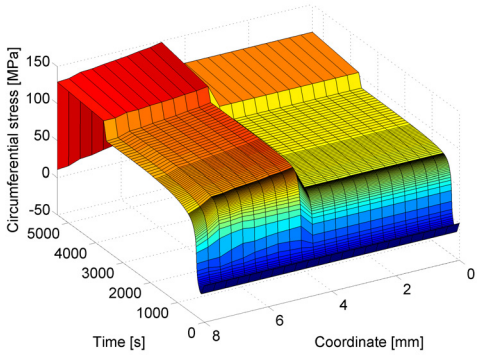

(c) Circumferential stress history from center to outside of fiber-matrix cylinder with 8 mm radius that has been constrained (Case b)

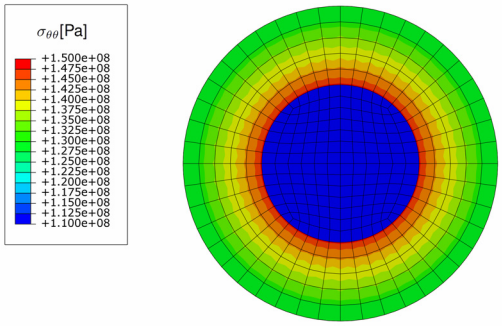

(d) Circumferential stress distribution after 5400 seconds in fiber-matrix cylinder with 8 mm radius that has been constrained (Case b)

Figure 4.12 Circumferential stress history in large constrained and unconstrained fiber-matrix cylinder

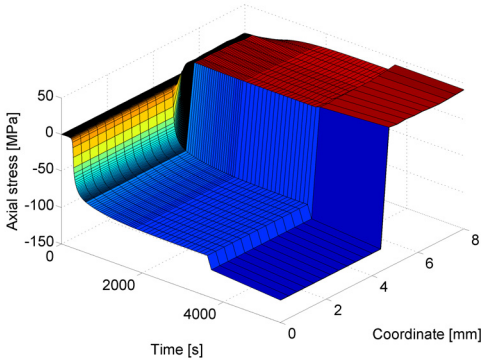

(a) Axial stress history from center to outside of fiber-matrix cylinder with 8 mm radius that has not been constrained (Case a)

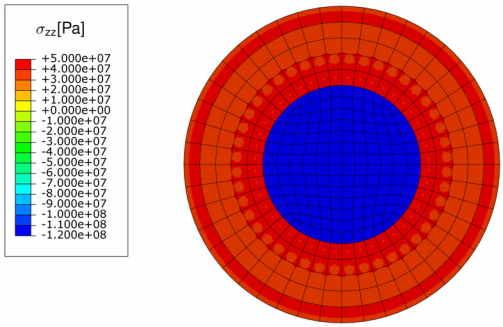

(b) Axial stress distribution after 5400 seconds in fiber-matrix cylinder with 8 mm radius that has not been constrained (Case a)

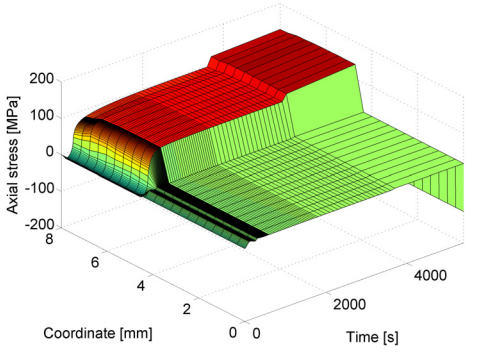

(c) Axial stress history from center to outside of fiber-matrix cylinder with 8 mm radius that has been constrained (Case b)

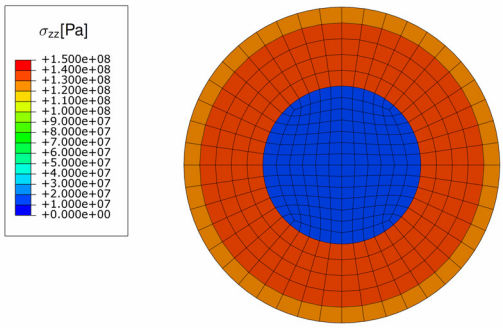

(d) Axial stress distribution after 5400 seconds in fiber-matrix cylinder with 8 mm radius that has been constrained (Case b)

Figure 4.13 Axial stress history in large constrained and unconstrained fiber-matrix cylinder

Material	Density kg/m^3	α_{11}	α_{22}	E_{11} GPa	E_{22}	ν_{21}	ν_{12}	G_{12} GPa	G_{23}	c_p J/kg/K	K W/m/K	Reference
E-Glass	2580	5.4	-	69	-	0.22	-	-	-	-	-	[4]
S2-Glass	2460	1.6	-	86.8	-	0.23	-	-	-	-	-	[4]
S2-Glass	2460	1.6	-	86.9	-	-	-	-	-	737	1.45	[80]
IM8	1800	-	-	310	-	0.2	-	-	-	-	-	[4]
IM7	1780	-0.38@400°C	6.94@400°C	276	19.5	0.01978	0.7	-	-	-	-	[81], [82]
IM7	-	-0.16	-	303	15	0.013	0.25	-	-	-	-	[83]
IM7	1780	-0.64	-	276	-	-	-	-	-	879	5.4	[84]
Carbon fiber	2120	-	-	-	-	-	-	-	-	1000	190	[85]
Carbon fiber	-	-	-	231	-	-	0.15	-	-	-	-	[5]
Carbon fiber	-	-	-	230	-	-	0.14	24	5.02	-	-	[8]
values used	1800	-0.64	6.94	230	15	0.49	0.14	24	5.02	879	5.4	

Table 4.1 Material properties for carbon and glass fibers

4.3 Cure of uniaxial fiber-matrix RUC

4.3.1 Comparison of small and large RUC

After investigating the stress evolution in a single fiber epoxy cylinder, a representative fiber-matrix tow in the form of a block is considered as shown in figure 4.14(a) and the coordinate system is shown in figure 4.14(b). The origin of the coordinate system is in the middle of the bottom surface in figure 4.14(b). Such a representative volume element corresponds to a fiber tow of a woven composite or a single lamina within multilayered laminate. To investigate size effects effectively, the fibers inside the RUC have been enlarged, but the outer dimensions of the element are on the length scale that can be found in a macroscopic part. Two sizes of cubes are considered; 1 mm and 20 mm side length, respectively. The fiber volume fraction is 60%. The outer surfaces of the cubes are maintained traction free throughout the curing analysis.

Consider the same thermal boundary conditions that have also been applied to the pure epoxy example earlier. The epoxy is at room temperature. It is heated up to 323 K within 100 seconds and held at that level for 3600 seconds. Then the temperature is decreased within 100 seconds to room temperature and another 1800 seconds may elapse to ensure uniform temperature upon cooling. The temperature boundary condition is applied on all six sides of the RUC.

Figure 4.15 shows the temperature evolution in the RUC as it cures. For this problem the

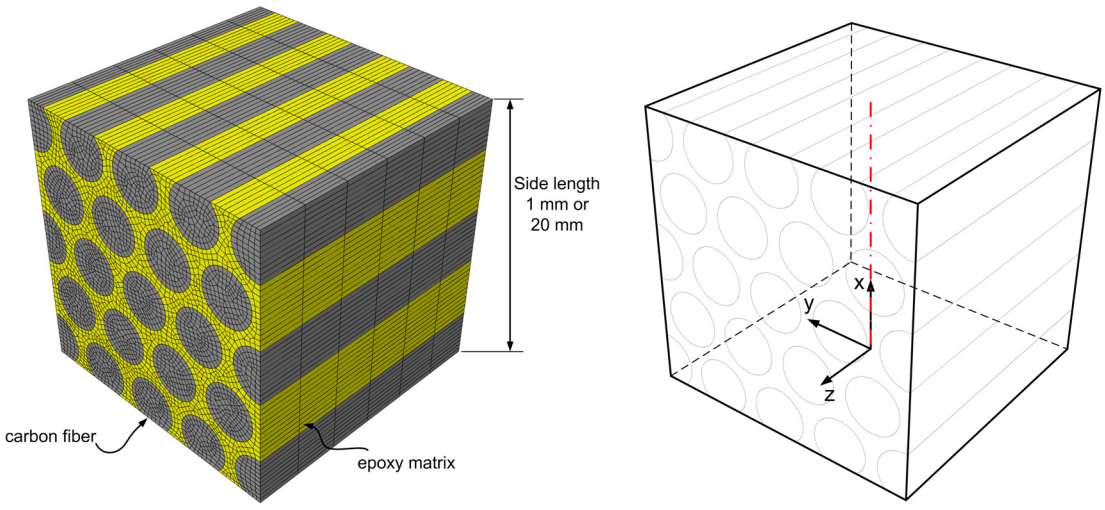

(a) RUC of uniaxial fibers and matrix meshed

(b) Sketch of RUC with coordinate system and origin indicated

Figure 4.14

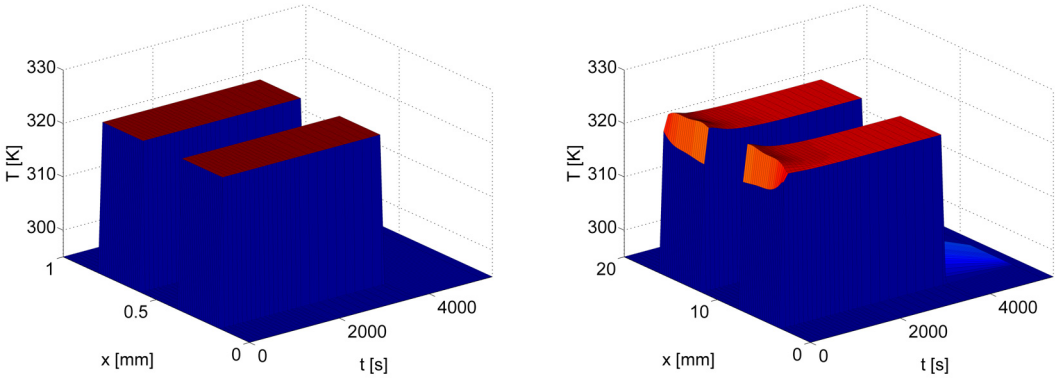

(a) Temperature history at centerline in fiber-matrix-RUC with 1 mm side length

(b) Temperature history at centerline in fiber-matrix-RUC with 20 mm side length

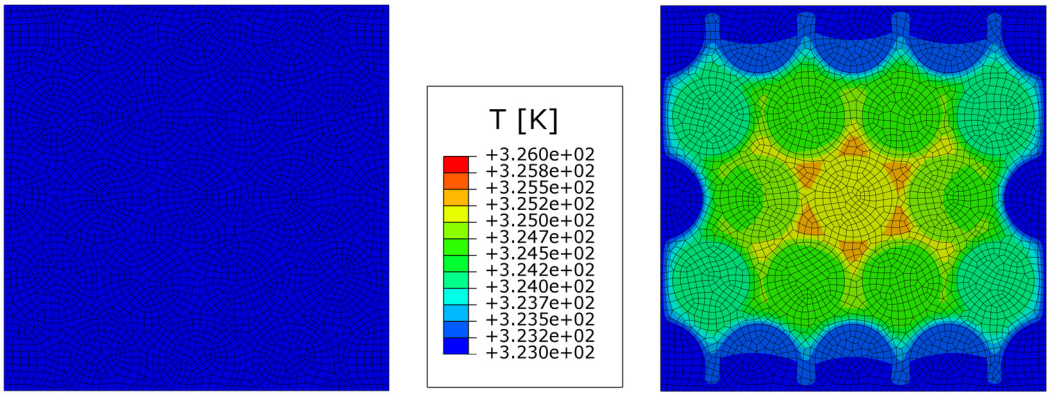

(c) Temperature distribution after 300 seconds in x-y-plane of fiber-matrix-RUC with 1 mm side length

(d) Temperature distribution after 300 seconds in x-y-plane of fiber-matrix-RUC with 20 mm side length

Figure 4.15 Temperature history and distribution in fiber-matrix-RUC

temperature can generally be regarded as homogeneous. A 3°C overshoot can be observed in the larger RUC due to the exothermic reaction.

Because the temperature variation in the larger RUC is small, the cure evolution in the two different sample sizes is comparable. The cure evolution is shown in figure 4.16. The curing histories in the small and the large RUC are comparable. In the large RUC a slightly faster curing can be observed towards the center of the RUC. For both RUC sizes, the time to full cure is about 1800 seconds. The center of the larger RUC cures slightly faster. While the pure epoxy shows a clear difference between different sized samples, the composite RUC does not do so. The reason lies in the good heat conductivity of the carbon fibers and the fact that they are part of the thermal boundary conditions. If the temperature was not prescribed at the ends of the fibers a larger rise in temperature will be observed. It is

therefore important to note the various aspects that have influence on the time to reach full cure. As discussed in section 2.7, larger parts cure faster than smaller ones, which stems from an elevation in temperature due to a strong exothermic reaction and poor conductivity. The effect is less strong when fibers are inserted, because they act as a reservoir that absorb heat from the curing reaction. High conductivity fibers, such as carbon, reduce the effect further. It is also important, which sides of the RUC have temperature boundary conditions applied. In the current example the temperature boundary conditions are applied on all sides, which reduces temperature increase due to the exothermic reaction and therefore does not lead to a decrease in curing time. On the other hand if insulation boundary conditions are prescribed on some faces of the unit cell, the temperature rises due to the exothermic reaction and thus a decrease in curing time can be observed as shown in section 4.3.3. To systematically investigate the influence of the various curing parameters, it is helpful to construct non-dimensional relationships. The time to full cure can then be expressed as a function of such a non-dimensional number. In section 2.7 it was seen that a plot of curing time versus other curing parameters shows large plateau regions and small regions of a steep transition. If it was possible to collapse these curves onto a single non-dimensional parameter, it could serve as a guide to estimate curing times and maximum temperature. Li and Tucker, [86], have given three dimensional groups to describe the thermochemical problem, but they did not further elaborate how they might be used to investigate the importance of the rise of temperature due to the exothermic reaction on the time to full cure.

As expected, the stresses in the two samples are comparable, as shown in figure 4.17. The maximum von Mises stresses in the 20 mm RUC are 2 MPa higher, compared to the 1 mm RUC, which is a negligible difference, considering that the maximum value of the von Mises stress is 58 MPa and 60 MPa respectively. It can be observed that the von Mises stresses are largest where fibers are closer together. Stress generation during cure has two causes: cure shrinkage of the epoxy and thermal mismatch. Both effects will be amplified when two fibers get closer together. Also the stresses are elevated closer to the fiber-matrix interface.

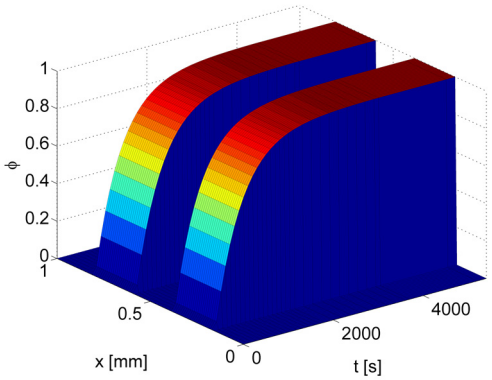

(a) Curing history at centerline in fiber-matrix-RUC with 1 mm side length

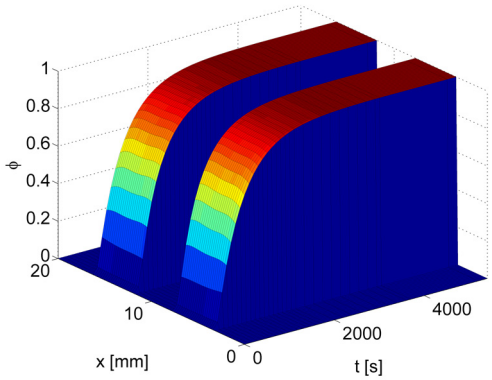

(b) Curing history at centerline in fiber-matrix-RUC with 20 mm side length

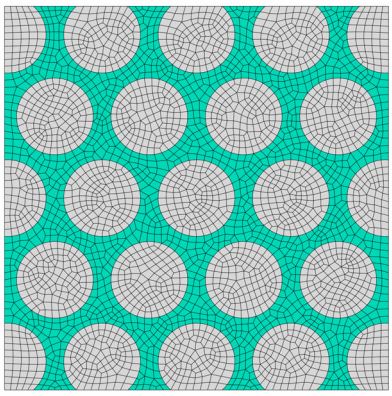

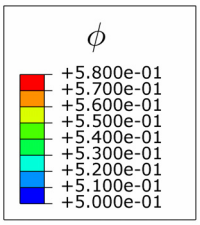

(c) Degree of cure after 500 seconds in x-y-plane of fiber-matrix-RUC with 1 mm side length

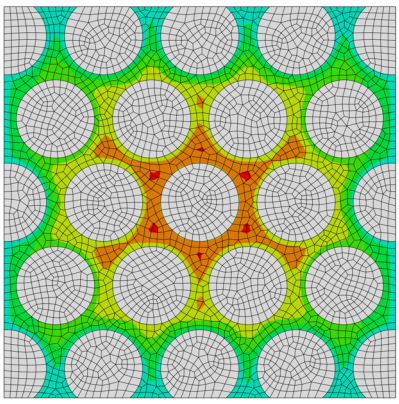

(d) Degree of cure after 500 seconds in x-y-plane of fiber-matrix-RUC with 20 mm side length

Figure 4.16 Curing history and distribution of degree of cure in fiber-matrix-RUC

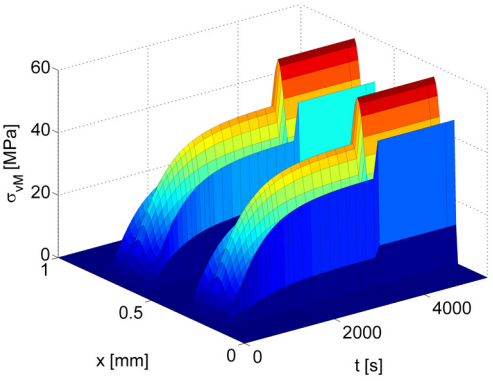

(a) von Mises stress history at centerline in fiber-matrix-RUC with 1 mm side length

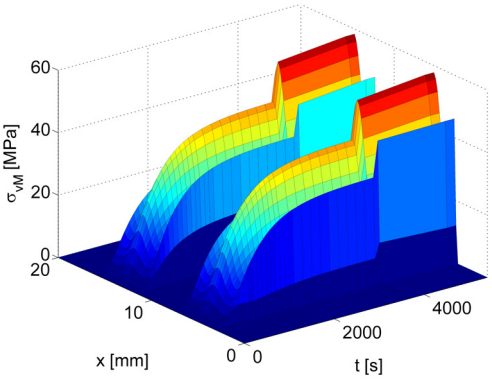

(b) von Mises stress history at centerline in fiber-matrix-RUC with 20 mm side length

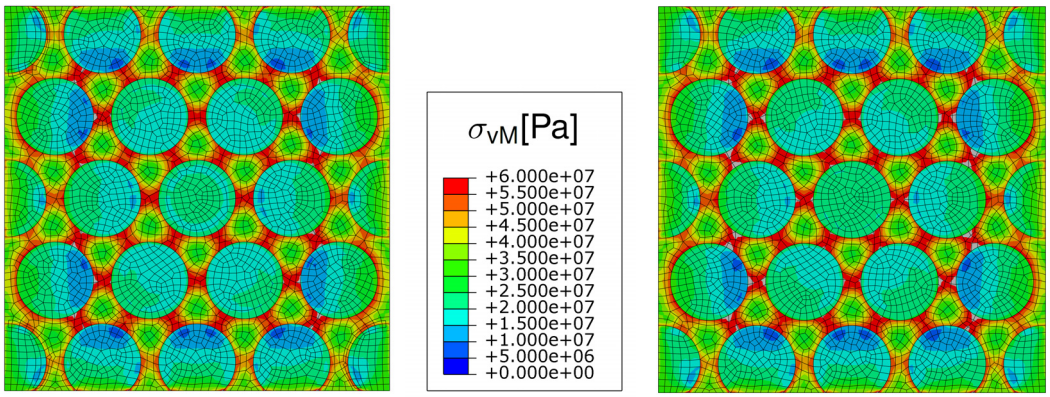

(c) von Mises stress after full cure in x-y-plane of fiber-matrix-RUC with 1 mm side length

(d) von Mises stress after full cure in x-y-plane of fiber-matrix-RUC with 20 mm side length

Figure 4.17 von Mises stress history and distribution in fiber-matrix-RUC

To investigate the various components of stress further, a cylindrical coordinate system is placed in the center of the fiber in the middle of the RUC. Figure 4.18 shows a polar plot of the radial stresses on at the surface around the center fiber, just inside and outside the fiber-matrix interface. The shrinkage during cure and subsequent cooling causes the matrix to press against the fiber. The result is a compressive radial stress. The radial stresses on the fiber-matrix interface inside the fiber and the matrix should be identical to satisfy force equilibrium in that direction. The mismatch that can be observed should be treated as interpolation error when the data was gathered. The compressive stresses are largest, where two fibers are closest together. Their maximum magnitude is at 16 MPa.

The circumferential stresses on the fiber-matrix interface of the center fiber are shown in figure 4.19. As in the case of a single fiber, the matrix is in tension in the circumferential direction and the fiber is in compression. During cure, the surrounding matrix shrinks which causes tensile stresses in the circumferential direction. This effect is further amplified by the thermal mismatch of the carbon and epoxy. There is directional dependence of the stress in the fiber and this is noticeable with respect to the location of the neighboring fibers. The circumferential compressive stresses are smallest, where fibers are close together. The circumferential stress in the matrix at the interface lacks such a dependence. The stress levels are at just over 40 MPa throughout.

Next, consider the σ_{zz}stresses shown in figure 4.20. Only slight directional dependence can be found in the matrix at the fiber-matrix interface. The matrix is again in tension and the fiber in compression. The tensile stresses in the matrix are comparable to the ones in the hoop direction. This comes as no surprise. Locally, one could examine an infinitesimally

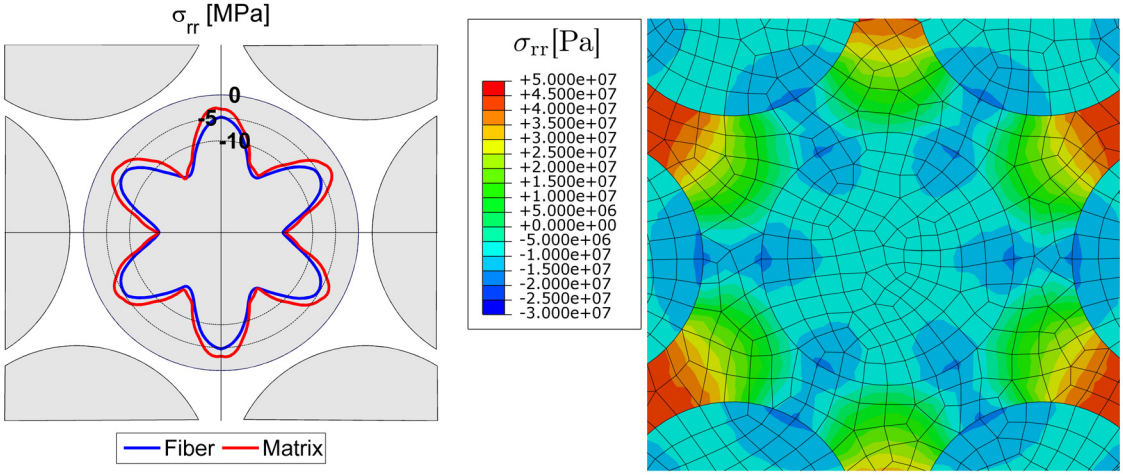

(a) Radial stresses on fiber-matrix interface of center fiber

(b) Radial stress contour around center fiber

Figure 4.18 Radial stresses around center fiber

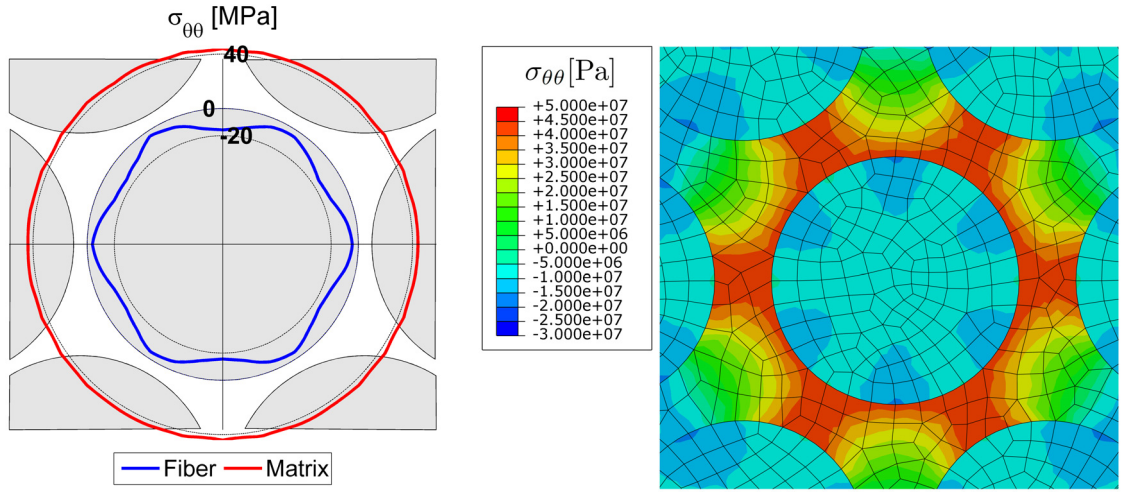

(a) Circumferential stresses on fiber-matrix interface of center fiber

(b) Circumferential stress contour around center fiber

Figure 4.19 Circumferential stresses around center fiber

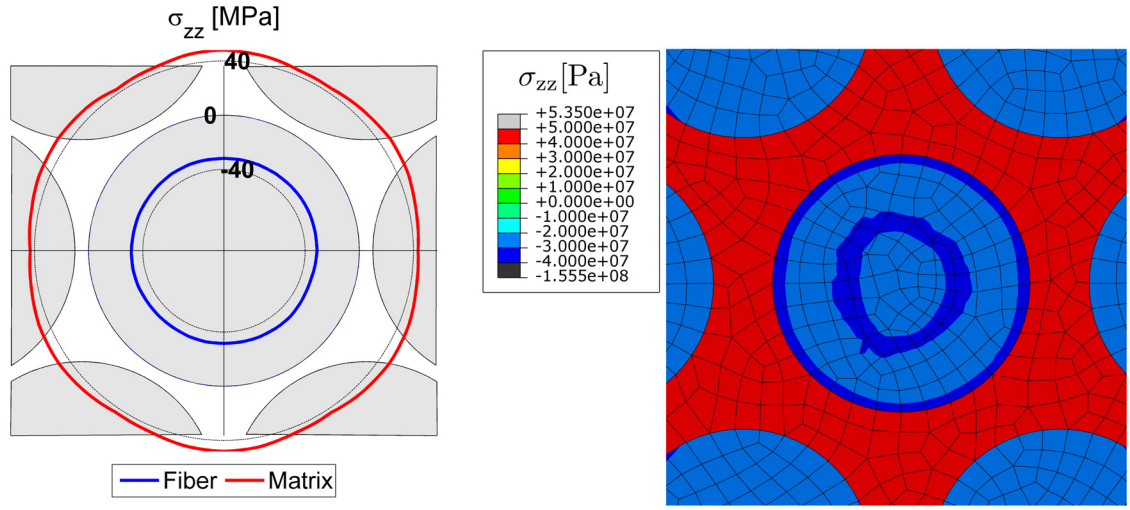

(a) Axial stresses on fiber-matrix interface of center fiber

(b) Axial stress contour around center fiber

Figure 4.20 Axial stresses around center fiber

small material element on the fiber-matrix interface. When considering such a small element, the curvature of the fiber can be neglected. The stress state can than be characterized as a biaxially stress state from the matrix point of view. That is, the matrix shrinks by the same amount in all directions due to cure and temperature change. The stress level in the fiber is higher in the axial direction compared to the circumferential one. The fiber axial stiffness is significantly larger compared to the in-plane stiffness. The tensile stress in the matrix is just over 40 MPa and the compressive stress in the fiber is just over -40 MPa.

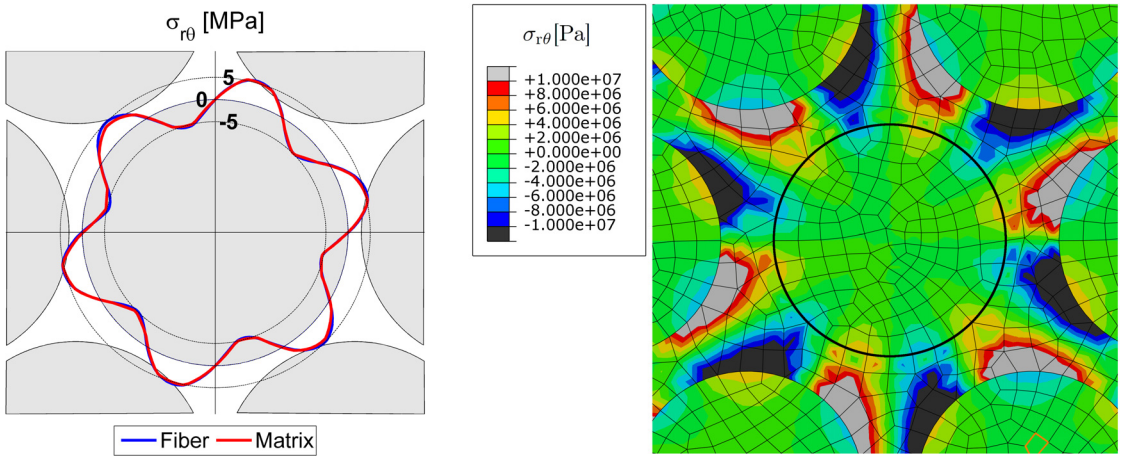

(a) Shear stresses on fiber-matrix interface of center fiber in plane perpendicular to the fiber direction

(b) Shear stress contour around center fiber in plane perpendicular to the fiber direction

Figure 4.21 Shear stresses around center fiber in plane perpendicular to the fiber direction

Finally consider the shear stress on the fiber-matrix interface in the circumferential direction shown in figure 4.21. The shear stresses show a clear periodicity and dependence on the location of the neighboring fiber. Stresses are zero when being closest and farthest away from the neighboring fiber. Elsewhere, the shear stresses are between -5 MPa and 5 MPa. Due to symmetry, the other two shear stress components, σ_{rz} and $\sigma_{\theta z}$, are zero.

4.3.2 Cure below room temperature

So far it has been seen that cure shrinkage and thermal mismatch can lead to stresses of appreciable size. The question that arises is, whether is possible to design the curing cycle in such a way to minimize stresses. So far the following was observed: both cure shrinkage and thermal mismatch increase stress levels. Specifically, the effect of cure shrinkage and curing at a temperature above operational temperature have the same influence. On the other hand, if the epoxy was cured below operational temperature, the thermal mismatch would partially cancel. To investigate this, consider the curing cycle where the epoxy is inserted into the mold at room temperature, cooled to 243 K (-30°C), held until full cure and heated back up to 295 K. This is of course purely a thought experiment. The curing time at the low temperature is more than three years! It can also be expected that the phenomenological curing law looses its validity at such low temperatures. Nevertheless, the result of such a curing cycle is a significant decrease in stresses. Figure 4.22(b) shows that the circumferential stresses in the matrix around the center fiber are reduced from over

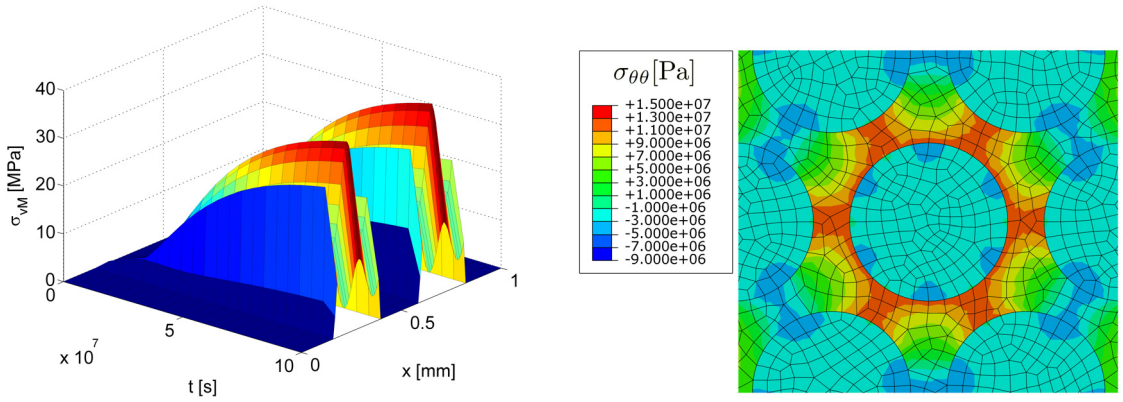

(a) von Mises stress evolution in sample cured at 243 K

(b) Circumferential stress around center fiber after curing at 243 K and heating up back to room temperature

Figure 4.22 Stress RUC cured at 243 K

40 MPa to less than 15 MPa. However, it should also been noted that these do not mark the largest stress magnitude that was felt by the epoxy during cure. In fact, the stresses at the end of the curing period, just before heating the sample up to room temperature, are significantly larger as shown in figure 4.22(a). This is consistent with the motivation of choosing this cure cycle in the first place. The stresses due to cure shrinkage are partially canceled out by the stresses due to thermal mismatch. However, if stresses exceeded the yield stress during cure before heating up to room temperature, this curing cycle would be insufficient.

To remove the large stress jump when the temperature ramps up at the end of the curing period consider the following: it was seen that when curing at temperatures below operational temperature, the stresses due to cure can be reduced. However the stresses were first built up due to shrinkage and then removed by heating. It would be desirable to do both at the same time. A good way to accomplish this is to have the cure shrinkage proportional to the thermal expansion. The thermal expansion coefficient is assumed to be independent of cure and the thermal expansion of pure epoxy is therefore a linear function of temperature. Thus, the cure shrinkage is proportional to the degree of cure in the current model. Therefore the requirement of cure shrinkage being proportional to the thermal expansion reduces to having the temperature change being proportional to the degree of cure. This is the same requirement that was stated earlier when considering the cure of the perfect insulator, with the exception, that this time the initial and the final temperatures are prescribed. To find the temperature history, start with the simplified version of the curing, equation 2.10, with n=1

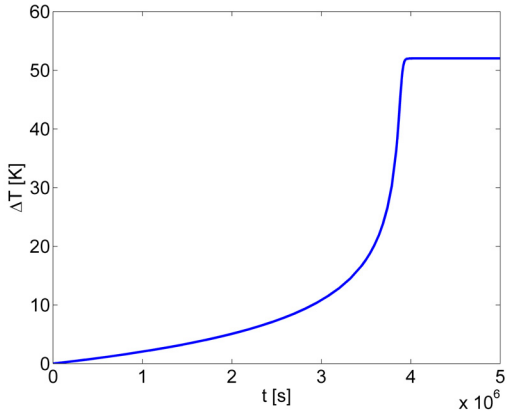

Figure 4.23 Temperature rise when cure is proportional to temperature

and m=A_2=0.

$$\frac{\mathrm{d}\phi}{\mathrm{d}t} = A_1 \exp\left(\frac{-\Delta E_1}{R(T_0+\Delta T)}\right)(1-\phi) \tag{4.4}$$

Now assume that the thermal expansion, and therefore the temperature, is proportional to the cure shrinkage or the degree of cure

$$\Delta T = (T_{\text{end}} - T_0)\phi = C\phi \tag{4.5}$$

The resulting differential equation can be either solved directly (numerically) using finite difference schemes or by finding roots to the following integral equation

$$t = \int_0^T \frac{\exp\left(\frac{\Delta E}{R(T_0+\tau)}\right)}{A_1(C-\tau)}\mathrm{d}\tau \tag{4.6}$$

The solution for a starting temperature of 243 K and a final temperature of 295 K is given in figure 4.23. The stress development is depicted in figure 4.24(a) and the circumferential stresses are given in figure 4.24(b). The stresses are small throughout large parts of the curing period and increase rapidly towards the end. This is tied in with the rapid rise of the degree of cure to the end. It can be noted that the goal of monotonically increasing stresses is achieved and there is no jump in stresses at the end of the curing process. Also the stresses are lower, compared to curing at 323 K. However, with a value of 24 MPa the final maximum circumferential stress is larger compared to the case discussed before. Previously all networks were assumed to have been formed at the same temperature and therefore all networks experienced the same temperature change and thermal expansion. Now, with ongoing time, new networks are formed at higher temperatures than previous

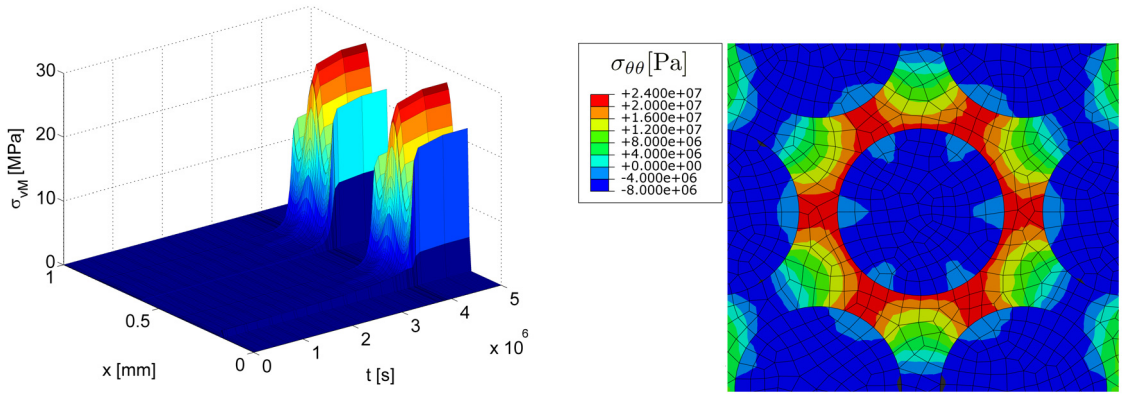

(a) von Mises stress evolution in sample cured from 243 K to room temperature and temperature rise is proportional to degree of cure

(b) Circumferential stress around center fiber after curing from 243 K to room temperature and temperature rise is proportional to degree of cure

Figure 4.24 Stress RUC cured from 243 K to room temperature and Temperature rise is proportional to degree of cure

ones. Therefore their thermal expansion between the state they are created in and the final state at room temperature will be lower. Consequently, stresses due to chemical shrinkage are reduced less, and thus, overall stress levels are higher. Which temperature profile is more desirable depends on whether stresses during constant low temperature cure are large enough to cause yield or damage in the matrix. If not, low temperature cure is preferential because it reduces residual stresses. Otherwise curing at a temperature profile proportional to cure is a better choice. It reduces the maximum tensile stress in the matrix.

It has been shown that curing at low temperatures can reduce stresses. However stresses are still tensile on the fiber interface and thus aide crack development. One way to produce compressive stresses in the matrix at the fiber-matrix interface is to have a cure shrinkage smaller than the subsequent thermal expansion (difference). So if it can be assumed that the epoxy is able to cure at very low temperatures and also that the volumetric cure shrinkage is 0.5% instead of 2%, compressive stresses can be obtained as seen in figure 4.25. Of course it is possible to get similar effects, if it were possible to chemically engineer an epoxy that swells during cure or if the fiber material observed large negative coefficient of thermal expansion.

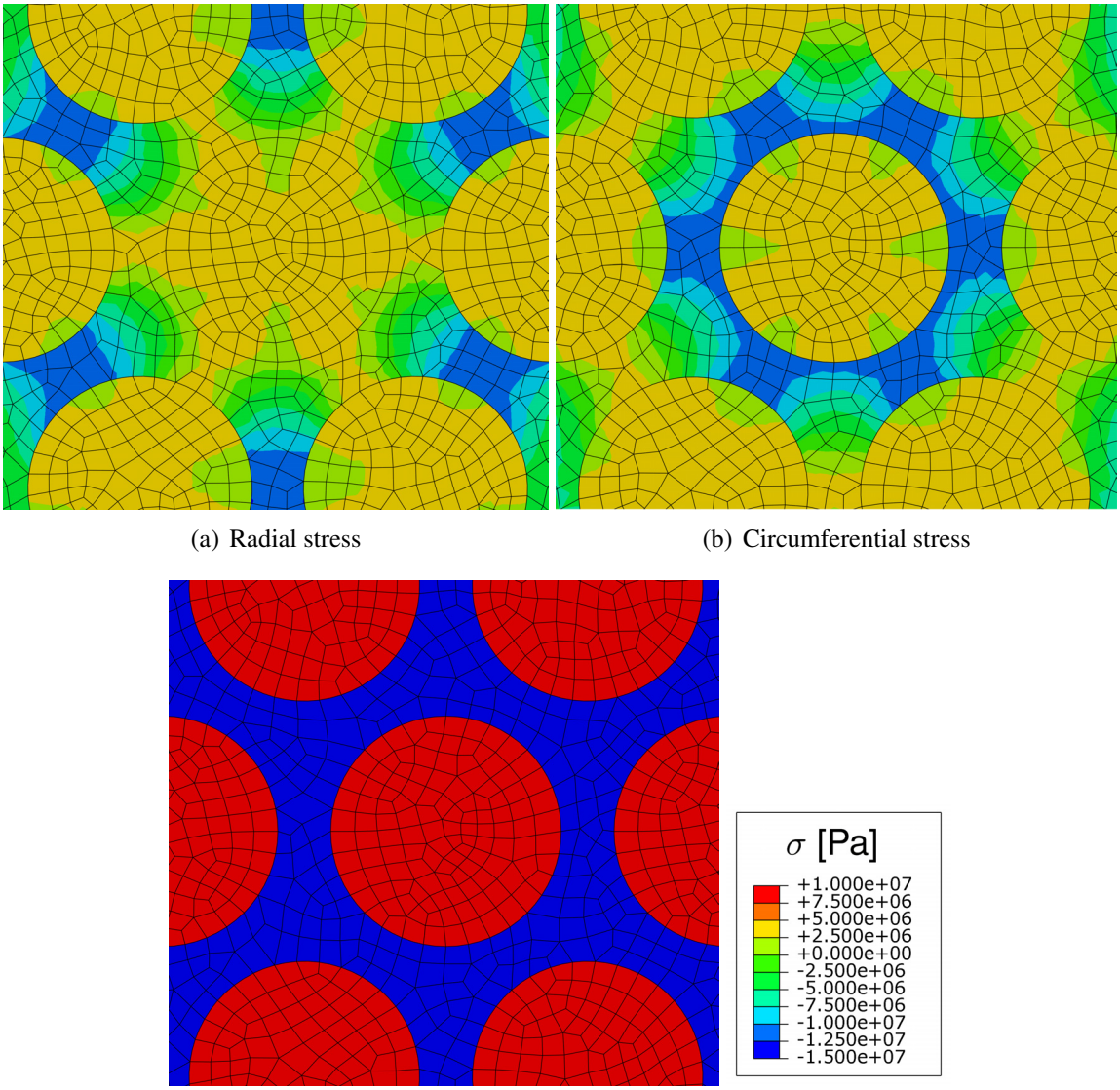

(a) Radial stress

(b) Circumferential stress

(c) Axial stress

Figure 4.25 Stress distribution around center fiber, cured at 243 K, volume shrinkage is reduced to 0.5%

4.3.3 Influence of curing on final shape

A further aspect that needs to be addressed when investigating the manufacturing of a composite is how much the final geometry will depend on the cure. For example, Zhu et al., [87], have investigated the dimensional accuracy of thermoset composites, especially circuit boards. Consider now the boundary value problem shown in figure 4.26. It shows a large unidirectional fiber composite plate, which might be manufactured through a VARTM process. The bottom of the plate is set to a certain temperature. The top side has only air and a vacuum bag surrounding it and is treated as an insulating wall. Perfect adhesion is assumed at the bottom of the plate, while the top can move freely up and down. The RUC captures the entire thickness of the plate, but only a limited amount in the length and width. To appropriately account for these directions, the periodic boundary conditions shown in figure 4.27 are applied. Displacements on front and back have to match, as well as the displacement on the left and right. While being in the mold, this equates to only up and down movement of the RUC. When being taken out of the mold, the plate is allowed to warp and bend, but the sides still have to stay flat due to periodic constraints.

Figure 4.28 shows the deformed shape of the unit cell when being taken out of the mold. The formerly rectangular shape deformed into a trapezoid and larger contractions can be observed on the top compared to the bottom. The deformation of the RUC for the BVP described is measured to have a radius of curvature of 37.7 m around an axis parallel to the fibers. This means, that a plate of 1 m side length would lift 3.3 mm on each side. The deformation in the plane perpendicular to the fibers is negligible. In this direction fibers provide strong support resisting deformation. The result is increased axial stress in the matrix in the direction parallel to the fibers.

A look at the temperature distribution during cure can give an insight into the causes for the final shape. Figure 4.29 shows the temperature distribution in the RUC after 600 seconds.

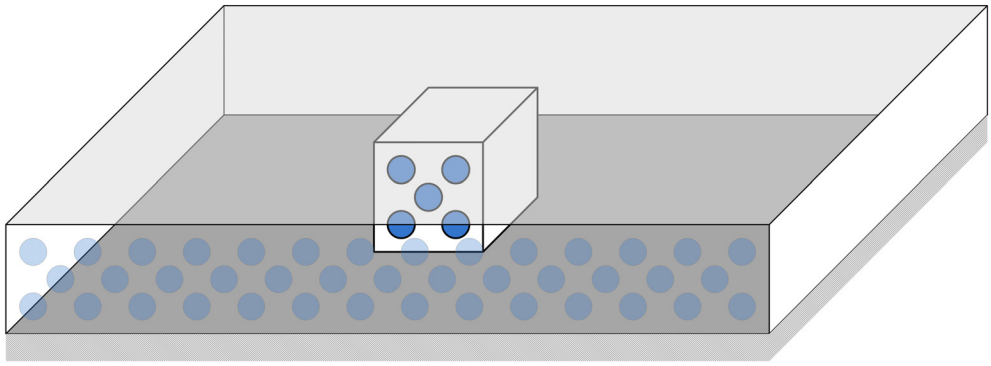

Figure 4.26 Schematic of the cure of a uniaxial composite plate

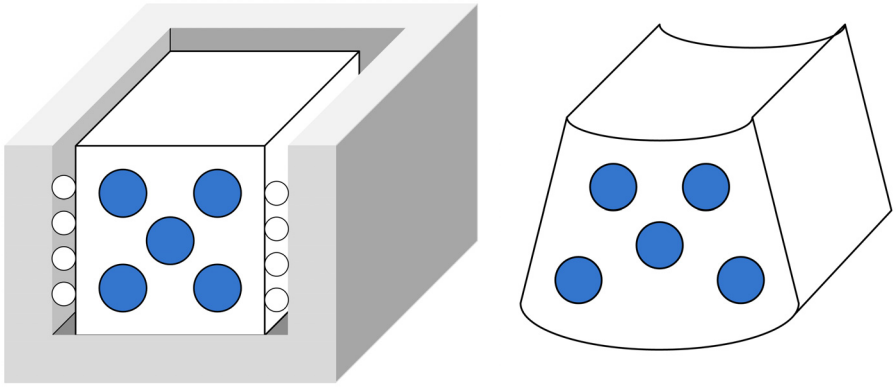

(a) In the mold (b) Removed from the mold

Figure 4.27 Boundary conditions in plate manufactured through VARTM

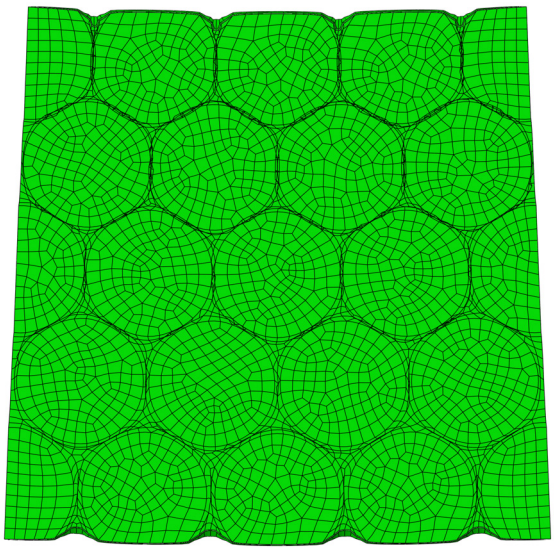

Figure 4.28 Deformed shape of RUC with 40X deformation scale factor

While the bottom of the mold is at the prescribed temperature of 323 K, the temperature at the top is 369 K. This results, as previously seen, in faster cure on the top compared to the bottom. At this top point, two opposing effects will occur. On the one hand, the top reaches full cure and therefore the final shape, before the bottom. The cure shrinkage of the later curing bottom causes compressive stresses on the top and tensile stresses on the bottom. The result is a downward curvature when the boundary conditions are relaxed. On the other hand the temperature on the top is higher and so is the reference temperature of the networks created there. Therefore, when the RUC is cooled down to room temperature at the end, these areas will exhibit a larger amount of cure shrinkage. This results in tensile stresses on the top and compressive stresses on the bottom. The result is an upward curvature. In the

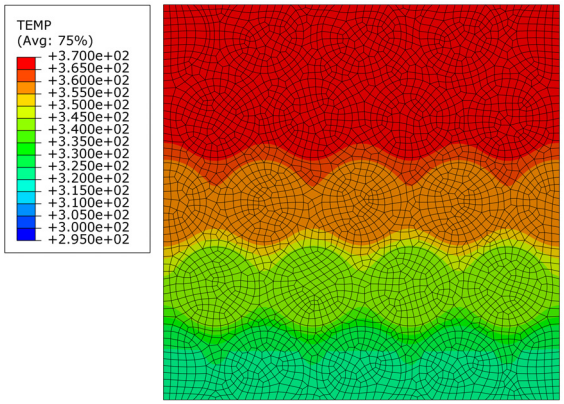

Figure 4.29 Temperature distribution after 600 seconds

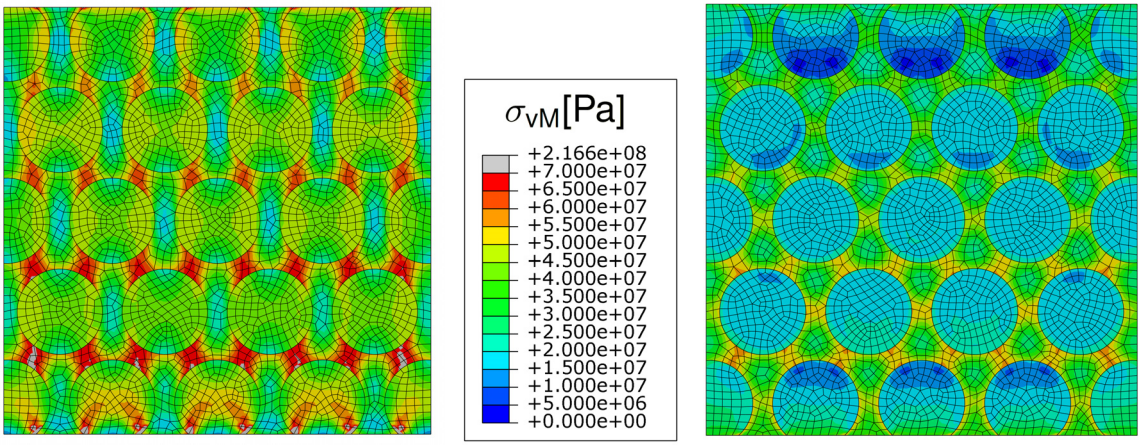

(a) In mold (b) Taken out of mold

Figure 4.30 von Mises stresses of RUC

example shown, the latter effects overweigh the former and the plate curves upward.

Finally, an account of the stresses should be given in figures 4.30 and 4.31. The von Mises stress and the maximum principal stress decreases from 72 MPa to 57 MPa and 82 MPa to 47 MPa respectively when allowing the RUC to assume a new shape. In all cases, a stress gradient is noticeable. The maximum stress measure is larger towards the bottom than at the top. Based on the above findings, which were limited to uniaxial cure of a composite, it appears that the overall thickness of the part that is being cured, together with the boundary conditions (heat from both sides or heating from one side, for example) can significantly contribute to the final geometrical tolerances.

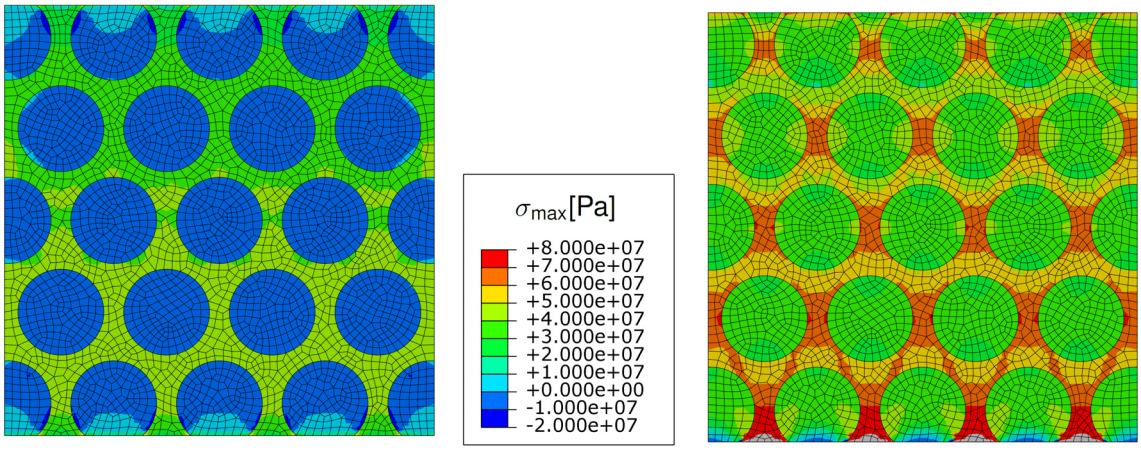

(a) (b)

Figure 4.31 Maximum principal stresses of RUC

4.4 Influence of Packing

So far only simple geometries and fiber arrangements have been considered, that is only a single fiber and a hexagonally packed array of fibers in the RUC studied in section 4.3. However, in any real fiber composite, the fibers are arranged to some degree in an arbitrary manner. At this point, the question arises how much the distribution of fibers affects the effective material properties. This is relevant for two problems. On one hand, homogenization techniques are used to find effective material properties, which in turn are used instead of the actual microstructure in subsequent calculations. Secondly, when fibers in a bundle are modeled, it would be helpful to know how many fibers are at least necessary to achieve a representative sample size. For example, can a fiber tow be modeled with tens of fibers instead of tens of thousands of fibers, as long as the degree of randomness and volume fraction are preserved and can the same end result still be achieved?

There are numerous techniques to extract the homogenized elastic and inelastic response of composite materials. A good summary of various homogenization techniques for the elastic response is given in [4]. These techniques include rule of mixtures, concentric cylinder assemblage [88], method of cells [89] and generalized method of cells [90]. These methods idealize the microstructure of the material and most of them assume a regular pattern of the fiber placement.

As stated, in reality the actual microstructure of the material is random in nature due to the manufacturing process and the manual steps involved in the process. The material will neither be entirely random nor entirely regular but instead fiber clusters and matrix pockets can be found [91]. When including non-linear effects, different microstructures can have a

profound impact on the overall result. Lissenden et al., [92], investigated the inelastic flow of fiber-reinforced metals having different microstructures . Specifically rectangular, hexagonal and square diagonal fiber packing arrays were investigated. It was found that the influence of microstructure is largest when fiber-matrix debonding is not an issue. Additionally, the effect of the microstructure increases with increasing fiber-volume fraction. A similar study was conducted by Brockenbrough et.al. [93]. Besides the effect of the fiber shape, they also included some microstructures with a random fiber distribution. It can be observed that there is a significant difference between the different packings investigated. It should be noted that the boundary conditions were chosen in such a way that straight boundary faces remained straight.

Recent studies of the micromechanical response of composites take a random distribution of fibers into account. These studies typically make use of the finite element method. Gonzáles et al. [94] investigated the mechanical behavior of unidirectional fiber-reinforced polymers under transverse compression. Interface decohesion between fiber and matrix, and matrix plastic deformation were included as damage modes.

A question that arises when taking into account randomly distributed fibers is how to quantify that randomness. Buryachenko et al. [95] used a digital image processing technique to measure the coordinates of fibers. Then they estimated the statistical parameters and used radial distribution functions describing the random nature of the composite. Ghosh et al. [96] noted that radial distribution function and second order intensity function are less suited to characterize the microstructure at higher volume fractions. Instead they employed Voronoi cells to model a multi phase material.

Using Voronoi tessellations, in conjunction with the finite element method, the effect of non-uniform fiber packing is studied next. A Voronoi tessellation with 9 distinct fibers is shown in figure 4.32 on the left. The actual RVE is shaded in gray. To calculate the size of the Voronoi polygons within the periodic unit cell, an image of the fiber positions have to be created around the unit cell. These shifted copies are lying in the white region of figure 4.32. The resulting FE model is shown on the right. The variation in the area of the Voronoi cells can be used to describe the deviation from regular packing.

The boundary conditions parallel to the fiber direction are periodic, [94] and are given below,

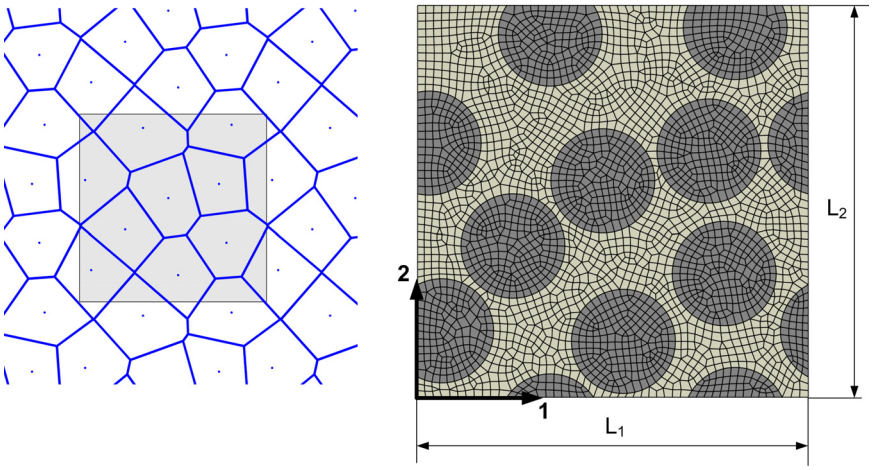

Figure 4.32 Voronoi cells and corresponding finite element model

$$u_1(L_1,x_2) - u_1(0,x_2) = E_{11}L_1 \tag{4.7}$$
$$u_2(L_1,x_2) - u_2(0,x_2) = 0 \tag{4.8}$$
$$u_1(x_1,L_2) - u_1(x_1,0) = 2E_{12}L_2 \tag{4.9}$$
$$u_2(x_1,L_2) - u_1(x_1,0) = E_{22}L_2 \tag{4.10}$$

where, E_{ij}, are the macroscopically measured/homogenized strains of the RVE and L_1 and L_2 are the side lengths of the RVE in the 1 and 2 direction, respectively, as shown in figure 4.32. The boundary conditions in the 3-direction were chosen such that plane sections remain plane, i.e. the displacement in the 3 direction was the same everywhere. The unit cell is considered small enough such that gradients in temperature are small. Based on the observation on of the earlier calculations, it now assumed the temperature field is uniform everywhere throughout the domain. Consequently, the temperature was prescribed to be the same at every material point within and on the boundary of the domain studied. When considering a composite part on the macroscopic level, i.e. the tow level, heat conduction has to be taken into account.

300 renditions of non-uniformly packed unit cells have been sampled over a range of 4 to 50 fibers per unit cell. The degree of randomness is chosen to be described by the relative standard deviation of the area of the Voronoi cells relative to the average area, i.e.

$$\overline{\sigma} = \sqrt{\frac{1}{n}\sum_{i=1}^{n}(A_i - \overline{A})^2} \Big/ \overline{A} \tag{4.11}$$

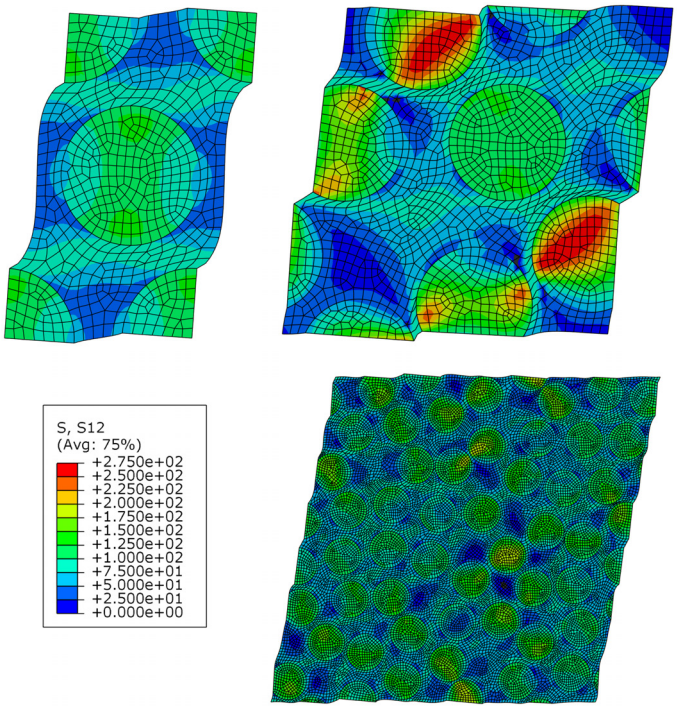

Figure 4.33 Shear response of hexagonal, 5-fiber and 50-fiber unit cell

where A_i is the area of each Voronoi polygon and $\overline{A}$ is the average area (arithmetic mean) of the Voronoi polygons.

The convergence of stresses in the curing unit cell as a function of fiber number is of interest. A similar study has also been conducted in connection with the shear response of a randomly packed unit cell with elastic-plastic material properties, subjected to in-plane shear loading, as similar problems have been discussed in the literature, [97]. In both cases the convergence of stress as a function of the fiber number is studied. It is to be noted that the shear BVP solution does not include the effects of the curing stresses.

The shear loading BVP simulations were done in the context of plane strain elastic-plastic behavior with J_2-flow theory, [98]. Whenever possible quadratic plane strain elements where used with quadratic triangles inserted whenever necessary to avoid mesh distortion. The material properties were comparable to carbon fiber and Hetron® epoxy.

The results of two different simulation cases (shear loading and curing)will be discussed in the following. The results for the shear response of a unit cell with 5 fibers (random), 50 fibers (random) and 2 fibers (hexagonal packing) are given in figure 4.33. The random unit cells had a "randomness" of $\overline{\sigma} = 10\%$ according to equation 4.11. All unit cells were sheared to a macroscopic strain $E_{12} = 0.02$. The average stresses and strains were calculated by summing the stresses and strains at the integration points, [99]. They were then normalized

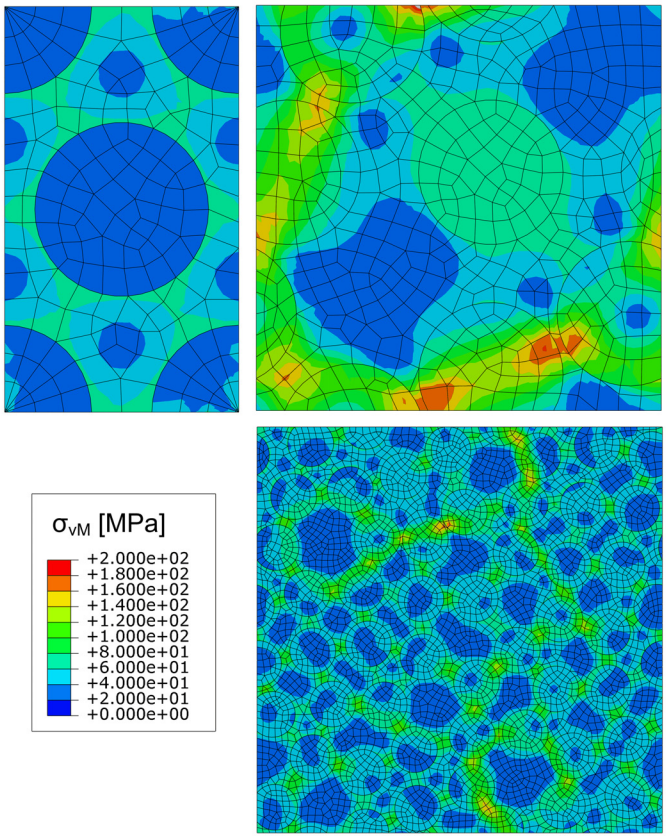

Figure 4.34 Residual stresses due to cure in hexagonal, 5-fiber and 50-fiber unit cell

by the total volume:

$$\Sigma_{ij} = \frac{1}{V}\int_V \sigma_{ij} \mathrm{d}V \tag{4.12}$$

$$E_{ij} = \frac{1}{V}\int_V \varepsilon_{ij} \mathrm{d}V \tag{4.13}$$

It is worth noting that the average shear strain E_{12} calculated using equation 4.13 is indeed identical to the strain imposed by the periodic boundary conditions (4.7) - (4.10). In general the average shear stress is largest in the smallest random unit cell as shown in figure 4.35. With increasing unit cell size and fiber number, the average shear stress decreases in the random unit cells. The hexagonal packing marks a lower bound for the response. This behavior is somewhat expected. Compared to a hexagonal packing arrangement, random packing places some fibers closer to each other than others. This causes stress concentrations and earlier yielding in these regions compared to the overall unit cell. On the other hand there are also larger homogeneous regions of matrix rich regions. Here stress concentrations

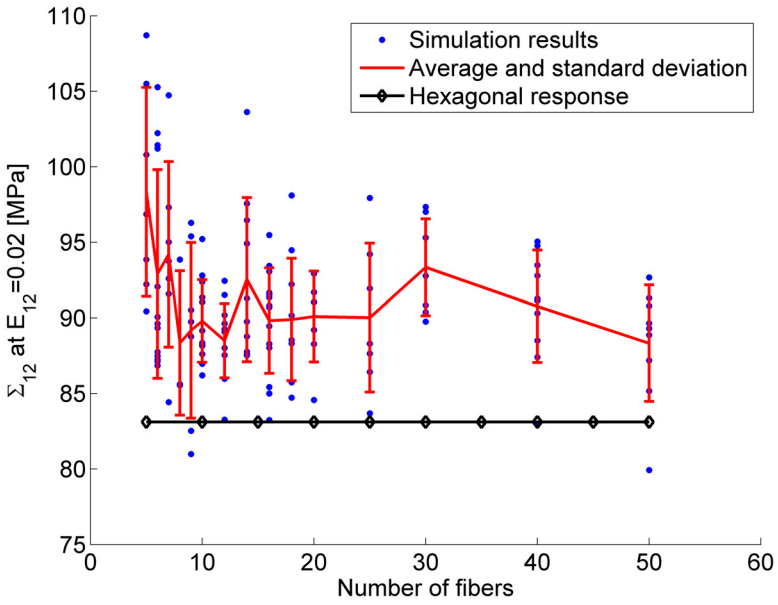

Figure 4.35 Average macroscopic shear stresses Σ_{12} when a macroscopic strain E_{12} of 0.02 is applied vs. number of fibers in a unit cell

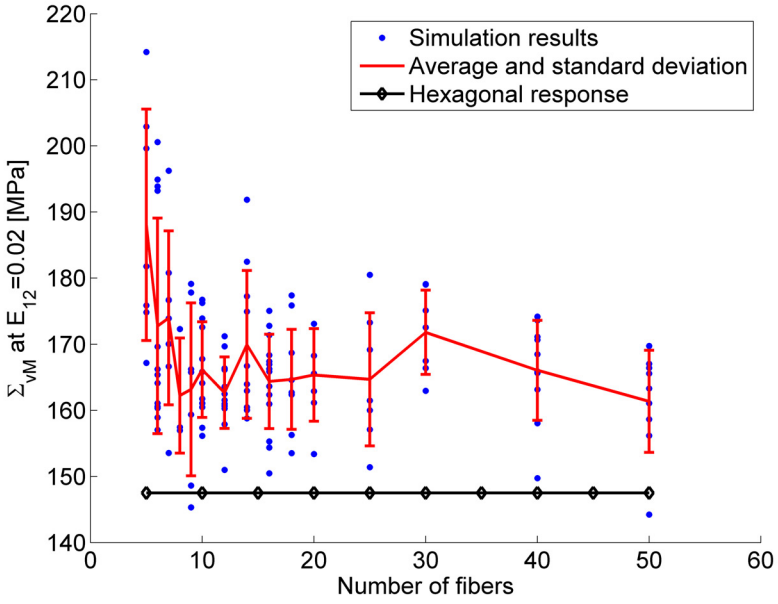

Figure 4.36 Average macroscopic von Mises stress Σ_{vM} when a macroscopic strain E_{12} of 0.02 is applied vs. number of fibers in a unit cell

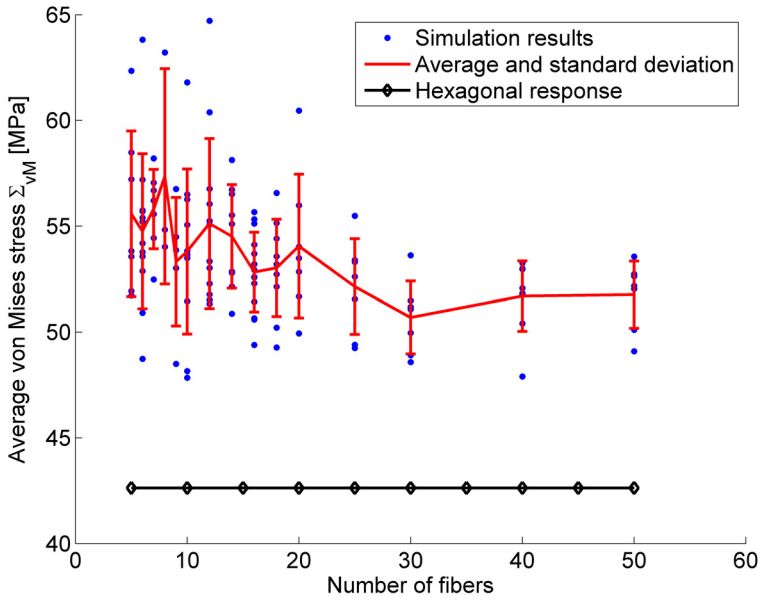

Figure 4.37 Average macroscopic von Mises stress Σ_{vM} after cure vs. number of fibers in a unit cell

are lowered and yield is delayed. Due to the non-linear nature of the problem, the reduced stresses in regions of less fibers combined with the increased stresses in regions of closer fibers do not reproduce the same results as regularly dispersed fibers. From a statistical point of view, the deviation in responses between different samples of the same unit cell size decreases with increasing fiber number. For larger samples, there are still regions where fibers are close to each other but for the same measure of randomness these regions of high stress appears less often than for small samples. What can be conclusively stated from the results of figure 4.35 is that as the number of fibers increases, the maximum average shear stress in the sample appears to show less deviation. Other stress measures, such as the von Mises stress, also show the same trend, as shown in figure 4.36

Now, similar observations can be made for the cured composite, as shown in figure 4.37. The residual stresses are large in small random unit cells and decreases when more fibers are added. Also, the spread between different samples of the same random unit cell size decreases with increasing amount of fibers. The hexagonal packing produces the lowest residual stresses. For the curing case, as well as the shear loading case, the largest variations in simulation outcomes can be found for unit cells that are smaller in size than 20 fibers. On the other hand neither case can be considered converged in terms of its response even for unit cells that contain 50 fibers. It should also be kept in mind that in the case of the curing model used here, only residual stress built up is investigated.

4.5 Cure of tow level RUC

The last example of stress evolution during cure will be concerned with a woven composite. In the previous studies, the tows which consist of matrix and fibers have been homogenized, so that a unit cell consisting of a few homogenized tows and the matrix material in between [5, 8], have been utilized for model development. For these models a viable homogenization technique needs to exist. The previous section gives several examples for techniques that can be used to obtain homogenized elastic or plastic tow properties. Due to the novel nature of the proposed curing model such a homogenization technique is not readily available. An exception is of course the use of a fine scale finite element model within a coarse scale finite element model. However, currently such an approach would be computationally very expensive. As an alternative to homogenization of the tows, they will be modeled using micromechanics. That is, the tows will be represented as a collection of a few discrete fibers and matrix. The size of the fibers is chosen such that the volume fraction and the outer dimension of the tow is equivalent to the dimensions of an actual tow. In the previous section it has been shown that for a particular class of material properties the response of a unit cell consisting of 20 fibers or more is insensitive to the packing. A similar behavior is expected when the fibers are arranged in undulating tows, instead of uniaxial RUCs. However, in order to keep the computational size manageable each tow will consist of 7 fibers, which are arranged in a compressed hexagon, as shown in figure 4.38(c).

One of the simplest braids is a plane weave. Here fiber tows run either in the 0° or 90° direction. A 2x2 unit cell model is shown in figure 4.38 where the woven fiber tows are also shown separately. The plane weave architecture has been chosen as an example, because the geometry creation is significantly easier, compared to a triaxial braid, that has been used in previous studies, [3]. Aside from a larger complexity in the geometry creation of a triaxially braided RUC no further differences exist in the application of the epoxy curing model.

The unit cell has been subjected to the same temperature cycle that has been discussed before in figure 4.2. The start and end temperature are room temperature and curing takes place at 50°C. The edges outer are free to move. No traction is applied on the outer edge surfaces. Only rigid body motion is prevented. The von Mises stresses and the maximum principle stresses at the end of the curing cycle are depicted in figures 4.39 and 4.40. Two different cross sections are considered. One in the middle of the 2x2 RUC (shown $\square ABCD$ in figure 4.38(b)) and the other a cross-section slightly removed from the center, $\square EFGH$, as shown in figure 4.38(b). Due to periodicity at the cross-section $\square JKMN$, the identical picture could be observed, as in the middle, at $\square ABCD$, just shifted by half a unit cell length, $L/2$. The location of the cross sections are marked by black cuts in figure 4.38(b).

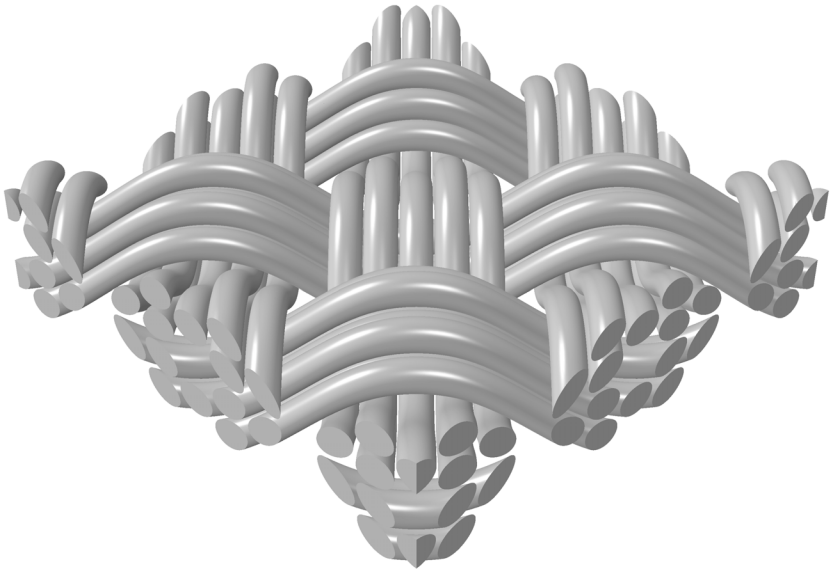

(a) Just fibers

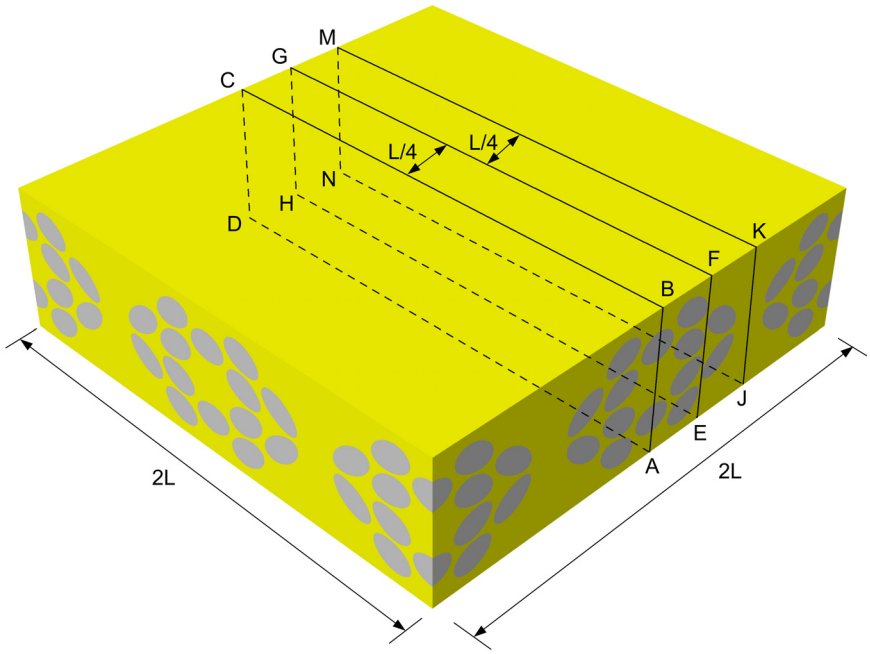

(b) Fibers in matrix

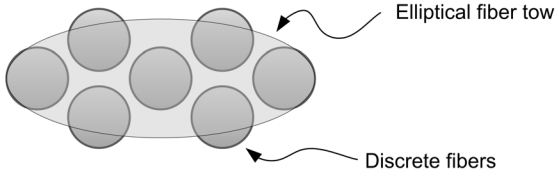

(c) Cross-section of idealized tow

Figure 4.38 2x2 Plane weave RUC

Figure 4.39 shows the von Mises stresses and maximum principal stress in the middle of the 2x2 RUC. The stresses are lowest at the surface, far away from the fiber. Here effects due to thermal mismatch and cure shrinkage are lowest. In the center two fiber tows cross, one on the top and on the bottom. In the middle a matrix rich region can be found. In that area, the fibers serve as an almost rigid constraint. Therefore the von Mises stress is quite low. However the maximum principal stresses are very large, due to the constrained thermal and cure shrinkage. Values of high principal stress can also be found in regions where fibers are close together. The same is true for the von Mises stress and maximum principal stress shown in figure 4.40. Areas of high principal stress are where fibers are close together. It should be noted that almost throughout the entire RUC the maximum principal stress in the matrix is at an elevated level of about 50 MPa and more. Thus, the matrix has an appreciable stress magnitude due to the cure and shrinkage of the manufacturing process, even prior to the application of service loads. Consequently, the magnitude and sign of the stresses (tension or compression) can play a significant role in influencing the subsequent deformation response under service loads. In particular, it is of interest to examine the possibility of the onset of matrix damage due to cure and shrinkage. This is addressed in the next chapter.

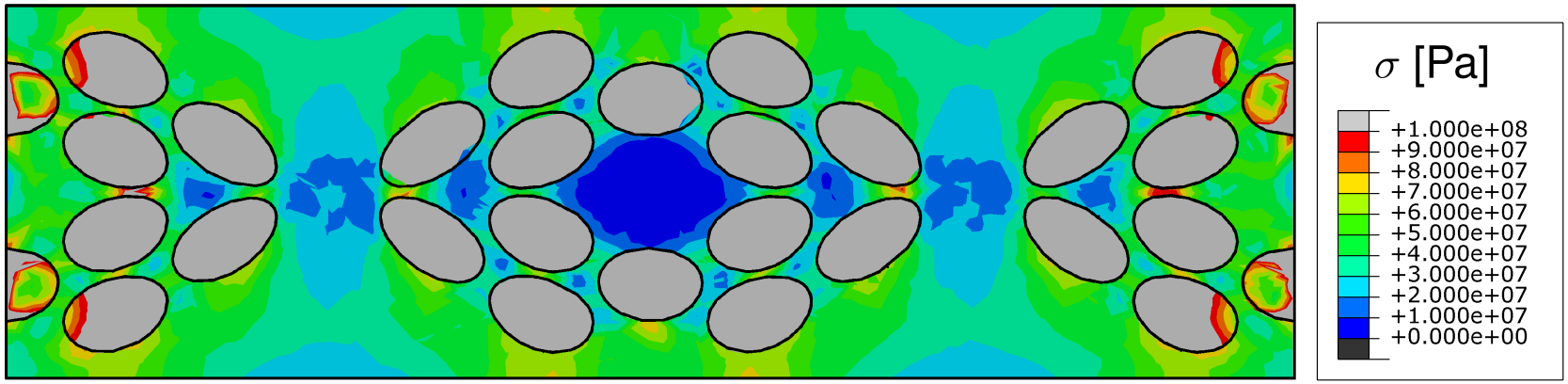

(a) Von Mises stress

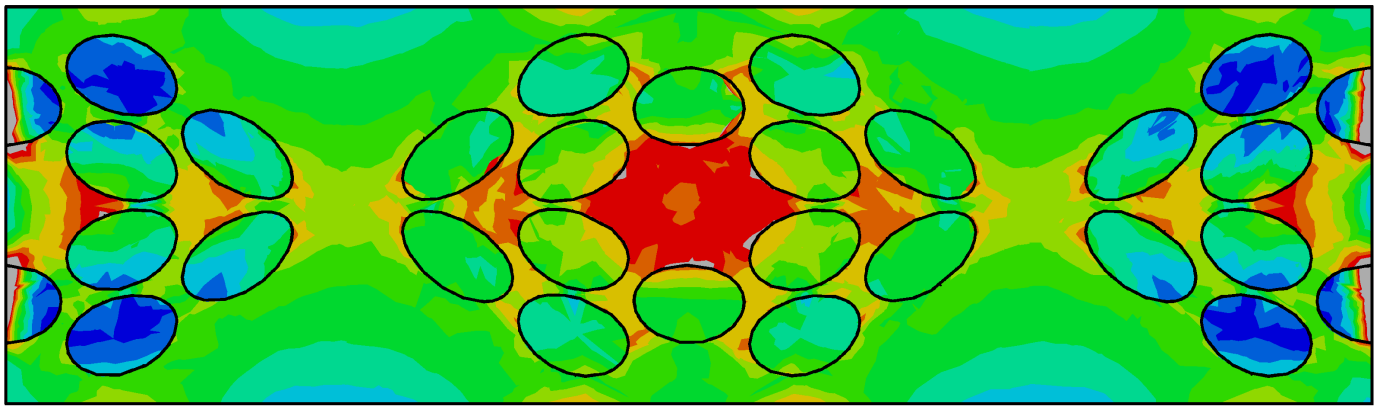

(b) Maximum principal stress

Figure 4.39 Stresses in cross-section □*ABCD*

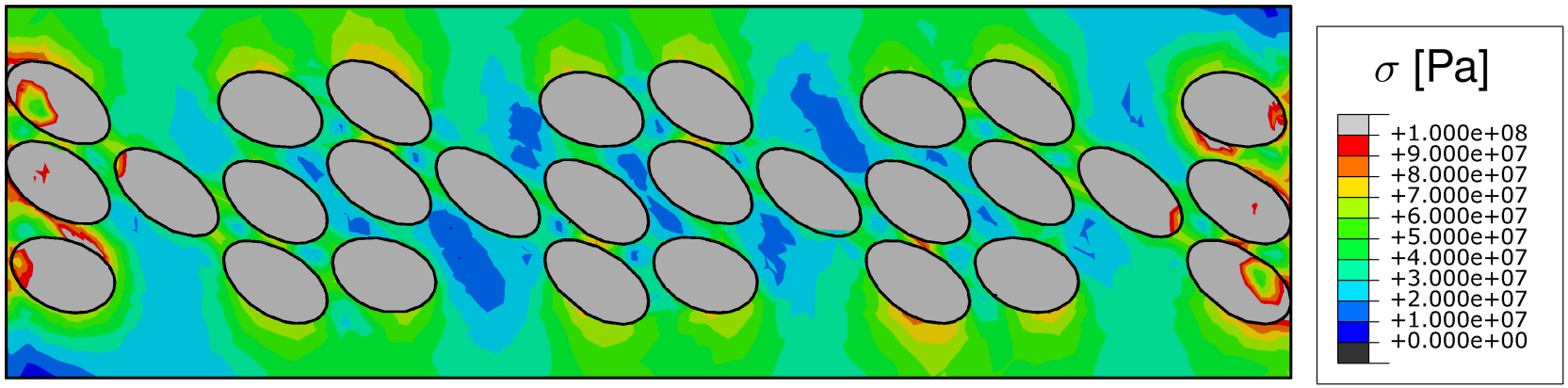

(a) Von Mises stress

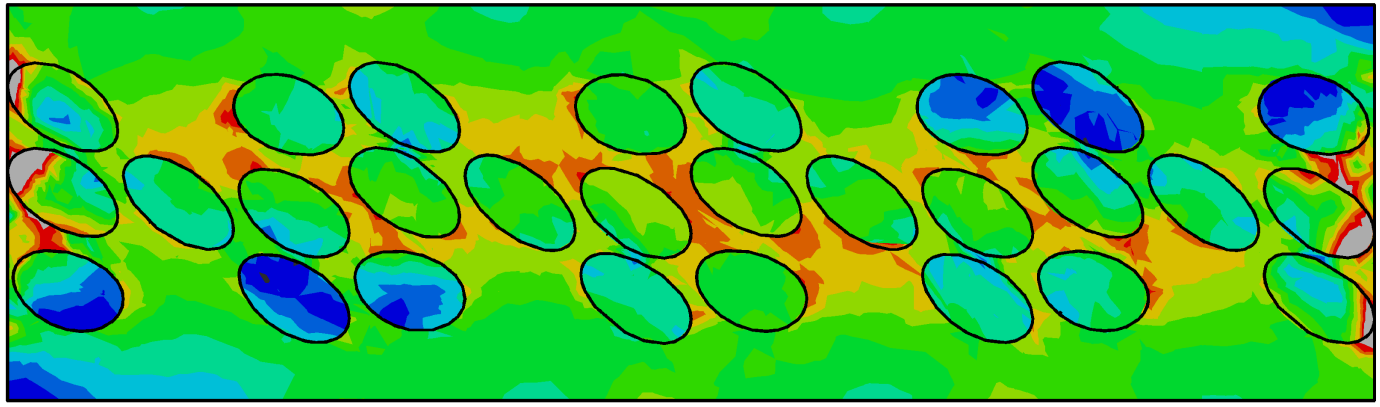

(b) Maximum principal stress

Figure 4.40 Stresses in cross-section $\square EFGH$

4.6 Conclusion

The creation of stress due to curing has been shown for various curing cycles, geometric arrangements and boundary conditions. Due to cure shrinkage and thermal mismatch manufacturing process induced stresses in the matrix can generally be expected. The magnitude of stresses are higher if the epoxy material is confined which is the case where fibers are close together or where the boundary is constrained, which is typically due to the constraints of the mold. Because epoxy expands significantly more upon heating compared to carbon fibers, stresses could theoretically be lowered by curing a part below operating temperature. Practically, this may not be viable, because it would drastically increase manufacturing time. Generally the stresses due to cure and shrinkage are quite appreciable and might locally already exceed limits for yield and fracture. Therefore it is necessary to examine the onset of damage in the matrix due to the curing process.

Chapter 5

Damage

The model proposed in chapter 3 for the creation of networks during cure shows linear elastic behavior upon full cure. It can therefore serve as a guide to curing conditions that will lead to small or large residual stresses, but it lacks the capability of predicting non-linear response during cure or in service. The results presented in chapter 4 show that the epoxy might already observe damage in the form of cracks during the curing process [20], [22]. This is also shown figure 5.1, which shows a cross section image of a fiber tow (carbon fiber and Hetron resin), [47], that shows damage in the form of crack present in the composite just after cure and prior to application of mechanical loads. Therefore, it is important to develop a model that allows the possibility of damage (non-reversible effects) to occur during the process of curing. Such a model is presented in this chapter and the implication of incorporating damage and the effects of damage on the curing process and subsequent mechanical loading are presented in chapter 6.

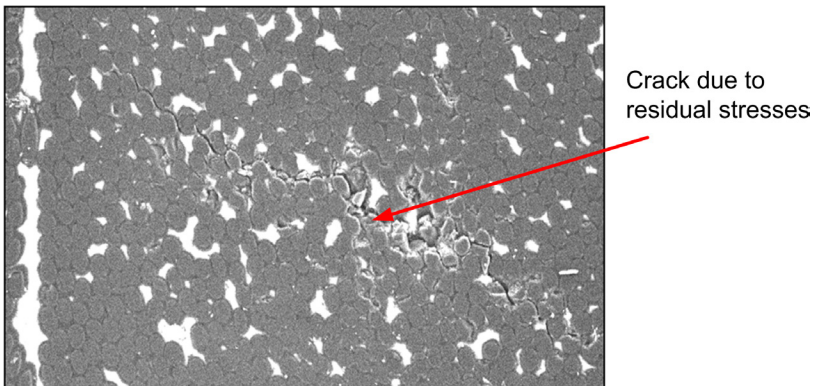

Figure 5.1 Crack in composite due to excessive stresses during cure

5.1 Damage in continuum mechanics

There is a multitude of ways to incorporate damage and failure into a material model. Some are shown in figure 5.2. The most convenient way is to model all non-linear effects within the framework of classical plasticity. Various plasticity models can be found in the literature, they are well understood and they have been widely implement into computer codes [55, 100, 101]. However, in light of the current study there are some shortcomings. The unloading slope of a plastically deformed "classical" solid will be proportional to the loading slope. That means, the elastic properties are not altered in classical plasticity. Also classical plasticity models are usually not capable of "ending" a stress-strain law. That means, continued loading will not lead to a decrease in stress, but will lead to continued flow, either with increasing stress (hardening) or constant stress (prefect plasticity). The most important consequence of damage is the *reduction* in stress with continued deformation. Models that incorporate reduction in stress beyond a peak stress are termed "softening" stress-strain laws. Naturally, these laws will need to accommodate a negative tangent stiffness in the stress-strain response as schematically shown in figure 5.2(d).

The physical significance of continuum damage can be explained both for metals and for polymers, [1]. In metals the damaging process might be regarded as the nucleation of microscopic cracks and voids. With increasing strain these will grow, coalesce and eventually form a macroscopic crack. In rubbery polymers on the other hand, damage can be seen as the rupture of polymer chains. Especially the last example gives a nice interpretation to the damage that will be investigated in the following: continued damage leads to continued breakage of bonds or springs and therefore loss of stiffness. The earliest work in the area of continuum damage mechanics is usually attributed to Kachanov (the translation can be found in [102]) who introduced an internal variable to model creep failure. Rabotnov [103] is attributed to giving physical meaning to the internal variable, although there has been some debate about whether such a thing should be attempted, [104]. Let us assume that damaged and undamaged load bearing cross sectional areas of a body are given by A and A_d respectively as shown in figure 5.5, [105]. Then the damage can be viewed as

$$D = \frac{A - A_d}{A}. \tag{5.1}$$

If $D = 0$, the material is completely damage free. $D = 1$ corresponds to a fully damaged or ruptured body, i.e. it is broken into two parts. Which means, the macroscopic crack in figure 5.3 fully advanced trough the entire cross-section. $0 < D < 1$ characterizes a damaged state. If one considers the force $\underline{F}$ acting normal to the surface A, the traction is given as

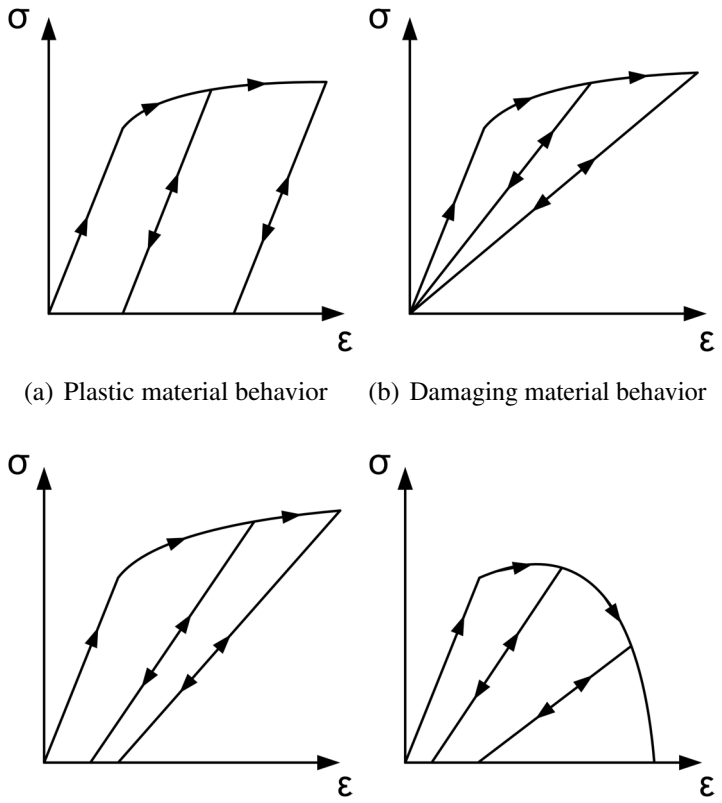

(a) Plastic material behavior

(b) Damaging material behavior

(c) Combined damage and plastic material behavior

(d) Softening material behavior, including damage and plasticity

Figure 5.2 Comparison of plastic and damaging material behavior

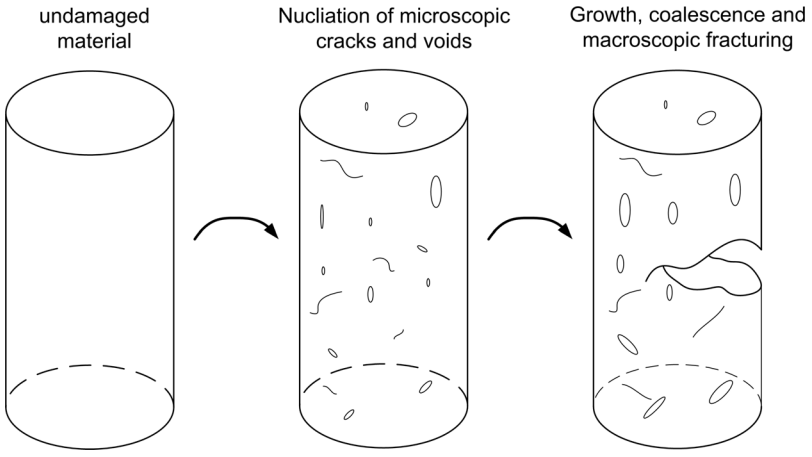

Figure 5.3 Ductile damage in metals [1]

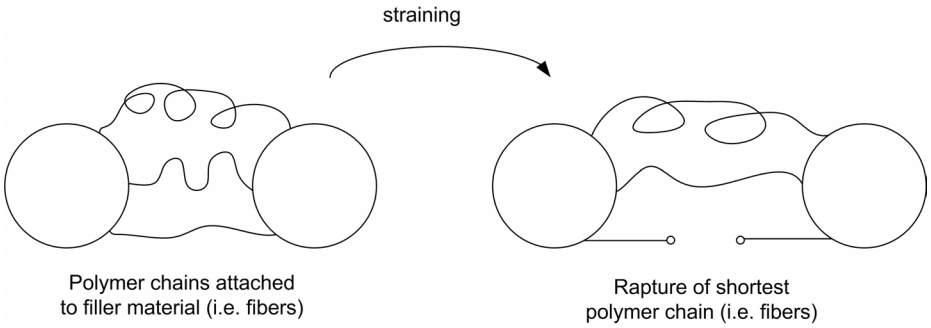

Figure 5.4 Damage of polymer chains [1]

$\underline{T} = \underline{F}/A$ ([106]). Then, an effective traction is given by

$$\underline{T}_{eff} = \frac{\underline{F}}{A_{eff}} = \frac{\underline{T}}{1-D}, \tag{5.2}$$

which leads by the usual definition of stress and traction, $\underline{T}_{eff} = \underline{\underline{\sigma}} \cdot \underline{n}$, to the effective stress

$$\underline{\underline{\sigma}}_{eff} = \frac{\underline{\underline{\sigma}}}{1-D}. \tag{5.3}$$

Using the linear elastic constitutive behavior, the relation between the stress and strain in the undamaged and damaged material, respectively are given by

$$\underline{\underline{\sigma}} = \underline{\underline{\underline{\underline{C}}}} : \underline{\underline{\varepsilon}} \tag{5.4}$$

$$\underline{\underline{\sigma}}_{eff} = \underline{\underline{\underline{\underline{C}}}}_{eff} : \underline{\underline{\varepsilon}} \tag{5.5}$$

This leads to the effective stiffness

$$\underline{\underline{\underline{\underline{C}}}}_{eff} = (1-D)\underline{\underline{\underline{\underline{C}}}} \tag{5.6}$$

With that, the final constitutive equation given by

$$\underline{\underline{\sigma}} = (1-D)\underline{\underline{\underline{\underline{C}}}} : \underline{\underline{\varepsilon}} \tag{5.7}$$

It should be noted that implicitly the assumption has been made, that damage can be

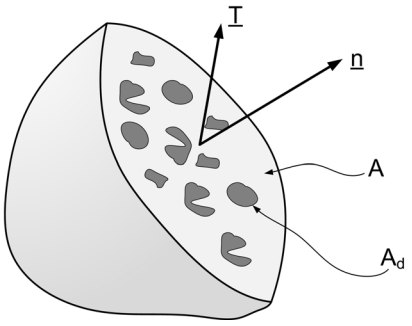

Figure 5.5 The effective stress concept, [2]

described by a scalar value. Furthermore, this scalar measure of damage D does not need to be monotonically varying with stress and/or strain. For example, it can be specified as a function of both, stress and strain in the form of a lookup table based on experimental observation. However, in this work it is assumed that the values of D, must conform to a reduction in stress with continued loading. That means, material healing is not allowed. Since D is a scalar, the hypothesis of isotropy has been used. It simplifies calculations significantly but higher order expressions might be suitable for more sophisticated theories. For example, it can be argued why strain in the normal direction should cause a reduction of material properties perpendicular to that direction. Distinguishing the direction in which damage occurs based on the direction and magnitude of some stress or strain measure will lead to anisotropic material behavior after the onset of damage. An example might be the following: assume that the material is initially isotropic. Damage initiation and direction is driven by the maximum principal strain. Then the stress-strain relation in the coordinate frame relative to the maximum principal strain at damage initiation can be described by

$$\begin{pmatrix} \sigma_{11} \\ \sigma_{22} \\ \sigma_{33} \\ \sigma_{12} \\ \sigma_{13} \\ \sigma_{23} \end{pmatrix} = \begin{bmatrix} (1-D_\perp)(\lambda+2\mu) & (1-D_\perp)\lambda & (1-D_\perp)\lambda & 0 & 0 & 0 \\ & \lambda+2\mu & \lambda & 0 & 0 & 0 \\ & & \lambda+2\mu & 0 & 0 & 0 \\ & & & 2(1-D_{||})\mu & 0 & 0 \\ & (\text{sym}) & & 0 & 2\mu & 0 \\ & & & 0 & & 2\mu \end{bmatrix} \begin{pmatrix} \varepsilon_{11} \\ \varepsilon_{22} \\ \varepsilon_{33} \\ \varepsilon_{12} \\ \varepsilon_{13} \\ \varepsilon_{23} \end{pmatrix} \tag{5.8}$$

where the damage can be different in the direction perpendicular or parallel to the evolving micro cracks. In this example, as shown in figure 5.6, it is assumed that the evolving cracks line up in one direction.

Once full damage occurs, effectively a crack will have formed on the plane normal

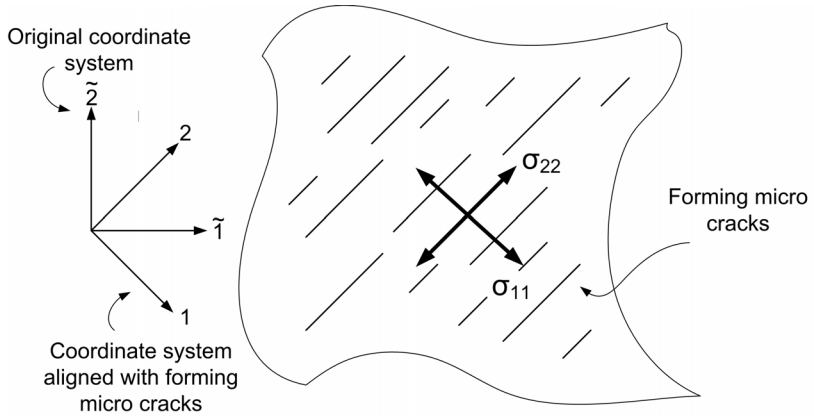

Figure 5.6 Example of anisotropic material properties due to micro cracks modeled by continuum damage

to the maximum principal strain. However the material is still able to carry load in the perpendicular direction. To account for such behavior, the damage needs to be described by a tensor quantity. This has been discussed for a second order tensor in [107] and for a fourth order tensor in [54]. Especially when looking at equation (5.6) choosing a fourth order damage tensor allows to degrade individual entries in the fourth order stiffness tensor. The damage tensor, $\underline{\underline{\underline{\underline{D}}}}$ is subject to major and minor symmetries, as the stiffness tensor is. More details are given in [108].

Continuum damage can be derived rigorously on a thermodynamic basis. In that case a thermodynamic potential is needed which may be decomposed into elastic and plastic parts [106, 109], assuming plasticity is also modeled. In that case, the damage response is absorbed into the elastic potential. It is also possible to split the thermodynamic potential into three parts: elastic, plastic and damage [110, 111]. In, [110], the strain was accordingly decomposed into elastic, plastic and damaging strains.

5.2 Strain softening behavior

5.2.1 Problem formulation

While a formulation using a thermodynamic potential is theoretically more sound, in the following a formulation like (5.7) will suffice to keep the derivation clearer. That is, it will be assumed that a uniaxial stress-strain curve of the type shown in figure 5.7 has been provided as material data. It will be assumed that the post-peak response is solely due to damaging behavior. Thus, the model development will be for an elastic-damaging solid,

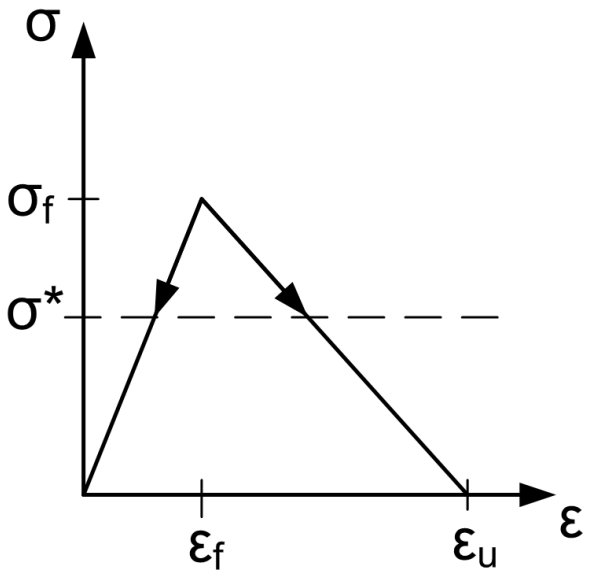

Figure 5.7 Softening stress-strain curve

whose uniaxial stress=strain response is described in figure 5.7.

It is often argued that a negative slope in the post-peak regime is physically not possible. It implies an imaginary speed of sound, [112]. However it can be argued, that the observed result is the combined response of structural changes of a representative volume of material. Little voids and cracks that cannot all be captured have formed within this volume. In between the voids and cracks, the speed of sound is real. Nevertheless, when considering the response of the entire material, softening can be observed. Imaginary speed of sound is not the only problem intrinsic to this stress-strain formulation. A loss of objectivity can be observed in numerical calculations that adopt any type of discretization scheme, [112]: when calculating a solution using finite element methods, the result will be strongly dependent on the mesh size. As an example consider the one dimensional bar in figure 5.8, [57, 112, 113]. Part of the beam consists of linear elastic material and a certain region of the beam has a softening material law.

Assume that the beam has a constant cross section. The displacement is prescribed and the force or stress is measured. The stress-strain relations for the two materials are given as

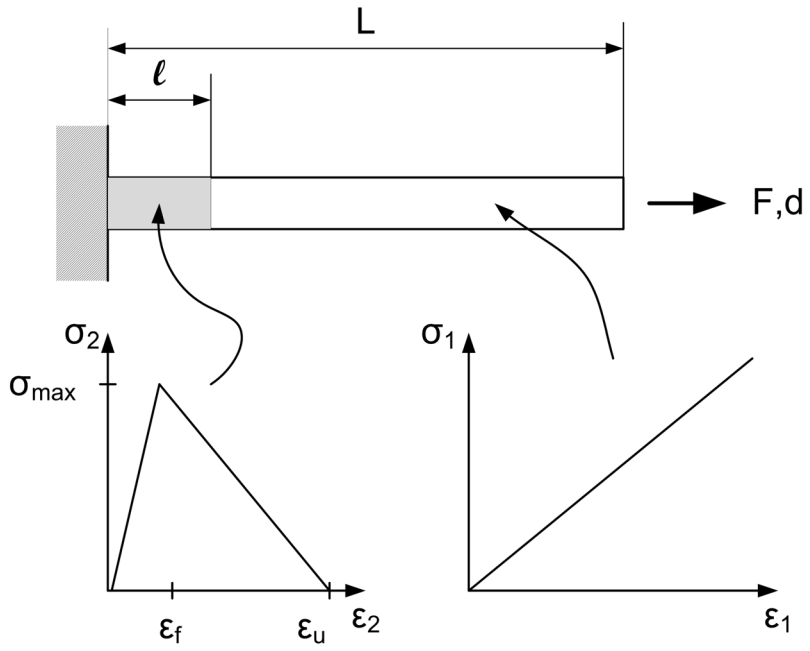

Figure 5.8 Beam under tension with some linear elastic material and softening material

$$\sigma_1 = E_1 \varepsilon_1 \tag{5.9}$$

$$\sigma_2 = \begin{cases} E_2 \varepsilon_2 & \text{if } \varepsilon_2 \leq \varepsilon_f \\ \varepsilon_f E_2 - \frac{E_2(\varepsilon_2 - \varepsilon_f)}{\varepsilon_u/\varepsilon_f - 1} & \text{if } \varepsilon_f < \varepsilon_2 \leq \varepsilon_u \\ 0 & \text{if } \varepsilon_u < \varepsilon_2 \end{cases} \tag{5.10}$$

Two cases can be distinguished. In the first case the strain in the softening material is below the failure strain $\varepsilon_2 < \varepsilon_f$.

$$F = \frac{AdE_2}{E_2/E_1(L-l)+l} \tag{5.11}$$

In the second, the initial failure strain has been exceeded in the strain softening material $\varepsilon_2 > \varepsilon_f$.

$$F = \frac{A(d - l\varepsilon_u)}{(L-l) - \frac{E_1}{E_2} l(\frac{\varepsilon_u}{\varepsilon_f} - 1)} E_1 \tag{5.12}$$

The above results are compared to a FE calculation as shown in figure 5.9. The analytical and numerical solutions match exactly. However, it should be noticed, that the softening region was always chosen to be only one element in size. If the mesh is refined in the

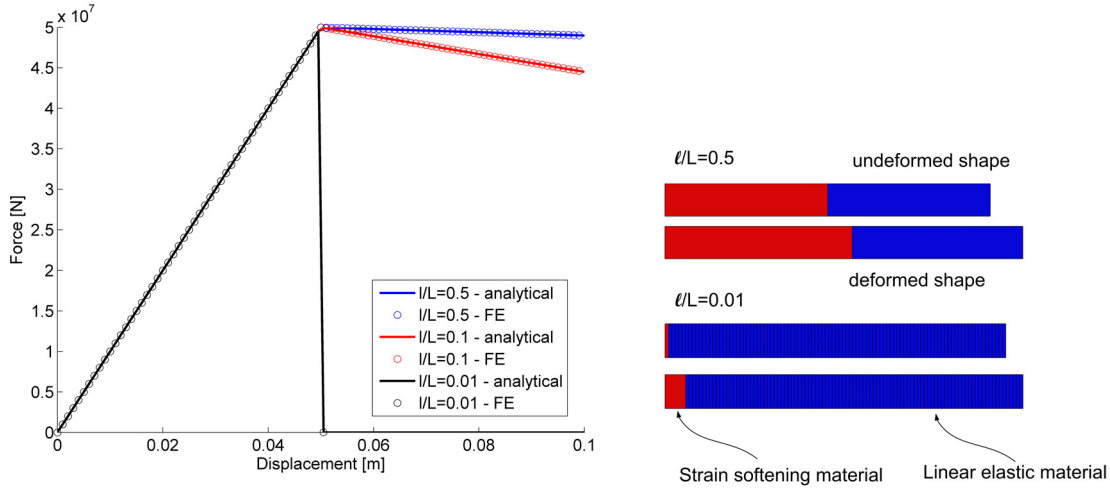

(a) Force vs. displacement for different length ratios of softening material to linear elastic material

(b) Deformed and undeformed shape of partially softening bar

Figure 5.9 Loading of partially softening bar

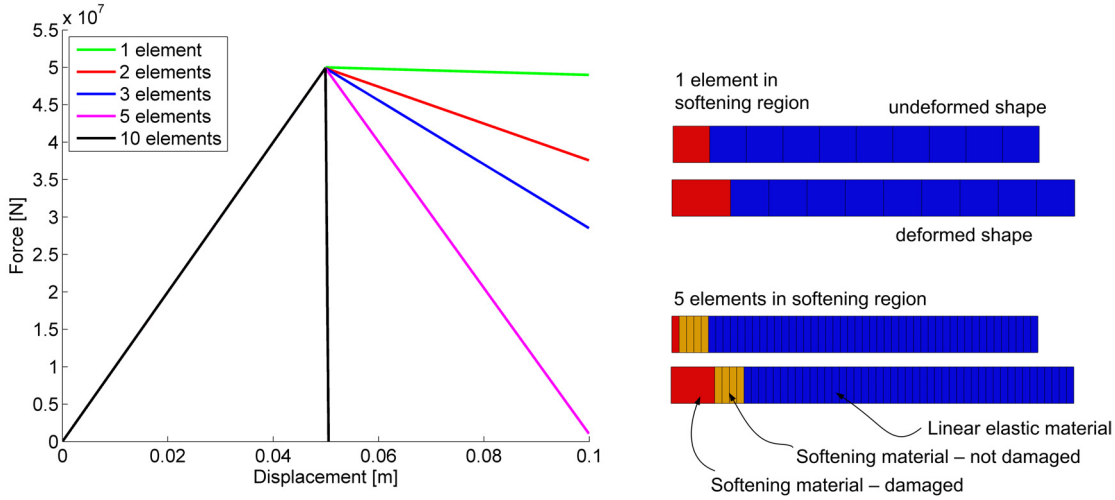

(a) Force vs. displacement of partially softening bar with different mesh sizes

(b) Deformed shape of partially softening bar with different mesh sizes

Figure 5.10 Loss of objectivity of partially softening bar

softening region, a loss of objectivity emerges. That is, different mesh sizes will lead to different results. This observation is detailed in figure 5.10. With increasing number of elements in the softening region, the reaction force in the post-damaged regime decreases. It can be observed that only one element always failed, despite that fact that a larger region has been designated as strain softening. When the failure strain ε_f is reached in the bar, bifurcation occurs. Several unloading paths are now open. The strain in each element can either decrease and follow the unloading path in figure 5.7 back to the origin or the strain can increase and the right unloading branch is chosen. At any given stress σ^* in the bar, two possible strain solutions exist. In fact, if the bar in figure 5.10 was continuous, a whole fan of solutions would exist between the unloading line of one element (the entire softening region fails) and the loading slope (only an infinitesimal portion of the damaging region fails). The latter statement can be also observed from equation (5.12). When the damaging length l approaches zero, the loading and the unloading curves coincide. The is the branch that will also be observed in reality upon mesh refinement. Here one element will fail first. This might be because the material properties have not everywhere been prescribed to be exactly the same, but there are small regions with infinitesimal deviations (within numerical precision). It might be that the calculated strain during an increment in the finite element simulation is slightly larger due to numerical errors, than the strains in the other elements. During subsequent iterations that element will follow the loading branch with increasing strains in figure 5.7. All other elements will follow the reverse loading branch back to the origin. Upon mesh refinement with infinitesimally small elements, the loading and unloading curves will coincide. This means, that upon failure the entire elastic energy is recovered, or in other words, there is no energy associated with damaging the material. This is of course, completely non-physical behavior. Mathematically speaking the described features are referred to as loss of ellipticity [57, 112, 114]. It occurs, when the acoustic tensor at a point within the region of interest (in this case within the bar volume) becomes singular. It should be mentioned, when calculating cases like the ones shown in figure 5.10, for small element sizes, a snapback is observed. To capture this behavior an arc length method must be applied as the solution scheme

5.2.2 Mesh adjusted modulus

So far it has been observed that calculating the response of a strain softening material using a standard finite element formulation will be mesh dependent and will lead to zero energy associated with fracture of the material in the limit of continued refinement of the mesh. One possible remedy to this problem is the so called mesh-adjusted softening modulus. Here the

softening modulus of each element needs to be changed depending on some characteristic length. This technique has been used for shear softening plasticity by Pietroszczak and Mróz, [115], and for tensile softening due to smeared cracking by Bažant and Oh, [116]. Franchi and Genna [117] proposed a self-adaptive model for structural softening of brittle materials. They considered softening plasticity. The goal of such studies is to retain the capability of using standard finite element procedures with the standard variables involved. For that, it needs to be accepted that the unloading slope is no longer a material property but rather a structural property that depends on the mesh and the loading conditions.

Reconsider the bar example from figure 5.10. This time, the softening slope is adjusted such that the energy during loading and subsequent failure is independent of mesh size, as shown in figure 5.11. That means that the single element must dissipate as much energy during failure, as all softening elements would do if the softening region were to fail in its entirety. The length of the softening region is given by l and the length of the failing element is denoted by l^e. The theoretically dissipated energy is given by

$$E = \frac{1}{2}\varepsilon_u \cdot l \cdot \sigma_{\max} \cdot A \tag{5.13}$$

This has to be equal to the energy dissipated in a single adjusted element

$$E = \frac{1}{2}\varepsilon_{u,new} \cdot l^e \cdot \sigma_{\max} \cdot A \tag{5.14}$$

Therefore the unloading modulus needs to be adjusted such that new mesh dependent ultimate strain is related to the original material dependent one by

$$\varepsilon_{u,new} = \varepsilon \frac{l}{l^e} \tag{5.15}$$

The result of the adjustment procedure is presented in figure 5.12. The unloading curves coincide and they are independent of the number of elements in the softening region. In all cases, only one element failed. All other elements unloaded elastically. While the correct choice of the characteristic element length and the adjustment procedure is quite straight forward in the one dimensional case, this might not be as trivial for 2D and 3D situations. Oliver, [118], derived a characteristic length for a smeared crack model by assuring that the energy dissipated within a crack band is preserved. A different way of looking at the problem is when the failing element of interest has no thickness. Then, effectively a traction separation law is prescribed, which will describe the decohesion process and the fracturing. This is known as the cohesive zone model [119, 120]. It has been used in many in FE analysis under the name Discrete Cohesive Zone Model to analyze fracture in composites [52]. When using DCZM's the expected location of the crack is usually known and the model is

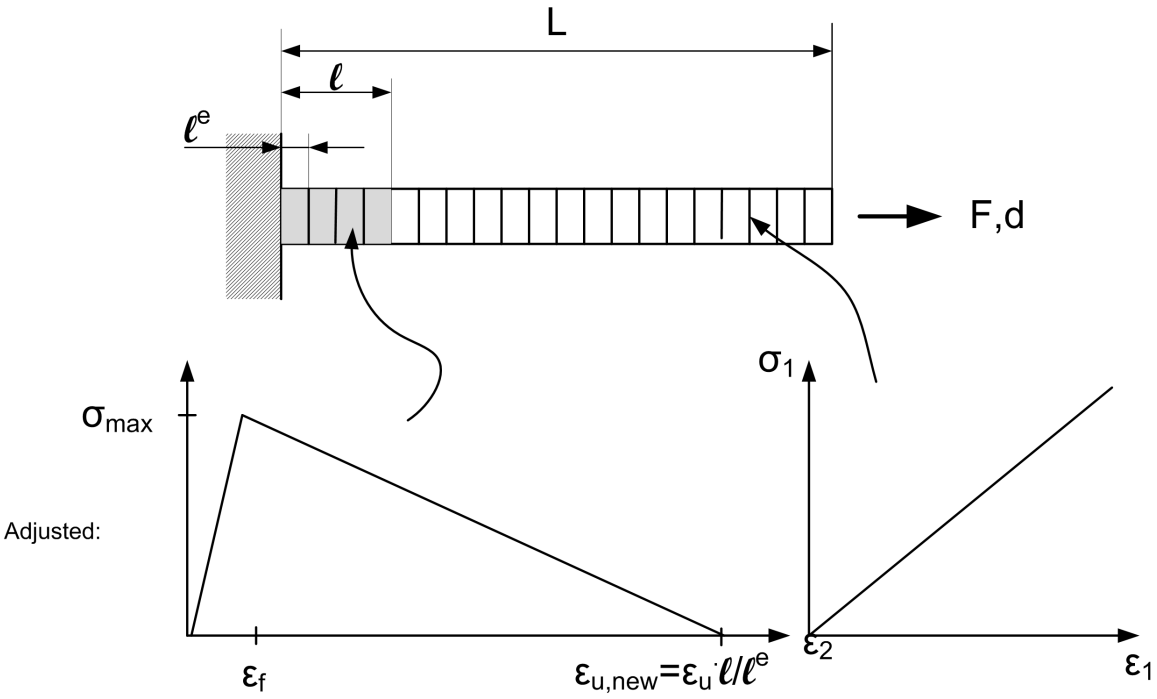

Figure 5.11 Partially strain softening bar with adjusted material properties

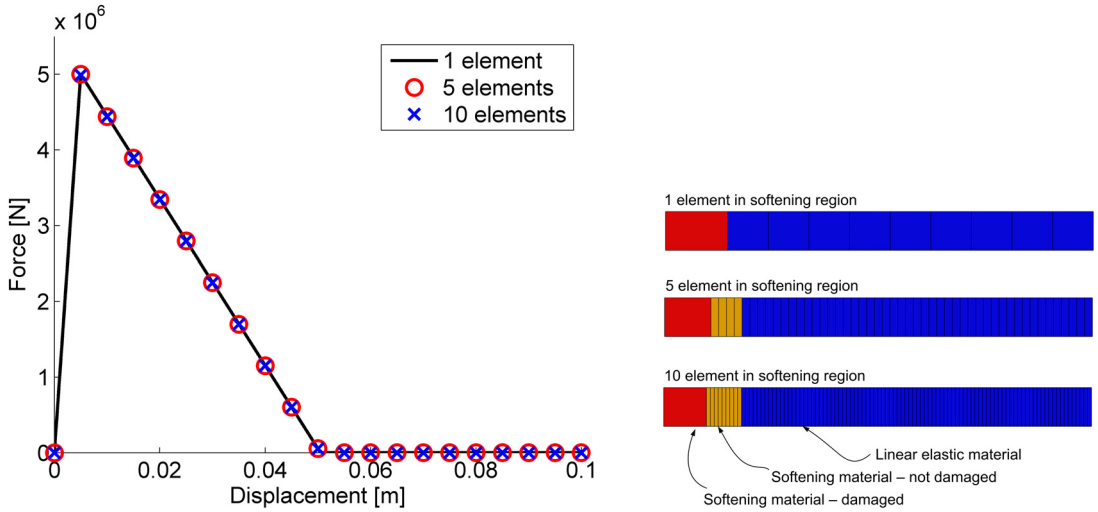

(a) Force vs. deflection of partially softening bar with mesh adjusted softening modulus

(b) Deformed shapes of partially softening bar

Figure 5.12 Partially softening bar with mesh adjusted modulus

prepared accordingly. This is not the case in the current study and is one of the reasons why a continuum damage model has been chosen.

5.2.3 Nonlocal material formulation

It is now clear that the response of a body that exhibits strain softening behavior cannot be successfully calculated using a standard finite element approach. In the previous section a mesh adjusted softening modulus has been described in order to obtain mesh independent results. However this approach transforms the meaning of the softening modulus from a material parameter to a structural parameter, that is dependent on the mesh size. It would be desirable to avoid the need to adjust material properties as a function of the mesh size. In order to do so, the governing equations need to incorporate some characteristic length scale associated with the softening modulus. This relates back to the original problem, that localization will occur upon strain softening on a certain length scale. The only length scale incorporated in standard FE solutions is the mesh size, hence the algorithm will choose this as the length scale to localize in. Therefore it should be possible to avoid the pathological issues of mesh size if a problem specific characteristic length scale can be provided elsewhere. A higher order continuum model is one remedy [121].

The Cosserat continuum is such a model that allows for the incorporation of an internal length scale [122]. Additional rotational degrees of freedom are incorporated, which cause the shear strains to be non-symmetric and additional micro curvature degrees of freedom are incorporated, which are tied to some length scale [123]. De Borst, [113], applied Cosserat theory to a material that exhibited shear softening plasticity. Upon mesh refinement the softening region of the stress-strain law converged to finite values.

Another popular way of achieving mesh objectivity of strain softening materials is the use of nonlocal theories. In nonlocal theories, it is assumed that the material response at a point is not only a function of the state at that point, but also of the state of surrounding points. In nonlocal theories, the field quantities describing the material response are replaced by their nonlocal equivalent through a volume averaging procedure, as,

$$\bar{f}(\underline{x}) = \frac{1}{V}\int_V w(\underline{x}-\underline{\xi})f(\underline{\xi})\mathrm{d}\underline{\xi} \tag{5.16}$$

Common choices for the weight function, $w(\underline{x}-\underline{\xi})$, include the Gauss distribution, the bell function, [116], and Green's function, [124]. They are shown in figure 5.13, and stated below.

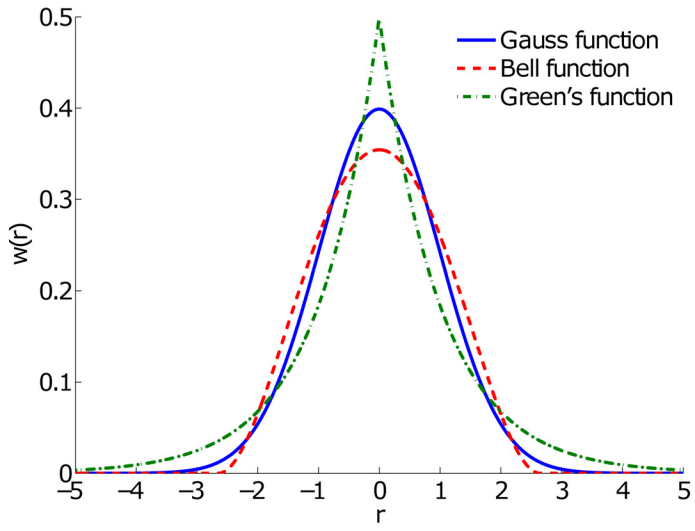

Figure 5.13 1D normalized nonlocal weight functions; $\int_{-\infty}^{\infty} w(r)\mathrm{d}r = 1$

$$w_{\text{Gauss}} = \exp\left(-\frac{n_{dim} r^2}{2\ell^2}\right) \tag{5.17}$$

$$w_{\text{Bell}} = \begin{cases} \left(1-\frac{r^2}{R^2}\right)^2 & \text{if } 0 \le r \le R \\ 0 & \text{if } r < R \end{cases} \tag{5.18}$$

$$w_{\text{Green}} = \frac{1}{2\ell}\exp\left(-\frac{|r|}{\ell}\right) \tag{5.19}$$

r is the distance between the point of interest, $\underline{x}$, and the surrounding points, $\underline{\xi}$, and it is called the interaction radius. ℓ and R are measures of the internal length scale. Jirásek and Bažant, [112], suggested that $\ell = R/\sqrt{7}$ in one dimension for the bell function. It should be noted that the choice of weighting function is to some degree arbitrary. The weight function needs to yield the local solution $\bar{f} = f$ when $f(\underline{x})$ is constant. Therefore $\int_V w(\underline{\xi})\mathrm{d}\underline{\xi} = V$. It can also be noted that when the weighting function equals the Dirac delta function, the local solution is obtained.

While nonlocal theories provide a theoretically sound way to incorporate a length scale into the equations governing the material response, the practical implementation into FE codes is quite cumbersome. Standard FE programs only require information at integration points or nodes. Further, information is only needed one element at a time. In the case of nonlocal theories, information from further away is needed and information from neighboring elements is required. Secondly, deriving and including boundary conditions is

not a trivial task either, [125, 126]. It is therefore desirable to find a representation of the governing equations that is related to the nonlocal continuum theory, but where variables in the finite element formulation and assembly can be done one element at a time and where boundary conditions can be applied in the classical way. To that end, expand the field of some strain measure η spatially through a Taylor series, [127–129],

$$\eta(\underline{x}+\underline{\xi}) = \eta(\underline{x}) + \nabla\eta(\underline{x})\underline{\xi} + \frac{1}{2!}\nabla^{(2)}\eta(\underline{x})\underline{\xi}\otimes\underline{\xi} + \frac{1}{3!}\nabla^{(3)}\eta(\underline{x})\underline{\xi}\otimes\underline{\xi}\otimes\underline{\xi} + \cdots + \frac{1}{n!}\nabla^{(n)}\eta(\underline{x})\underline{\xi}^{(n)} \tag{5.20}$$

with ∇^n denoting the nth order gradient operator and $\underline{\xi}^{(n)}$ is a dyadic product of n terms. Substituting this into the definition of a nonlocal field (5.16) yields

$$\overline{\eta}(\underline{x}) = \eta(\underline{x}) + c_1^2\nabla^2\eta(\underline{x}) + c_2^4\nabla^4\eta + \cdots \tag{5.21}$$

c_1 and c_2 are expansion parameters. They have the dimension of length. Therefore in (5.20), a length scale parameter is present. By retaining only low order terms, one obtains the simplest approximation to nonlocal theory as

$$\overline{\eta}(\underline{x}) = \eta(\underline{x}) + c_1^2\nabla^2\eta(\underline{x}) \tag{5.22}$$

Due to the symmetry of the weighting function only even terms are retained, [114]. (5.22) is also termed the explicit second gradient formulation. The nonlocal variable depends explicitly on its local counterpart, which makes the evaluation especially easy. However this formulation is less suited for finite element implementation, because it requires $\mathscr{C}^1$-continuity in the nonlocal variable. That means, that at the finite element nodes, the variable and its derivative need to be continuous. This is necessary to ensure that the second derivative in equation (5.22) is evaluated with a non-trivial value. This type of formulation is well known from the FE solutions of Euler-Bernoulli beam equations, where displacements and their derivatives have to be continuous. The explicit gradient formulation has been used by Askes and co-workers [130, 131] to calculate the solution to gradient enhanced damage mechanics in a bar. However their numerical implementation used element free Galerkin solutions that has no requirements on continuity. Dorgan and Voyiadjis [111] used explicit gradients and a mixed finite element formulation of the evolution of damage and isotropic and kinematic plasticity to calculate the formation of shear bands. It should also be noted that the explicit gradient formulation is only weakly nonlocal. That is, the nonlocality is limited to an infinitesimal volume. From a finite element point of view this means that information of the nonlocal field is only important with respect to the neighboring

elements and the exchange of that information is ensured by the $\mathscr{C}^1$-continuity requirement. Values from elements further away are not important. To remove these restrictions, implicit nonlocal formulations can be adopted, [124, 129–133]. To that end, apply the second order gradient operator to equation (5.22).

$$\nabla^2\overline{\eta} = \nabla^2\eta + c_1^2\nabla^4\eta \tag{5.23}$$

$$\nabla^2\eta = \nabla^2\overline{\eta} - c_1^2\nabla^4\eta \tag{5.24}$$

and insert the result into the original equation (5.22). Then,

$$\overline{\eta} = \eta + c_1^2(\nabla^2\overline{\eta} - c_1^2\nabla^4\eta) \tag{5.25}$$

Rename the constant c_1 to ℓ to signify its meaning as an internal length parameter, rearrange and neglect higher order terms to finally find,

$$\overline{\eta}(\underline{x}) - \ell^2\nabla^2\overline{\eta}(\underline{x}) = \eta(\underline{x}) \tag{5.26}$$

This is termed an implicit formulation, because the nonlocal field cannot be written anymore directly but is instead implicitly stated through a differential relationship with the local field variable. While equation (5.22) is weakly nonlocal, equation (5.26) is strongly nonlocal. The nonlocal field variable now depends on a finite neighborhood around it. This can also been seen from a finite element point of view: like all elliptic partial differential equations that are solved with an implicit FE scheme, the entire body has to be considered at once. That is, all degrees of freedom of the FE formulation are solved for simultaneously. In the same manner it is necessary to consider the entire local field in the body to find the nonlocal field. Peerlings et al., [124], have shown that implicit gradient models provide physically meaningful solutions when analyzing wave propagation. The wave speed in a bar was bounded for nonlocal and implicit gradient models, whereas that was not the case for an explicit nonlocal model. Note that during the derivation of the implicit gradient formulation, the assumption was made that the characteristic length parameter ℓ is small. However, Peerlings et al., [124] , have shown that the solution to equation (5.26) is identical to a nonlocal model when Green's function has been used as the weighting function. In that case there is no restriction on the length parameter ℓ. Physically a larger length parameter increases the area in which damage will occur. It will smooth out the transition from undamaged to damaged material because higher weight is given to derivatives. Further discussion of the length parameter ℓ is given in the context of a 1D damage model in the next section.

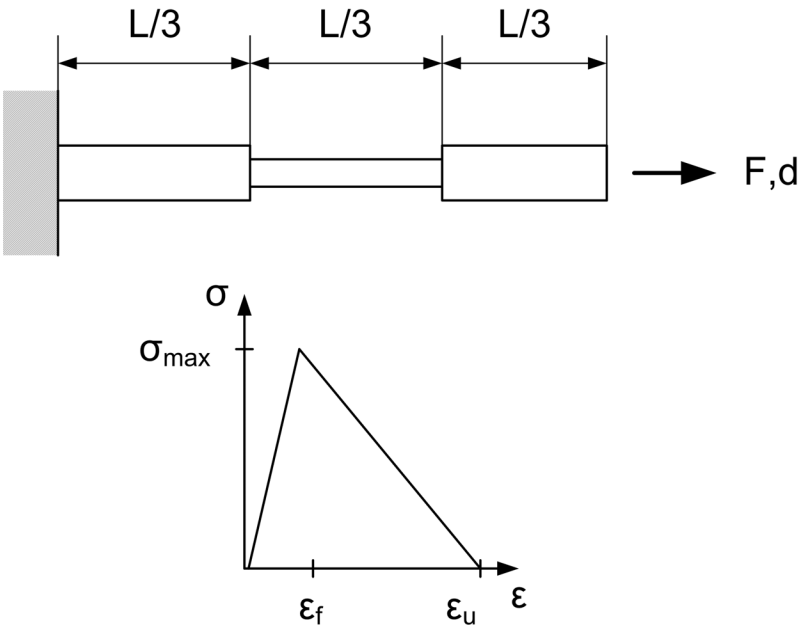

Figure 5.14 Description of nonlocal bar problem

Having obtained the definition of the nonlocal field variable, it is possible to restate the stress-strain relationship of the damaging law in equation (5.7), as,

$$\underline{\underline{\sigma}}(\underline{x}) = (1 - D(\overline{\eta}(\underline{x})))\underline{\underline{\underline{\underline{C}}}} : \underline{\underline{\varepsilon}}(\underline{x}) \tag{5.27}$$

The damage is now a function of the nonlocal strain measure, $\overline{\eta}$, which may be either obtained through the explicit or the implicit gradient formulation. As opposed the damage, stress and strain are treated as local variables. Pijaudier-Cabot and Bažant, [126], commented on this by stating that without any damage present, the classical solution of elasticity should be obtained. A similar formulation has been used by Challamel, [134]. However he used the nonlocal damage field $\overline{D}$ directly instead of evaluating the nonlocal strain measure and than evaluating the damage locally, $D(\overline{\eta})$.

5.3 1D damage

As a first example, consider again a one dimensional bar problem given in figure 5.14. The bar is divided into three equal sections with identical strain softening material properties, but the cross section in the center part of the bar is different. In this one dimensional case the strain measure η is simply the uniaxial strain ε. The uniaxial stress-strain law is also given in figure 5.14. It should be noted, that if damage occurs uniformly the stress-strain

law of a local and nonlocal description are identical.

Assume that $E = 1000$ MPa, $A = 1$ mm^2 and 0.9 mm^2 respectively, $\ell^2 = 0.01$, L =40 mm, ε_f=0.0001 and ε_u=0.01. The response of force versus displacement of the nonlocal softening bar as a function of element size is given in figure 5.15. With increasing element number, the solution converges to a non-zero value of fracture energy. That is, the area under the unloading curve is finite.

Figure 5.16 shows the distribution of stresses along the bar. As expected, the stresses in the middle portion are larger, than on the outside and they are piecewise constant, ensuring force equilibrium. With increasing amount of damage, the stresses reduce. Due to the numbers chosen in this example the stresses are very low. When solving such a problem using the commercial FE package, ABAQUS, it is necessary to make the tolerances of the solution algorithm stricter. In cases where that was not done it has been observed that the stresses had slight variations in each section despite the fact that the solver claimed equilibrium was achieved.

In figure 5.17, the displacements of material points in the bar are shown. With increasing amount of damage, a large change in displacement can be noticed in the center section. However the change is not abrupt, but instead retains a certain amount of smoothness. The (local) strains $\varepsilon = \partial u/\partial x$ are depicted in figure 5.18. In accordance with the large displacement in the region with a smaller cross section, the strain localizes in that area. The elevated strain can be found across several elements due to the nonlocal formulation of the finite element problem.

The nonlocal strains are given in figure 5.19. They are similar to the local strains. However the maximum nonlocal strain, which eventually drives the damage is lower and the entire curve is spread out. This fact is detailed in figure 5.20. Assume that, instead of the implicit, the explicit gradient formulation is used. The second derivative of local strain is negative near the peak of the strain and positive away from the peal. Therefore the addition of the second derivative of (local) strain will effectively lower the maximum nonlocal strain.

The damage along the softening bar is depicted in figure 5.21. It is widely spread in the center section. The damage is driven by nonlocal strain, which is large at the thinner cross section . Although the damage is directly a function of nonlocal strain, it is less localized than the nonlocal strain. Instead it is further spread out. This is mainly due to the fact that damage cannot decrease. As shown in figure 5.19, at the beginning of the damaging process the nonlocal strain is less localized and therefore increasing the damage value more uniformly. Only towards higher values of damage it can be seen that the strain localizes in the center and hence increases the damage in the area further.

Finally, the question of the importance of the length scale parameter ℓ^2 is addressed

in figure 5.22. With increasing length scale parameter the area under the unloading curve increases. Mathematically, an increasing ℓ will give greater importance to higher derivatives of (local) strain and thus reduce the maximum nonlocal strain. It will spread the region of elevated nonlocal strain. Damage occurs in a larger region. From a formulation point of view, one can see that both the stress-strain curve and the length parameter are necessary, to prescribe the fracture energy. The stress-strain curve alone gives information per unit volume. However, as pointed out earlier, the classical continuum mechanics formulation does not provide a volume or length scale and thus the softening was reduced to an infinitesimal volume as the mesh was refined. Together with the length parameter, a fixed energy can be specified. That means that the fracture energy can be adjusted two ways: either change the stress-strain law to change the fracture energy per unit volume, or change the volume by changing the length scale ℓ. Therefore, the length scale parameter serves two purposes. On the one hand it introduces a length scale into the continuum mechanics formulation of the problem and it suppresses spurious strain localization during the calculation of the problem. From a physical stand point, ℓ is related to the spread and progression of damage in the structure that is considered. It is related to the size of the damage zone. To properly determine ℓ experiments at different size scales are needed. Because ℓ is only of importance in the softening regime and therefore damage related part of stress-strain relations, such experiments should be related to traditional experiments that are used to investigate damage and fracture behavior. An experiment to extract ℓ could be double cantilever beam (DCB) tests of different sizes. The results of these experiments need to be compared to numerical simulations to find the appropriate softening behavior of the stress-strain relations and length scale parameter. After this is done, ℓ can be treated as a material parameter of the epoxy system that is independent of fiber architecture, fiber volume fraction, fiber material and the numerical discretization.

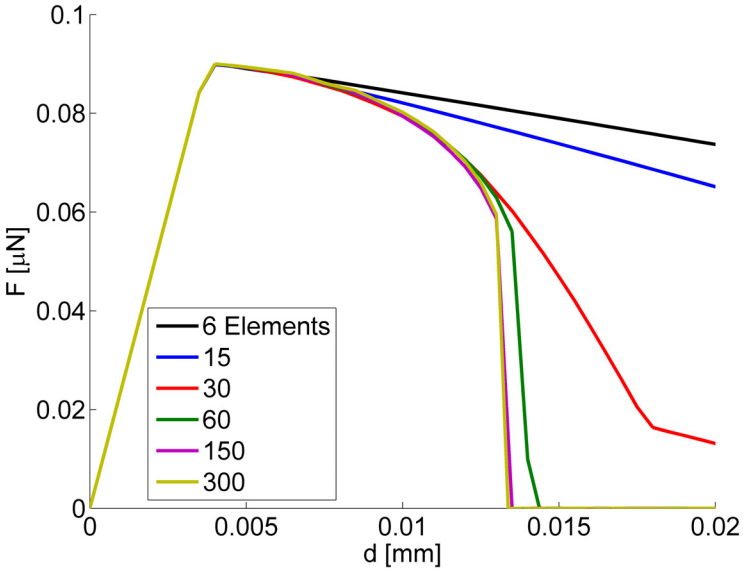

Figure 5.15 Force vs displacement of strain softening bar for various element numbers

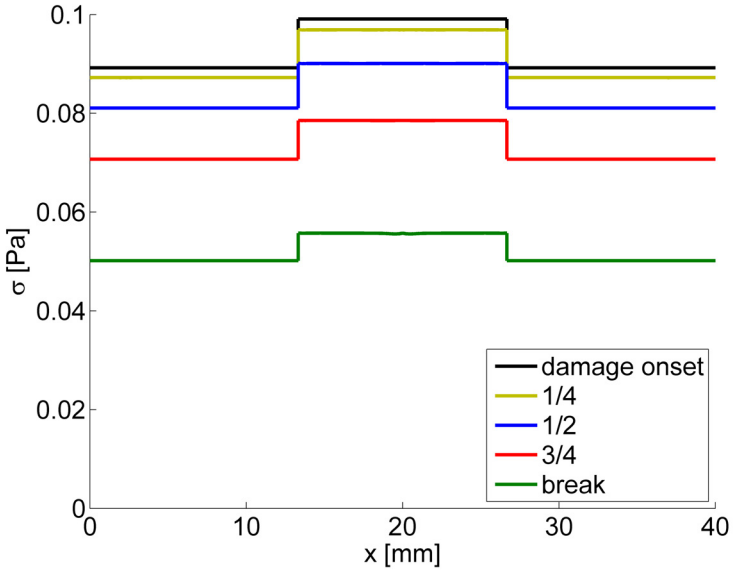

Figure 5.16 Distribution of stress in strain softening bar

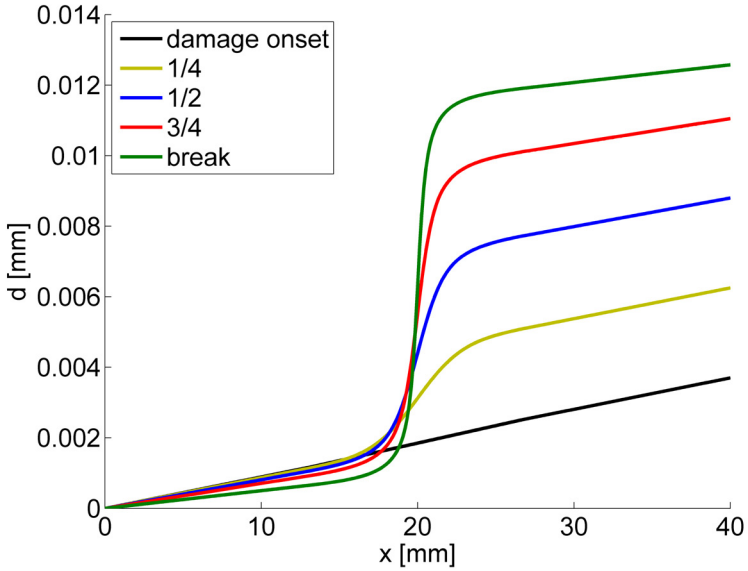

Figure 5.17 Displacement in strain softening bar

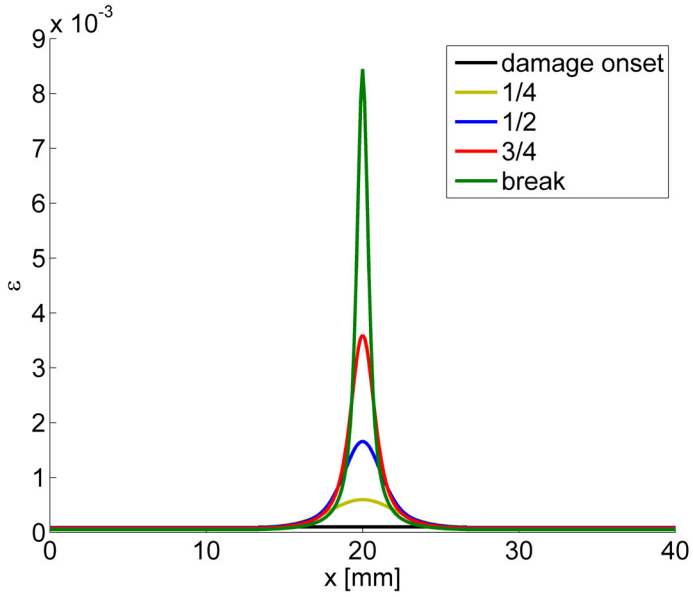

Figure 5.18 Distribution of strain in strain softening bar

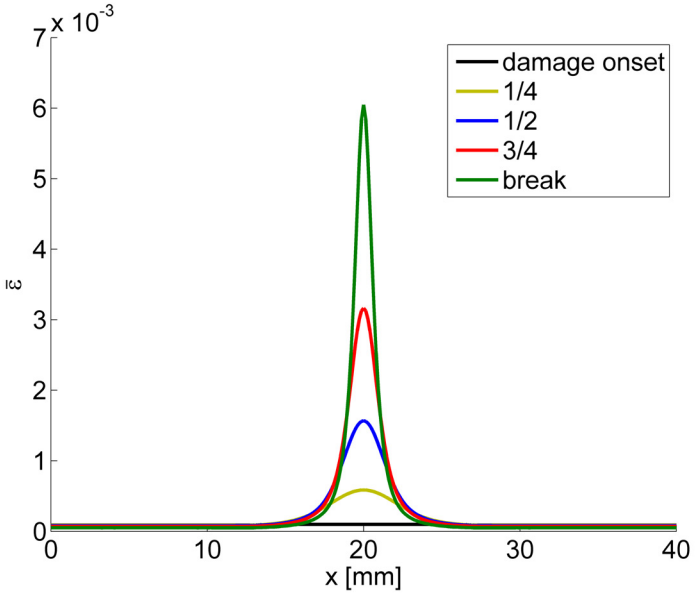

Figure 5.19 Distribution of nonlocal strain in strain softening bar

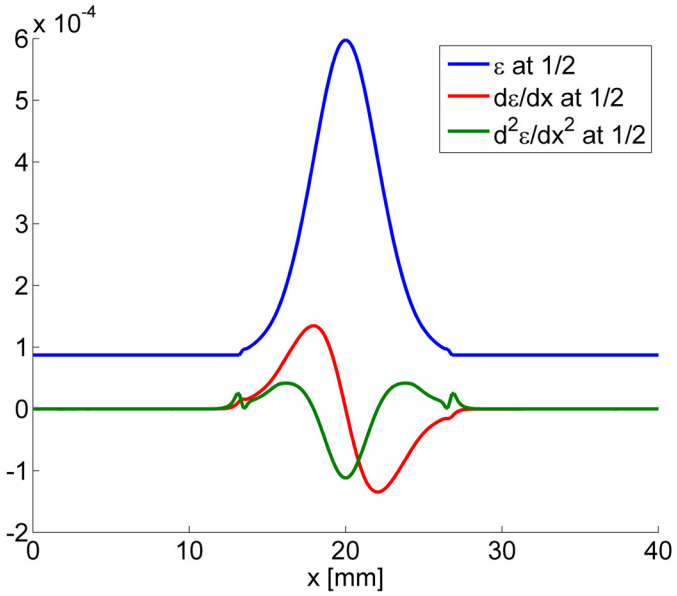

Figure 5.20 Distribution of strain and first and second derivative of strain half way between damage onset and full failure

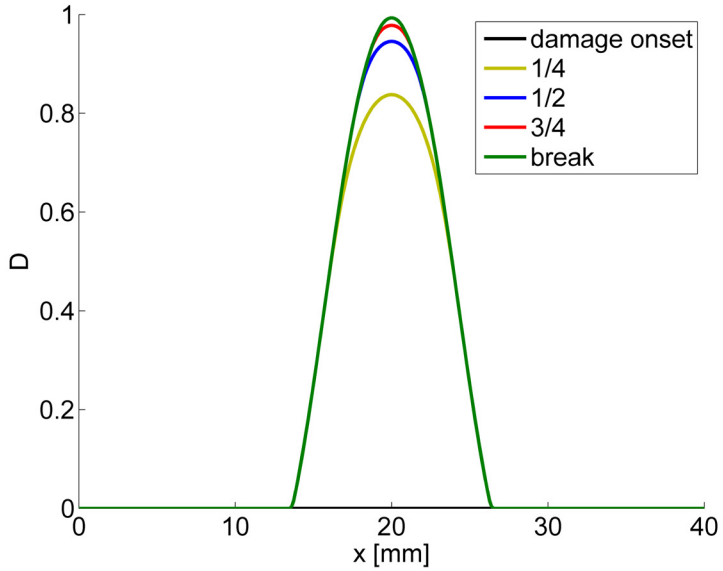

Figure 5.21 Distribution of damage in strain softening bar

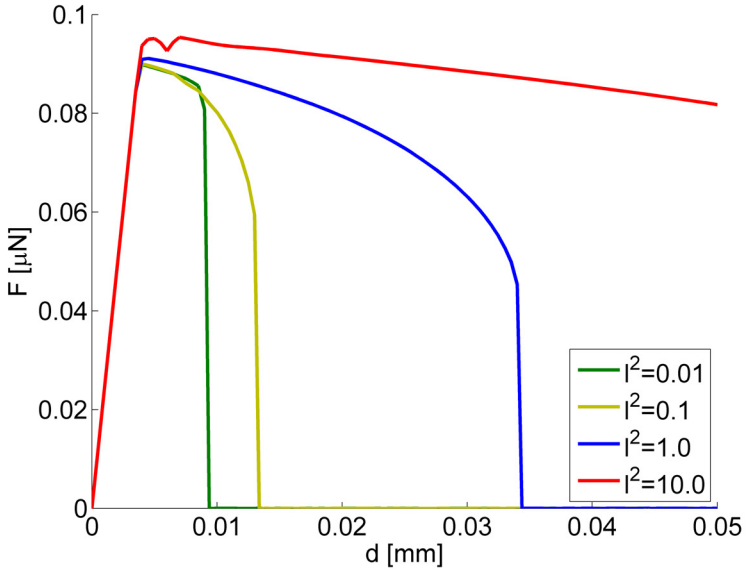

Figure 5.22 Force vs displacement of strain softening bar for various length parameters

5.4 3D damage with cure

5.4.1 Governing equations

In the following the ideas of continuum damage will be combined with the ideas of the network creation during cure. Previously, every network was treated as a linear isotropic solid with unique elastic properties, cure shrinkage, thermal expansion coefficient and stress free reference configuration in chapter 3. Now each network will also have some damage D associated with it. Specifically, recall the stress-strain relation from equation (3.15) and allow all networks to damage individually by premultiplying the per-network bulk modulus $K(s)$ and the per-network shear modulus $\mu(s)$ with a damage term of the form $(1-D(t,s))$.

$$\begin{aligned}\underline{\underline{\sigma}}(t) &= \int_0^t \dot{\phi}(s)(1-D(t,s))\Big[K(s)\mathrm{tr}\left(\underline{\underline{\varepsilon}}(t)-\underline{\underline{\varepsilon}}(s)+\underline{\underline{\varepsilon_c}}(s)-\underline{\underline{1}}\alpha(s)\Delta T(t,s)\right) \\ &\quad +2\mu(s)\left(\underline{\underline{\varepsilon}}(t)-\underline{\underline{\varepsilon}}(s)+\underline{\underline{\varepsilon_c}}(s)-\underline{\underline{1}}\frac{1}{3}\mathrm{tr}\left(\underline{\underline{\varepsilon}}(t)-\underline{\underline{\varepsilon}}(s)+\underline{\underline{\varepsilon_c}}(s)\right)\right)\Big] \\ &\quad +(1-\phi(t))K_{liq}\mathrm{tr}(\underline{\underline{\varepsilon}}(t)-\underline{\underline{1}}\alpha_{liq}\Delta T(t))\underline{\underline{1}}\end{aligned} \tag{5.28}$$

The damage parameter $D(t,s)$ depends on the current state at time t as well as on the history at times s. Specifically it depends on the nonlocal field variable $\overline{\eta}(t,s)$. The nonlocal field variable depends on the local field variable through equation (5.26). That is,

$$\overline{\eta}(t,s)-\ell^2\nabla^2\overline{\eta}(t,s)=\eta(t,s) \tag{5.29}$$

The nonlocal field variables at different times in history are independent of each other. Each network created at time $s=t_i$, is independent from the network created at time $s=t_j$. That means equation (5.29) has to be solved for all histories $0\leq s\leq t$, leading to an infinite number of equations. At this point another problem regarding the numerical formulation of equation (5.28) should be mentioned: taking the integral with respect to time becomes increasingly difficult. In the absence of damage, it was possible to split up the integral into different terms and evaluate it using a running update. That means the integral could be divided into parts only depending on the current state at time t and other parts that depend only on the history at times s. This is not possible anymore. The dependence of damage on the current state as well as the history makes it necessary to save the histories of stress, strain, cure, curing rate, temperature and damage during a FE simulation. It should be noticed, that the integral only needs to be evaluated during a finite time interval, $0<t<t_{cure}$. At the curing time, t_{cure}, the curing process is regarded to be complete. Mathematically full cure is

approached asymptotically. Therefore $\phi_{cure} = 95\%$ has been chosen for convenience such that $t_{cure} = t(\phi = \phi_{cure})$. At full cure the rate of cure is zero and the portion of the integral relating to subsequent times will be zero, as well. It is now possible to numerically evaluate the integral using for example the trapezoidal or Simpson's rule. Here, the kernel of the integral only needs to be known at selected time intervals $0 = t_0 < t_1 < t2 < \cdots < t_N = t_{cure}$. The amount of history information saved needs to be stated prior to performing a FE simulation. On the other hand it is not known a priori how and when full cure will be achieved. Therefore the curing process is divided into equal intervals with respect to degree of cure. That is, if N time slots are allotted to save history information, the times are given by $t_0 = t(\phi = 0) = 0$, $t_1 \geq t(\phi = \phi_{cure}/(1-N))$, ..., $t_{N-1} \geq t_{cure}$. The time steps are chosen by the finite element program and generally do not coincide with the times when the prescribed curing stages are reached. Therefore, the times when to save the history information don't usually follow entirely the desired even spacing in degree of cure. Inherent to this proposed integration scheme is the assumption that during the curing, the loading and boundary conditions are sufficiently smooth and not subject to oscillations, which is true for any realistic curing and loading scenario.

Finally, the nonlocal field variable only needs to be determined at the times that are used to numerically evaluate the integral. That is,

$$\begin{aligned} \overline{\eta}(t,t_0) - \ell^2\nabla^2\overline{\eta}(t,t_0) &= \eta(t,t_0) \\ \overline{\eta}(t,t_1) - \ell^2\nabla^2\overline{\eta}(t,t_1) &= \eta(t,t_1) \\ &\vdots \\ \overline{\eta}(t,t_{N-1}) - \ell^2\nabla^2\overline{\eta}(t,t_{N-1}) &= \eta(t,t_{N-1}) \end{aligned}$$

In the finite element program, the nodal variables will be grouped by times. That is, $\underline{\overline{\eta}} = [\underline{\overline{\eta}}(t_0), \underline{\overline{\eta}}(t_1), \ldots, \underline{\overline{\eta}}(t_{N-1})]^{\mathrm{T}}$, where $\underline{\overline{\eta}}(t_i)$ are the nodal values of the nonlocal field variable belonging to the network formed at time t_i. The damage should only depend on the mechanical strain in a network. Therefore the (local) field variable $\eta(t,s)$ needs to be some invariant of the mechanical strain $\underline{\varepsilon}^m(t,s)$. The two most promising choices are the maximum principal mechanical strain or the von Mises mechanical strain (the deviatoric part of the strain tensor) given by

$$\eta_{vM}(t,s) = \sqrt{2}\left[(\varepsilon^m_{11}(t,s)-\varepsilon^m_{22}(t,s))^2+(\varepsilon^m_{22}(t,s)-\varepsilon^m_{33}(t,s))^2+(\varepsilon^m_{33}(t,s)-\varepsilon^m_{11}(t,s))^2 + \frac{3}{2}((\gamma^m_{12}(t,s))^2+(\gamma^m_{13}(t,s))^2+(\gamma^m_{23}(t,s))^2)\right]^{1/2} \quad (5.30)$$

Both von Mises strain and maximum principal strain collapse to the uniaxial strain in a one dimensional tension problem when only end loads or displacements are prescribed. Other invariants of the strain might be possible to be used, for example the mean hydrostatic strain.
The mechanical strain can be written as,

$$\underline{\underline{\varepsilon}}^m(t,s) = \underline{\underline{\varepsilon}}(t) - \underline{\underline{\varepsilon}}(s) + \underline{\underline{\varepsilon}}_c(s) - \alpha(s)(T(t)-T(s)) \quad (5.31)$$

where, $\underline{\varepsilon}(t)$ is the total strain at current time, t, $\underline{\varepsilon}(s)$ is the total strain at the time of the creation of the network, s, $\underline{\varepsilon}_c$ is the cure shrinkage of the network created at time s, $\alpha(s)$ is the coefficient of thermal expansion and $T(t)$ and $T(s)$ are the current temperature and the temperature at the time the network was created.

5.4.2 Finite element formulation

The weak forms of the governing equations will be derived, that will subsequently be solved using the finite element program. To that end, let the components of the stress tensor be arranged into vector form

$$\underline{\sigma} = [\sigma_{11}, \sigma_{22}, \sigma_{33}, \sigma_{12}, \sigma_{13}, \sigma_{23}] \quad (5.32)$$

The equilibrium equation is given by

$$L^{\mathrm{T}}\underline{\sigma} + \underline{b} = 0 \quad (5.33)$$

where L is a linear operator such that, [130, 135] ,

$$L^{\mathrm{T}} = \begin{bmatrix} \frac{\partial}{\partial x_1} & 0 & 0 & \frac{\partial}{\partial x_2} & \frac{\partial}{\partial x_3} & 0 \\ 0 & \frac{\partial}{\partial x_2} & 0 & \frac{\partial}{\partial x_1} & 0 & \frac{\partial}{\partial x_3} \\ 0 & 0 & \frac{\partial}{\partial x_3} & 0 & \frac{\partial}{\partial x_1} & \frac{\partial}{\partial x_2} \end{bmatrix} \quad (5.34)$$

Multiplying by a weighting function $\delta\underline{u}^{\mathrm{T}}$, integrating by parts, and use of the divergence

theorem, results in,

$$\int_V (L\delta\underline{u})^{\mathrm{T}}\underline{\sigma}\mathrm{d}V = \int_V \delta\underline{u}^{\mathrm{T}}\underline{b}\mathrm{d}V + \int_A \delta\underline{u}^{\mathrm{T}}\underline{t}\mathrm{d}A \tag{5.35}$$

Here $\underline{b}$ is the body force and $\underline{t}$ are the tractions acting on the traction boundary. In the finite element analysis, the displacement field and the weight functions are approximated by $\underline{u} = \underline{N_u}\underline{U}$ and $\delta\underline{u} = \underline{N_u}\delta\underline{U}$ respectively. $\underline{U}$ and $\delta\underline{U}$ are the displacements and the trial function displacement at the nodes of the element. $\underline{N_u}$ are the shape functions for the displacement. Then,

$$\int_V \delta\underline{U}^{\mathrm{T}}\underline{N_u}\underline{b}\mathrm{d}V + \int_A \delta\underline{U}^{\mathrm{T}}\underline{N_u}\underline{t}\mathrm{d}A - \int_V (L\underline{N_u}\delta\underline{U})^{\mathrm{T}}\underline{\sigma}\mathrm{d}V = 0 \tag{5.36}$$

The product of the linear operator L and the displacement shape function is denoted by $L\underline{N_u} = B_u$, leading to

$$\delta\underline{U}^{\mathrm{T}}\left(\int_V \underline{N_u}\underline{b}\mathrm{d}V + \int_A \underline{N_u}\underline{t}\mathrm{d}A - \int_V B_u^{\mathrm{T}}\underline{\sigma}\mathrm{d}V\right) = 0 \tag{5.37}$$

The trial function displacement at nodes, $\delta\underline{U}$, is arbitrary. Therefore the residual that needs to be driven to zero by the FE program is

$$\underline{F_u} = \left(\int_V \underline{N_u}\underline{b}\mathrm{d}V + \int_A \underline{N_u}\underline{t}\mathrm{d}V - \int_V B_u^{\mathrm{T}}\underline{\sigma}\mathrm{d}A\right) \tag{5.38}$$

Next the weak forms of the governing equation to find the nonlocal field variable are derived. The nonlocal field variable is denoted by $\bar{\eta}$ and the differential equation of the implicit gradient nonlocal theory is given by equation (5.26)

$$\overline{\eta} - \ell^2\nabla^2\overline{\eta} = \eta \tag{5.39}$$

Multiply with a weighting function $\delta\bar{\eta}$ and integrate over the domain

$$\int_V \delta\overline{\eta}(\overline{\eta} - \ell^2\nabla^2\overline{\eta})\mathrm{d}V = \int_V \delta\overline{\eta}\cdot\eta\mathrm{d}V \tag{5.40}$$

Integrate by parts, and make use of the divergence theorem. Then,

$$\int_V (\delta\overline{\eta}\cdot\overline{\eta} + \ell^2(\nabla\delta\overline{\eta})^{\mathrm{T}}\nabla\overline{\eta})\mathrm{d}V - \int_A \ell^2\delta\overline{\eta}\underline{n}^{\mathrm{T}}\nabla\overline{\eta}\mathrm{d}A = \int_V \delta\overline{\eta}\cdot\eta\mathrm{d}V \tag{5.41}$$

The order of the governing equation was reduced from two to one, but a new boundary condition emerged. Either, the nonlocal variable is zero at the boundary or the gradient of

the nonlocal variable normal to the boundary of the domain is zero. In the following, the second condition will be assumed. To explain this further, investigate a one dimensional bar problem. In this case the nonlocal field variable is the nonlocal strain. Further assume that the displacement field is linear. Then the strain is constant and the (local) strain and nonlocal strain are identical. The boundary of the bar is marked by the two end points. There, the nonlocal strain is non-zero, but its gradient is zero. The local and nonlocal field variables, together with the weight function are interpolated by $\eta = \underline{N}_{\overline{\eta}}\underline{\eta}$, $\overline{\eta} = \underline{N}_{\overline{\eta}}\underline{\overline{\eta}}$ and $\delta\overline{\eta} = \underline{N}_{\overline{\eta}}\delta\underline{\overline{\eta}}$. Thus,

$$\int_V (\delta\underline{\overline{\eta}}^{\mathrm{T}}\underline{N}_{\overline{\eta}}^{\mathrm{T}} \cdot \underline{N}_{\overline{\eta}}\underline{\overline{\eta}} + \ell^2(\nabla\underline{N}_{\overline{\eta}}\delta\underline{\overline{\eta}})^{\mathrm{T}}\nabla\underline{N}_{\overline{\eta}}\underline{\overline{\eta}})\mathrm{d}V = \int_V \delta\underline{\overline{\eta}}^{\mathrm{T}}\underline{N}_{\overline{\eta}}^{\mathrm{T}} \cdot \underline{N}_{\overline{\eta}}\underline{\eta}\mathrm{d}V \tag{5.42}$$

The gradient operator acting on the interpolation function will be expressed by $B_{\overline{\eta}}$. Rearranging and noting that the variation of the weighting function is arbitrary yields the residual of the weak form of the governing equations that are used to find the nonlocal field variable.

$$\underline{F}_{\overline{\eta}} = \int_V (\underline{N}_{\overline{\eta}}^{\mathrm{T}} \cdot \underline{N}_{\overline{\eta}} + \ell^2\underline{B}_{\overline{\eta}}^{\mathrm{T}}\underline{B}_{\overline{\eta}})\underline{\overline{\eta}} - \underline{N}_{\overline{\eta}}^{\mathrm{T}} \cdot \underline{N}_{\overline{\eta}}\underline{\eta}\mathrm{d}V \tag{5.43}$$

The aim of the finite element program is to drive the residuals in equations (5.38) and (5.43) to zero. While the routines for achieving force equilibrium are readily available in ABAQUS, this is not the case for the governing equations of the nonlocal field variable. To add this, a user defined element, UEL, was developed. At this point it is worth remembering, that historically the finite element procedure first has been used in structural applications. However, in general it is merely a tool to solve any set of partial differential equations numerically. In this particular case, the capabilities of the ABAQUS solver will be used to establish not only force equilibrium, but to also solve the PDE relating the local and nonlocal field variables.

The ABAQUS UEL provides the user with estimates of the nodal variables that are solved for, which are in this particular case, the nodal displacements $\underline{U}$ and the nodal value of the nonlocal field variable $\underline{\overline{\eta}}$. In turn it requires the user to specify a vector of residuals and the Jacobian/ stiffness matrix. In the ABAQUS convention the stiffness matrix is ***defined*** as the negative of the derivative of the residuals with respect to the nodal values. In this particular case, let the force vector be the stacking of the residuals from the force equilibrium and the PDE describing the nonlocal field variable, $F = [\underline{F}_u, \underline{F}_{\overline{\eta}}]^{\mathrm{T}}$. Then the stiffness matrix

is given by

$$K = \begin{bmatrix} K_{uu} & K_{u\overline{\eta}} \\ K_{\overline{\eta}u} & K_{\overline{\eta}\overline{\eta}} \end{bmatrix} = \begin{bmatrix} -\frac{\partial \underline{F}_u}{\partial \underline{U}} & -\frac{\partial \underline{F}_u}{\partial \underline{\overline{\eta}}} \\ -\frac{\partial \underline{F}_{\overline{\eta}}}{\partial \underline{U}} & -\frac{\partial \underline{F}_{\overline{\eta}}}{\partial \underline{\overline{\eta}}} \end{bmatrix}. \tag{5.44}$$

The four individual parts of the stiffness matrix can found with the aid of equations (5.38) and (5.43). The stiffness matrix relating force equilibrium and nodal displacement is

$$\begin{aligned} K_{uu} &= -\frac{\partial}{\partial \underline{U}} \left(\int_V \underline{N}_u \underline{b} \mathrm{d}V + \int_A \underline{N}_u \underline{t} \mathrm{d}A - \int_V B_u^{\mathrm{T}} \underline{\sigma} \mathrm{d}V \right) && (5.45) \\ &= \int_v B_u^{\mathrm{T}} \frac{\partial \underline{\sigma}}{\partial \underline{U}} \mathrm{d}V && (5.46) \end{aligned}$$

The stress is directly a function of the strain and the nonlocal field variable. The strains will depend on the displacements at the nodes, whereas the nonlocal field variable depends on the value of the nonlocal variable at the nodes. Therefore $\underline{\sigma} = \underline{\sigma}(\underline{\varepsilon}(\underline{U}), \overline{\eta}(\underline{\overline{\eta}}))$. With that, the derivatives in K_{uu} can be further expanded.

$$K_{uu} = \int_v B_u^{\mathrm{T}} \frac{\partial \underline{\sigma}}{\partial \underline{\varepsilon}} \frac{\partial \underline{\varepsilon}}{\partial \underline{U}} \mathrm{d}V \tag{5.47}$$

Now, use engineering shear strains and order the strain components in a vector in the same manner as the stress components have been ordered previously, $\underline{\varepsilon} = [\varepsilon_{11}, \varepsilon_{22}, \varepsilon_{33}, \gamma_{12}, \gamma_{13}, \gamma_{23}]$. The strain can be calculated from the displacement field using the previously defined linear operator L.

$$\underline{\varepsilon} = L\underline{u} = L\underline{N}_u \underline{U} = B_u \underline{U} \tag{5.48}$$

This yields the familiar small strain finite element stiffness matrix.

$$K_{uu} = \int_v B_u^{\mathrm{T}} \frac{\partial \underline{\sigma}}{\partial \underline{\varepsilon}} B_u \mathrm{d}V \tag{5.49}$$

The Jacobian $\frac{\partial \underline{\sigma}}{\partial \underline{\varepsilon}}$ has a very similar form to the one shown in section 3.4.2. Using the

same arguments as presented in section 3.4.2 the Jacobian can be derived in the form

$$\frac{\partial \underline{\sigma}}{\partial \underline{\varepsilon}} = \begin{bmatrix} \tilde{\lambda}(t)+2\tilde{\mu}(t) & \tilde{\lambda}(t) & \tilde{\lambda}(t) & 0 & 0 & 0 \\ \tilde{\lambda}(t) & \tilde{\lambda}(t)+2\tilde{\mu}(t) & \tilde{\lambda}(t) & 0 & 0 & 0 \\ \tilde{\lambda}(t) & \tilde{\lambda}(t) & \tilde{\lambda}(t)+2\tilde{\mu}(t) & 0 & 0 & 0 \\ 0 & 0 & 0 & \tilde{\mu}(t) & 0 & 0 \\ 0 & 0 & 0 & 0 & \tilde{\mu}(t) & 0 \\ 0 & 0 & 0 & 0 & 0 & \tilde{\mu}(t) \end{bmatrix} \tag{5.50}$$

where

$$\tilde{\lambda}(t) = \int_0^t \dot{\phi}(s)(1-D(t,s))(K(s)-\frac{2}{3}\mu(s))\mathrm{d}s + (1-\phi(t))K_{liq} \tag{5.51}$$

$$\tilde{\mu}(t) = \int_0^t \dot{\phi}(1-D(t,s))\mu(s)\mathrm{d}s \tag{5.52}$$

Next, the stiffness matrix, $K_{\overline{\eta}\,\overline{\eta}}$, only involving terms due to the nonlocal field variable and its governing equation will be stated.

$$K_{\overline{\eta}\,\overline{\eta}} = -\frac{\partial \underline{F}_{\overline{\eta}}}{\partial \underline{\overline{\eta}}} = \mathrm{diag}\left[-\frac{\partial \underline{F}_{\overline{\eta}}(t_i)}{\partial \underline{\overline{\eta}}(t_i)}\right] = \begin{bmatrix} C & 0 & \cdots \\ 0 & C & \\ \vdots & & \ddots \end{bmatrix} \tag{5.53}$$

where the constant is given by $C = \int_V (\underline{N}_{\overline{\eta}}^{\mathrm{T}} \cdot \underline{N}_{\overline{\eta}} + \ell^2 \underline{B}_{\overline{\eta}}^{\mathrm{T}} \underline{B}_{\overline{\eta}})\mathrm{d}V$. As stated previously the nonlocal field variables of the networks formed at various times are independent. Therefore the resulting stiffness matrix is block diagonal. Due to the linear nature of the nonlocal field equation the stiffness matrix is constant.

The cross term $K_{\overline{\eta}u}$ in the stiffness matrix can again be calculated noting that the nonlocal field variable of networks created at different times are independent.

$$K_{\overline{\eta}u} = \begin{bmatrix} K_{\overline{\eta}u}(t_0) \\ K_{\overline{\eta}u}(t_1) \\ \vdots \\ K_{\overline{\eta}u}(t_{N-1}) \end{bmatrix} \tag{5.54}$$

To find the stiffness matrix related to the networks created at different times, $K_{\overline{\eta}u}(t_i)$, it is important to note that the (local) field variable $\eta(t_i)$ is an invariant of the current mechanical strain in the network created at time t_i, which in turn is a function of the displacement. Thus,

$\eta = \eta(\underline{\underline{\varepsilon}}) = \eta(\underline{\underline{\varepsilon}}^m(\underline{U}))$. Therefore,

$$K_{\overline{\eta}u}(t_i) = -\int_V N_{\overline{\eta}}^{\mathrm{T}} \frac{\partial \eta(t_i)}{\partial \underline{U}} \mathrm{d}V \tag{5.55}$$

If the (local) field variable η is related to the maximum principal strain, an eigenvalue problem needs to be solved. If it is related to the deviatoric strain, equation (5.30) needs to be evaluated. In either case, finding the derivative of the (local) field variable η with respect to the nodal displacements as a closed form solution is an almost futile task. Therefore the change of the (local) field variable $\eta(t_i)$ of the network formed at time t_i with respect to the change in nodal degree of freedom, $\partial\eta(t_i)/\partial\underline{U}$, is done using a finite difference scheme.

$$\frac{\partial \eta(t_i)}{\partial U_j} \approx \frac{\eta(t_i, \underline{U} + \underline{e}_i \Delta U) - \eta(t_i, \underline{U})}{\Delta U} \tag{5.56}$$

Here e_j is the unit vector of the jth component. Finally the last entry of the stiffness matrix can be found as,

$$K_{u\overline{\eta}} = -\frac{\partial \underline{F}_u}{\partial \underline{\overline{\eta}}} = \int_V B_u^{\mathrm{T}} \frac{\partial \underline{\underline{\sigma}}}{\partial \underline{\overline{\eta}}} \mathrm{d}V = \int_V B_u^{\mathrm{T}} \frac{\partial \underline{\underline{\sigma}}}{\partial \overline{\eta}(t_i)} \frac{\partial \overline{\eta}(t_i)}{\partial \underline{\overline{\eta}}} \mathrm{d}V \tag{5.57}$$

The derivative of the nonlocal field variable with respect to its values at the nodes, $\partial\overline{\eta}(t_i)/\partial\underline{\overline{\eta}}$,will lead to a block diagonal matrix.

$$\frac{\partial \overline{\eta}(t_i)}{\partial \underline{\overline{\eta}}} = \begin{bmatrix} N_{\overline{\eta}} & 0 & \cdots \\ 0 & N_{\overline{\eta}} & \\ \vdots & & \ddots \end{bmatrix} \tag{5.58}$$

For further evaluation, define the stress in each network in the absence of damage, $\underline{\underline{\tilde{\sigma}}}$, such that

$$\begin{aligned} \underline{\underline{\tilde{\sigma}}}(t,s) &= K(s)\mathrm{tr}\left(\underline{\underline{\varepsilon}}(t) - \underline{\underline{\varepsilon}}(s) + \underline{\underline{\varepsilon_c}}(s) - \underline{\underline{1}}\alpha(s)\Delta T(t,s)\right) \\ &\quad + 2\mu(s)\left(\underline{\underline{\varepsilon}}(t) - \underline{\underline{\varepsilon}}(s) + \underline{\underline{\varepsilon_c}}(s) - \underline{\underline{1}}\frac{1}{3}\mathrm{tr}\left(\underline{\underline{\varepsilon}}(t) - \underline{\underline{\varepsilon}}(s) + \underline{\underline{\varepsilon_c}}(s)\right)\right) \end{aligned} \tag{5.59}$$

When rearranging that stress tensor in matrix form, the curing stress in each network reads,

$$\underline{\sigma}(t) = \int_0^t (1 - D(\overline{\eta}(t, s = t_i)))\underline{\tilde{\sigma}}(s)\mathrm{d}s \tag{5.60}$$

Thus,

$$\frac{\partial \underline{\sigma}}{\partial \overline{\eta}(t_i)} = \int_0^t -e_i^{\mathrm{T}} \frac{\partial D(\overline{\eta}(t, s=t_i))}{\partial \overline{\eta}(t, s=t_i)} \underline{\tilde{\sigma}}(s) \mathrm{d}s \tag{5.61}$$

where e_i is again the unit vector of the ith component. To give meaning to the above expression, it should be kept in mind, that the integral is evaluated numerically. For all but one time point, the kernel of the integral is zero, but the one non-zero time point will lead to a finite value of the integral. If it was possible to evaluate the nonlocal field at all times, and if the integral could be represented exactly, the unit tensor would be replaced by a dirac delta function. Finally the derivative of the damage with respect to the nonlocal field variable, η, will depend on the choice of the stress-strain relation for each network, as well as the damage history in that network. If the stress-strain curve is chosen as presented in figure 5.7 and equation (5.10), then the damage can be expressed by

$$D = \begin{cases} 0 & \text{if } \eta < \varepsilon_f \\ \frac{\varepsilon_u(\eta - \varepsilon_i)}{\eta(\varepsilon_u - \varepsilon_i)} & \text{if } \varepsilon_f < \eta < \varepsilon_u \\ 0 & \text{if } \varepsilon_u < \eta \end{cases} \tag{5.62}$$

Due to the restriction that the material cannot heal, $\dot{D} > 0$, the change of damage with respect to the nonlocal field variable becomes

$$\frac{\partial D}{\partial \overline{\eta}} = \begin{cases} \frac{\varepsilon_f \varepsilon_u}{\overline{\eta}^2(\varepsilon_u - \varepsilon_f)} & \text{if } \varepsilon_f < \eta < \varepsilon_u \text{ and } \dot{D} > 0 \\ 0 & \text{otherwise} \end{cases} \tag{5.63}$$

At this point all necessary information to construct the residuals and stiffness matrix of the FE formulation are stated. The concrete implementation of the various terms will be deferred to appendix E. In the current study, the displacements are approximated through quadratic shape functions, and the nonlocal field through linear shape functions. This is mainly because the nonlocal field is related to the strain, which is related to the derivative of the displacement. To allow for a general geometry, a tetrahedron has been chosen as the element shape. For the evaluation of the time integral during cure, 12 different networks are used. Therefore the resulting element has 30 degrees of freedom for the calculation of displacement and 48 degrees of freedom to find the nonlocal field. The resulting stiffness matrix is 78x78 in size.

Chapter 6

Macroscopic Deformation Response of an Idealized Woven Textile Composite Unit Cell After Curing

The various thermal, kinetic and mechanical models that have been developed in this thesis are now combined to study the deformation response of an idealized, woven textile composite unit cell that is first cured and subsequently subjected to mechanical loads.

6.1 Material properties

In addition to the elastic properties as a function of cure which are obtained through BLS and RLS, properties relating the onset and evolution of damage response need to be found. Specifically, the characteristic length, ℓ, the strain at which damage initiates, ε_f, and the ultimate strain, where full damage is reached, ε_u, are needed. Ideally, these values are determined for each network individually. To achieve such a task, a corresponding experiment would need to be conducted at various stages of the curing process. Possible experiments include a double cantilever beam experiment as described below, or a compact tension test. For a first estimate of the damaging material properties, assume the following: no cure strain ($\underline{\underline{\varepsilon}}_c = 0$) and external strain are applied to the specimen during cure, the temperature is constant throughout and all networks experience the same damage behavior. Then the stress as given in equation (3.43) can be simplified to give,

$$\underline{\underline{\sigma}}(t > t_{cure}) = (1 - D(t)) \left[\left(\underline{\underline{1}} \frac{1}{3} \mathrm{tr} \underline{\underline{\varepsilon}}(t) \right) \int_0^{t_{cure}} \dot{\phi} K(s) \mathrm{d}s + \left(\underline{\underline{\varepsilon}}(t) - \underline{\underline{1}} \frac{1}{3} \mathrm{tr} \underline{\underline{\varepsilon}}(t) \right) \int_0^{t_{cure}} \dot{\phi} 2\mu(s) \mathrm{d}s \right] \tag{6.1}$$

This means the cured epoxy will be regarded as a classical isotropic solid, and equation (6.1) has now the same form as equation (5.7).

The remaining question is the proper choice of the length scale parameter, ℓ, and the ultimate strain, ε_u. ℓ, has influence on the size of the zone or volume in which damage occurs. The shape of the stress-strain curve, and thus the value of ε_u prescribes how much energy (area under the curve, shown in figure 6.3) is dissipated per unit volume during the damage process. ℓ and ε_u combined will provide a value of energy that is dissipated during the damage. Therefore the length scale parameter ℓ is chosen to be 0.1 mm. To find a corresponding ultimate strain value, an estimate of energy is needed, that is related to damage process and a BVP is needed to connect it the material model. This has been investigated on the laminate level using Shapery theory [136–138]. For pure epoxy such values are not readily available. However, fracture energy is an energetic value related to failure, that has been thoroughly studied. It will therefore be used to obtain a value of ε_u though a simulation of a double cantilever beam (DCB) test. Here a layer of epoxy is inserted between two aluminum beams. A displacement is prescribed at the end of the beams and the force is measured. The geometry of the problem is given in figure 6.1. The displacement is increased until at some external prescribed displacement (and load), damage initiation strain in the epoxy is reached. From that moment on, damage sets in and starts progressing from the outer edge of the epoxy (right side in figure 6.2) away from the point where the load is applied. With increasing displacement more damage is accumulated and the material softens locally. Eventually this will also lead to a negative slope in the global force-displacement curve, as shown in figure 6.3. Once the tangent of the loading slope approaches $-\infty$, the simulation needs to be stopped because no further equilibrium solutions can found. In an actual experiment this point would mark the onset of unstable crack growth and the force would suddenly drop.

In the present DCB simulation, that uses Aluminum adherents and EPON 862 resin, the damage zone advanced by 0.0546 mm, at which the onset of unstable fracture was initiated. The projected damage area was 0.0168 mm^2. The geometry of the DCB is shown in figure 6.1 and the material properties used in the simulation are given in table 6.2. The recoverable (elastic) work and non-recoverable (inelastic) energy in the DCB simulation are shown in figure 6.3. The inelastic energy was determined to be 5.7 μJ. The inelastic energy per projected damage area yielded 350 J/m^2, which falls well into the range of fracture energy found in the literature. Data for EPON Resin 862 with EPIKURE Curing Agent 3234 from the literature are given in table 6.1. It should be noted that when applying an idealized stress-strain curve, as shown in figure 5.7, the yield strain calculated from the manufacturer data presented is 2.55%. This value was used for the failure onset strain, ε_f.

Property	Value	Unit	Reference
Modulus	3.24	GPa	[64]
	2.76	GPa	[139]
Yield Strength	82.7	MPa	[64]
	86	MPa	[139]
Yield strain	6.6	%	[64]
Fracture energy	606	J/m^2	[139]
	280	J/m^2	[140]

Table 6.1 Properties of EPON 862, obtained from literature

Property	Value	Unit
Final elastic modulus E	4.95	GPa
Damage initiation strain ε_f	2.55	%
Ultimate strain ε_u	5.0	%
Length parameter ℓ	0.1	mm

Table 6.2 Damage related properties of EPON 862 used in simulations

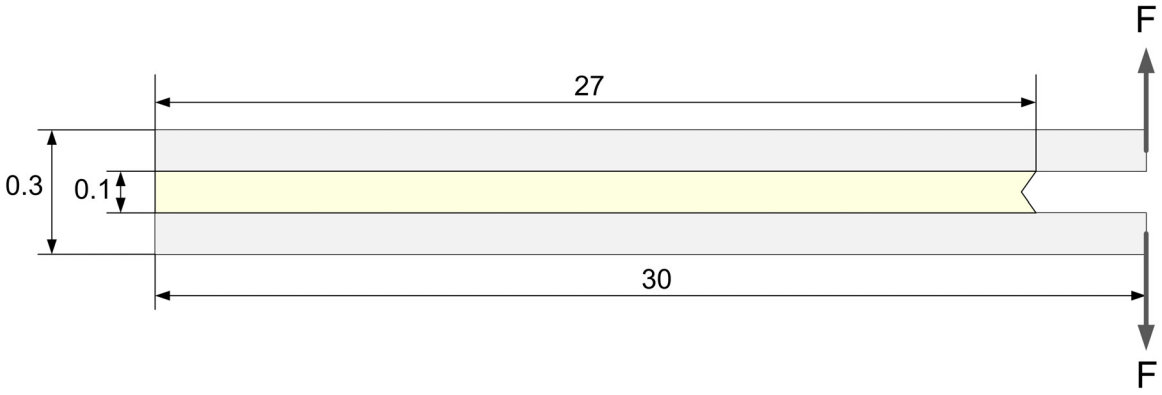

Figure 6.1 Geometry of Double cantilever beam

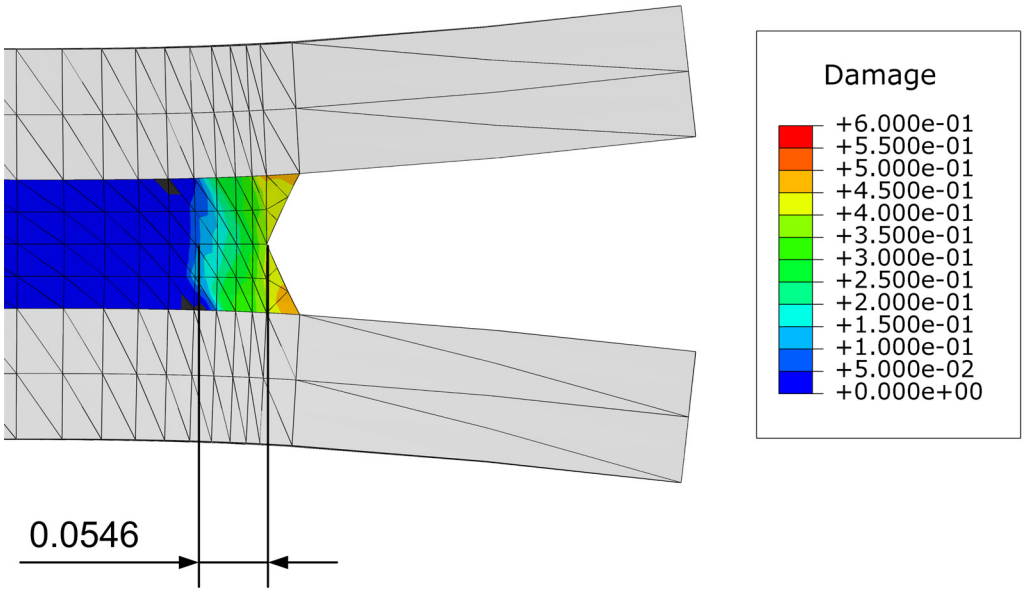

Figure 6.2 Progression of damage in epoxy

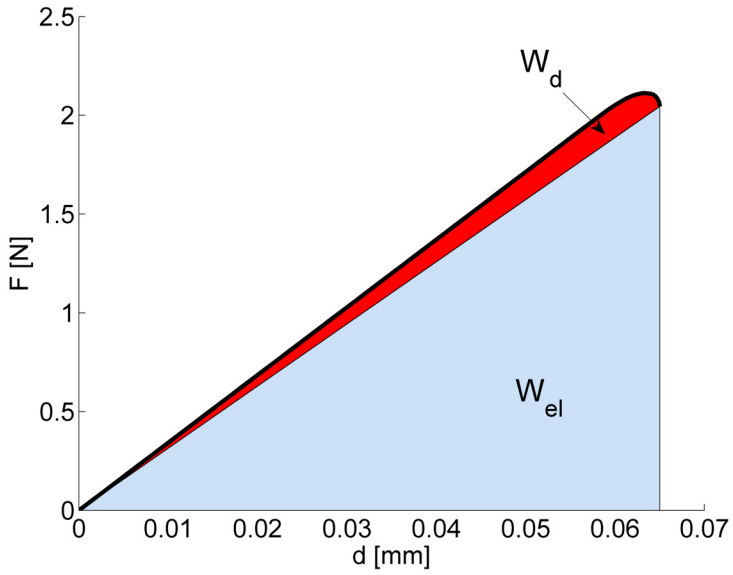

Figure 6.3 Force vs. (total) displacement of DCB specimen. Elastic and "damage" work during are shown.

6.2 Example - Woven RUC

6.2.1 Problem description

As in section 4.5, a woven RUC will be considered. However, due to computational constraints only a single RUC will be considered. First, the RUC is fully cured, than a uniaxial displacement controlled tension test is performed. To allow for the tension test subsequent to cure, the boundary conditions needed to be slightly modified compared to section 4.5. They are depicted in figure 6.4. The surfaces in the 2-direction and 3-direction are unconstrained and traction free at all times. The two surfaces with a normal along the 1-direction are also free to move in the 2-direction and 3-direction. However, one of the two surfaces is completely constrained in the 1-direction. The other surface with a normal in the 1-direction is constrained such that plane sections remain plane. During cure that plane is free to expand and contract. During loading a concentrated force is applied to a reference node, which in turn is coupled to that surface. These constraints are necessary, because during cure the RUC deforms due to shrinkage and thermal effects, and boundary conditions are always applied with respect to the undeformed shape, which is initially flat.

Figure 6.6 shows the normalized results of a cure and tension simulation. The displacement applied at one side of the unit cell has been normalized by the RUC length to give an average strain. The total reaction force has been normalized by the cross-sectional area to give an average strain. Five different cases have been considered in figure 6.6. They are

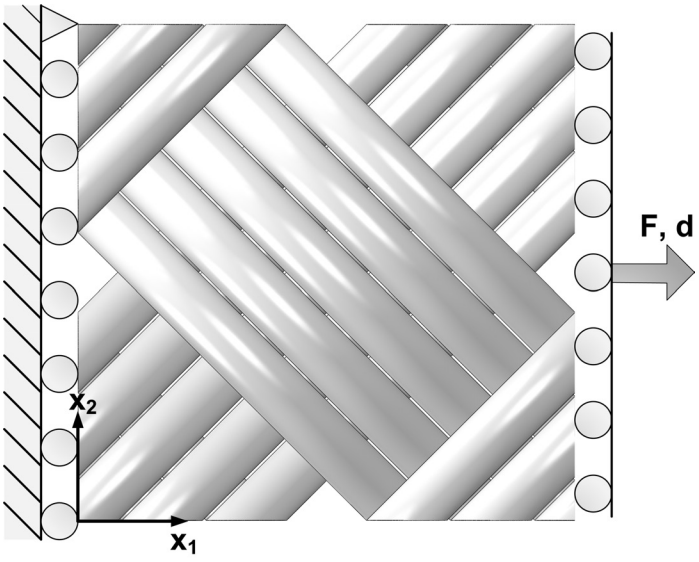

Figure 6.4 Top view of RUC to show boundary conditions applied during and after cure (only fibers are shown)

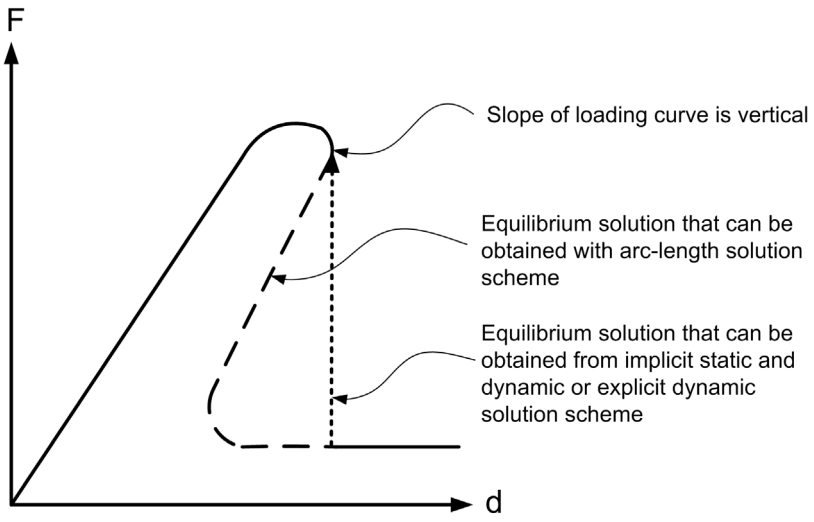

Figure 6.5 Snap-back and snap-through in damaging models

summarized in table 6.3. In Case 1, the RUC has been cured at 50°C according to the cure cycle shown in figure 4.2. The inelastic material properties used are shown in table 6.2 and the evolution of elastic properties is shown in figures 3.7 and 3.8. Case 2 is identical to Case 1, except the global cure shrinkage has been increased from 2% to 6%. This cure shrinkage is comparable to the one seen in HETRON resin, which has been used as a matrix material in previous studies [3,5–8]. In Case 3, neither cure shrinkage nor thermal expansion occurs, which is equivalent to $\alpha(s) = 0$ and $\varepsilon_c = 0$. Therefore the fiber and matrix are stress free prior to mechanical loading it. In Case 4, only cure shrinkage is considered which is a material state, that can be obtained by curing and loading at the same temperature. Finally, Case 5 does not allow for any damage to occur during the cure and also during subsequent mechanical loading. In this case the loading response is entirely linear.

6.2.2 Results and discussion

In Cases 1-4, a large linear regime was observed and followed by a small non-linear regime. The lack of prolonged softening behavior can be explained with the help of figure 6.5. It has been seen in the literature, [129, 141], that upon tensile loading a snap-back of the load deflection curve can be observed. That means that with continued softening due to accumulated damage, the load and displacement have to be lowered in subsequent iterations to find an equilibrium position. To successfully calculate such a snap back behavior an arc-length method needs to employed, such as the RIKS method, [142, 143]. If a standard implicit finite element solution scheme is used, it is not possible to predict such a snap-back

Case	Cure shrinkage	ΔT at the end curing step	Damage included	Comments
1	2%	30°C	yes	EPON 862 Baseline
2	6%	30°C	yes	This case corresponds to an elevated cure shrinkage that is found in HETRON resin
3	0%	0°C	yes	Room temperature cure
4	2%	0°C	yes	Room temperature cure
5	2%	30°C	no	Linear properties and response

Table 6.3 The 5 cases simulated for a woven RUC with carbon fibers and EPON 862 resin

behavior. Instead a snap-trough type behavior, when the loading slope becomes vertical leads to solution divergence. At this point, a drop in load is observed and the subsequent equilibrium solution cannot be found by an implicit finite element solver. If the solver is an explicit solver, than a solution can be found, but there is additional kinetic energy, that enters the problem. In the current work, that models the evolution of material properties with time, the use of the RIKS method to solve the equilibrium equations is not straight forward, because time is not an explicit input to such a solution scheme.

Figure 6.6 shows the macroscopic stress, σ, and the macroscopic strain E for the 5 cases that were studies. The maximum stresses, Σ, in Case 1, 3 and 4 are similar. The maximum Σ is largest in Case 3, where no built-in stresses due to cure are present. The next largest maximum Σ occurs in Case 4, where only internal stresses due to chemical shrinkage were considered, but not thermal gradients in time because the curing and loading were performed at the same temperature. Case 1 contains stresses before mechanical loading due to both chemical shrinkage and temperature changes in time. The maximum Σ is therefore lower. However, in Case 1,2 and 4 no damage was observed at the end of the curing cycle. Case 2 is different in that regard. Here damage occurs already during cure and the matrix material starts to soften locally prior to the application of mechanical load. This is shown in figure 6.9(c). This RUC also shows a significantly reduced maximum Σ in figure 6.6. While the maximum Σ for Case 3 is 142 MPa, the maximum for Case 2 is 94 MPa, which is an effective reduction of over 30% of the maximum Σ.

To further investigate the reduction in maximum Σ, the internal stress and damage states of Case 1 and Case 2 at the end of the curing process and shortly before reaching the maximum macroscopic strain, E, due to mechanical loading are shown in figures 6.8 and

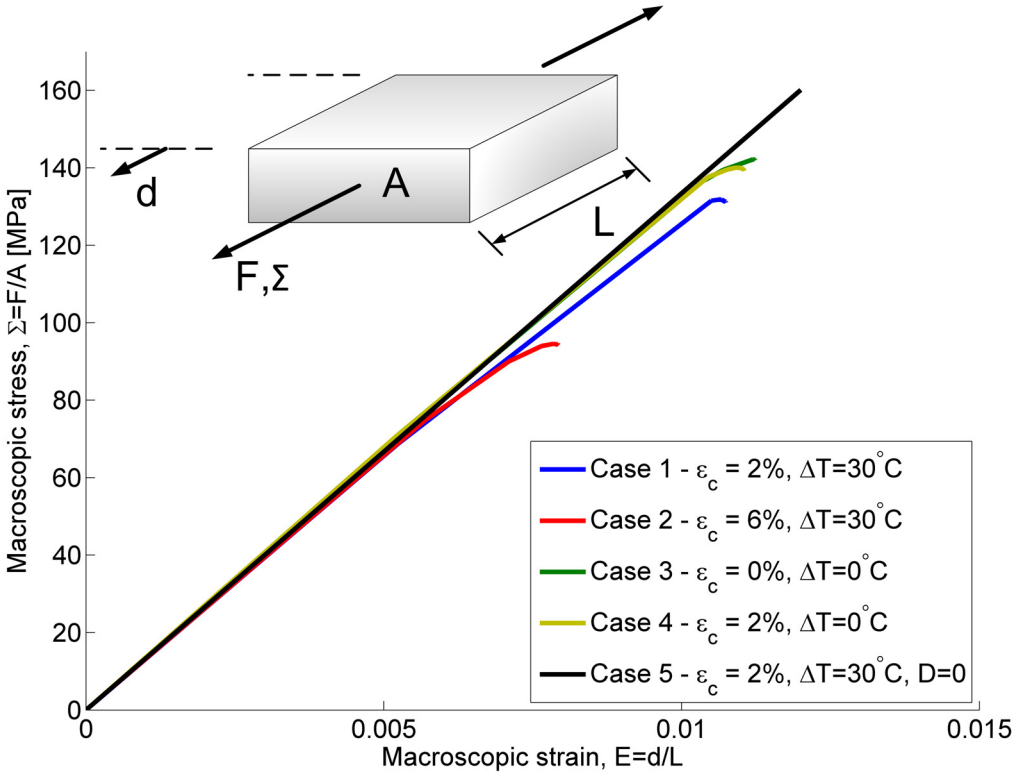

Figure 6.6 Global deformation response of woven RUC

6.9. Figure 6.8(a) shows the internal maximum principle stresses, $\sigma_{max,1}$, in Case 1 due to cure, before external loads are applied. $\sigma_{max,1}$ is largest in the center of the fiber tow and is smallest away from the fibers. In the center of the fiber tow, the fibers act as a constraints that prevent the matrix from shrinking as cure progresses and therefore stresses build up in that region. These observations are identical to the ones in figure 4.39(b). From figure 6.9(a) it can be seen that no damage is present before external mechanical loading is applied. Figure 6.8(b) shows $\sigma_{max,1}$ in Case 1 after applying mechanical load and shortly before unstable damage growth occurs. The maximum principal stress, $\sigma_{max,1}$, is largest where fibers are close together. However, these areas of high $\sigma_{max,1}$ do not correspond to the damaged areas as shown in figure 6.9(b) shortly before unstable damage growth occurs . Damage is largest at the boundary of the unit cell. The difference between location of maximum damage and largest $\sigma_{max,1}$ has two reasons. First, damage initiation and progression is dependent on strain, not on stress. Secondly, by definition, areas of increased damage have softened and will only be able to hold a reduced amount of stress.

Figure 6.8(c) shows the maximum principle stress, $\sigma_{max,2}$, due to cure effects in Case 2 prior to applying external mechanical loads. The stress pattern is similar to the one that can be found for Case 1 in figure 6.8(a). However, due to larger cure shrinkage the amount of

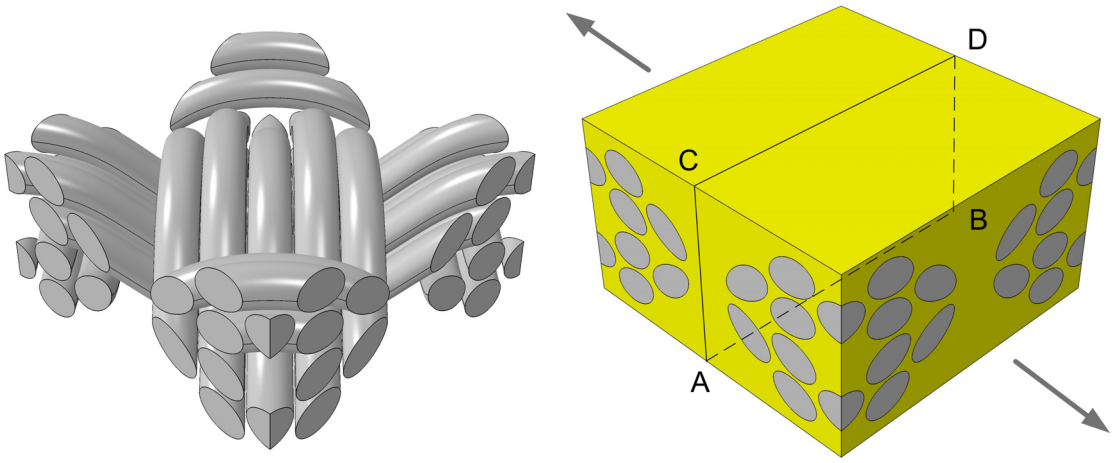

(a) Only fibers shown

(b) Fibers and matrix show, loading direction indicated

Figure 6.7 1x1 RUC

$\sigma_{\max,2}$ is generally larger, than $\sigma_{\max,1}$ at the end of cure. It can be seen from figure 6.9(c) that damage is already existent in the cured part, prior to applying external load. The location of the damage is identical to the one found in Case 1 after loading, as shown in figure 6.9(b). The maximum principle stress shortly before failure in Case 2 are shown in figure 6.8(d). Stresses are largest in the center of the fiber tow and where fibers are close together. Low $\sigma_{\max,2}$ can be found towards the edge of the RUC. In this region significant amount of damage and softening took place, as shown in figure 6.9(d). Here the damage found before applying mechanical load has progressed. The damage volume and the magnitude of damage have increased.

Due to the incorporation of damage during and after cure through continuum damage mechanics fiber debonding cannot be observed. Instead the decrease of elastic modulus that might be equivalent to such a debonding is spread out though the epoxy that occupies the volume between the fibers.

To further investigate the evolution of stress and damage during cure, consider Point A as shown in figure 6.10. At this point damage already develops during cure in Case 2. The evolution of damage in Case 2 at Point A is depicted in figure 6.12. The figure shows the damage in the network that was created at the beginning of the curing process. To also characterize the total combined damage in all networks by a single value, a compound damage is introduced that weighs the damage in each network with the rate of cure. Thus,

$$D_{\text{tot}}(t) = \int_0^t \dot{\phi}(s) D(t,s) \mathrm{d}s \tag{6.2}$$

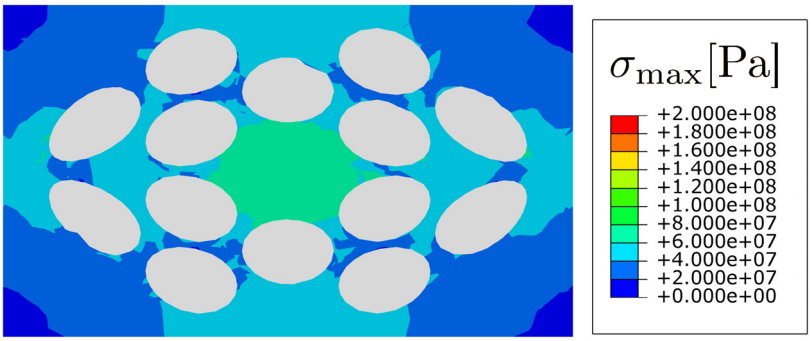

(a) Case 1, maximum principal stress at end of cure

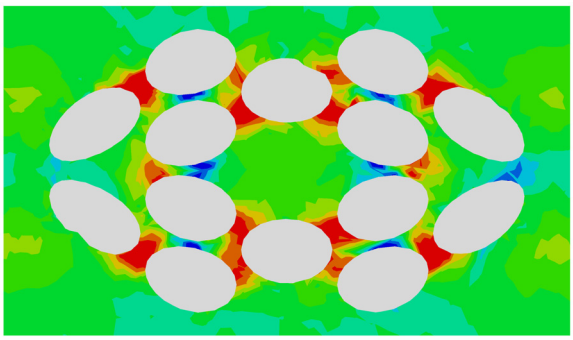

(b) Case 1, maximum principal stress at failure

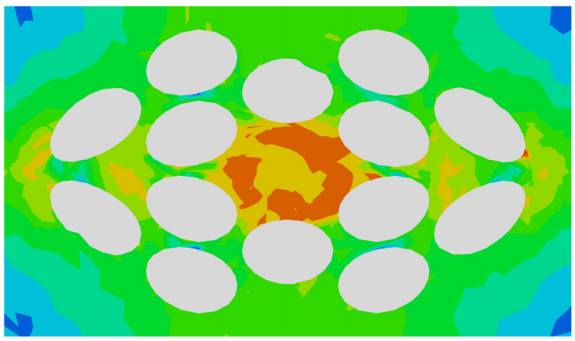

(c) Case 2, maximum principal stress at end of cure

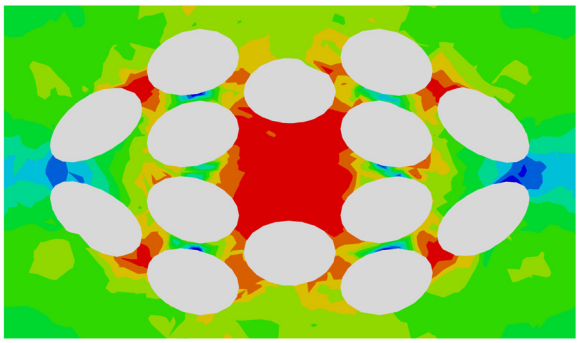

(d) Case 2, maximum principal stress at failure

Figure 6.8 Maximum principle stress in cross section $\square ABCD$

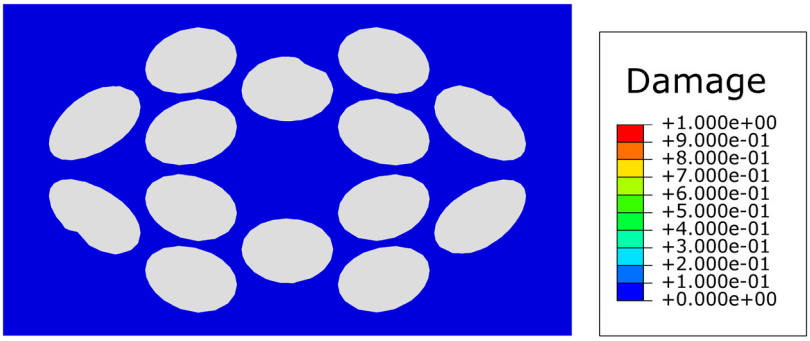

(a) Case 1, damage at end of cure

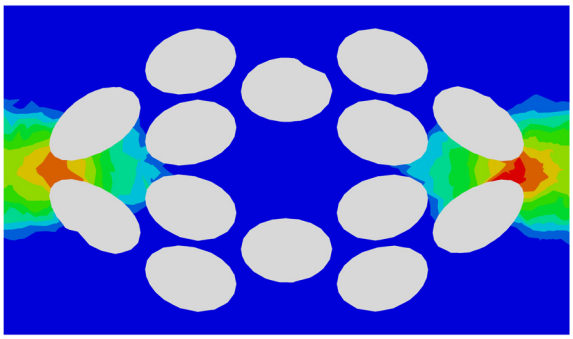

(b) Case 1, damage at failure

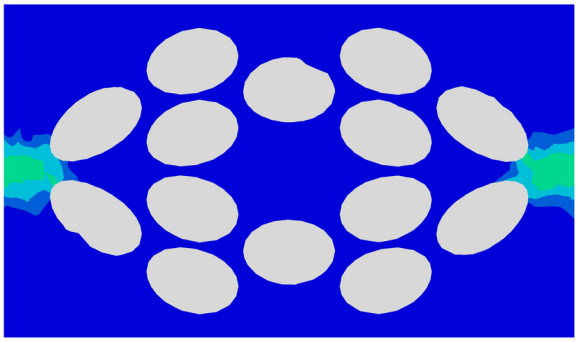

(c) Case 2, damage at end of cure

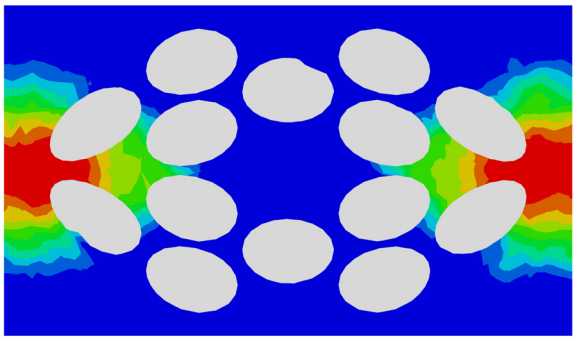

(d) Case 2, damage at failure

Figure 6.9 Damage in cross section $\square ABCD$

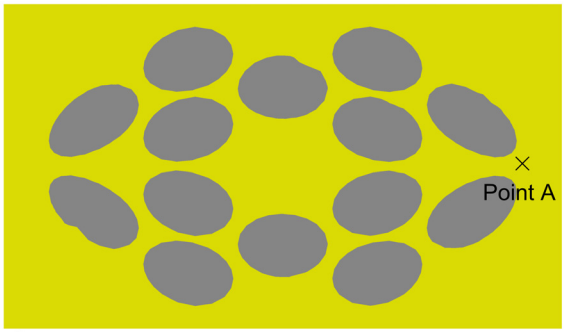

Figure 6.10 Location where evolution stress and damage is investigated

The evolution of maximum principle stress is shown in figure 6.13. To properly interpret the results it is also necessary to consider the evolution of temperature and degree of cure at that point as shown in figure 6.11. The evolution of stress and damage can be divided into several stages. For the first 200 seconds no significant maximum principle stress can be seen due to vanishing shear modulus. At this point gelation occurs and the continued chemical shrinkage leads to increasing stresses. Due to slower curing rates at later times, as shown in figure 6.11, the creation of stresses also slows down. After 700 seconds the strains in the first network exceed damage onset strain. Continued cure shrinkage leads to an increase in damage. After 1800 seconds full cure is reached and no further increase in damage or maximum principle strain due to chemical effects can be observed. After 3600 seconds the temperature in the specimen is lowered. This leads to further damage and stress generation. Strictly speaking, if the cured epoxy was treated as a solid with stress-strain relations as described in figure 5.7, an increase in damage due to an increase in strain should be accompanied by a reduction in stress. This does not have to be the case in the curing of an epoxy. Networks created at different times have a different damage state. Therefore, while the networks created at the beginning accumulated a significant amount of damage, the networks created at the end continue to carry load. Generally it can be expected that networks created at the beginning show larger damage compared to networks created at later times, because they show the largest differential mechanical strain relative to their initial configuration. It should be noted that despite the sharp decrease of temperature in figure 6.11 after 3600 seconds, the increase of damage in figure 6.12 and maximum principal stress in figure 6.13 is spread out over the time from 3000 seconds to 4000 seconds. This due to the time discretization of the FE simulation. Smaller time steps will resolve the cooling down phase better, but the computational time will accordingly increase.

Next the influence of mold pressure will be investigated for Case 1. First it is important to state the pressures present in the mold during the manufacturing of a textile composite.

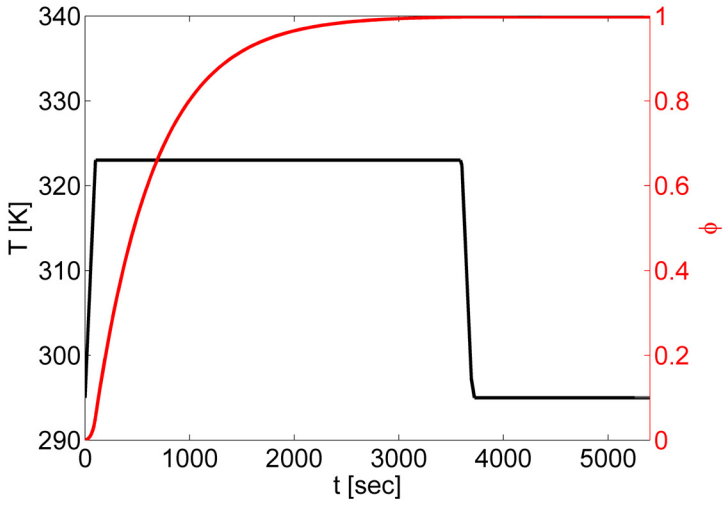

Figure 6.11 Temperature and degree of cure at Point A

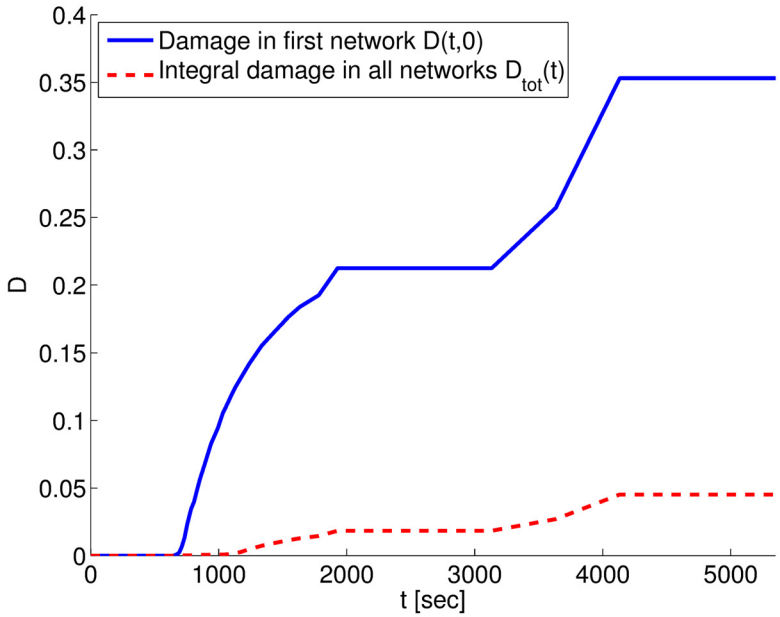

Figure 6.12 Evolution of damage at Point A

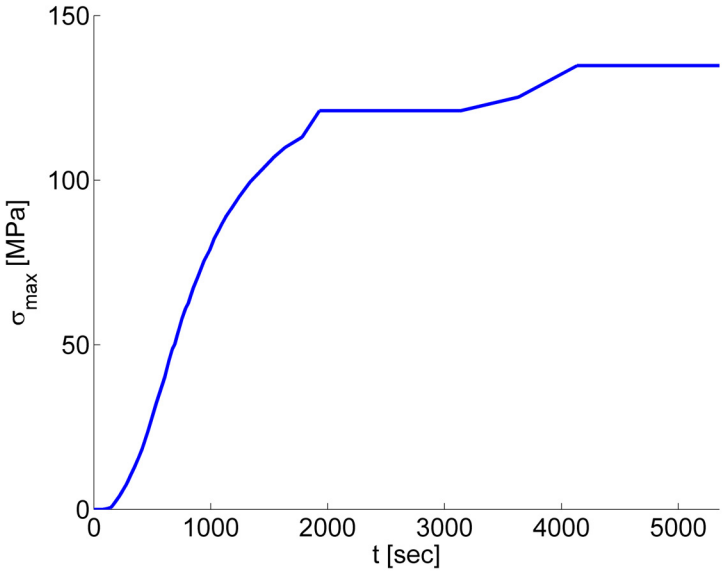

Figure 6.13 Evolution of maximum principle stress at Point A

Rudd, [144], gives mold pressures of up to 15 bar for RTM after injection. Ikegawa et al., [71], cite a mold pressure of 20-50 bar for structural resin transfer molding after applying the resin to the fiber mat. Revello, [72], extends the value to 35-140 bar. However these values are obtained for compression molding of sheet molding compound, which usually consists of fiber glass and polyester compound. Also the impregnation process is different compared to RTM. Finally Charrier, [145], quotes pressure of 35-700 bar for compression molding. However these values were discussed in the context of pure polymeric materials without fibers. The values given by Rudd and Ikegawa provide reasonable estimates for maximum mold pressure.

To account for mold pressure, the boundary value problem described in figure 6.4 is augment as follows: during cure all sides are fixed and a 5 MPa mold pressure is applied on the top surface. This simulates the part being in the mold. After cure, the same boundary conditions as shown in figure 6.4 are present. However due to the way the boundary conditions are enforced in the FE model during cure, all surfaces have to remain flat after the RUC is removed from the mold. The RUC may however expand and contract, when external loads are applied.

The results are shown in figures 6.14 and 6.15. Figure 6.14 shows the comparison of global force and deformation curves for Case 1 with and without mold pressure being applied. The most notable difference is a changed stiffness. However this is not due to the curing process. Instead it is due to details of the FE simulation. The proper application of mold pressure during the FE simulation requires that surfaces stay flat even after the

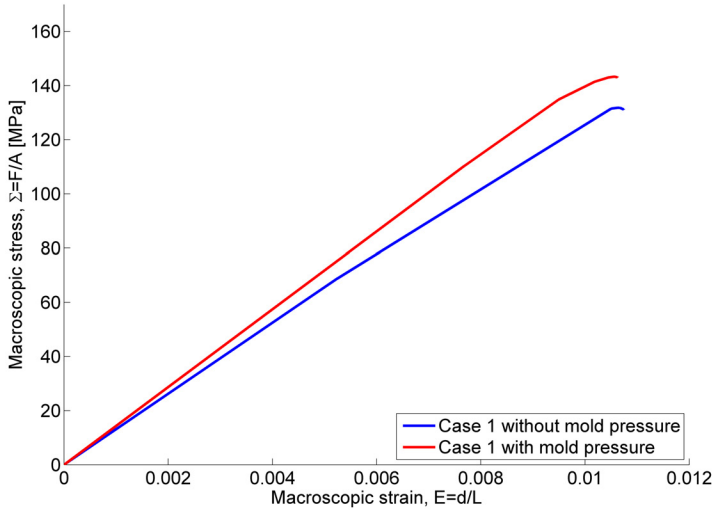

Figure 6.14 Global deformation response of woven RUC in Case 1 with and without mold pressure applied during cure

pressure is released. This enforces additional constraints on the RUC that makes it appear stiffer compared to the cases discussed previously. On the other hand it can be seen that the ultimate macroscopic strain is comparable for the cases with and without mold pressure. Therefore the ultimate strain is unaffected by the application of a 5 MPa cure pressure.

Figures 6.15(a) and 6.15(b) show the damage at the end of cure and at failure for Case 1 with mold pressure applied during cure. The results are comparable to the ones without mold pressure as shown in figures 6.9(a) and 6.9(b).

Figures 6.15(c) and 6.15(d) show the maximum principle stresses in Case 1 with mold pressure being applied during cure at the end of cure and at failure. Stress distribution and magnitude are comparable to the case shown in figure 6.8(a) and 6.8(b). However the stresses after cure are more evenly distributed and increased towards the edge of the unit cell.

Overall the application of mold pressure during cure has a negligible influence on the overall response of the RUC. Compared to the internally generated stresses of over 60 MPa, an external stress of 5 MPa is too small to have a significant impact.

The findings of the 5 different cases can be compared with previous studies by Song [3]. The major result of that study is repeated in figure 6.16. It shows the compression response of a triaxially braided RUC with carbon fiber and Hetron matrix. The fiber tows were modeled using the CCM model as a homogenization technique. The matrix material included plastic and damage effects, where the damage was closely related to the equivalent plastic strain. Stresses due to cure are not accounted for. Instead the effective material properties of

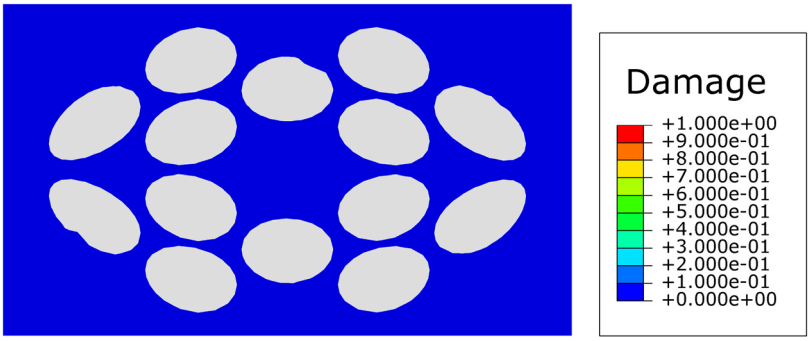

(a) Case 1 with mold pressure, damage at end of cure

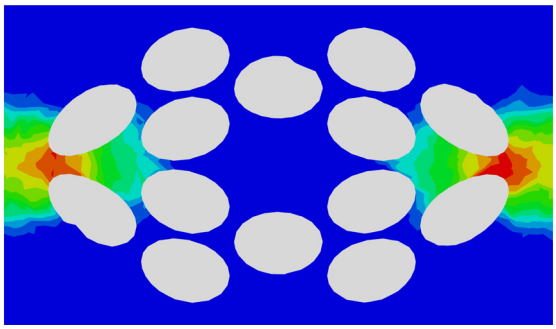

(b) Case 1 with mold pressure, damage at failure

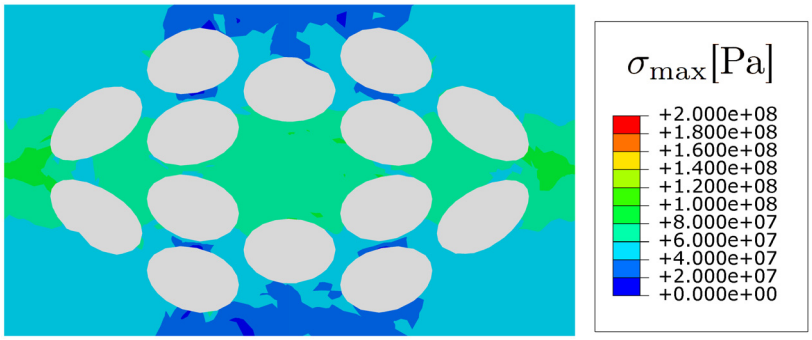

(c) Case 1 with mold pressure, maximum principle stress at end of cure

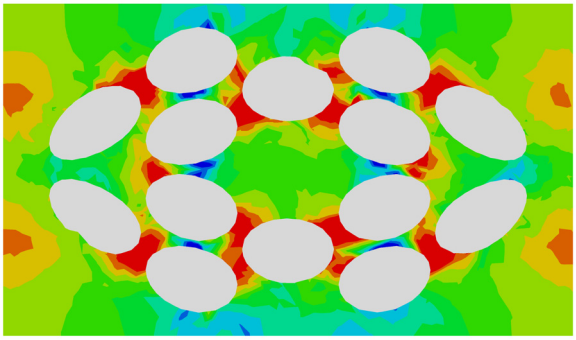

(d) Case 1 with mold pressure, maximum principle stress at failure

Figure 6.15 Damage and maximum principle stress in cross section $\square ABCD$ for Case 1 with mold pressure applied during cure

the matrix material are lowered to obtain agreement between experimental result and the numerical models. The maximum stress with "virgin" properties, that do not account for residual stresses due to cure, is 700 MPa. The maximum stress with "in-situ" properties that include corrections for residual stresses is 300 MPa, thus leading to a reduction in maximum stress of 57%.

The current study, as well as the one by Song, [3], aims to find the response of a braided composite in the presence of manufacturing induced stresses. In the calculations by Song the stress state after complete cure was not known. Therefore, the effective "in-situ" material properties needed to be calibrated through further experiments. The aim of the current study is to find the material properties through "first principles". All material properties used were found from experiments only involving single constituents, either carbon fiber or epoxy. Only in the simulation step, the materials are combined into a composite model and their combined response is determined. There was no need to find "in-situ" properties, because the evolution of stresses is explicitly accounted for. On a historical side note, it is worth mentioning, that two similar view points have long been used in the determination of structural integrity and fatigue of notched steel bars and shafts. Here a nominal stress approach and a local stress approach exist, [146]. In the nominal stress approach the effective material properties have been lowered based on experimental values to account for stress concentrations in parts with complicated geometries. This is comparable to finding "in-situ" properties, when the post-cure stress field is not known. On the other hand, in the local stress approach, the actual stresses concentrations, that occur at notches have to be calculated, but the material properties used can be found through simpler experiments, that do not need to contain information about the geometry of the part that is considered. This is comparable to the approach taken in the current study, where the material properties of the epoxy has been determined in bulk and the evolution of stress and damage needs to be accounted for in the FE simulation.

It should be noted that figures 6.6 and 6.16 should only be compared qualitatively. The epoxy material, fiber architecture, fiber volume fraction and loading direction are different. However they qualitatively show the same trend. An increase in chemical shrinkage and thermal gradients can lead to significantly reduced maximum global stress.

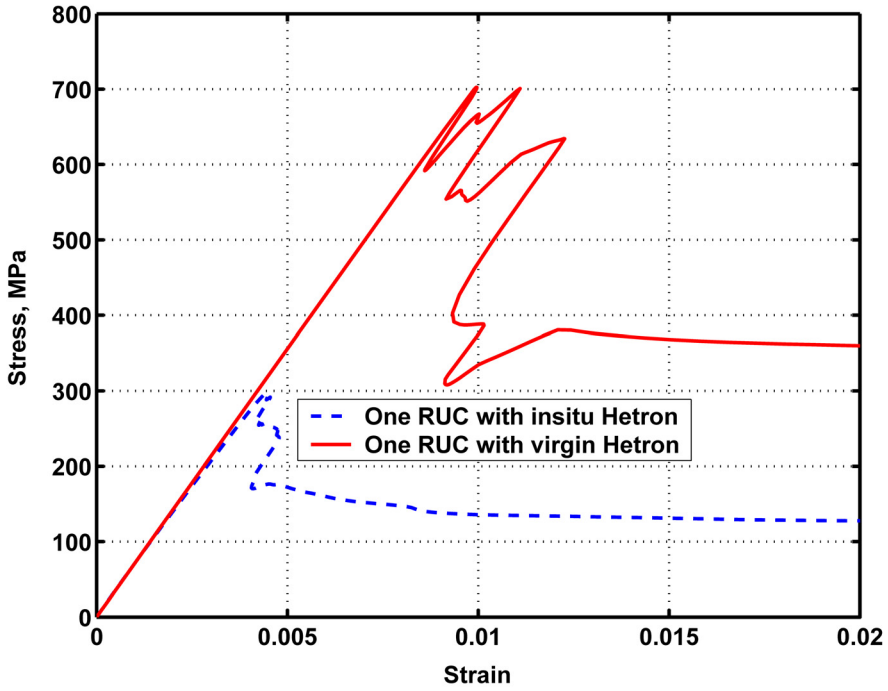

Figure 6.16 Comparison of macroscopic stress-strain curve of uniaxial compression test of triaxially braided composite with "virgin" and "in-situ" Hetron matrix material, [3]

Chapter 7
Concluding remarks

7.1 Summary

The aim of this thesis was to understand the role of the curing process of matrix materials (polymer resin) in textile composites and the influence of stresses generated during the curing process due to chemical shrinkage and thermal effects on subsequent performance of textile composites when service loads are applied. Of especial importance was to eliminate the need of "in-situ" material properties by accounting for stresses due to cure in the matrix material explicitly. Another goal was to characterize the elastic and inelastic properties of a cured composite, only with the knowledge of material properties of the individual constituents and the geometrical arrangement of the fibers in the final part. To that end, several physical aspects needed to be accounted for, including thermal, chemical and mechanical effects. The evolution of temperature was coupled to a phenomenological curing model. Both effects depend strongly on each other and the corresponding equations were solved simultaneously. It has been quantified to what extent geometry, thermal conductivity, parameters of the curing equation and boundary conditions influence the maximum temperature and rate of cure.

A model was developed to describe the phase transition of a liquid epoxy resin and hardener mixture. The idea of continuously developing networks has been used. These networks interpenetrate each other, but do not otherwise interact with each other. Different networks may have different thermal, elastic and inelastic properties and states. Especially, different networks have different stress free reference configurations. Due to thermal gradients in time and space and cure shrinkage of newly generated networks, stresses develop. These stresses may reduce (or increase) the margin of external loads that can be applied before the epoxy starts failing. The application of the network curing model has been shown for pure epoxy, unidirectional composites and woven composites. Thermal gradients should only be expected in geometries where the wall thickness exceeds several millimeters. However,

stresses generated during cure have an appreciable magnitude regardless of the size of the composite considered.

Inelastic response during and after cure was modeled using a damage model. The damage state can be different for each network. A non-local damage model was used to prevent strain localization when the curing process is simulated using the finite element method. The extended curing-damage model has been applied to a woven composite made of carbon fibers and epoxy matrix. The woven tows have been modeled using representative fibers, thus eliminating the need for a homogenization scheme of the curing and damaging fibers tows. For this representative unit cell, the effect of cure shrinkage and cure at different temperatures have been quantified.

The material properties of the curing model was derived from BLS and RLS data. It was also shown how the material properties necessary to describe damage can be related to the fracture energy.

7.2 Future work

There are several extensions to the proposed curing and damage model the seem quite obvious to do. These include the extension of the model to finite deformation. This is especially important, because toughened epoxies may show strains of several percent before full failure. It would also be interesting to investigate whether plasticity can be included into the model formulation to allow for permanent deformation. Visco-elastic effects have been neglected in the current model. However it is known that polymeric material do exhibit this type of behavior. Especially when considering the strong dependence of visco-elastic effects on the temperature and observing that large temperature changes can be found during the curing cycle, the role of visco-elastic effects is not entirely clear. Finally, it should be mentioned that the current presentation of the curing and damage model was based on arguments related to the mechanics of materials. It should be possible to find an alternative and more rigorous derivation based on thermodynamic arguments.

7.2.1 Experimental validation and material properties

When considering the various extensions of the curing and damage model to plasticity and visco-elasticity it becomes obvious that an extensive experimental procedure is necessary to derive all required material properties. This includes tests relating the inelastic properties to the degree of cure. For example it would be necessary to perform tension tests or tests

on compact tension specimens at various stages of the curing program to find the inelastic response of the epoxy. It would also be advisable to perform these tests with differently sized specimens, so that the characteristic length scale ℓ can be found.

7.2.2 Micromechanics and multiscale analysis

Currently, the woven composite is modeled using representative tows. This is computationally very expensive. In order to model the response of multiple RUCs or larger structures in general with current computing resources the use of some multiscale computing models seem inevitable. Therefore, it can be investigated whether the curing and damage model can be incorporated into some homogenization or multiscale scheme to model the micromechanical response of the fiber tows. Due to the complexity of the governing equations, such a multiscale scheme will have to be of computational nature such as the method of cells, [89, 147], or additional finite element simulations on the finer scale.

7.2.3 Optimize cure cycle and geometry

With the presented curing and damage model at hand, various optimization studies can be conducted. For example the curing cycle might be optimized for short time, while cure stresses or maximum temperature may not exceed a certain value. Also the fiber layout can be optimized to achieve desired performance while reducing weight. When optimizing the curing cycle, the epoxy system is usually already chosen and treated as an input to the optimization problem and the optimal cure temperature and pressure cycle are the outputs, [30, 44–46]. However it is also possible to treat the cure cycle and especially the total curing time as well as the minimum requirement on the ultimate strength as an input to the optimization problem. In that case, finding a proper material system which can be characterized in terms of curing constants in equation (2.4), mechanical properties in equations (3.71) and (3.73) and cure shrinkage would be the output. It is of course another problem to find the proper chemical structure of the resin and hardener mixture to achieve such a goal.

An aspect that has not been addressed in the current study is a shift in mechanical properties when the temperature exceeds the glass transition temperature, T_g. Plepys and Farris [22] noted that the coefficient of thermal expansion is larger above T_g, but the modulus is significantly larger below T_g, thus leading to larger stresses when the material is cured below T_g. It is worth including such effects when considering an optimized curing cycle.

7.2.4 Biological growth

The model presented in this work aimed to predict the development of stress and evolution of material properties in a curing epoxy. However, such a model might also be of interest when investigating growth or healing of biological tissue. For example, it may be possible to treat the creation and growth of cells on top of other already existing tissue through the same idea of newly forming networks as it has been done for the creation of networks in an epoxy. Such cells can have different stress free reference configurations compared to the tissue they are created on. Due to the nature of biological tissue, such a model would need to be able to account for large deformation and anisotropy because the growth of the cells is assumed to have a preferential direction based on the deformation and stress state of the underlying tissue.

Appendices

Appendix A
Nanoindenation

A.1 Introduction

To develop further understanding of the matrix material properties in fiber tow between individual fibers, a tool is needed to extract material properties on a small scale. Such a tool that has been used to determine the Young's modulus, yield strength and hardness of materials on small scales is nanoindentation, [148]. These methods have been developed to measure the material properties of elastic-plastic materials, that do not exhibit time dependent properties. Besides the use of analytical methods, numerical investigations were also undertaken, [149, 150]. Doa et al. [151] and Chollacoop et al. [152] used FE to model the reverse analysis of the nanoindentation problem using one and two indenters. They also made use of dimensional analysis and representative stress and strain in order to reduce the amount of unknowns in the problem. Most work so far was concerned with elastic plastic behavior. Nevertheless, basing on the work of Lee and Radok [153], Lu and co-workers described methods to extract one [154] or two [155] linear viscoelastic properties through analytic expressions. For non-linear viscoelastic behavior or viscoelastic-viscoplastic behavior one has to resort to FE. Anand and Ames [156] described the forward indentation problem with a very general material model. Oveart [157] used a four parameter model that could also account for viscoplastic response to investigate the property of surface coating.

Lee et al. [158] investigated the interphase properties in a cellulose fiber-reinforced polypropylene composite. They noted that in a region eight times the length of their flat punch indenter radius, fiber and matrix properties both influence the outcome of the experiment and have to be deconvoluted. Quasmi et al. [159] used FE analysis and a modified three parameter viscoelastic model to quantify graded viscoelastic properties due to electron irradiation. They used the Levenberg-Marquardt Method from the MATLAB optimization toolbox [62] to optimize and match their numerical results with the values obtained from experiments. In summary: a way for separating the effects of fibers and matrix in a nanoindentation experiment in a composite is to make use of FE analysis and to match numerical

and experimental results. This will be done in the following. First the computational method is introduced. The material model, its implementation within the FE model is shown. Next surrogate modeling is discussed to speed up the numerical calculations. Finally the surrogate model is validated against additional simulations and the quality of its predictive capability is analyzed.

A.2 Computational Modeling

A.2.1 Material Model

The matrix material is modeled as a viscoelastic-plastic hardening material. The elastic part is time dependent whereas the plastic part is time independent. More general material models for polymers have been constructed, i.e. [156]. Unfortunately these models also involve more parameters that need to be calibrated to describe the material behavior. The advantage of the material model used in this study is, that the amount of variables are limited. It can also be easily specialized to be compared with previous results: when removing the time dependance, comparison with the Oliver-Pharr Method [148] is possible. If the yield stress is set to be infinite the model yields results similar to linear viscoelastic analysis. They are not the same since the FE implementation will capture geometric non-linearities.

A one dimensional model of the material is depicted in figure A.1. The time dependent part is modeled as a three parameter solid. The time independent part is constituted of a isotropic non-linear hardening sliding element.

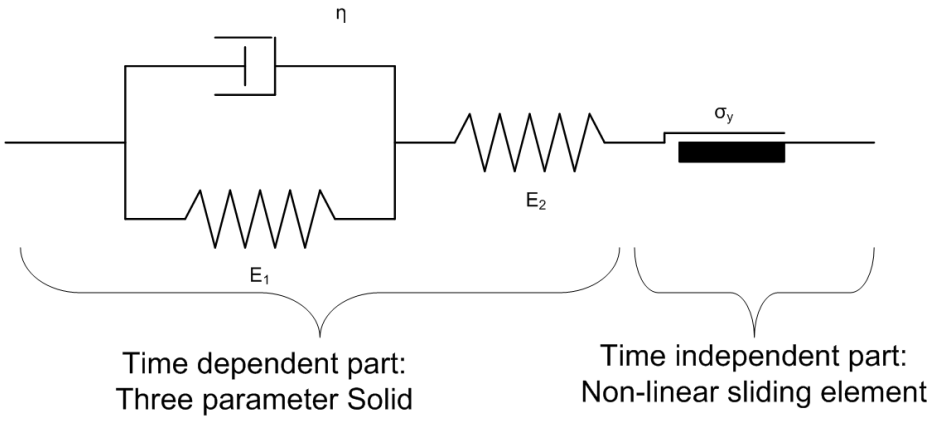

Figure A.1 One dimensional analog of visco-elastic perfectly plastic element used

Based on the one dimensional model the generalization to three dimensions is as fol-

lows [55] for the visco elastic portion:

$$\sigma_{ij} + \tilde{\nu}\dot{\sigma}_{ij} = \lambda\varepsilon_{kk}\delta_{ij} + 2\mu\varepsilon_{ij} + \tilde{\lambda}\dot{\varepsilon}_{kk}\delta_{ij} + 2\tilde{\mu}\dot{\varepsilon}_{ij} \tag{A.1}$$

So in the normal directions one obtains:

$$\sigma_{11} + \tilde{\nu}\dot{\sigma}_{11} = \lambda\left(\varepsilon_{11} + \varepsilon_{22} + \varepsilon_{22}\right) + 2\mu\varepsilon_{11} + \tilde{\lambda}\left(\dot{\varepsilon}_{11} + \dot{\varepsilon}_{22} + \dot{\varepsilon}_{33}\right) + 2\tilde{\mu}\dot{\varepsilon}_{11} \tag{A.2}$$

etc.
In the shear directions:

$$\sigma_{12} + \tilde{\nu} = \mu\gamma_{12} + \tilde{\mu}\dot{\gamma}_{12} \tag{A.3}$$

etc.
It is important to remember the definition of shear strain used by ABAQUS [55] when implementing the material model. It is engineering shear strains for Abaqus/Standard, but tensorial strains in Abaqus/Explicit, in which the material model was implemented.

A discretization scheme for the time part is the central difference operator. Where the point of interest is in the middle of the interval and the slope is evaluated with respect to the beginning and end of the interval:

$$\dot{f}_{t+1/2\Delta t} = \frac{\Delta f}{\Delta t} \tag{A.4}$$

$$f_{t+1/2\Delta t} = f_t + \frac{\Delta f}{2} \tag{A.5}$$

$$\tag{A.6}$$

With that the formerly time dependent stresses and strains vanish and one obtains the following discretization for every time increment.

$$\left(\frac{\Delta t}{2} + \tilde{\nu}\right)\Delta\sigma_{11} = \left(\Delta t\frac{\lambda}{2} + \tilde{\lambda}\right)\Delta\varepsilon_v + \left(\Delta t\mu + 2\tilde{\mu}\right)\Delta\varepsilon_{11} + \Delta t\left(\lambda\varepsilon_V + 2\mu\varepsilon_{11} - \sigma_{11}\right)_t \tag{A.7}$$

To give more meaning to the variables, introduce the following definitions for the volumetric strains, the relaxation time, the Lamé constants where '0' depicts instantaneous and '∞' depicts long term behavior, respectively.

$$\varepsilon_V = \varepsilon_{11} + \varepsilon_{22} + \varepsilon_{33} \tag{A.8}$$

$$\tilde{\nu} = \tau \tag{A.9}$$

$$\tilde{\lambda} = \tau\lambda_0 \tag{A.10}$$

$$\lambda = \lambda_\infty \tag{A.11}$$

$$\mu = \mu_\infty \tag{A.12}$$

$$\tilde{\mu} = \tau\mu_0 \tag{A.13}$$

To see if the material model gives reasonable results set $\tau = 0, \quad \Rightarrow \tilde{\nu} = \tilde{\lambda} = 0$. So the material relaxes instantaneously.

$$\Delta\sigma_{11} = \lambda_\infty \Delta\varepsilon_V + 2\mu_\infty \Delta\varepsilon_{11} \tag{A.14}$$

The material behavior is governed by its long term behavior.

If one assumes $\tau \to \infty$, so the relaxation time is large compared to the time of the increment/ experiment:

$$\Delta\sigma_{11} = \lambda_0 \varepsilon_V + 2\mu_0 \Delta\varepsilon_{11} \tag{A.15}$$

Here the material is governed by its short term behavior. Both cases work as expected.

The following abbreviations can be introduced:

$$\Delta\sigma_{11} = A_{1111}\Delta\varepsilon_{11} + A_{1122}\Delta\varepsilon_{22} + A_{1133}\Delta\varepsilon_{33} + B_{1111}\Delta\varepsilon_{11} + C_{11} \tag{A.16}$$

Doing the time discretization also for the shear part one finds:

$$\Delta\sigma_{12} = \frac{\Delta\mu/2 + \tilde{\mu}}{\Delta t/2 + \tilde{\nu}} 2\Delta\varepsilon_{12} + \Delta t \frac{(\mu 2\varepsilon_{12} - \sigma_{12})_t}{\Delta t/2 + \tilde{\nu}} \tag{A.17}$$

$$\Delta\sigma_{12} = A_{1212}\Delta\varepsilon_{12} + C_{12} \tag{A.18}$$

The equations in normal and shear direction can be put in tensor form by noting

$$A_{1111} = A_{1212} =: A(\Delta t) \tag{A.19}$$

$$B_{1111} = B_{1122} =: B(\Delta t) \tag{A.20}$$

$$\Delta\sigma_{ij} = A(\Delta t)\Delta\varepsilon_{ij} + B(\Delta t)\Delta\varepsilon_{kk}\delta_{ij} + C_{ij} \tag{A.21}$$

If one replaces $A = 2G$ and $B = \lambda$ one recognizes a form similar to one from linear elasticity. The time dependence has been moved away from the stresses and strains to the materials constants in the constitutive behavior. By noting the similarity of the so far obtained constitutive law with classical elasticity earlier derived algorithms for plasticity can be used [100, 160],

The radial return algorithm will be employed. The strains are split up into viscoelastic parts and plastic parts:

$$\Delta\varepsilon_{ij} = \Delta\varepsilon_{ij}^{VE} + \Delta\varepsilon_{ij}^{P} \Leftrightarrow \Delta\varepsilon_{ij}^{VE} = \Delta\varepsilon_{ij} - \Delta\varepsilon_{ij}^{P} \tag{A.22}$$

The strains in equation A.21 are all assumed to be purely viscoelastic.

$$\Delta\sigma_{ij} = A\left(\Delta\varepsilon_{ij} - \Delta\varepsilon_{ij}^{P}\right) + B\left(\Delta\varepsilon_{kk} - \Delta\varepsilon_{kk}^{P}\right)\delta_{ij} + C_{ij} \tag{A.23}$$

Note that the definition of C_{ij} contains information about previous strains. Since it is based upon the assumption of viscoelastic behavior only such strains should be used when recalculating C_{ij} in every time step.

A standard assumption is that the plastic part of the deformation is incompressible. Taking the deviatoric part of the plastic strain to be trace free one can rearrange the change in stress into an elastic predictor and plastic corrector.

$$\Delta\sigma_{ij} = \underbrace{A\Delta\varepsilon_{ij} + B\Delta\varepsilon_{kk}\delta_{ij} + C_{ij}}_{\text{elastic predictor:}=\Delta\sigma_{ij}^{trial}} - \underbrace{A\Delta\varepsilon_{ij}^{P}}_{\text{plastic corrector}} \tag{A.24}$$

An associative flow rule is used

$$\dot{\varepsilon}_{ij}^{P} = \dot{\gamma}\frac{\partial f}{\partial\sigma_{ij}} \tag{A.25}$$

where $\dot{\varepsilon}_{ij}^{P}$ are the plastic strain rate components, $\dot{\gamma}$ is the consistency parameter and f is the yield function.

The plastic strain increment is normal to the yield surface

$$\Delta\varepsilon_{ij}^{P} = \Delta\gamma n_{ij} \tag{A.26}$$

Where $\underline{\underline{n}} = \underline{\underline{s}}/||\underline{\underline{s}}||$ is the normal unit tensor. The yield criterion is dependent upon the deviatoric part $\underline{\underline{s}}$ of the stress tensor and an isotropic hardening function which depends upon

the equivalent plastic strain, ε^P_{eqv}.

$$f(\underline{\underline{\sigma}}, \varepsilon^P_{eqv}) = ||\underline{\underline{s}}|| - \sqrt{\frac{2}{3}} K(\varepsilon^P_{eqv}) \tag{A.27}$$

The hardening function is given by

$$K(\varepsilon^P_{eqv}) = \sigma_Y + H \cdot \left(\varepsilon^P_{eqv}\right)^n \tag{A.28}$$

where H is the hardening modulus and n is a hardening coefficient. For $n = 1$, one recovers linear hardening behavior and for $H = 0$, perfectly plastic behavior.

If the yield condition is satisfied, so $f(\underline{\underline{\sigma}}^{trial}, \varepsilon^P_{eqv}) > 0$ then the consistency parameter can be found by solving

$$||\underline{\underline{e}}^{trial}|| - \sqrt{\frac{2}{3}} K(\varepsilon^P_{eqv}) = A \cdot \Delta\gamma \tag{A.29}$$

where $||\underline{\underline{e}}^{trial}||$ is the deviatoric part of the strain at the beginning of the increment. Finally the stress increment and the equivalent plastic strain have to be corrected:

$$\Delta\sigma_{ij} = \sigma_{trial} - A\Delta\gamma \frac{\underline{\underline{s}}^{trial}}{||\underline{\underline{s}}^{trial}||} \tag{A.30}$$

$$\Delta\varepsilon^P_{eqv} = \Delta\gamma \frac{\underline{\underline{s}}^{trial}}{||\underline{\underline{s}}^{trial}||} \tag{A.31}$$

The material model has been implemented into an Abaqus/Explicit user material model (VUMAT).

A.2.2 Finite Element Model

The numerical simulations have been carried out in Abaqus/Explicit 6.8. It is a solver mostly used for transient dynamic problems, but can also be used for quasi-static problems if the kinetic energy compared to the potential energy is small. It is also the suggested solution method (as opposed to Abaqus/Standard) for problems with non-linear material behavior and contact. A drawback of the method is a stability limit on the maximum size of the time increments. An estimate of the stable time increment is:

$$\Delta t \approx \frac{L_{\min}}{\sqrt{\frac{\lambda+2\mu}{\rho}}} \tag{A.32}$$

Where $L_{\min}$ is the smallest side length of the element and $\sqrt{\frac{\lambda+2\mu}{\rho}}$ is the dilatational wave speed. For typical material values of epoxy (E=3 GPa, ν=0.35, ρ=1200 kg/m^3) and an element length under the tip of less then 0.1 μm, this results in a stable time increment of the order of 10^{-10} which is unacceptable. A possibility is to speed up the event time, reduce the modulus or increase the density in the FE model. Since the assumption was that the experiment is performed quasi statically, the latter can be performed without changing the physics of the entire process drastically. This consideration led to the use of the non-homogeneous mass scaling feature in ABAQUS. This scales the densities of the elements to match the numerical stability criterion.

If one wants to model the fibers and matrix individually, the maximum element size would have an upper limit, which is necessary to fully resolve the fiber shape. Together with the need to model a reasonable large sample to correctly represent the indented half space one would arrive at a large model with fine discretization away from the region of interest. Therefore the sample has been divided into two pieces. The area under the indenter is represented by fibers and matrix material individually. Further away, the concentric cylinder method has been used to create a orthotropic homogenized representation [4]. In that area large element sizes can obtained.

In the non-homogeneous area under the indenter the fibers were placed on a hexagonal grid to ensure a prescribed volume fraction. Then fibers under the indentor were removed. This is due to manufacturing imperfections and the indents will be made there in order for the indenter to avoid touching the fibers during indentation. Figure A.2 shows a typical scanning electron microscope (SEM) image. The projected area of a 1μm deep indent with a Berkovich indenter is shown. The ellipse with its half axes a and b and the fiber volume density are used to describe the geometry of the experiment.

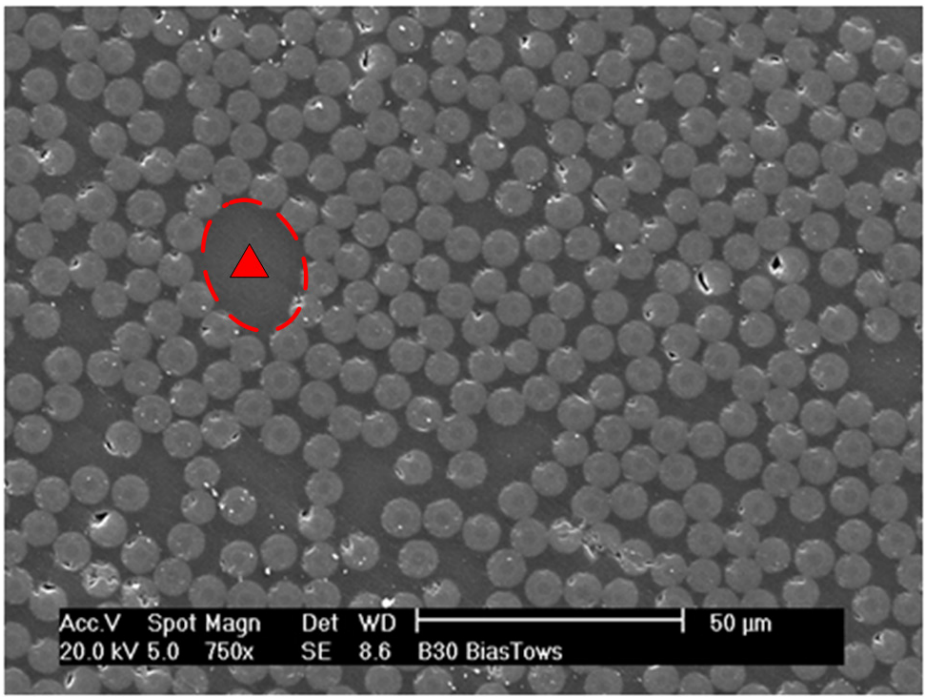

Figure A.2 SEM image of fiber tow, to scale: footprint of 1 μm deep indent with Berkovich indenter

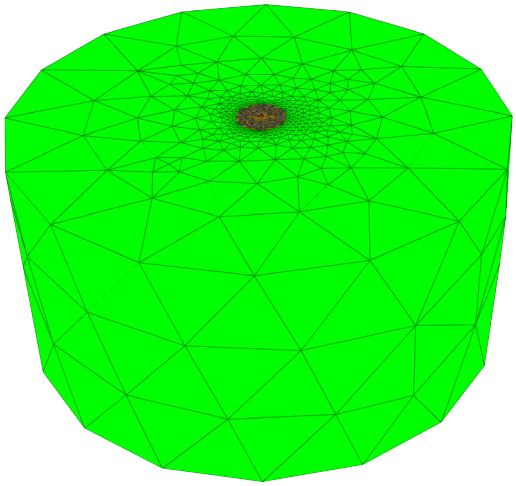

Figure A.3 Far away snapshot of the composite and indenter assembly

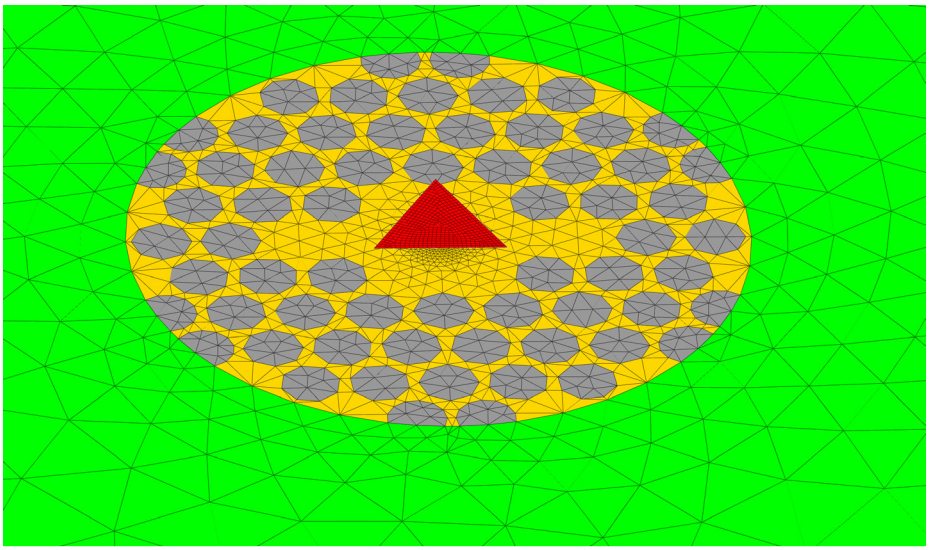

Figure A.4 Close up of the composite and assembly - green: homogenized material, yellow:matrix, grey: fiber, red: indenter

The FEM simulations consisted of a loading and holding step. In both cases the displacement of the indenter was prescribed which leads to more reliable solutions of the software compared to prescribing the reaction forces. While the loading step is believed to give better insight into the plastic properties, the holding part is supposed to provide more information about the viscoelastic material properties.

The elements used were linear tetrahedral, which were necessary to capture the geometry sufficiently. A parametric study has been preformed to ensure convergence with respect to element number as well as amount of mass scaling. The contact was modeled as hard/ kinematic contact with no friction.

A.2.3 Surrogate modeling

Since the computation of a load displacement curve for each guess of material properties takes on the order of hours, an optimization procedure involving possibly hundreds of function evaluations would take too long. Therefore it is desirable to create a function that can be evaluated quickly, but gives results that are comparable to the outcome of the FE simulation. This can be achieved through surrogate modeling [161]. Here a model of the model is created based on some training data. Even though there are initial computational costs involved in creating the meta model by evaluating the costly FE simulation, the increase in performance of the following surrogate based optimization, outweighs that.

Design of (Computer) Experiments (DOE)

An algorithm is needed to create the initial evaluation sites for the surrogate model. The easiest way is the so called full factorial sampling. Here one can specify at what points in each dimension the data should be taken, and then a design matrix containing all possible variations is created. The size of the design matrix increases exponentially with the dimensionality of the problem. Therefore this procedure can only be used for 3 or 4 input parameters. A commonly used solution lies in Latin Hypercube Sampling (LHS). Here each design variable is partitioned equally along its dimensions. The entries of the resulting vectors are randomly combined to give the design sites. A disadvantage of LHS is that design points might cluster together due to the random nature of the process by which they were created. To prevent this Optimal Latin Hyper Cube sampling [162] is used. This creates a more uniform spreading than LHS by optimizing a spreading criteria [161]. To generate the OLH grid, the Isight software package was used [163].

Kriging

The training data is provided at the N sites $\underline{\underline{x}} = [\underline{x}^{(1)}..\underline{x}^{(N)}]$ and it yields the results $\underline{y} = [y_1..y_N]$. Now one has to choose a model to predict the outcome $\hat{y}$ at the trial site $\underline{\hat{x}}$. The easiest way to do this are polynomial fits. While this is easy in one and two dimensions it gets very cumbersome tiresome for higher dimensional input data. A very successful scheme, that works for higher dimensions is Kriging [164–167]. An assumption of Kriging is that errors are correlated. This implies that the errors of two points close together are close. The assumption of uncorrelated error is in fact appropriate, if the sources of error are random, which is the case for actual experiments, but not for a deterministic computer code. The observation data is assumed to come from a function of the form

$$y(\underline{x}) = \mathscr{F}(\underline{\beta}, \underline{x}) + z(\underline{x}) \tag{A.33}$$

Where $\mathscr{F}$ is a regression model with regression parameters $\underline{\beta}$, and $z(\underline{x})$ is a stochastic process. Let us assume that the regression model is a linear combination of chosen functions

$$\mathscr{F}(\underline{\beta}, \underline{x}) = \beta_1 f_1(\underline{x}) + ... + \beta_P f_P(\underline{x}) = \underline{f}(\underline{x})^{\mathrm{T}} \underline{\beta} \tag{A.34}$$

The regression model can be thought of as describing the overall global behavior and the stochastic process describes the local variations. The stochastic process is assumed to

have zero mean and a covariance of

$$\mathrm{Cov}[z(\underline{x}^{(i)}), z(\underline{x}^{(j)})] = \sigma^2 \mathscr{R}(\underline{\theta}, \underline{x}^{(i)}, \underline{x}^{(j)}) \tag{A.35}$$

where σ^2 is the process variance, $\mathscr{R}$ is the correlation model and θ are some correlation parameters. To find the Kriging predictor define the matrix of the stochastic process correlations:

$$R_{ij} = \mathscr{R}(\underline{\theta}, \underline{x}^{(i)}, \underline{x}^{(j)}) \tag{A.36}$$

The vector of correlation between the design sites and the newly added site $\underline{\hat{x}}$ is

$$\underline{r}(\underline{\hat{x}}) = [\mathscr{R}(\underline{\theta}, \underline{x}^{(1)}, \underline{\hat{x}}), ..., \mathscr{R}(\underline{\theta}, \underline{x}^{(N)}, \underline{\hat{x}})]^{\mathrm{T}} \tag{A.37}$$

The Kriging prediction of the unknown output $\hat{y}$ with the inputs of interest $\underline{\hat{x}}$ is given by

$$\hat{y}(\underline{\hat{x}}) = \underline{f}^{\mathrm{T}} \underline{\beta}^* + \underline{r}\underline{\underline{R}}^{-1}(\underline{y} - \underline{\underline{F}}\underline{\beta}^*) \tag{A.38}$$

where the generalized least square estimate of $\underline{\beta}$ is

$$\underline{\beta} = (\underline{\underline{F}}^{\mathrm{T}} \underline{\underline{R}}^{-1} \underline{\underline{F}})^{-1} \underline{\underline{F}} \underline{\underline{R}}^{-1} \underline{y} \tag{A.39}$$

The variance of the stochastic process is

$$\sigma^2 = \frac{1}{N}(\underline{y} - \underline{\underline{F}}\underline{\beta}^*)^{\mathrm{T}} \underline{\underline{R}}^{-1}(\underline{y} - \underline{\underline{F}}\underline{\beta}^*) \tag{A.40}$$

The optimal choice of the regressions parameter $\underline{\theta}$ can be obtained from maximizing the likelihood

$$-\frac{1}{2}(N \ln \sigma^2 + \ln |\underline{\underline{R}}|)) \tag{A.41}$$

It turns out that in many cases the correlation term is so powerful, and the regression is of such low importance, so that it is set to be a constant. This model gives the stochastic process approach and can be recovered from the previous consideration by replacing the regression function with the mean estimate.

$$\underline{\mathscr{F}}(\beta, \underline{x}) = \hat{\mu} \tag{A.42}$$

This leads to

$$\underline{f}(\underline{x}) = 1 \tag{A.43}$$

$$\underline{\beta}^* = \hat{\mu} \tag{A.44}$$

$$\underline{\underline{F}}(\underline{x}) = \underline{1} \tag{A.45}$$

$$\hat{\mu} = \frac{\underline{1}^{\mathrm{T}}\underline{\underline{R}}^{-1}\underline{y}}{\underline{1}^{\mathrm{T}}\underline{\underline{R}}^{-1}\underline{1}} \tag{A.46}$$

$$\sigma^2 = \frac{1}{N}(\underline{y}-\underline{1}\hat{\mu})^{\mathrm{T}}\underline{\underline{R}}^{-1}(\underline{y}-\underline{1}\hat{\mu}) \tag{A.47}$$

These equations are identical to the ones given in [161, 166]. For the current study the DACE computer code has been used [164, 165]. Here Gaussians for the correlation term and second order regression functions yield the best results.

The upper and lower bounds to the OLH construction are given in table A.1 . Note that $E_0 < E_\infty$, $a > b$, $r = 1$ (linear hardening). Outside of these bounds the Kriging predictions cannot be used .

	E_0 [MPa]	E_∞ [MPa]	τ [s]	σ_Y [MPa]	H [MPa]	$\dot{d}$ [μm/s]	$d_{\max}$ [μm]	a [μm]	b [μm]	v_f
lower bound	1000	500	0	40	0	0.090	0.8	4.8	4.8	0.5
upper bound	15000	5000	1000	200	30000	0.011	1.2	35	35	0.78

Table A.1 Range of parameters to construct surrogate model of nanoindentation experiment

A.3 Experimental Setup

The composite of interest is 2D triaxially braided composite (2STBC). The fiber material is carbon and the matrix is EPON 862. The composite was manufactured in 8 mm thick plates and cut with a diamond saw. The pieces were then machine polished with an ABRAMIN machine by Strues with grid size 500 and 1000. It was then hand polished one a Buehler Ecomet 6 with 2400 grid sand paper and 1 μm and 0.05 μm Metadi Diamond Suspension. The nanoindentation experiments have been performed by a NanoInstruments Nanoindenter XP at Michigan Technical University, [168].

The experiment was divided into two steps; a loading and a holding step. It is believed, that this division helps signify the material properties. The loading part gives more information about the parameter involving plastic deformation (E_0,σ_Y,H), while the holding part reveals insight into the visco-elastic properties (E_0,E_∞,τ).

Due to the size of the indents and the tight packing of the fibers, indents have been made

in imperfections in between the fibers. A.2 shows and SEM image of a fiber tow region with the footprint of a 1 μm deep indent with a nanoindenter. Around the fiber is drawn an ellipse. The size of the ellipse axis' and the volume fraction serve as input parameters to the FE calculation later on to describe the geometric properties of the experiment. As one can see if the same indent is made in a region without any imperfection the indenter would touch the fiber and the resulting load displacement curve is largely influence by its properties. This is of course still true for the tightly confined matrix rich region, but less so. The remaining influence of the fiber is supposed to be divided out through the FEM calculations.

For this choice of indentation depth on can only obtain one measurement per region. If one was to set several indents next to each other the plastic deformations of the earlier ones would influence the result of the later ones. A suitable tool of decreasing indentation depth and increasing the resolution is using an atomic force microscope [169].

A.4 Evaluation of Surrogate Quality and Virtual Experiment

Before using the proposed procedure to extract actual material information from a composite it is important to check if the surrogate model actually reproduces the underlying FE procedure. A second question is what are the errors involved in the surrogate not being fully able to reproduce the FE model.

To answer the first question, the Kriging approximation has been set up using the majority trial sites evaluated though FE analysis. Fifteen calculation have been used to check the Kriging model.

A typical error measure is the root square mean error (RSME):

$$RSME = \sqrt{\sum_{i=1}^{N} \left(\frac{y^{(i)} - \hat{y}(i)}{y^{(i)}} \right)^2 \Big/ N} \tag{A.48}$$

The RSME has been equally divided between a loading and the holding part of the experiment and evaluated at ten points during each step. The results are shown in table A.2

The RSME of the surrogate of the trial sites lies between 0.9% and 7.3%, with an average of 2.9% where, as a rough quality estimate, a number of $<$10% is considered reasonable and $<$2% is considered very good by Forrester et al. [161].

A second question is how well does the Surrogate serve in recovering material properties. For that the FE results that were set aside previously are used to serve as experimental data. The curves were then matched using non-linear least squares curve fit capabilities of

No	E_0 [MPa]	E_∞ [MPa]	τ [s]	σ_Y [MPa]	H [MPa]	$\dot{d}$ [μm/s]	$d_{\max}$ [μm]	a [μm]	b [μm]	v_f	RSME %
1	2519	2259	871	93	25131	0.0107	0.82	23.8	17.1	0.70	1.5
2	6200	3161	794	53	23431	0.0090	0.87	28.4	23.8	0.60	0.9
3	12769	1846	245	66	13636	0.0108	1.20	27.6	17.9	0.65	4.8
4	11222	2369	259	127	26715	0.0099	0.85	17.7	6.6	0.77	3.0
5	10867	2373	323	106	8093	0.0109	0.82	22.6	14.7	0.50	1.8
6	9566	4494	243	130	5278	0.0094	1.15	34.2	12.1	0.64	1.3
7	4790	1956	66	69	22580	0.0098	0.84	15.3	6.3	0.65	7.3
8	7719	3491	766	81	9413	0.0104	0.86	33.7	29.2	0.76	1.2
9	3834	2217	795	151	25249	0.0106	0.89	21.7	5.5	0.67	2.1
10	4626	3695	865	96	1876	0.0099	0.10	26.0	15.3	0.52	2.0
11	4722	3196	191	178	12434	0.0095	0.81	34.5	20.4	0.62	3.4
12	4612	1217	609	86	3372	0.0093	0.92	25.6	16.8	0.50	5.3
13	5694	4410	755	147	22903	0.0110	1.00	30.1	28.0	0.73	1.9
14	1561	1313	502	167	17741	0.0105	0.10	11.4	5.5	0.57	3.5
15	4982	609	389	89	12873	0.0092	1.14	15.5	11.6	0.54	3.2

Table A.2 Trial sites to obtain predictive capabilities of surrogate model

MATLAB [62]. Table A.3 shows the RSME of the calculations

	E_0	E_∞	τ
RSME	9.4%	9.8%	26.0%

Table A.3 Errors for backing out material properties that served as input to FE simulations

As one can see the suggested procedure does a reasonable job on predicting the elastic properties with an error of 9.4% for the short term modulus and 9.8% for the long term modulus. The properties governing the yield behavior have a larger error associated with them and conclusions regarding the yield behavior should be made with caution. This is a problem that has already been seen in other studies [151, 170]. One solution for that obstacle lies in using multiple indenter tips which drastically enhances the quality of the predictions. Unfortunately that is only an option for homogeneous material or thin films. Another solution might be the use of an indenter tip, or a different sequence of loading or holding cycles which causes the yield strength to have a greater outcome on the experiment.

A.5 Experimental results

The results of the inverse procedure to extract material data is shown in table A.4. Compared with manufacturer data, [64], the short term modulus is drastically over predicted. However

	E_0 [GPa]	E_∞ [GPa]	τ [s]	σ_Y [MPa]	H [MPa]
Bulk material	5.7±1.1	2.4±0.6	140	73±11	7.7±3.2
Composite tow	6.3±1.7	2.6±0.9	310	68±14	5.9±2.6

Table A.4 Values and standard deviation of inversely extracted bulk epoxy material and of matrix material properties inside fiber tow

it is comparable to other experimental data. Song, [3] determined a value of 9 GPa of the "in-situ" elastic modulus through inverse modeling of the braided RUC. Aldridge, [58], determined the short term modulus to be 4.95 GPa through light scattering. The short term modulus of the epoxy material inside the fiber tow is slightly higher than the same value in the bulk material.

It is interesting to note, that the relaxation time in the bulk epoxy material is only about half of the one found inside the composite tow. This might be explained by the built up of stresses inside the epoxy tow during cure. These stresses cause creep of the matrix material inside the fiber tow before the nanoindentation experiments are performed.

The yield stress value predicted by method is comparable to the manufacturing data. The yield stress and linear hardening modulus of the matrix material inside the tow are lower compared to the corresponding values of bulk epoxy. This suggest that the matrix material yield earlier and hardens less. However, the large standard deviation and the reduced capabilities of the surrogate modeling when applied to yield properties should be kept in mind, when considering the implications of these numbers.

Except the drastic increase in relaxation time, the material properties of bulk epoxy and material inside the fiber tows are not significantly different. This could be attributed to the fact, that material properties were measured inside matrix pockets inside the tow, To get data that is truly between two fibers an instrument with a higher resolution is needed, such as an atomic force microscope, [169].

A.6 Concluding remarks

A procedure has been introduced that enables nanoindentation to be used to measure viscoelastic properties of matrix material in a composite. A material model was introduced capable of capturing basic viscoelastic-plastic properties but low enough in parameters to be used in a parametric study. Kriging was introduced to predict the outcome of the simulations of the experiment and to enable a fast curve fitting between experimental and numerical data. The predictive error of the surrogate with respect to the underlying FE simulation was 2.9 %

for the selected trial sites. A increases in predictive quality can be achieved by adding more training data. The short term modulus was recovered with an error of 9.4 % and the long term modulus with an error of 9.8%. Experimental data was obtained for bulk epoxy and for epoxy inside a woven composite tow. The measured data is similar for the two cases. A notable difference is the increase in stress relaxation time of epoxy inside the tow, pointing to already existing stresses inside the composite and already progressed relaxation.

Appendix B

Finite difference discretization of equations governing radial heat conduction and cure

Because it is not possible to solve the heat and curing equation for arbitrary geometries in closed form it is necessary to solve the equations numerically. The system of interest is an infinitely long cylinder with prescribed initial and boundary temperature. The resembles the laboratory set-up of a glass tube filled with curing epoxy.

The governing equation of heat conduction in cylindrical coordinates assuming constant conductivity and no angular dependence can be found from equation 2.9 as,

$$\rho c \frac{\partial T}{\partial t} = K\left(\frac{1}{r}\frac{\partial T}{\partial r} + \frac{\partial^2 T}{\partial r^2}\right) + \rho H_r \frac{\partial \phi}{\partial t}. \tag{B.1}$$

A Taylor series expansion for forward and backward finite difference yields

$$T(r+\Delta r_+) = T(r) + \frac{(\Delta r_+)}{2!}\frac{\partial T}{\partial r} + \frac{(\Delta r_+^2)}{3!}\frac{\partial^2 T}{\partial r^3} + \mathscr{O}(\Delta r^2) \tag{B.2}$$

$$T(r-\Delta r_-) = T(r) - \frac{(\Delta r_-)}{2!}\frac{\partial T}{\partial r} + \frac{(\Delta r_-^2)}{3!}\frac{\partial^2 T}{\partial r^3} + \mathscr{O}(\Delta r^2) \tag{B.3}$$

Considering i the point of interest and replacing $T(r+\Delta r_+) = T_{i+1}$ and $T(r-\Delta r_-) = T_{i-1}$ accordingly yields,

$$\left.\frac{\partial^2 T}{\partial r^2}\right|_i = T_{i+1}\left(\frac{2}{(\Delta r_+ + \Delta r_-)(\Delta r_+)}\right) - T_i\left(\frac{2}{\Delta r_+ \Delta r_-}\right) + T_{i-1}\left(\frac{2}{(\Delta r + + \Delta r_-)(\Delta r_-)}\right) + \mathscr{O}(\Delta r^2) \tag{B.4}$$

Where

$$\Delta r_- = r_i - r_{i-1} \tag{B.5}$$

$$\Delta r_+ = r_{i+1} - r_i \tag{B.6}$$

In the same fashion one obtains for the first derivative using central differences

$$\frac{\partial T}{\partial r} = \frac{T_{i+1} - T_{i-1}}{\Delta r_+ + \Delta r_-} + \mathscr{O}(\Delta r^2) \tag{B.7}$$

The time is approximated by a backward difference scheme. This way unconditional stability of the algorithm is guaranteed.

$$T(r,t+\Delta T) = T(r,t) + \frac{\Delta t}{2!}\frac{\partial T}{\partial t} + \mathscr{O}(\Delta t) \tag{B.8}$$

or

$$T_i^{l+1} = T_i^l + \frac{\Delta t}{2}\frac{\partial T}{\partial t} \tag{B.9}$$

This yields the implicit finite difference scheme, that has to be solved for every new time step $l+1$

$$\begin{pmatrix} B_1 & B_2 & \cdots & & 0 \\ \vdots & \ddots & & & \\ & C_{i-1} & C_i & C_{i+1} & \vdots \\ & & & \ddots & \\ 0 & & & 0 & B_N \end{pmatrix} \cdot \begin{bmatrix} T_1^{l+1} \\ \vdots \\ T_{i-1}^{l+1} \\ T_i^{l+1} \\ T_{i+1}^{l+1} \\ \vdots \\ T_N^{l+1} \end{bmatrix} = \begin{bmatrix} f_1^{l+1} \\ \vdots \\ f_{i-1}^l \\ f_i^l \\ f_{i+1}^l \\ \vdots \\ f_N^{l+1} \end{bmatrix} \tag{B.10}$$

where

$$C_{i-1} = \frac{\Delta t\,\kappa}{(\Delta r_+ + \Delta r_-) r_i} + \frac{-2\Delta t\,\kappa}{(\Delta r_+ + \Delta r_-)\Delta r_-} \tag{B.11}$$

$$C_i = \frac{2\Delta t\,\kappa}{\Delta r_+ \Delta r_-} + 1 \tag{B.12}$$

$$C_{i+1} = \frac{-\Delta t\,\kappa}{(\Delta r_+ + \Delta r_-) r_i} + \frac{-2\Delta t\,\kappa}{(\Delta r_+ + \Delta r_-)\Delta r_+} \tag{B.13}$$

$$f_i^l = \Delta t \frac{H_r}{c}\frac{\partial \phi}{\partial t}\bigg|_i^l + T_i^l \tag{B.14}$$

The evolution of degree of cure is found by

$$\phi_i^{l+1} = \phi_i^l + \Delta t \left[\left(k_1 \left(T_i^l + \frac{\Delta t}{2} \Delta T_i^l \right) + k_2 \left(T_i^l + \frac{\Delta t}{2} \Delta T_i^l \right) \left(\phi_i^l \right)^m \right) \left(1 - \phi_i^l \right)^n \right] \tag{B.15}$$

The rate of cure is approximated by

$$\left. \frac{\partial \phi}{\partial t} \right|_i^l = \left[\left(k_1 \left(T_i^l + \frac{\Delta t}{2} \Delta T_i^l \right) + k_2 \left(T_i^l + \frac{\Delta t}{2} \Delta T_i^l \right) \left(\phi_i^l \right)^m \right) \left(1 - \phi_i^l \right)^n \right] \tag{B.16}$$

The boundary conditions are symmetry of the temperature with respect to the center line, or no heat flow in the middle (both for a solid cylinder) and the temperature is fixed on the outer boundary:

$$K \left. \frac{\partial T}{\partial r} \right|_{r=0} = 0 \tag{B.17}$$

$$T|_{r=R_o} = T_0 \tag{B.18}$$

therefore

$$B_1 = -B_2 = 1 \tag{B.19}$$

$$B_N = 1 \tag{B.20}$$

$$f_1^l = 0 \tag{B.21}$$

$$f_N^l = T_0^l \tag{B.22}$$

$$\tag{B.23}$$

Appendix C
Consistent units

A common mistake is to neglect consistent units. Computer codes such as ABAQUS do not poss any knowledge of the units used to describe the problem that is being solved. They only require that a unit system is chosen, that is consistent. When working with RUCs that are only millimeters or potentially micrometers in size the units have to be altered accordingly. Ideally numerical values used to describe the geometry and material properties are of the order of $10^{-3} - 10^{3}$ to make best use of the machine precision offered by the computer and to reduce rounding errors. A suitable unit system used in this thesis is:

- Mass (M) in grams
- Length (L) in millimeters
- Time (T) in seconds
- Temperature (θ) in Kelvin

All other units can be calculated accordingly. They are given in table C.1, where in the definition column 'F' and 'J' represent the force and energy.

Quantity	Definition	SI unit	Consistent unit	Conversion (SI x ? =CU)
Force	ML/T^2	$N=kgm/s^2$	$\mu N=gmm/s^2$	10^6
Stress	F/L^2	N/m^2	N/m^2	10^0
Density	M/L^3	kg/m^3	g/mm^3	10^{-6}
Energy	FL	J	nJ	10^9
Specific heat	$J/M/\theta$	J/kg/K	mJ/kg/K	10^6
Flux	$J/T/L^3$	$J/s/m^3$	$J/s/m^3$	10^0
Conductivity	$J/T/L/\theta$	W/m/K	mW/m/K	10^6

Table C.1 Consistent units for the curing studies

Appendix D

Testing of user subroutines

D.1 Heat generation

The correct implementation of the curing model has been tested for the perfect conductor and perfect insulator as shown in figures D.1 and D.2.

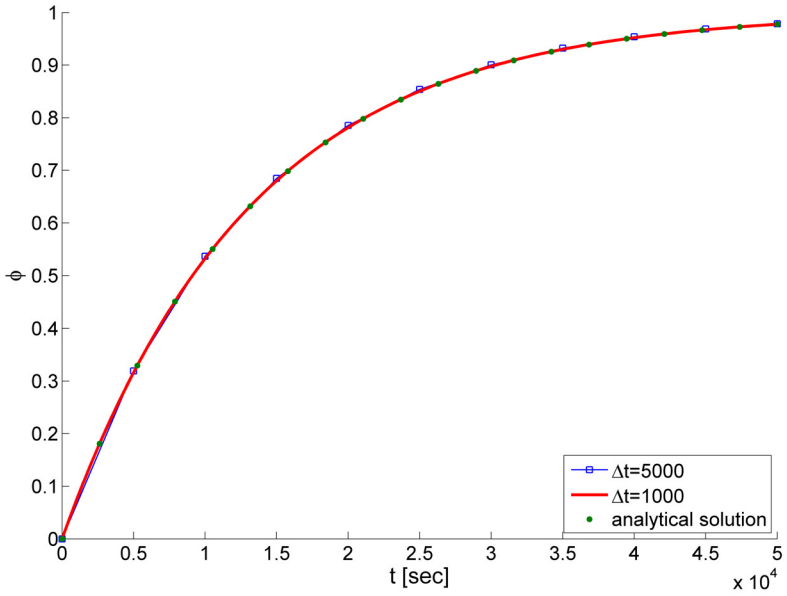

Figure D.1 Comparing the FE solution of the perfect conductor to the closed form solution

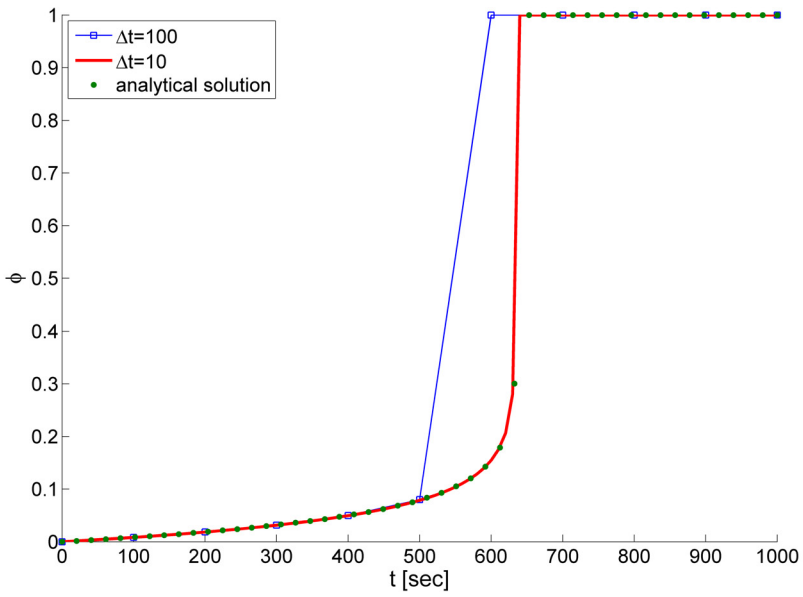

Figure D.2 Comparing the FE solution of the perfect insulator to the closed form solution

D.2 Curing without damage

To ensure that the per-network moduli are applied the epoxy is cured in a plain strain condition. At different stages a step strain is applied. The response of the curing epoxy to such an input is equivalent to the response of a linear elastic isotropic body that has material properties to the ones of the sum of all networks. Therefore the material properties as measured by RLS and BLS should be recovered:

$$\Delta\varepsilon_{11} \neq 0, \text{ all other strains} = 0 \tag{D.1}$$

$$\Delta\sigma_{11} = M\Delta\varepsilon_{11} = (K + \frac{4}{3}\mu)\Delta\varepsilon_{11} \tag{D.2}$$

$$\Delta\sigma_{22} = (K - \frac{2}{3}\mu)\Delta\varepsilon_{11} \tag{D.3}$$

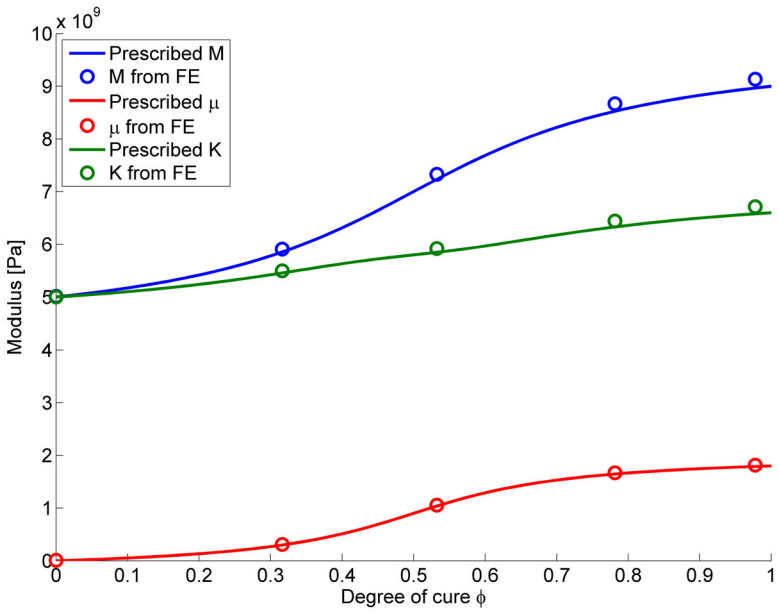

Figure D.3 Comparing the measure moduli from the FE model to the desired total network properties

$$M = \frac{\Delta\sigma_{11}}{\Delta\varepsilon_{11}} \tag{D.4}$$

$$\mu = \frac{\Delta\sigma_{11} - \Delta\sigma_{22}}{2\Delta\varepsilon_{11}} \tag{D.5}$$

$$K = \frac{\Delta\sigma_{11} + 2\Delta\sigma_{22}}{3\Delta\varepsilon_{11}} \tag{D.6}$$

The cure shrinkage is prescribed to be linear. For that the epoxy was allowed to cure in a plain strain field, where the stress in the non-zero strain direction is zero.

Finally a non-trivial strain and temperature history has been prescribed. The solution cannot be obtained in a closed form, but due to the uniaxial strain nature of the problem, a solution can be found using Matlab's ODE45 solver and numerical integration.It should be noted, that the solutions converge towards each other for smaller time steps.

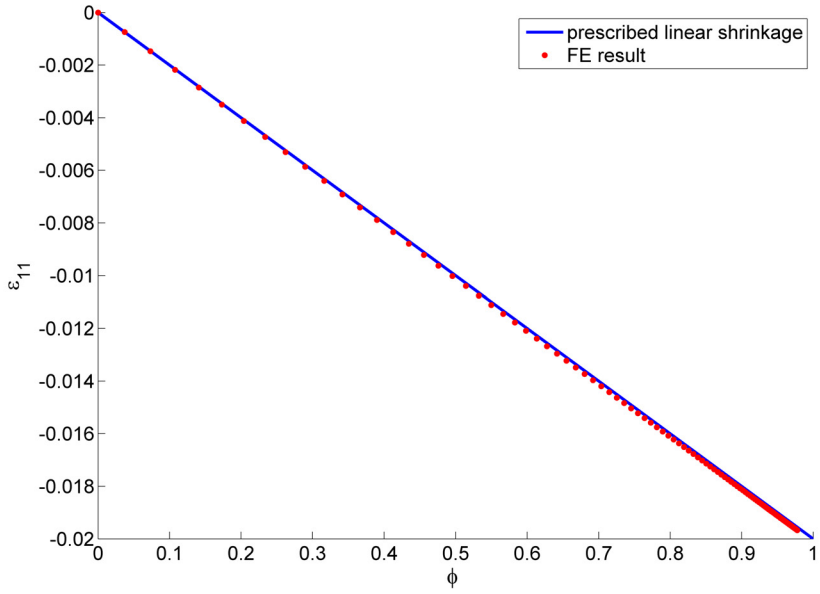

Figure D.4 Comparing the measured cure shrinkage to the desired cure shrinkage

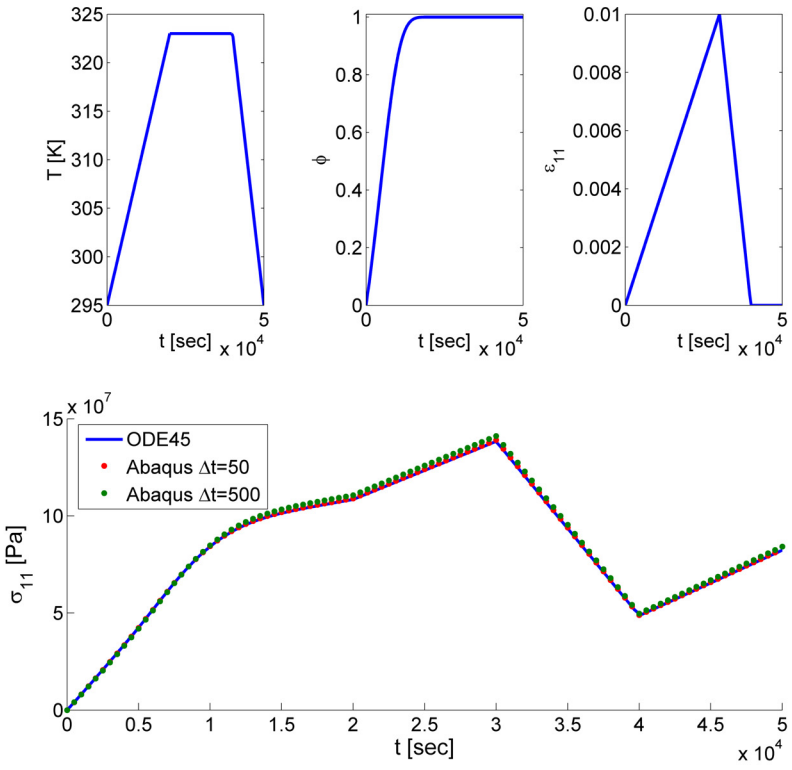

Figure D.5 Comparing the stress obtained from ABAQUS with a second solution from Matlab

Appendix E

Finite element implementation of cure with damage

Most finite element textbooks, [171] [135, 172], describe the derivation of higher order tetrahedral elements in a very broad manner. Therefore the important pieces are repeated here for completeness. Tetrahedral elements are used, as these allow for very general geometries. A quadratic interpolation scheme will be used for the displacements, as it has been noted, that linear tetrahedrons can show too stiff behavior, [135]. Because the nonlocal field is related to the strain and therefore the derivative of the displacement, it will be interpolated linearly . The node numbering scheme is related to the one used in ABAQUS, which will allow to use that program for pre- and post-processing. However, the node numbering shown in figure E.1(a) only allows for displacement interpolation, but not for interpolation of the nonlocal field. To calculate the history of the nonlocal field variable, 12 representative "time points" or networks are chosen. Each node has three degrees of freedom associated with it, therefore 4 additional nodes are required. To efficiently construct the augmented elements from a given ABAQUS mesh all node numbers were multiplied by ten. Then, after each of the first four nodes, four additional nodes were inserted. Therefore all nodes containing information about the displacement end in "0". All nodes with nonlocal field history information end in "1"-"4" in the ABAQUS input file. This is shown in figure E.1(b) The element is formulated in an isoparametric fashion.
The interpolation of the displacement field is given by

$$\underline{u} = N_u \underline{U}, \tag{E.1}$$

where $\underline{U}$ are all the nodal displacement degrees of freedom

$$\underline{U} = [U_1^{(1)}, U_2^{(1)}, U_3^{(1)}, \ldots, U_3^{(10)}]^{\mathrm{T}} \tag{E.2}$$

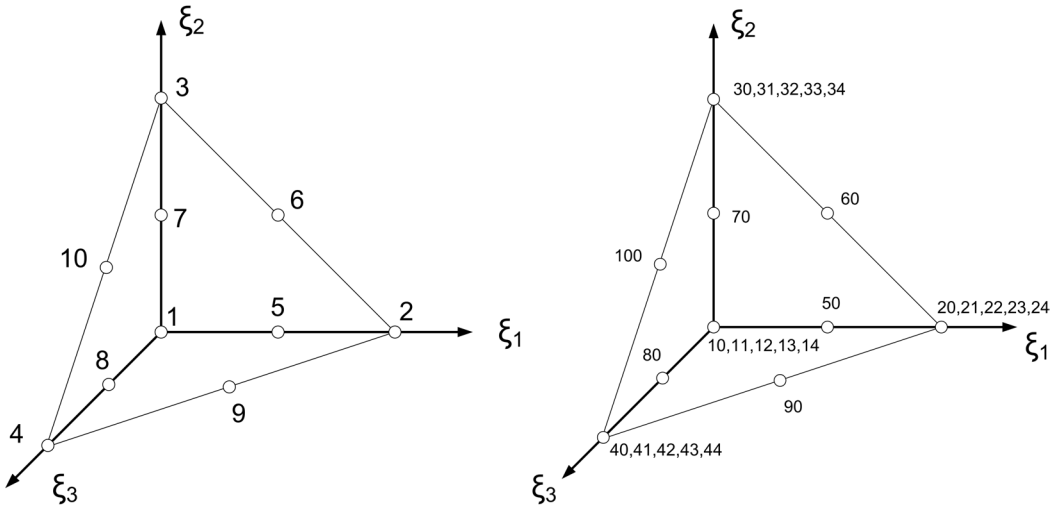

(a) Node numbering scheme of standard quadratic tetrahedron

(b) Node numbering scheme of augmented tetrahedron

Figure E.1 Node numbering scheme of tetrahedron

and N_u is the matrix of interpolation functions

$$N_u = \begin{bmatrix} N_u^{(1)} & 0 & 0 & N_u^{(2)} & 0 & & 0 \\ 0 & N_u^{(1)} & 0 & 0 & N_u^{(2)} & \cdots & 0 \\ 0 & 0 & N_u^{(1)} & 0 & 0 & & N_u^{(10)} \end{bmatrix} \tag{E.3}$$

To formulate the shape functions, consider the following intermediate variables,

$$\zeta_1 = 1 - \xi_1 - \xi_2 - \xi_3 \tag{E.4}$$

$$\zeta_2 = \xi_1 \tag{E.5}$$

$$\zeta_3 = \xi_2 \tag{E.6}$$

$$\zeta_4 = \xi_3 \tag{E.7}$$

The shape functions of the displacements are given as,

$$
\begin{aligned}
N_u^{(1)} &= \zeta_1(2\zeta_1 - 1) && \text{(E.8)}\\
N_u^{(2)} &= \zeta_2(2\zeta_2 - 1) && \text{(E.9)}\\
N_u^{(3)} &= \zeta_3(2\zeta_3 - 1) && \text{(E.10)}\\
N_u^{(4)} &= \zeta_4(2\zeta_4 - 1) && \text{(E.11)}\\
N_u^{(5)} &= 4\zeta_1\zeta_2 && \text{(E.12)}\\
N_u^{(6)} &= 4\zeta_2\zeta_3 && \text{(E.13)}\\
N_u^{(7)} &= 4\zeta_3\zeta_1 && \text{(E.14)}\\
N_u^{(8)} &= 4\zeta_1\zeta_4 && \text{(E.15)}\\
N_u^{(9)} &= 4\zeta_2\zeta_4 && \text{(E.16)}\\
N_u^{(10)} &= 4\zeta_3\zeta_4 && \text{(E.17)}
\end{aligned}
$$

The derivatives of the shape function in the isoparametric domain are found to be,

$$
\left[\frac{\partial \underline{N}_u}{\partial \underline{\xi}}\right] = \begin{bmatrix}
-3+4(\xi_1+\xi_2+\xi_3) & -3+4(\xi_1+\xi_2+\xi_3) & -3+4(\xi_1+\xi_2+\xi_3)\\
4\xi_1-1 & 0 & 0\\
0 & 4\xi_2-1 & 0\\
0 & 0 & 4\xi_3-1\\
4(1-2\xi_1-\xi_2-\xi_3) & -4\xi_1 & -4\xi_1\\
4\xi_2 & 4\xi_1 & 0\\
-4\xi_2 & 4(1-\xi_1-2\xi_2-\xi_3) & -4\xi_2\\
-4\xi_3 & -4\xi 3 & 4(1-\xi_1-\xi_2-2\xi_3)\\
4\xi_3 & 0 & 4\xi_1\\
0 & 4\xi_3 & 4\xi_2
\end{bmatrix}^{\mathrm{T}} \qquad \text{(E.18)}
$$

The Jacobian is given by,

$$
J_{u,ij} = \frac{\partial N_u^{(j)}}{\partial \xi_i} \cdot x_{u,j}|_{\text{at node } i} \qquad \text{(E.19)}
$$

or in matrix form

$$
[J_u] = \left[\frac{\partial \underline{N}_u}{\partial \underline{\xi}}\right] \cdot [x_u] \qquad \text{(E.20)}
$$

where $x_{u,ji}$ is the jth coordinate component of the ith node. Now the derivative of the shape

functions in the physical domain are given by,

$$\left[\frac{\partial \underline{N}_u}{\partial \underline{x}_u}\right] = [J_u]^{-1}\left[\frac{\partial \underline{N}_u}{\partial \underline{\xi}}\right] \tag{E.21}$$

The interpolation of the strains in the physical domain can be found through the linear operator L defined in chapter 5

$$\underline{\varepsilon} = B\underline{U} \tag{E.22}$$

$$\tag{E.23}$$

where,

$$B_u = L\underline{N}_u \tag{E.24}$$

This leads to

$$
B_u^{\mathrm{T}} = \begin{bmatrix}
\partial N_u^{(1)}/\partial x_{u,1} & 0 & 0 & \partial N_u^{(1)}/\partial x_{u,2} & \partial N_u^{(1)}/\partial x_{u,3} & 0 \\
0 & \partial N_u^{(1)}/\partial x_{u,2} & 0 & \partial N_u^{(1)}/\partial x_{u,1} & 0 & \partial N_u^{(1)}/\partial x_{u,3} \\
0 & 0 & \partial N_u^{(1)}/\partial x_{u,3} & 0 & \partial N_u^{(1)}/\partial x_{u,1} & \partial N_u^{(1)}/\partial x_{u,2} \\
\partial N_u^{(2)}/\partial x_{u,1} & 0 & 0 & \partial N_u^{(2)}/\partial x_{u,2} & \partial N_u^{(2)}/\partial x_{u,3} & 0 \\
0 & \partial N_u^{(2)}/\partial x_{u,2} & 0 & \partial N_u^{(2)}/\partial x_{u,1} & 0 & \partial N_u^{(2)}/\partial x_{u,3} \\
0 & 0 & \partial N_u^{(2)}/\partial x_{u,3} & 0 & \partial N_u^{(2)}/\partial x_{u,1} & \partial N_u^{(2)}/\partial x_{u,2} \\
\partial N_u^{(3)}/\partial x_{u,1} & 0 & 0 & \partial N_u^{(3)}/\partial x_{u,2} & \partial N_u^{(3)}/\partial x_{u,3} & 0 \\
0 & \partial N_u^{(3)}/\partial x_{u,2} & 0 & \partial N_u^{(3)}/\partial x_{u,1} & 0 & \partial N_u^{(3)}/\partial x_{u,3} \\
0 & 0 & \partial N_u^{(3)}/\partial x_{u,3} & 0 & \partial N_u^{(3)}/\partial x_{u,1} & \partial N_u^{(3)}/\partial x_{u,2} \\
\partial N_u^{(4)}/\partial x_{u,1} & 0 & 0 & \partial N_u^{(4)}/\partial x_{u,2} & \partial N_u^{(4)}/\partial x_{u,3} & 0 \\
0 & \partial N_u^{(4)}/\partial x_{u,2} & 0 & \partial N_u^{(4)}/\partial x_{u,1} & 0 & \partial N_u^{(4)}/\partial x_{u,3} \\
0 & 0 & \partial N_u^{(4)}/\partial x_{u,3} & 0 & \partial N_u^{(4)}/\partial x_{u,1} & \partial N_u^{(4)}/\partial x_{u,2} \\
\partial N_u^{(5)}/\partial x_{u,1} & 0 & 0 & \partial N_u^{(5)}/\partial x_{u,2} & \partial N_u^{(5)}/\partial x_{u,3} & 0 \\
0 & \partial N_u^{(5)}/\partial x_{u,2} & 0 & \partial N_u^{(5)}/\partial x_{u,1} & 0 & \partial N_u^{(5)}/\partial x_{u,3} \\
0 & 0 & \partial N_u^{(5)}/\partial x_{u,3} & 0 & \partial N_u^{(5)}/\partial x_{u,1} & \partial N_u^{(5)}/\partial x_{u,2} \\
\partial N_u^{(6)}/\partial x_{u,1} & 0 & 0 & \partial N_u^{(6)}/\partial x_{u,2} & \partial N_u^{(6)}/\partial x_{u,3} & 0 \\
0 & \partial N_u^{(6)}/\partial x_{u,2} & 0 & \partial N_u^{(6)}/\partial x_{u,1} & 0 & \partial N_u^{(6)}/\partial x_{u,3} \\
0 & 0 & \partial N_u^{(6)}/\partial x_{u,3} & 0 & \partial N_u^{(6)}/\partial x_{u,1} & \partial N_u^{(6)}/\partial x_{u,2} \\
\partial N_u^{(7)}/\partial x_{u,1} & 0 & 0 & \partial N_u^{(7)}/\partial x_{u,2} & \partial N_u^{(7)}/\partial x_{u,3} & 0 \\
0 & \partial N_u^{(7)}/\partial x_{u,2} & 0 & \partial N_u^{(7)}/\partial x_{u,1} & 0 & \partial N_u^{(7)}/\partial x_{u,3} \\
0 & 0 & \partial N_u^{(7)}/\partial x_{u,3} & 0 & \partial N_u^{(7)}/\partial x_{u,1} & \partial N_u^{(7)}/\partial x_{u,2} \\
\partial N_u^{(8)}/\partial x_{u,1} & 0 & 0 & \partial N_u^{(8)}/\partial x_{u,2} & \partial N_u^{(8)}/\partial x_{u,3} & 0 \\
0 & \partial N_u^{(8)}/\partial x_{u,2} & 0 & \partial N_u^{(8)}/\partial x_{u,1} & 0 & \partial N_u^{(8)}/\partial x_{u,3} \\
0 & 0 & \partial N_u^{(8)}/\partial x_{u,3} & 0 & \partial N_u^{(8)}/\partial x_{u,1} & \partial N_u^{(8)}/\partial x_{u,2} \\
\partial N_u^{(9)}/\partial x_{u,1} & 0 & 0 & \partial N_u^{(9)}/\partial x_{u,2} & \partial N_u^{(9)}/\partial x_{u,3} & 0 \\
0 & \partial N_u^{(9)}/\partial x_{u,2} & 0 & \partial N_u^{(9)}/\partial x_{u,1} & 0 & \partial N_u^{(9)}/\partial x_{u,3} \\
0 & 0 & \partial N_u^{(9)}/\partial x_{u,3} & 0 & \partial N_u^{(9)}/\partial x_{u,1} & \partial N_u^{(9)}/\partial x_{u,2} \\
\partial N_u^{(10)}/\partial x_{u,1} & 0 & 0 & \partial N_u^{(10)}/\partial x_{u,2} & \partial N_u^{(10)}/\partial x_{u,3} & 0 \\
0 & \partial N_u^{(10)}/\partial x_{u,2} & 0 & \partial N_u^{(10)}/\partial x_{u,1} & 0 & \partial N_u^{(10)}/\partial x_{u,3} \\
0 & 0 & \partial N_u^{(10)}/\partial x_{u,3} & 0 & \partial N_u^{(10)}/\partial x_{u,1} & \partial N_u^{(10)}/\partial x_{u,2}
\end{bmatrix} \tag{E.25}
$$

In a similar fashion, the nonlocal field is interpolated by

$$\overline{\eta} = \underline{N_{\overline{\eta}}}\,\underline{\overline{\eta}} \tag{E.26}$$

Where $\underline{\overline{\eta}}$ are the nodal values of the nonlocal field in the kth network,

$$\underline{\overline{\eta}} = [\overline{\eta}^{(1)}(t_k), \overline{\eta}^{(2)}(t_k), \overline{\eta}^{(3)}(t_k), \overline{\eta}^{(4)}(t_k)]^{\mathrm{T}} \tag{E.27}$$

$\underline{N_{\overline{\eta}}}$ is the vector or interpolation functions,

$$\underline{N_{\overline{\eta}}} = [N_{\overline{\eta}}^{(1)}, N_{\overline{\eta}}^{(2)}, N_{\overline{\eta}}^{(3)}, N_{\overline{\eta}}^{(4)}] \tag{E.28}$$

with,

$$N_{\overline{\eta}}^{(1)} = \zeta_1(2\zeta_1 - 1) \tag{E.29}$$
$$N_{\overline{\eta}}^{(2)} = \zeta_2(2\zeta_2 - 1) \tag{E.30}$$
$$N_{\overline{\eta}}^{(3)} = \zeta_3(2\zeta_3 - 1) \tag{E.31}$$
$$N_{\overline{\eta}}^{(4)} = \zeta_4(2\zeta_4 - 1) \tag{E.32}$$

The Jacobian is,

$$J_{\overline{\eta},ij} = \frac{\partial N_{\overline{\eta}}^{(j)}}{\partial \xi_i} \cdot x_{\overline{\eta},j}\big|_{\text{at node } i} \tag{E.33}$$

with

$$\left[\frac{\partial \underline{N_{\overline{\eta}}}}{\partial \underline{\xi}}\right] = \left[\frac{\partial N_{\overline{\eta}}^{(j)}}{\partial \xi_i}\right] = \begin{bmatrix} -1 & 1 & 0 & 0 \\ -1 & 0 & 1 & 0 \\ -1 & 0 & 0 & 1 \end{bmatrix} \tag{E.34}$$

The matrix of the derivative of the nonlocal shape function is given by,

$$\left[B_{\overline{\eta}}\right] = \left[\frac{\partial N_{\overline{\eta}}^{(i)}}{\partial x_j}\right] = \left[J_{\overline{\eta}}\right]^{-1} \left[\frac{\partial \underline{N_{\overline{\eta}}}}{\partial \underline{\xi}}\right] \tag{E.35}$$

To evaluate any of the volume integrals, a change in variables has to be performed to describe the integration in isoparametric coordinates.

$$\int_V F(\underline{x})\mathrm{d}V = \int_V F(\underline{\xi})\,\det J \mathrm{d}V \tag{E.36}$$

The integration over the element volume in the isoparametric domain is done by Gaussian

Quadrature. The same integration scheme was chosen for the displacement field and the nonlocal field. For a quadratic function four integration points are necessary, [135]. They are located at

$$\underline{\xi}^1 = [\alpha,\beta,\beta]^{\mathrm{T}} \tag{E.37}$$
$$\underline{\xi}^2 = [\beta,\alpha,\beta]^{\mathrm{T}} \tag{E.38}$$
$$\underline{\xi}^3 = [\beta,\beta,\alpha]^{\mathrm{T}} \tag{E.39}$$
$$\underline{\xi}^4 = [\beta,\beta,\beta]^{\mathrm{T}} \tag{E.40}$$
$$\tag{E.41}$$

where,

$$\alpha = \frac{5+3\sqrt{(5)}}{20} \tag{E.42}$$
$$\beta = \frac{5-\sqrt{(5)}}{20} \tag{E.43}$$

The weights at the integration points are all identical,

$$w^i = 0.25 \tag{E.44}$$

The volume integral of the tetrahedron can now be evaluated numerically,

$$\int_V F(\underline{x})\mathrm{d}V \approx \sum_{i=1}^{4} \frac{\det J}{6} F(\underline{\xi}^i) w^i \tag{E.45}$$

Bibliography

[1] E. A. de Souza Neto, D. Perić, and D. R. J. Owen. *Computational Methods for Plasticity: Theory and Applications*. John Wiley & Sons, Ltd, 2008.

[2] Jean Lemaitre and Rodrigue Desmorat. *Engineering Damage Mechanics: Ductile, Creep, Fatigue and Brittle Failures*. Springer-Verlag, 2005.

[3] Shunjun Song. *Compression Response of Tri-axially Braided Textile Composites*. PhD thesis, University of Michigan, Ann Arbor, 2007.

[4] Carl T. Herakovich. *Mechnics of Fibrous Composites*. Wiley, 1997.

[5] Shunjun Song, Anthony M. Waas, Khaled W. Shahwan, Xinran Xiao, and Omar Faruque. Braided textile composites under compressive loads: Modeling the response, strength and degradation. *Composites Science and Technology*, 67(15-16):3059 – 3070, 2007.

[6] Shunjun Song, Anthony M. Waas, Khaled W. Shahwan, Omar Faruque, and Xinran Xiao. Compression Response of 2D Braided Textile Composites: Single Cell and Multiple Cell Micromechanics Based Strength Predictions. *Journal of Composite Materials*, 42(23):2461–2482, 2008.

[7] Shunjun Song, Anthony M. Waas, Khaled W. Shahwan, Omar Faruque, and Xinran (Sharon) Xiao. Compression response, strength and post-peak response of an axial fiber reinforced tow. *International Journal of Mechanical Sciences*, 51(7):491 – 499, 2009.

[8] Shunjun Song, Anthony M. Waas, Khaled W. Shahwan, Omar Faruque, and Xinran Xiao. Effects of Matrix Microcracking on the Response of 2D Braided Textile Composites Subjected to Compression Loads. *Journal of Composite Materials*, 44(2):221–240, 2010.

[9] Chou Tsu-Wei Ishikawa, Takashi. One-dimensional micromechanical analysis of woven fabric composites. *AIAA journal*, 21(12):1714–1721, 1983. cited By (since 1996) 142.

[10] N.K. Naik and P.S. Shembekar. Elastic Behavior of Woven Fabric Composites: Lamina Analysis. *Journal of Composite Materials*, 26(15):2196–2225, 1992.

[11] Bhavani V. Sankar and Ramesh V. Marrey. A unit-cell model of textile composite beams for predicting stiffness properties. *Composites Science and Technology*, 49(1):61 – 69, 1993.

[12] N.K. Naik and V.K. Ganesh. Prediction of on-axes elastic properties of plain weave fabric composites. *Composites Science and Technology*, 45(2):135 – 152, 1992.

[13] Y. C. Zhang and J. Harding. A numerical micromechanics analysis of the mechanical properties of a plain weave composite. *Computers & Structures*, 36(5):839 – 844, 1990.

[14] Ryan L. Karkkainen and Bhavani V. Sankar. A direct micromechanics method for analysis of failure initiation of plain weave textile composites. *Composites Science and Technology*, 66(1):137 – 150, 2006.

[15] Stephen W. Tsai and H. Thomas Hahn. *Introduction to composite materials*. Technomic Publishing Company, Inc., Lnacaster, PA, 1980.

[16] John Whitcomb and Kanthikannan Srirengan. Effect of various approximations on predicted progressive failure in plain weave composites. *Composite Structures*, 34(1):13 – 20, 1996.

[17] Shu Ching Quek, Anthony M. Waas, Khaled W. Shahwan, and Venkatesh Agaram. Analysis of 2d triaxial flat braided textile composites. *International Journal of Mechanical Sciences*, 45(6-7):1077 – 1096, 2003.

[18] Shu Ching Quek, Anthony Waas, Khaled W. Shahwan, and Venkatesh Agaram. Compressive response and failure of braided textile composites: Part 2–computations. *International Journal of Non-Linear Mechanics*, 39(4):649 – 663, 2004.

[19] R. Hill. A theory of the yielding and plastic flow of anisotropic metals. *Proceedings of the Royal Society of London. Series A, Mathematical and Physical Sciences*, 193(1033):pp. 281–297, 1948.

[20] N. Rabearison, Ch. Jochum, and J.C. Grandidier. A fem coupling model for properties prediction during the curing of an epoxy matrix. *Computational Materials Science*, 45(3):715 – 724, 2009. Proceedings of the 17th International Workshop on Computational Mechanics of Materials - IWCMM-17.

[21] T. J. Corden, I. A. Jones, D. T. Jones, and V. Middleton. The mechanisms of interlaminar cracking in thick resin transfer moulded composite cylinders. *Composites Part A: Applied Science and Manufacturing*, 29(4):455 – 464, 1998.

[22] A.R. Plepys and R.J. Farris. Evolution of residual stresses in three-dimensionally constrained epoxy resins. *Polymer*, 31(10):1932 – 1936, 1990.

[23] Yu. A. Chekanov, V. N. Korotkov, B. A. Rozenberg, E. A. Dhzavadyan, and L. M. Bogdanova. Cure shrinkage defects in epoxy resins. *Polymer*, 36(10):2013 – 2017, 1995.

[24] David A. Darrow and Lloyd V. Smith. Isolating Components of Processing Induced Warpage in Laminated Composites. *Journal of Composite Materials*, 36(21):2407–2419, 2002.

[25] G. Fernlund, N. Rahman, R. Courdji, M. Bresslauer, A. Poursartip, K. Willden, and K. Nelson. Experimental and numerical study of the effect of cure cycle, tool surface, geometry, and lay-up on the dimensional fidelity of autoclave-processed composite parts. *Composites Part A: Applied Science and Manufacturing*, 33(3):341 – 351, 2002.

[26] Carolyne Albert and Gran Fernlund. Spring-in and warpage of angled composite laminates. *Composites Science and Technology*, 62(14):1895 – 1912, 2002.

[27] Andrew Johnston, Reza Vaziri, and Anoush Poursartip. A Plane Strain Model for Process-Induced Deformation of Laminated Composite Structures. *Journal of Composite Materials*, 35(16):1435–1469, 2001.

[28] Jong Woon Kim, Ji Hyung Lee, Hyoung Geun Kim, Hak Sung Kim, and Dai Gil Lee. Reduction of residual stresses in thick-walled composite cylinders by smart cure cycle with cooling and reheating. *Composite Structures*, 75(1-4):261 – 266, 2006. Thirteenth International Conference on Composite Structures - ICCS/13.

[29] K.S. Kim and H.T. Hahn. Residual stress development during processing of graphite/epoxy composites. *Composites Science and Technology*, 36(2):121 – 132, 1989.

[30] S.R. White and H.T. Hahn. Cure Cycle Optimization for the Reduction of Processing-Induced Residual Stresses in Composite Materials. *Journal of Composite Materials*, 27(14):1352–1378, 1993.

[31] P. Shrotriya, N. R. Sottos, and A. F. Skipor. Residual Stress Development during Relamination of Woven Composite Circuit Boards. *Journal of Composite Materials*, 35(10):905–927, 2001.

[32] T.W. Capehart, Nouman Muhammad, and Hamid G. Kia. Compensating thermoset composite panel deformation using corrective molding. *Journal of Composite Materials*, 41(14):1675–1701, 2007.

[33] Musa R. Kamal. Thermoset characterization for moldability analysis. *Polymer Engineering and Science*, 14(3):231–239, 1974.

[34] Anthony Plepys, Menas S. Vratsanos, and Richard J. Farris. Determination of residual stresses using incremental linear elasticity. *Composite Structures*, 27(1-2):51 – 56, 1994. Special Issue Advances in Fiber Reinforced Composites Technology.

[35] Travis A. Bogetti and John W. Gillespie. Process-Induced Stress and Deformation in Thick-Section Thermoset Composite Laminates. *Journal of Composite Materials*, 26(5):626–660, 1992.

[36] D. B. Adolf, J. E. Martin, R. S. Chambers, S. N. Burchett, and T. R. Guess. Stresses during thermoset cure. *Journal of Materials Research*, 13:530–550, 1998.

[37] Douglas Adolf and Robert Chambers. Verification of the capability for quantitative stress prediction during epoxy cure. *Polymer*, 38:5481–5490, 1997.

[38] S.R. White and H.T. Hahn. Process Modeling of Composite Materials: Residual Stress Development during Cure. Part I. Model Formulation. *Journal of Composite Materials*, 26(16):2402–2422, 1992.

[39] Jakob Lange, Staffan Toll, Jan-Anders E. Mnson, and Anders Hult. Residual stress build-up in thermoset films cured above their ultimate glass transition temperature. *Polymer*, 36(16):3135 – 3141, 1995.

[40] Douglas B. Adolf and Robert S. Chambers. A thermodynamically consistent, nonlinear viscoelastic approach for modeling thermosets during cure. *Journal of Rheology*, 51(1):23–50, 2007.

[41] Douglas B. Adolf, Robert S. Chambers, and James M. Caruthers. Extensive validation of a thermodynamically consistent, nonlinear viscoelastic model for glassy polymers. *Polymer*, 45(13):4599 – 4621, 2004.

[42] Yuhai Mai, Albert F. Yee, Alna S. Wineman, and Chaodong Xiao. Streff evolution during thermoset cure. In *Material Research Society Symposia Proceedings*, volume 515, 1998.

[43] Yuhai Mei. *Stress Evolution in a Conductive Adhesive during Curing and Cooling*. PhD thesis, University of Michigan, Ann Arbor, Michigan, 2000.

[44] Min Li, Qi Zhu, Philippe H. Geubelle, and Charles L. Tucker III. Optimal curing for thermoset matrix composites: Thermochemical considerations. *Polymer Composites*, 22(1):118 – 131, 2001.

[45] Ajith K. Gopal, Sarp Adali, and Viktor E. Verijenko. Optimal temperature profiles for minimum residual stress in the cure process of polymer composites. *Composite Structures*, 48(1-3):99 – 106, 2000.

[46] Qi Zhu and Philippe H. Geubelle. Dimensional Accuracy of Thermoset Composites: Shape Optimization. *Journal of Composite Materials*, 36(6):647–672, 2002.

[47] Amit Salvi and Anthony M. Waas. Report to the Automotive Composite Consortium: Static and dynamic fracture of carbon fiber reinforced braided composites. Technical report, University of Michigan, January 2005.

[48] Chandra S. Yerramalli and Anthony M. Waas. In situ matrix shear response using torsional test data of fiber reinforced unidirectional polymer composites. *Journal of Engineering Materials and Technology*, 124(2):152–159, 2002.

[49] B. Ramakrishnan, L. Zhu, and R. Pitchumani. Curing of composites uning internal resistive heating. *Journal of Manufacturing Sciences and Egnieering*, 122:124–131, 2000.

[50] R. Shanku, J.G. Vaughan, and J.A. Roux. Rheological characteristics and cure kinetics of EPON 862/W epoxy used in pultrusion. *Advances in Polymer Technology*, 16(4):297–311, 1997.

[51] Daniel J. O'Brien and Scott R. White. Cure kinetics, gelation, and glass transition of bisphenol f epoxide. *Polymer Engineering and Science*, 43(4):863–874, 2003.

[52] De Xie and Anthony M. Waas. Discrete cohesive zone model for mixed-mode fracture using finite element analysis. *Engineering Fracture Mechanics*, 73(13):1783 – 1796, 2006.

[53] De Xie, Amit G. Salvi, Ce Sun, Anthony M. Waas, and Ari Caliskan. Discrete Cohesive Zone Model to Simulate Static Fracture in 2D Triaxially Braided Carbon Fiber Composites. *Journal of Composite Materials*, 40(22):2025–2046, 2006.

[54] J.-L. Chaboche. Continuous damage mechanics - a tool to describe phenomena before crack initiation. *Nuclear Engineering and Design*, 64(2):233–247, 1981.

[55] Simulia. *ABAQUS 6.9 manual*. Dassault Systems, 2009.

[56] Y.C. Fung. *A First Course in Continuum Mechanics*. Prentence Hall, Englewood Cliffs, 3 edition, 1994.

[57] Issam Doghri. *Mechanics of Deformable Solids*. Springer Verlag, Berlin, 2000.

[58] Michael Aldridge. Personal communication.

[59] K. E. Chike, M. L. Myrick, R. E. Lyon, and S. M. Angel. Raman and near-infrared studies of an epoxy resin. *Appl. Spectrosc.*, 47(10):1631–1635, 1993.

[60] L. Merad, M. Cochez, S. Margueron, F. Jauchem, M. Ferriol, B. Benyoucef, and P. Bourson. In-situ monitoring of the curing of epoxy resins by raman spectroscopy. *Polymer Testing*, 28(1):42 – 45, 2009.

[61] A. Yousefi, P. G. Lafleur, and R. Gauvin. Kinetic studies of thermoset cure reactions: A review. *Polymer Composites*, 18(2):157–168, 1997.

[62] The Mathworks. *Matlab R2009a*, 2009.

[63] Vikas Varshney, Soumya S Patnaik, Ajit K. Roy, and Barry L. Farmer. Molecular dynamics study of thermal transport phenomena in cross-linked polymer: Epon 862 with curing agent W (DETDA).

[64] Hexion Specialty Chemicals, Inc. Diglycidyl Ether of Bisphenol F (DGEBF) - Performance Properties.

[65] B. Garnier and A. Sommier. Thermal Property Measurements During Curing of Thermoset Resins Using Steady Periodic Conditions. *Journal of Reinforced Plastics and Composites*, 21(13):1193–1203, 2002.

[66] P. Bujard, G. Kuhnlein, S. Ino, and T. Shiobara. Thermal conductivity of molding compounds for plastic packaging. In *Electronic Components and Technology Conference, 1994. Proceedings., 44th*, pages 159 –163, May 1994.

[67] Junhua Wu and D.D.L Chung. Calorimetric study of the effect of carbon fillers on the curing of epoxy. *Carbon*, 42(14):3039 – 3042, 2004.

[68] Sabyasachi Ganguli, Ajit K. Roy, and David P. Anderson. Improved thermal conductivity for chemically functionalized exfoliated graphite/epoxy composites. *Carbon*, 46(5):806 – 817, 2008.

[69] J.A. Ramos, N. Pagani, C.C. Riccardi, J. Borrajo, S.N. Goyanes, and I. Mondragon. Cure kinetics and shrinkage model for epoxy-amine systems. *Polymer*, 46(10):3323 – 3328, 2005.

[70] Martin K. Beyer and Hauke Clausen-Schaumann. Mechanochemistry:the mechanical activation of covalent bonds. *Chemical Reviews*, 105:2921 – 2948, 2005.

[71] Naoto Ikegawa, Hiroyuki Hamada, and Zenichiro Maekawa. Effect of compression process on void behavior in structural resin transfer molding. *Polymer Engineering & Science*, 36(7):953–962, 1996.

[72] M. Revello, L. Saggese, and E. Gaiero. *Comprehensive Composite Materials*, chapter Compression Molding of SMCs, pages 763–805. Elsevier, Amsterdam, 2000.

[73] M. Hossain, G. Possart, and P. Steinmann. A small-strain model to simulate the curing of thermosets. *Computational Mechanics*, 43:769 – 779, 2009.

[74] Hiroshi Yamura, Mami Matsukawa, Takahiko Otani, and Norikazu Ohtori. Brillouin scattering study on the elastic properties of epoxy adhesive layer. *Japanese Journal of Applied Physics*, 38(Part 1, No. 5B):3175–3178, 1999.

[75] Daniel J. O'Brian, Patrick T. Mather, and Scott R. White. Viscoelastic properties of an epoxy resin during cure. *Journal of Composite Materials*, 35:883 – 904, 2001.

[76] Chun Li, Kevin Potter, Michael R. Wisnom, and Graeme Stringer. In-situ measurement of chemical shrinkage of my750 epoxy resin by a novel gravimetric method. *Composites Science and Technology*, 64(1):55 – 64, 2004.

[77] Jakob Lange, Staffan Toll, Jan-Anders E. Månson, and Anders Hult. Residual stress build-up in thermoset films cured below their ultimate glass transition temperature. *Polymer*, 38(4):809 – 815, 1997.

[78] B. Yates, B. A. McCalla, L. N. Phillips, D. M. Kingston-Lee, and K. F. Rogers. The thermal expansion of carbon fibre-reinforced plastics. *Journal of Materials Science*, 14:1207–1217, 1979. 10.1007/BF00561306.

[79] Amit Salvi. Personal communication.

[80] AGY. High strength glass fibers.

[81] Raghav Shrikant Kulkarni. Characterization of carbon fibers: Coefficient of thermal expansion and microstructure. Master's thesis, Texas A&M University, December 2004.

[82] Raghav Kulkarni and Ozden Ochoa. Transverse and Longitudinal CTE Measurements of Carbon Fibers and their Impact on Interfacial Residual Stresses in Composites. *Journal of Composite Materials*, 40(8):733–754, 2006.

[83] J. A. Barnes. Thermal expansion behaviour of thermoplastic composites. *Journal of Materials Science*, 28:4974–4982, 1993. 10.1007/BF00361164.

[84] Inc. Hexcel. Hextow im7 product data, March 2010.

[85] Jun Fukai, Yuichi Hamada, Yoshio Morozumi, and Osamu Miyatake. Improvement of thermal characteristics of latent heat thermal energy storage units using carbon-fiber brushes: experiments and modeling. *International Journal of Heat and Mass Transfer*, 46(23):4513 – 4525, 2003.

[86] Min Li and Charles L. Tucker. Modeling and simulation of two-dimensional consolidation for thermoset matrix composites. *Composites Part A: Applied Science and Manufacturing*, 33(6):877 – 892, 2002.

[87] Qi Zhu, Phillippe H. Geubelle, Min Li, and Charles L. Tucker III. Dimensional accuracy of thermoset composites: Simulation of process-induced residual stresses. *Jounal of Composite Materials*, 35(24):2171–2203, 2001.

[88] R. Hill. Theory of mechanical properties of fibre-strengthened materials: I. elastic behaviour. *Journal of the Mechanics and Physics of Solids*, 12(4):199 – 212, 1964.

[89] Jacob Aboudi. Micromechanical analysis of composites by the method of cells. *Applied Mechanics Reviews*, 42(7):193–221, 1989.

[90] M. Paley and J. Aboudi. Micromechanical analysis of composites by the generalized cells model. *Mechanics of Materials*, 14(2):127 – 139, 1992.

[91] Cecilia Grufman and Fernand Ellyin. Determining a representative volume element capturing the morphology of fibre reinforced polymer composites. *Composites Science and Technology*, 67(3-4):766 – 775, 2007.

[92] Cliff J. Lissenden, Steven M. Arnold, and Saiganesh K. Iyer. Flow/damage surfaces for fiber-reinforced metals having different periodic microstructures. *International Journal of Plasticity*, 16(9):1049 – 1074, 2000.

[93] J.R. Brockenbrough, S. Suresh, and H.A. Wienecke. Deformation of metal-matrix composites with continuous fibers: geometrical effects of fiber distribution and shape. *Acta Metallurgica et Materialia*, 39(5):735 – 752, 1991.

[94] Carlos Gonzlez and Javier LLorca. Mechanical behavior of unidirectional fiber-reinforced polymers under transverse compression: Microscopic mechanisms and modeling. *Composites Science and Technology*, 67(13):2795 – 2806, 2007.

[95] V. A. Buryachenko, N. J. Pagano, R. Y. Kim, and J. E. Spowart. Quantitative description and numerical simulation of random microstructures of composites and their effective elastic moduli. *International Journal of Solids and Structures*, 40(1):47 – 72, 2003.

[96] Somnath Ghosh, Zdzislaw Nowak, and Kyunghoon Lee. Quantitative characterization and modeling of composite microstructures by voronoi cells. *Acta Materialia*, 45(6):2215 – 2234, 1997.

[97] Andreas Rossoll, Benedikt Moser, and Andreas Mortensen. Longitudinal deformation of fibre reinforced metals: influence of fibre distribution on stiffness and flow stress. *Mechanics of Materials*, 37(1):1 – 17, 2005.

[98] C.Heinrich, M. Aldridge, A.S. Wineman, J. Kieffer, and A.M. Waas. The influence of fiber packing on the homogenized response of cured fiber composites. In *25th Annual Technical Conference American Society for Composites*, 2010.

[99] Andre Zaoui. Continuum micromechanics: Survey. *Journal of Engineering Mechanics*, 128(8):808–816, 2002.

[100] J.C. Simo and T.J.R. Hughes. *Computational Inelasticity*, volume 7 of *Interdisciplinary Applied Mathematics*. Springer, 2nd edition, 2000.

[101] ANSYS. *ANSYS 13.0*. ANSYS, Inc, 2011.

[102] Lazar Kachanov. Rupture time under creep conditions. *International Journal of Fracture*, 97:11–18, 1999. 10.1023/A:1018671022008.

[103] Y.N. Rabotnov. On the equations of state for creep. *Proceedings of the Institution of Mechanical Engineers, Conference Proceedings 1964-1970 (vols 178-184), Various titles labelled Volumes A to S*, pages 117–122.

[104] F.A. Leckie and D.R. Hayhurst. Constitutive equations for creep rupture. *Acta Metallurgica*, 25(9):1059 – 1070, 1977.

[105] Jean Lemaitre and Jean-Louis Chaboche. *Mechanics of Solid Materials*. Cambridge University Press, 1994.

[106] Jean Lemaitre. A continuous damage mechanics model for ductile fracture. *Journal of Engineering Materials and Technology*, 107(1):83–89, 1985.

[107] J.P. Cordebois and F. Sidoroff. Endommagement anisotrope en élasticité. *Journal de Méchanique Théorique et Apllicquée*, (Spécial):45–60, 1982.

[108] S. Nemat-Nasser and M. Hori. *Micromechanics: Overall Properties of Heterogeneous Materials*. North-Holland Series in Applied Mathematics and Mechanics. North Holland, 2 edition, January 1999.

[109] J.C. Simo and J.W. Ju. Strain- and stress-based continuum damage models–i. formulation. *International Journal of Solids and Structures*, 23(7):821 – 840, 1987.

[110] Francisco Armero and Sergio Oller. A general framework for continuum damage models. i. infinitesimal plastic damage models in stress space. *International Journal of Solids and Structures*, 37(48-50):7409 – 7436, 2000.

[111] Robert J. Dorgan and George Z. Voyiadjis. A Mixed Finite Element Implementation of a Gradient-enhanced Coupled Damage Plasticity Model. *International Journal of Damage Mechanics*, 15(3):201–235, 2006.

[112] Milan Jirásek and Zdeněk P. Bažant. *Inelastic Analysis of Structures*. John Wiley & Sons, Ltd, 2002.

[113] R. de Borst. Computation of post-bifurcation and post-failure behavior of strain-softening solids. *Computers & Structures*, 25(2):211 – 224, 1987.

[114] Robert J. Dorgan. *A nonlocal model for coupled damage-plasticity incorporating gradients of internal state variables at multiscales*. PhD thesis, Louisiana State University, Baton Rouge, Louisiana.

[115] St. Pietruszczak and Z. Mróz. Finite element analysis of deformation of strain-softening materials. *International Journal for Numerical Methods in Engineering*, 17:327–334, 1981.

[116] Zdeněk Bažant and B. Oh. Crack band theory for fracture of concrete. *Materials and Structures*, 16:155–177, 1983. 10.1007/BF02486267.

[117] Alberto Franchi and Francesco Genna. Self-adaptive model for structural softening of brittle materials. *Journal of Engineering Mechanics*, 115(7):1543–1558, 1989.

[118] J. Oliver. A consistent characteristic length for smeared cracking models. *International Journal for Numerical Methods in Engineering*, 28:461–474, 1989.

[119] A. Needleman. A continuum model for void nucleation by inclusion debonding. *Journal of Applied Mechanics*, 54(3):525–531, 1987.

[120] Viggo Tvergaard and John W. Hutchinson. The relation between crack growth resistance and fracture process parameters in elastic-plastic solids. *Journal of the Mechanics and Physics of Solids*, 40(6):1377 – 1397, 1992.

[121] René de Borst. Simulation of strain localization: A reappraisal of the cosserat continuum. *Engineering Computations*, 8:317–332, 1991.

[122] E. Cosserat and F. Cosserat. *Théore des corps déformables*. Harman, Paris, 1909.

[123] H. B. Mühlhaus. Application of cosserat theory in numerical solutions of limit load problems. *Archive of Applied Mechanics*, 59:124–137, 1989. 10.1007/BF00538366.

[124] R. H. J. Peerlings, M. G. D. Geers, R. de Borst, and W. A. M. Brekelmans. A critical comparison of nonlocal and gradient-enhanced softening continua. *International Journal of Solids and Structures*, 38(44-45):7723 – 7746, 2001.

[125] Zdeněk Bažant. Imbricate continuum and its variational derivation. *Journal of Engineering Mechanics*, 110:1693–1712, 1984.

[126] Gilles Pijaudier-Cabot and Zdeněk P. Bažant. Nonlocal damage theory. *Journal of Engineering Mechanics*, 113:1512–1533, 1987.

[127] H.-B. M˙ A variational principle for gradient plasticity. *International Journal of Solids and Structures*, 28(7):845 – 857, 1991.

[128] David Lasry and Ted Belytschko. Localization limiters in transient problems. *International Journal of Solids and Structures*, 24(6):581 – 597, 1988.

[129] R.H.J. Peerlings, R. de Borst, W. A. M. Brekelmans, and J. H. P. de Vree. Gradient enhanced damage for quasi-brittle materials. *International Journal for Numerical Methods in Engineering*, 39:3391–3403, 1996.

[130] Harm Askes, Jerzy Pamin, and Ren de Borst. Dispersion analysis and element-free galerkin solutions of second- and fourth-order gradient-enhanced damage models. *International Journal for Numerical Methods in Engineering*, 49, 2000.

[131] H. Askes and L. J. Sluys. Explicit and implicit gradient series in damage mechanics. *European Journal of Mechanics - A/Solids*, 21(3):379 – 390, 2002.

[132] M. G. D. Geers, R. L. J. M. Ubachs, and R. A. B. Engelen. Strongly non-local gradient-enhanced finite strain elastoplasticity. *International Journal for Numerical Methods in Engineering*, 56:2039–2068, 2003.

[133] Roy A. B. Engelen, Marc G. D. Geers, and Frank P. T. Baaijens. Nonlocal implicit gradient-enhanced elasto-plasticity for the modelling of softening behaviour. *International Journal of Plasticity*, 19(4):403 – 433, 2003.

[134] Noël Challamel. A variationally based nonlocal damage model to predict diffuse microcracking evolution. *International Journal of Mechanical Sciences*, 52(12):1783 – 1800, 2010.

[135] O. C. Zienkiewicz and Robert L. Taylor. *Finite Element Method for Solid and Structural Mechanics*. Elsevier, Burlington, Mass., 6 edition, 2005.

[136] R.A. Schapery. Mechanical characterization and analysis of inelastic composite laminates with growing damage. In *Proceedings of the Third ASCE/ASME Joint Mechanics Conference*, San Diego, July 1989.

[137] R.A. Schapery. A theory of mechanical behavior of elastic media with growing damage and other changes in structure. *Journal of the Mechanics and Physics of Solids*, 38(2):215 – 253, 1990.

[138] R.A. Schapery and S.L. Sicking. On nonlinear constitutive equations for elastic and viscoelastic composites with growing damage. In *Mechanical behavior of materials; invited papers presentet at the Seventh International Conference on Mechanical Behavior of Materials - ICM7*, 1995.

[139] Chenggang Chen, Ryan S. Justice, Dale W. Schaefer, and Jeffery W. Baur. Highly dispersed nanosilica-epoxy resins with enhanced mechanical properties. *Polymer*, 49(17):3805 – 3815, 2008.

[140] Suraj C. Zunjarrao and Raman P. Singh. Characterization of the fracture behavior of epoxy reinforced with nanometer and micrometer sized aluminum particles. *Composites Science and Technology*, 66(13):2296 – 2305, 2006.

[141] M. G. D. Geers, R. de Borst, W. A. M. Brekelmans, and R. H. J. Peerlings. Strain-based transient-gradient damage model for failure analyses. *Computer Methods in Applied Mechanics and Engineering*, 160(1-2):133 – 153, 1998.

[142] E. Riks. The application of newton's method to the problem of elastic stability. *Journal of Applied Mechanics*, 39(4):1060–1065, 1972.

[143] E. Riks. An incremental approach to the solution of snapping and buckling problems. *International Journal of Solids and Structures*, 15(7):529 – 551, 1979.

[144] C.D. Rudd. *ASM Handbook*, volume 21–Composites, chapter Resin transfer modling and strutural reaction injection molding, pages 493–500. ASM International, 2001.

[145] Jean-Michel Charrier. *Polymeric Materials and Processing*. Hanser Publishers, Munich, Vienna, New York, 1990.

[146] Wolfgang Beitz and Karl-Heinrich Grote. *DUBBEL - Taschenbuch für den Maschinenbau*. Springer, Berlin, 20 edition, 2001.

[147] Evan Pineda, Anthony Waas, Brett Bednarcyk, Craig Collier, and Phillip Yarrington. Progressive damage and failure modeling in notched laminated fiber reinforced composites. *International Journal of Fracture*, 158:125–143, 2009. 10.1007/s10704-009-9370-3.

[148] W C Oliver and G M Pharr. An improved technique for determining hardness and elastic modulus using load and displacement sensing indentation experiments. *Journal of Materials Research*, 7:1564 – 1583, 1992.

[149] Hsiang-Yung Yu and J. C. M. Li. Computer simulation of impression creep by the finite element method. *Journal of Materials Science*, 12(11):2214 – 2222.

[150] Bertil Storkers and Per-Lennart Larsson. On brinell and boussinesq indentation of creeping solids. *Journal of the Mechanics and Physics of Solids*, 42(2):307 – 332, 1994.

[151] M. Dao, N. Chollacoop, K. J. Van Vliet, T. A. Venkatesh, and S. Suresh. Computational modeling of the forward and reverse problems in instrumented sharp indentation. *Acta Materialia*, 49(19):3899 – 3918, 2001.

[152] N. Chollacoop, M. Dao, and S. Suresh. Depth-sensing instrumented indentation with dual sharp indenters. *Acta Materialia*, 51(13):3713 – 3729, 2003.

[153] E H Lee and J R M Radok. The contact problem for viscoelastic bodies. *Journal of Applied Mechanics*, 27:438 – 444, 1960.

[154] H. Lu, B. Wang, J. Ma, G. Huang, and H. Viswanathan. Measurement of creep compliance of solid polymers by nanoindentation. *Mechanics of Time-Dependent Materials*, 7(3):189–207.

[155] G. Huang and H. Lu. Measurements of two independent viscoelastic functions by nanoindentation. *Experimental Mechanics*, 47(1):87–98.

[156] L. Anand and N.M. Ames. On modeling the micro-indentation response of an amorphous polymer. *International Journal of Plasticity*, 22(6):1123 – 1170, 2006.

[157] Timothy C. Ovaert, Byung Ro Kim, and Jianjun Wang. Multi-parameter models of the viscoelastic/plastic mechanical properties of coatings via combined nanoindentation and non-linear finite element modeling. *Progress in Organic Coatings*, 47(3-4):312 – 323, 2003.

[158] Seung-Hwan Lee, Siqun Wang, George M. Pharr, and Haitao Xu. Evaluation of interphase properties in a cellulose fiber-reinforced polypropylene composite by nanoindentation and finite element analysis. *Composites Part A: Applied Science and Manufacturing*, 38(6):1517 – 1524, 2007.

[159] M. Qasmi, P. Delobelle, F. Richard, C. Brun, and M. Fromm. Viscoelastic mechanical properties determined by nanoindentation tests and its numerical modelling of polypropylene modified by he+ particle implantation and e- irradiation. *Progress in Organic Coatings*, 51(3):195 – 204, 2004.

[160] Fionn Dunne and Nick Petrinic. *Introduction to computatinal plasticity*. Oxford University Press, 2005.

[161] Alaxander Forrester, Adras Sobester, and Andy Keane. *Engineering Design via Surrogate Modelling: A Practical Guide*. Wiley, 2008.

[162] Nestor V. Queipo, Raphael T. Haftka, Wei Shyy, Tushar Goel, Rajkumar Vaidyanathan, and P. Kevin Tucker. Surrogate-based analysis and optimization. *Progress in Aerospace Sciences*, 41(1):1 – 28, 2005.

[163] Simulia. *Isight manual*. Dassault Systems, 2006.

[164] Søren N. Lophaven, Hans Brunn Nielen, and Jacob Sondergaard. Dace - a matlab kriging toolbox. Technical Report IMM-TR-2002-12, Informatics and Matehmatical Modelling - Technical Universtiy of Denmark, 2002.

[165] Søren N. Lophaven, Hans Brunn Nielen, and Jacob Sondergaard. Aspects of the matlab toolbox dace. Technical Report IMM-REP-2002-13, Informatics and Matehmatical Modelling - Technical Universtiy of Denmark, 2002.

[166] Donald R. Jones, Matthias Schonlau, and William J. Welch. Efficient global optimization of expensive black-box functions. *Journal of Global Optimization*, 13(4):455–492, 1998.

[167] Bryan Glaz, Peretz P. Friedmann, and Li Liu. Surrogate based optimization of helicopter rotor blades for vibration reduction in forward flight. *Structural and Multidisciplinary Optimization*, 35(4):341 – 363.

[168] Benjamin D. Jensen. Personal communication.

[169] Phil Attard. Measurement and interpretation of elastic and viscoelastic properties with the atomic force microscope. *Journal of Physics: Condensed Matter*, 19(47):473201 (33pp), 2007.

[170] C. Heinrich, A.M. Waas, and A.S. Wineman. Determination of material properties using nanoindentation and multiple indenter tips. *International Journal of Solids and Structures*, 46(2):364 – 376, 2009.

[171] K.-J. Bathe. *Finite Element Procedures*. Prentice-Hall, New Jersey, 1996.

[172] Tirupathi R. Chandrupatla and Ashok D. Belegundu. *Introduction to Finite Elements in Engineering*. Prentice-Hall, Inc., 3rd edition, 2002.